Exciton Localization and Diffusion in Low-Dimensional Nanostructures Formed on Non-Planar Substrates

THÈSE N^O 4070 (2008)

ÉCOLE POLYTECHNIQUE FÉDÉRALE DE LAUSANNE

POUR L'OBTENTION DU GRADE DE DOCTEUR ÈS SCIENCES

PAR

Nicolas MORET

ingénieur physicien diplômé EPF
de nationalité suisse et originaire de Ollon (VD)

acceptée sur proposition du jury:

Prof. R. Schaller, président du jury
Prof. E. Kapon, directeur de thèse
Prof. H. Akiyama, rapporteur
Prof. V. Savona, rapporteur
Prof. W. Wegscheider, rapporteur

EPFL

ÉCOLE POLYTECHNIQUE
FÉDÉRALE DE LAUSANNE

Suisse
2008

Résumé

Les puits quantiques, les fils quantiques, ainsi que les boîtes quantiques sont des hétérostructures à base de matériaux semiconducteurs dont les dimensions sont de l'ordre de quelques nanomètres. A cette échelle, leurs propriétés sont fixées par les lois de la mécanique quantique. Le grand intérêt pour ces *nanostructures* est motivé par des applications dans les domaines de l'électronique et de l'opto-électronique: les puits quantiques sont déjà largement utilisés dans des diodes et des lasers; les boîtes quantiques sont maintenant l'objet de nombreuses recherches grâce à la possibilité de contrôler précisément leur interaction avec la lumière. A mi-chemin entre puits et boîtes quantiques, les fils quantiques sont des structures dans lesquelles le déplacement des charges électriques est restreint à une seule dimension (1D). Ils ont bénéficié de moins de considération en raison des difficultés rencontrées pour fabriquer des structures homogènes dans lesquelles les propriétés électroniques et photoniques sont proches de systèmes 1D idéaux.

La *croissance épitaxiale* est une technique répandue pour la fabrication de nanostructures quantiques à base de semiconducteurs. Une de ses principales implémentations est l'épitaxie en phase gazeuse à partir de précurseurs organo-métalliques (Metalorganic vapor phase epitaxy, MOVPE), qui permet notamment d'utiliser des mécanismes d'*auto-organisation* pour contrôler la croissance d'une surface cristalline. Dans ce travail de thèse, nous mettons à profit ces phénomènes pour améliorer l'homogénéité de puits et de fils quantiques à base de GaAs et $Al_xGa_{1-x}As$.

Dans le cas des puits quantiques, nous avons étudié la croissance de structures $GaAs/Al_xGa_{1-x}As$ sur des *substrats vicinaux*. Ce terme désigne les substrats dont l'orientation s'écarte légèrement d'une direction cristallographique donnée, et à la surface desquels les plans atomiques sont discontinus. Nous avons montré que le mode de croissance est très sensible à l'angle de déviation initial. Cela nous a permis de créer plusieurs configurations de désordre à l'interface des puits quantiques. Nous avons notamment déterminé des conditions permettant de fabriquer des puits quantiques dont les propriétés optiques ont une qualité jusqu'alors inégalée pour des structures crues par MOVPE. De plus, en utilisant une technique d'attaque chimique sélective, nous avons pu relier l'étroite largeur spectrale des meilleurs puits à une morphologie particulière des interfaces. Cette morphologie consiste en un arrangement de la surface en terraces séparées par des marches mono-atomiques, et qui sont lisses à l'échelle de l'exciton.

Les fils quantiques que nous avons étudiés se forment lors de la déposition de couches de $Al_xGa_{1-x}As$ sur des substrats gravés de *sillons en V*. Un phénomène d'auto-organisation conduit à la formation d'une région quasi-1D au centre des sillons, avec une section caractéristique en forme de croissant. Ces structures pâtissent des importantes inhomogenéités de leurs interfaces le long de l'axe du fil. Nous nous sommes intéressés à la possibilité de réduire l'influence de ce désordre en diminuant la hauteur des barrières de potentiel qui confinent les porteurs. En ajustant de façon adéquate les paramètres de croissance pour des couches avec une faible teneur en aluminium, nous avons obtenu une importante réduction de la largeur spectrale de l'émission des fils.

Pour améliorer l'homogénéité des fils crus dans des sillons en V tout en maintenant un confinement important, nous avons également investigué l'opportunité de croître des fils quantiques sur des substrats vicinaux gravés. Nous avons mis en évidence une importante modification des vitesses de croissance sur les différentes facettes formant le fil, ainsi qu'une diminution significative de la largeur spectrale de l'émission du fil. Cette amélioration offre de nouvelles possibilités pour l'étude de phénomènes 1D.

Finalement, nous nous sommes interessés à la question de la *diffusion* des excitons dans les fils quantiques. Ce sujet a fait l'objet de nombreuses études théoriques, mais les données expérimentales sont rares. Nous présentons une étude systématique de la diffusion excitonique en fonction de la température du réseau cristallin. A l'aide de mesures résolues en temps, nous avons mis en évidence une activation de la diffusion à des températures de l'ordre de 50 K. Nos données suggèrent que les excitons sont localisés en dessous de cette température, et que la diffusion est limitée par la rugosité des interfaces de la structure.

En synthèse, cette thèse présente d'importants progrès relatifs aux propriétés optiques de puits et de fils quantiques crus par MOVPE. Pour les deux types de structures, nous avons obtenus des valeurs record de la largeur spectrale de l'émission. Comme indiqué par nos mesures de diffusion, la rugosité des interfaces est le facteur qui limite la mobilité des excitons à basse température. Toutefois, les mécanismes de croissance que nous avons mis en évidence peuvent être utilisés pour encore améliorer l'homogénéité des fils quantiques crus dans les sillons en V.

Mots-clés:

Semiconducteur, hétérostructure, GaAs, micro-processing, nanostructure, puits quantique, fil quantique, épitaxie, MOVPE, auto-organisation, substrat vicinal, désordre, localisation, diffusion, exciton, propriétés optiques, photoluminescence, photoluminescence résolue en temps.

Abstract

Quantum wells (QWs), quantum wires (QWRs) and quantum dots (QDs) are semi-conductor heterostructures with nanoscopic dimensions. At this length scale, their properties are governed by quantum mechanics. The interest in these *nanostructures* is motivated by applications in the domain of electronics and opto-electronics. QWs are widely used in diodes and lasers. QDs now attract much attention because of the ability to precisely tailor their interaction with light. With carrier dimensionality in between, QWRs have been less considered, partly because of their higher sensitivity to disorder and the difficulties in fabricating homogeneous structures approaching ideal electronic and photonic 1D systems.

The common technique for fabricating semiconductor quantum nanostructures is *epitaxial growth*. Metalorganic vapor phase epitaxy (MOVPE) is one of the major implementations of the epitaxial process. One of the exciting aspects of this technique is that one can make use of *self-organization* mechanisms to control the growth front of a crystalline surface. In this thesis, we make use of these phenomena to improve the homogeneity of $GaAs/Al_xGa_{1-x}As$ QWs and QWRs.

In the case of QWs, we investigated the growth of $GaAs/Al_xGa_{1-x}As$ structures on *vicinal substrates*. Discontinuities of the atomic planes are known to occur on the surface of such structures. We found that the growth mode is very sensitive to the initial miscut angle. It allowed us to create very different configurations of the disorder at the interfaces of QWs. In particular, we determined conditions for which the optical characteristics of QWs grown by MOVPE reached unprecedented quality. Moreover, by using a selective etching technique, we were able to correlate the narrow optical linewidth observed to a step-flow morphology of the hetero-interfaces. In that case, terraces are smooth over the length scale determined by the exciton radius.

The $GaAs/Al_xGa_{1-x}As$ QWRs that we studied are formed at the center of *V-grooves* patterned onto the substrate. A lateral self-ordering mechanism creates a quasi one-dimensional (1D) region with a crescent-shaped cross-section. These structures suffer from strong fluctuations of the interfaces along the QWR axis. We investigated the possibility of reducing the effects of this disorder by decreasing the potential height of the confining barriers. By properly adjusting the growth conditions to grow $Al_xGa_{1-x}As$ barriers with low Al concentration, we obtained a strongly reduced spectral linewidth of the emission. When the probed area is of the order of one micron, the spectral line

of the QWR decomposes into two main components, the origin of which are discussed.

To improve the homogeneity of V-groove QWRs while retaining a strong confinement, we also investigated the effect of growing these structures on vicinal patterned substrates. We evidenced a strong modification of the relative growth rates of the facets forming the QWRs and a narrower spectral linewidth for QWRs grown on substrates with a large miscut angle. This narrower linewidth offers new possibilities for the study of 1D physics.

Finally, we also addressed the question of *exciton diffusion* in QWRs. This subject has been at the center of important theoretical efforts, but experimental data have been scarce so far. We present a systematic study of the exciton diffusion as a function of the lattice temperature. Using a time-of-flight technique, we have evidenced an activation of the diffusion at intermediate temperatures ($\sim$50 K). We present data suggesting that excitons are localized below this temperature and that the diffusion is determined by interface roughness.

In summary, this thesis presents important improvements of the properties of QWs and QWRs grown by MOVPE. Record low spectral linewidths of the emission are obtained for both types of structures. Yet, diffusion measurements in QWRs indicate that the interface roughness is still the dominant factor in limiting the exciton mobility at low temperatures. The growth mechanisms that we evidenced offer new routes for further improvement of the homogeneity of V-groove QWRs.

Keywords:

Semiconductor, heterostructure, GaAs, micro-processing, nanostructure, quantum well, quantum wire, epitaxy, MOVPE, self-organization, vicinal substrate, disorder, localization, diffusion, exciton, optical properties, photoluminescence, time-resolved photoluminescence.

Contents

à Kozue

Chapter 1

Introduction

1.1 Nanotechnology

The reduction of the size of components, devices or of entire systems was initially motivated by benefits in integration, weight, power consumption and costs. Nanotechnologies are therefore natural contenders for markets challenged by the leitmotiv 'smaller, faster, cheaper'. On top of that, the size of some systems has been reduced so much that they are now subject to, and consequently make use of, different physical laws related to their nanoscale dimensions.

Nanotechnology has flooded markets as diverse as medical, textile, sustainable energy and consumer electronics, and their expansion should even accelerate in the near future [1]. Nanomaterials encompass a broad range of systems. Carbon nanotubes (CNT) are well known for their large catalog of outstanding properties. Liquid crystals have revolutionized our display devices and more generally an increasing number of devices make use of organic materials [2]. In the domain of life science, biological markers or drug delivery systems of extremely small dimensions are starting to be used clinically and even DNA is now engineered [3].

The improving ability to individually address nano-systems and to manipulate their properties is the driving force of the recent burst in nanotechnologies. The tools now available for the observation of nanosystems also strongly contribute to making them more concrete. Imaging technologies, such as confocal, electronic, or holographic microscopes, yield high-resolution structural information, and some of them even allow *in-situ* manipulation of nanostructures.

Fabrication technologies of nano-systems roughly split into two categories. *Bottom-up* approaches rely on the self-assembly of the system components. They are often assimilated to various schemes of chemical synthesis. *Top-down* methods start from large pieces of materials and reduce or transform them to form substructures. This path has been the one followed during the last 60 years in the pionneering domain of miniaturization: microelectronics [4].

Electronic circuits have now reached dimensions, which place them within the limits of the nanoworld. The width of the circuits produced by 2010 should be as small as 45 nm [5]. Yet the CMOS technology is close to reaching a limit and new paradigms have to be developed to maintain the technological development rate. Bottom-up approaches and/or the integration of systems of lower dimensionality are the choice alternatives that are currently investigated [6,7].

In the case of electronics, it could be envisioned to replace the motion of electrons by their tunneling across thin layers. That type of structures has been investigated for many years in the sister industry of opto-electronics. Although some contenders made out of organic materials exist, light emitting diodes and lasers are mainly based on semiconductor crystals, whose dimensions may correspond to only a few atomic layers.

1.2   Epitaxial growth

The production of semiconductor crystals has benefited from huge advances throughout the second part of the last century. A groundbreaking fabrication technique developed in the 60's, Molecular Beam Epitaxy (MBE), first allowed to grow crystals monolayer by monolayer. It triggered important progresses in fundamental solid-states physics and stimulated the transformation of laboratory curiosities into functional devices [8].

In MBE, elemental sources are evaporated at a controlled rate onto a heated substrate under ultra-high vacuum conditions. The ensuing crystal growth is epitaxial: the deposited layers reproduce the crystalline structure of the substrate. By modifying the sources, it becomes possible to *locally* change the composition of the crystal, thus modifying its properties. The most important *heterostructure* formed this way is the *quantum well* (QW): a thin layer of low bandgap material grown between two layers of higher bandgap material. In such a structure, the charge carriers are trapped in the central layer. If the latter is thin enough, comparable to the quantum mechanical wavelength of the particle, *quantum confinement* takes place.

Since the first demonstration of this effect in 1974 [9], the quality of the QW hetero-interfaces has been at the center of intense debates. Pioneers suggested that interfaces could be flat within one crystal monolayer (ML) [10]. Domains (referred to as *islands*) defined by such discrete ML variations could then be expected to translate into separated photoluminescence lines, with energy separation determined solely by the structure composition and dimensions. As a matter of fact, this model did not explain completely the experimental observations and the disorder at the interfaces was found to manifest itself over different length scales [11–14] and to result in complex features of the optical spectra.

Metalorganic Vapor Phase Epitaxy (MOVPE, also often referred to as MOCVD: Metalorganic Chemical Vapor Deposition) is the main alternative to MBE [15, 16]. The main difference lies in the fact that atoms are not directly evaporated onto the substrate, but delivered by the breaking of precursors in the vicinity of the substrate surface. MOVPE, then, does not require ultra-high vacuum and is preferred by the semiconductor industry for its lower cost and higher yield.

Yet MBE still sets the standard of growth quality of semiconductor heterostructures, as it is considered to produce smoother interfaces than MOVPE. MBE growth of high quality QWs usually relies on growth interruptions (G.I.) at the interfaces [17, 18]. The diffusion length of adatoms increases with increasing interruption time, which allows them to migrate toward more energetically stable sites and flatten the surface. However, the island size is ultimately limited by thermodynamics. Some results suggest that correlations between the interfaces might be lost during the G.I., which would then be detrimental to the structure quality [19, 20]. G.I. effects in MOVPE process are not as well characterized, as the gain in interface smoothness is often counterbalanced by an increased incorporation of impurities.

Many investigations have also aimed at unveiling the *mechanisms* underlying epitaxial growth [21–23]. They are better established for MBE than for MOVPE [24]; first because of the fewer stages involved in the MBE process and second because of the better in-situ diagnostic tools routinely used in that case.

1.3   Semiconductor quantum nanostructures

Beyond its fundamental interest as the experimental realization of a model quantum mechanical system, the quantum well structure rapidly found applications in opto-electronic devices. Scientists rapidly identified the interest of further confining the carriers in additional directions in order to form one-dimensional (1D) *quantum wires* (QWRs) and zero-dimensional *quantum dots* (QDs) [25]. The suppression of the motion in the confined directions imposes severe constraints on the kinetic energy of the particles and strongly modifies the density of states of the system. The effects of Coulomb interactions in those systems are also dramatically enhanced and appear to dominate many of their properties [26].

These particular properties can be turned into advantages to improve multiple characteristics of devices. For opto-electronic applications, from a *spectral* point of view, the optical transitions and the gain spectrum get narrower because of the sharper 1D and 0D density of states [27]. Polarization properties can also be controlled, which can be used in detectors or emitters [28, 29]. Recently, many-body effects have been exploited to produce entangled photons [30–33] and to control the light emission statistics, as in single photon sources [34, 35]. In addition, for lasers, the threshold *current* should be

reduced [36] and its dependence on temperature attenuated [37]. Finally the *dynamics* of these devices is also expected to be improved: higher modulation speeds are expected in lower dimensional structures.

One- and zero-dimensional systems have also been investigated for electronic applications. The former are natural channels to transport carriers and higher mobilities were predicted in relation to reduced elastic scattering [38], which promises faster speed and wider modulation bandwidth. Yet performances at room temperature are mainly determined by phonon interactions, and possible improvement in those conditions is more likely to be related to reduced signal-to-noise ratio [39]. As for QDs, their discrete energy levels are used in single electron transistors [40, 41].

Some of these properties are only improvements of those existing in 2D or bulk materials. They are not always linked to quantum effects but can simply arise from the reduced dimensions or the particular geometry of the systems. Yet, the control and engineering of quantum effects opens new fields of research in light-matter interaction, leading to new applications in quantum communication and quantum information [42, 43].

Many approaches were investigated to achieve experimental realizations of one- and zero dimensional semiconductor systems [44, 45]. The difficulty lies in achieving sufficiently small dimensions while keeping an overall homogeneity sufficient to distinguish between inhomogeneously broadened confined states. Top-down approaches include:
  - Creating an electrostatic confinement, either through gates deposited on the surface of hetero-junction by lithography [46, 47] or through ion-beam implantation [48];
  - Etching walls to laterally reduce the size of QWs [49] and possibly re-growing barriers around the structure;
  - Modifying the crystal potential with stressors [50, 51].

The control and reliability of epitaxy also motivated bottom-up methods, for example:
  - Growth of QWR lattices on vicinal [52, 53] or faceted [54] substrates;
  - Growth of *nanowires* on masked or catalyzed substrates [55, 56];
  - Overgrowth on a cleaved edge of a QW structure [57];
  - Strain induced self-ordering [58];
  - Stranski-Kastranov growth of QDs, which also relies on strain [59].

The mixed approach developed in our group combines the advantages of the lithographic control of the nanostructure position and of the bangap engineering allowed by epitaxy. In a first step, the substrates are processed to create pyramidal recesses or V-shaped grooves. The subsequent MOVPE growth of (In)GaAs/AlGaAs layers on such non-planar substrates is designed to form nanostructures with self-limited interfaces and potential barriers of tunable height. QDs [60] and vertical QWRs (VQWRs) [61] are formed in the center of the pyramids, whereas QWRs are obtained after growth

on V-groove substrates. QDs and QWRs are surrounded by structures of higher dimensionality (Fig. 1.1), which also play important roles in the confinement of the carriers [62].
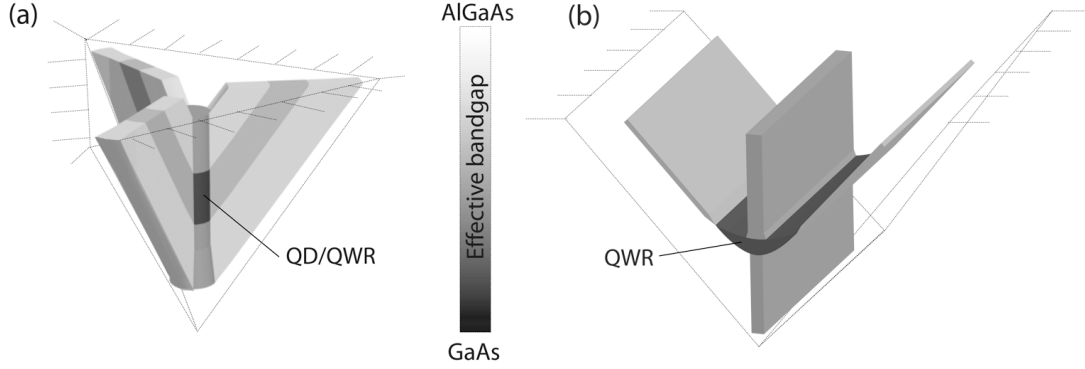
Figure 1.1: Schematic view of nanostructures grown in pyramidal recess (a) or V-groove (b). The QWR corresponds to the region of lowest effective bandgap (i.e. accounting for the confinement energy) and are surrounded by barriers, which height and dimensionality vary. In the first case (a) reducing the thickness of the QWR results in a QD.

VQWRs are useful systems to probe dimensional effects of confinement [63] and the coupling between structures. V-groove QWRs, which can be stacked to achieve large densities and whose length is in principle only limited by the substrate size, are preferred for transport studies [64, 65] or integration into devices [66, 67]. Nevertheless, their homogeneity is not yet sufficiently controlled, and their properties correspond in many aspects to chains of QDs.

1.4 Physics of one-dimensional systems

A characteristic landmark of 1D systems is their peaked, singular density of states decaying as $E^{-1/2}$. Yet, beyond this characteristic, the specificities of many physical phenomena mainly stem from the modified interactions among particles in 1D systems [68]. For electronic systems, it is manifested in the collective behavior of a *Luttinger liquid*. For electron-hole pairs, the Coulomb interaction is enhanced; it results in strongly bound *excitonic* states at energies below the free carriers continuum.

As for the optical features, excitons govern many of the properties of 1D systems. Yet, it is often hard to distinguish them from QD states. Only few systems exhibited clear 1D quantum behavior. Some convincing results were obtained on organic semiconductors. The luminescence of a rather long polymer chain ($\sim 10\mu m$) exhibited very small inhomogeneous broadening and fast charge transport [69]. Even more striking was the observation of macroscopic coherence across such samples [70].

Nevertheless, some significant results were also reported in 1D crystalline semiconductor nanostructures. Most of them were obtained on two class of systems already mentioned: the T-shape QWRs obtained by the MBE cleaved-edge overgrowth technique [57] and the crescent-shape QWRs grown, usually by MOVPE, on substrates patterned with V-grooves [45]. These systems have the advantage of being easily doped, or even better, to allow the control of the charge density through Schottky contacts [53, 71].

Optical spectroscopy measurements on T-shape QWRs benefit from the high spatial homogeneity obtained by MBE and a specific annealing procedure [72]. It allowed to resolve states from the 1D continuum [73, 74], as well as the singular density of states of 1D systems [75]. Nevertheless, the first observation of the intrinsic optical anisotropy of 1D systems was reported from V-groove QWRs [76], as well as was the first QWR laser in 1989 [77].

Since then, the debate on the nature of optical gain in 1D semiconductor has been lively [57, 78–80], and linked to the controversy around an hypothetic Mott transition in 1D systems [81–83]. The latest results tend to show that such a transition does not exist, but that instead there is a continuous transition from excitons toward an electron-hole plasma, mediated by exciton complexes. The actual existence of a bandgap renormalization (BGR) is also an open question, as it seems to be exactly cancelled by a reduction of the exciton binding energy [81, 84, 85].

The observation of excitonic complexes (excitons charged negatively [71, 86] and positively [86] and biexcitons [57, 82, 87]) in QWRs has been reported in the last few years. But the disorder of the structure was shown to have a major effect on their stability [87, 88]. Actually, disorder acts on most of the optical features measured in 1D systems; namely, the broadening of the density of states, the exciton lifetime [81, 89, 90] or relaxation [91–93] are all strongly affected by disorder.

One-dimensional transport is the subject of sustained activities, which address in particular systems in the ballistic regime. It is motivated by evident applications in electronic devices, but transport measurements have unveiled intriguing phenomena, in particular the quantization of the electrical conductance [94], which can now be studied in high-quality 1D systems [95] among which are the V-groove QWRs [64, 65]. Nevertheless, the transport properties of QWRs [95–97] are also altered by disorder, and the specificities of 1D motion have been only observed in the ballistic regime, but not yet in the diffusive one.

1.5 Thesis goal and outline

The global uniformity of V-groove QWRs is presently insufficient: fluctuations of the potential along the QWR direction localize charge carriers and prevent them from ex-

hibiting true 1D behavior. Improved samples showing properties closer to 1D have been recently reported [98], but the progress in the fabrication of the structure relies essentially on the processing steps. Obtaining similar improvement directly during the growth, by better mastering it, would be more efficient in terms of yield and reproducibility.

Improving the quality of V-groove QWRs demands a deeper understanding of both the growth processes and of the effects of the resulting disorder on the optical properties. Yet, the task is complex because the interfaces of this system are formed by several facets of different crystalline orientations, presenting very different characteristics.

It is the goal of this thesis to better understand the formation mechanism of disorder, and its effect on the optical properties of GaAs/AlGaAs heterostructures (QW and V-groove QWRs), in order to better control it.

Chapter 2 is a general introduction to GaAs/AlGaAs quantum nanostructures. It explains how Coulomb interactions and disorder modify the ideal picture of low-dimensional systems and affect their optical and transport properties. Several reviews have been published [99–101], and are good complements to the overview presented in this chapter.

In chapter 3, we describe the process of epitaxy, and the procedure followed for the sample fabrication. We briefly describe the experimental techniques: atomic force microscopy and optical spectroscopies.

Chapter 4 reports the study of QWs as model systems to better understand the relation between growth mechanism, sample morphology and optical properties. In particular, we show the topmost utility of vicinal surfaces to control disorder.

A the beginning of chapter 5, we first present state of the art V-groove QWRs, affected by disorder, and investigate routes toward disorder control. Here also, QWRs grown on vicinal substrates are shown to be promising candidates.

Finally, chapter 6 addresses the transition from localization to delocalization of V-groove QWR excitons, principally through diffusion measurements.

The last chapter (7) reviews what has been achieved and makes proposals for further investigations.

Chapter 2

Theory of GaAs semiconductor nanostructures

This chapter presents an overview of the physical properties of semiconductor nanostructures. Although the physics and methods presented below are more general, the discussion is focused on systems based on $Al_xGa_{1-x}As$ materials (Sec. 2.1). These systems hold an important position for practical applications and fundamental research purpose. The theory presented is directly related to the structures studied in this thesis, which are all GaAs/AlGaAs heterostructures.

We describe the theoretical framework used in the study of those nanostructures, with an accent on the effects of confinement. After introducing the characteristics of ideal structures (Sec. 2.2), we discuss the modifications due to the disorder inherent to real systems (Sec. 2.3).

2.1 GaAs / AlGaAs crystal

Gallium (Ga) and Aluminum (Al) are chemical elements with three valence electrons, thus belonging to the column III of the periodic table of elements. With five valence electrons, Arsenic (As) takes place in the column V. The (Al)GaAs compounds then belong to the so-called III/V class of semiconductor crystals. This section reviews some of its properties.

2.1.1 Crystallography

GaAs crystals usually form in the zinc blende structure. Each group of atoms forms a face-centered cubic lattice of parameter a (= 5.653 Å) and they are displaced one from another by $a/4$ along the cube diagonal. This structure is schematized in Fig. 2.1 with the indication of the main crystallographic directions.

Fig. 2.1 also highlights some atomic planes of particular importance. The [001] axis corresponds to the usual growth direction during epitaxy. Most of the crystal properties are usually referred relatively to this direction. Two adjacent (001) layers of the same element are separated by a distance $a/2 = 2.83$ Å, which is referred to as the crystal monolayer (ML) thickness. The planes orthogonal to the [111] direction also play a determinant role in our studies, as they also serve as parts of the templates for the growth of nanostructures. In particular, they have different physical properties depending on their termination, which can be A (Ga) or B (As).
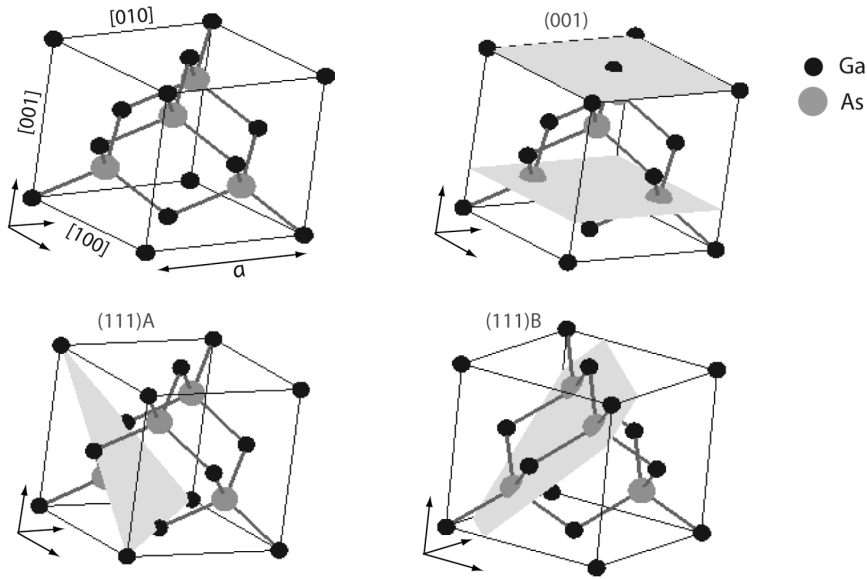
Figure 2.1: Zinc blende structure of GaAs, with the main crystallographic directions and the lattice parameter a. Some of the principal planes are also drawn.

By substituying a fraction x of the Ga atoms by Al atoms, a ternary alloy is obtained: $Al_xGa_{1-x}As$. The lattice parameter of $Al_xGa_{1-x}As$ only weakly depends on x ($a = 5.660$ Å for x = 1). The physical properties of the $Al_xGa_{1-x}As$ alloy, in particular its band structure, are slightly modified compared to those of GaAs. Yet, these slight modifications may have dramatic effects on the electronic and optical properties of the crystal.

2.1.2   Band Structure

The valence electrons of each atom constituent of a crystal are shared through covalent bonds. Their motion can be regarded relatively to a fixed potential $V(\mathbf{r})$ determined by the static ions of the crystal and their electronic clouds. The Schrödinger equation describing the motion of these electrons reads:

$$-\frac{\hbar^2}{2m}\nabla^2\psi_n(\mathbf{k},\mathbf{r}) + V(\mathbf{r})\psi_n(\mathbf{k},\mathbf{r}) = E_{n,k}\psi_n(\mathbf{k},\mathbf{r}) \qquad (2.1)$$

The wavefunction can be written as a product, $\psi_n(\mathbf{k}, \mathbf{r}) = u_n(\mathbf{k}, \mathbf{r}) \cdot e^{i\mathbf{kr}}$, in which the function u_n has the periodicity of the lattice and is known as a Bloch function. Eq. 2.1 can be solved analytically for $k = 0$, but more sophisticated approaches have to be used to compute the solutions in k-space. The *tight-binding* model allows to get a rather intuitive idea of the solutions. If one considers that electrons are tightly bound to the ions, their states are affected by the overlaps with the wavefunctions of electrons on adjacent lattice sites, which result in a splitting into bonding and anti-bonding states. When considering the whole crystal, these states assemble into bands: the one corresponding to the bonding states is the *valence band* (VB) and is fully occupied, whereas the anti-bonding states (the *conduction band*, CB) are empty. No states are available in between, forming a *bandgap*, which energy is of the order of 1 eV in the case of III-V semiconductors. The bandgap energy depends on temperature and for GaAs follows Eq. 2.2:

$$E(T) = E(0) - 5.4 \cdot 10^{-4} \frac{T^2}{204 + T} \tag{2.2}$$

The band structure of GaAs is depicted in Fig. 2.2(a) [102]. It depends on the crystal direction through the Bloch functions, and is represented along various k-space directions in the figure. The minimum of the CB is at the so-called Γ-point, and coincides with the VB maximum, which makes GaAs a *direct* semiconductor. Around this extrema corresponding to $k = 0$, the dispersion $E(k)$ is nearly parabolic. It is generally approximated by: $E = \frac{\hbar^2 k^2}{2m_{e,h}}$, where m_e (m_h) are *effective masses* for CB (VB) electrons (holes).
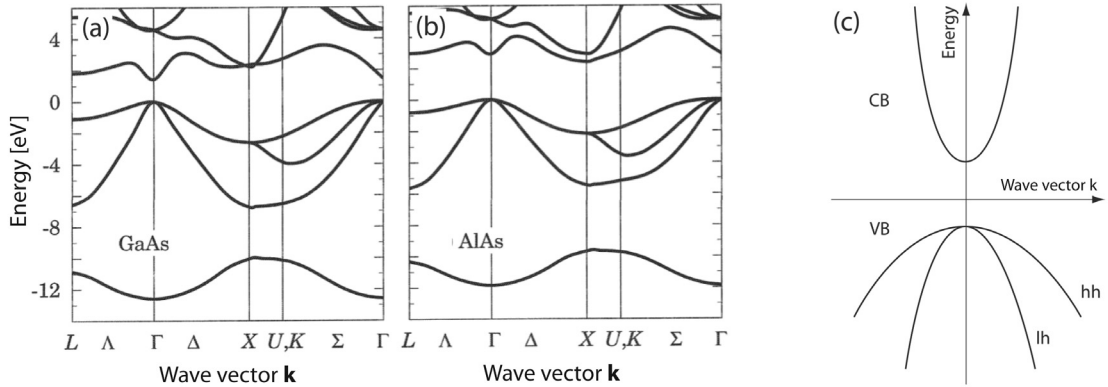
Figure 2.2: First Brillouin zone band structure of (a) GaAs and (b) AlAs, from Ref. [102]. (c) Simplified model around the Γ-point, for small k. The bands are approximated by parabola, and limited to heavy (hh) and light (lh) holes contributions in the valence band.

The calculation of more exact solutions $E(k)$ requires demanding methods, in particular for the VB states. Solutions in the vicinity of $k = 0$ are usually obtained by a perturbative treatment of the Schrödinger equation (the $\mathbf{k} \cdot \mathbf{p}$ method). Sophisticated approaches have yet to be employed for the VB states, which are degenerate at $k = 0$. These states are labeled by their angular momentum $\boldsymbol{J}$ and its component along a given direction J_z. The states $(|\|\boldsymbol{J}\|; J_z\rangle)$ $|3/2; \pm 3/2\rangle$ are called *heavy hole* (hh) states due to

Bandgap	$E(x) = 1.5194 + 1.36 \, x + 0.22 \, x^2 \; [eV]$
Dielectric constant	$\epsilon = 12.9 - 2.84 \, x \; [\epsilon_0]$
Effective masses	$m_e = 0.067 + 0.083 \, x$
	$m_{hh} = 0.62 + 0.14 \, x$
	$m_{lh} = 0.087 + 0.063 \, x$

Table 2.1: Dependence of some $Al_x Ga_{1-x}As$ parameters on the aluminium content x. From Ref. [103, 104]

the small curvature of the band that they form, whereas the states $|3/2; \pm 1/2\rangle$ are *light hole* (*lh*) states. Their degeneracy is accounted for in the Luttinger formalism that expresses their coupling and allows to define the effective masses through the so-called *Luttinger parameters*.

Most of the interest in the band structure lies in the vicinity of $k = 0$, in particular because optical transitions occur between these states. The two *hh* and *lh* valence bands and the conduction band are then the three most important bands, and other contributions can often be neglected. This simplified model of band structure is represented in Fig. 2.2(c).

The band structure of the $Al_x Ga_{1-x}As$ alloy is modified, as illustrated by the extreme case of AlAs ($x = 1$) in Fig. 2.2(b). The CB minimum here lies at the X-point, and does not coincide with the VB maximum anymore. This semiconductor is therefore *indirect*; in fact, $Al_x Ga_{1-x}As$ alloys with $x > 0.42$ are indirect. States corresponding to the bottom of the X band are optically inactive as they cannot recombine without involving other interaction to carry out their excess momentum. Indirect materials will not be considered further in this thesis. The dependence of some of their properties on the Al content x are given in Table 2.1.

2.2 Ideal quantum nanostructures

2.2.1 Heterostructures

Techniques of crystal growth (Sec. 3.1) allow to spatially change the characteristics of a crystal. One of the first examples realized was the p-n homojunction (Fig. 2.3(a)): part of the atoms in the crystal are replaced by impurities, which release excess charge carriers. By controlling the type of impurity, the material can be n- (electrons in excess) or p-doped (electron vacancies, or holes). At an interface between the two types of materials, the charge distribution is rearranged and creates an internal electric field used for instance in diodes or photovoltaïc cells.

Assembling semiconductors with different bandgaps allows to further control the
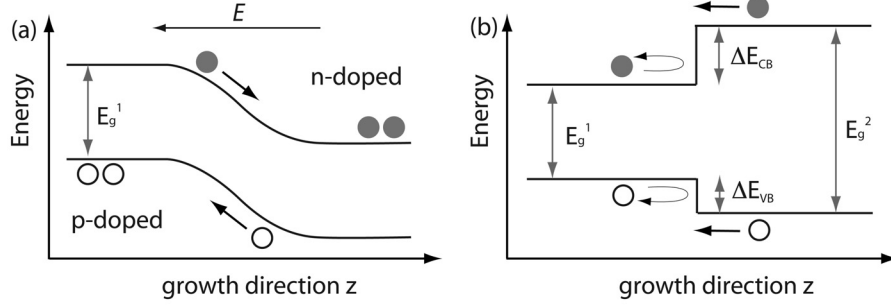
Figure 2.3: Schematic band structure of (a) a p-n homojunction, with the electric field **E** created at the interface; (b) an heterojunction.

charge flow and distribution. The bandgap mismatch is distributed between the CB and the VB (in the ratio $\Delta E_{VB}/\Delta E_{CB} \simeq 32/68$ for $Al_xGa_{1-x}As$ systems). Electrons and holes then encounter potential discontinuities at the material interfaces (Fig. 2.3(b)). This is a situation identical to the textbook examples of particles facing potential barriers (see for example Ref. [105]).

2.2.1.1 Confinement

Assembling two inverted heterojunctions creates potential wells, in which carriers are trapped. Quantum confinement occurs when the *width* of such a well approaches the De Broglie wavelength ($\lambda^{th} \approx \sqrt{\frac{2\pi\hbar^2}{m_{e,h}k_BT}}$). In semiconductor, it is of the order of a few nanometers ($\simeq 25$ nm in GaAs at room temperature), because of the small effective mass of electrons. If the width of the potential well is comparable to λ^{th}, the CB and VB split into separated energy surfaces in **k**-space. In that case, the Schrödinger equation reads:

$$-\frac{\hbar^2}{2}\nabla\frac{1}{m_{e,h}(z)}\nabla\psi_n(\mathbf{k},\mathbf{r}) + \widetilde{U}(\mathbf{r})\psi_n(\mathbf{k},\mathbf{r}) = E_{n,k}\psi_n(\mathbf{k},\mathbf{r}) \qquad (2.3)$$

The potential $\widetilde{U}(\mathbf{r}) = V(\mathbf{r}) + U(z)$ includes a component $U(z)$ due to the bandgap mismatch. The effective mass $m_{e,h}(z)$ also becomes dependent on the coordinate z of the confined direction. The slowly varying Bloch functions can be considered identical in the various materials and the wave function can therefore be written as $\psi(\mathbf{k},\mathbf{r}) = u(\mathbf{k},\mathbf{r})\,\chi(z)$. The function $\chi(z)$ is the *envelope function* of the state. The Bloch functions can be factored out of the Schrödinger equation to yield:

$$-\frac{\hbar^2}{2}\nabla\frac{1}{m_{e,h}(z)}\nabla\chi_n(z) + U(z)\chi_n(z) = E_{n,0}\chi_n(z) \qquad (2.4)$$

For infinitely high barriers, the energy of the nth electronic state confined in a rectangular well of width L_z is given by:

$$E_{n,0} = n^2\frac{\pi^2\hbar^2}{2m_eL_z{}^2} \qquad (2D) \qquad (2.5)$$

The electron may have some kinetic energy in the QW plane, corresponding to $E_{kin}^{2D} = \frac{\hbar^2(k_x^2+k_y^2)}{2m_{e,h}}$, in the effective mass approximation.
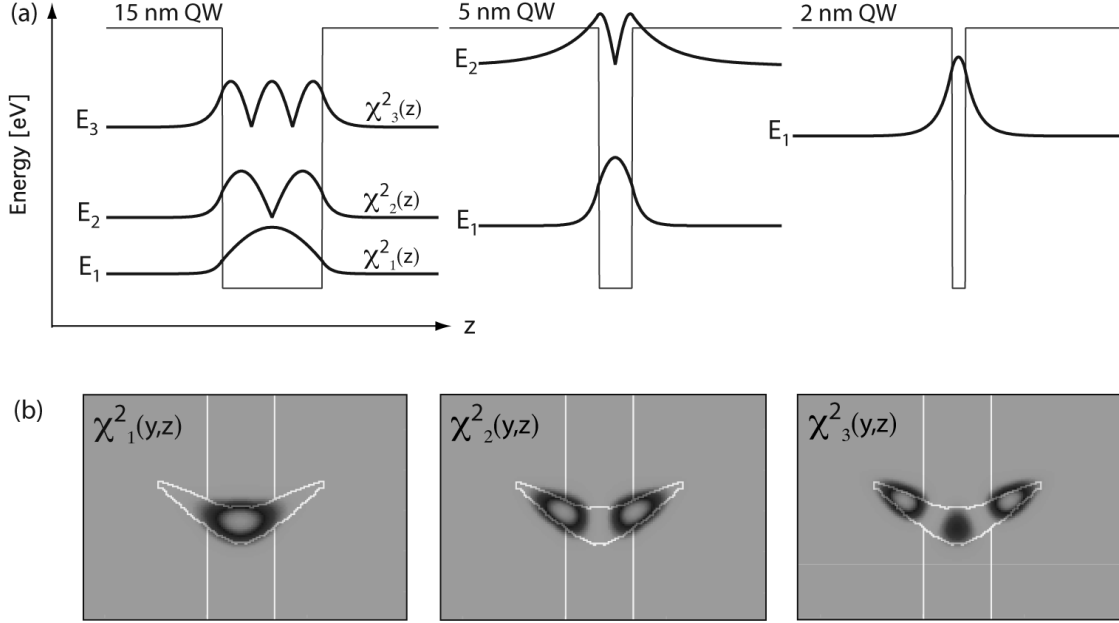
Figure 2.4: Density of probability of electrons confined in GaAs (a) QWs of different thicknesses; (b) crescent-shaped QWR.

The *dimensionality* of the system can be further reduced by confining the particles in additional directions. The *quantum wires* (QWR) and *quantum dots* (QD), which are thus created correspond to one- or zero-dimensional systems. The same kind of decompositions apply and the confinement energy for $k = 0$ electrons confined by infinite barriers reads:

$$E_{n_y,n_z} = \frac{\pi^2\hbar^2}{2m_e}\left(\frac{n_y^2}{L_y{}^2} + \frac{n_z^2}{L_z{}^2}\right) \qquad (1D) \qquad (2.6)$$

$$E_{n_x,n_y,n_z} = \frac{\pi^2\hbar^2}{2m_e}\left(\frac{n_x^2}{L_x{}^2} + \frac{n_y^2}{L_y{}^2} + \frac{n_z^2}{L_z{}^2}\right) \qquad (0D) \qquad (2.7)$$

An electron in a QWR still has one degree of liberty, with a corresponding kinetic energy $E_{kin}^{1D} = \frac{\hbar^2(k_x^2)}{2m_e}$. In a QD the k-space dispersion disappears because all spatial degrees of freedom are lifted.

The decomposition of the wavefunction into a product of an envelope function and a Bloch function can be generalized to states of different dimensionalities and to the valence band states. In the latter case, the coupling between the bands has to be taken into consideration. The spin m_s induces a degeneracy. The general expressions for the

CB wavefunction $\psi_{m_s}^e$ and VB wavefunction ψ^h are [106]:

$$\psi_{m_s}^e(\mathbf{r}) = \chi^e(z)\,u_{m_s}^e(x,y) \qquad \text{with } m_s = \pm\frac{1}{2} \tag{2.8}$$

$$\psi^h(\mathbf{r}) = \sum_{m_j} \chi_{m_j}^h(z)\,u_{m_j}^h(x,y) \qquad \text{with } m_j = \pm\frac{3}{2}, \pm\frac{1}{2} \tag{2.9}$$

In Ch. 5 we compute the wavefunctions and energy levels of our experimental QWR structures. In order to do so, we solve a 1D Schrödinger equation similar to Eq. 2.4 to obtain the envelope functions χ^e and χ^h and the single particle energies, with a 4x4 Luttinger hamiltonian to describe VB states and a parabolic CB for electrons [107]. The potential $U(y,z)$ is defined using a TEM image of the QWR cross-section[1].

2.2.1.2 Density of states

An important quantity deriving from the above considerations is the density of states (DOS), which depends critically on the dimensionality. It corresponds to the number of solutions to the Eq. 2.3 corresponding to an eigenvalue (energy) E. From bulk (3D) to QD (0D), they are given by:

$$\rho_{3D} = \frac{m}{\pi^2\hbar^3}\sqrt{2mE} \tag{2.10}$$

$$\rho_{2D} = \frac{m}{\pi\hbar^2\,L_z}\sum_{n_z}\theta(E-E_{n_z}) \tag{2.11}$$

$$\rho_{1D} = \frac{\sqrt{2m}}{\pi\hbar\,L_yL_z}\sum_{n_y,n_z}\sqrt{\frac{1}{E-E_{n_y,n_z}}} \tag{2.12}$$

$$\rho_{0D} = \frac{2}{L_xL_yL_z}\sum_{n_x,n_y,n_z}\delta(E-E_{n_x,n_y,n_z}) \tag{2.13}$$

The DOS corresponding to the different dimensionalities are represented in Fig. 2.5 and compared to the bulk case.

In QWs, the degeneracy of hh and lh is lifted. At $k \neq 0$, the heavy and light characters are mixed, which adds complications to the ideally staircase-like DOS of Fig. 2.5.
The DOS of QWRs is strongly peaked and decays characteristically as $1/\sqrt{E}$. From this shape follow many specificities of QWRs, discussed later. In contrast to QWs, heavy and light hole subbands are mixed even for $k = 0$. It is therefore not possible to ascribe a pure character to holes in a QWR due to the coupling between the bands [108].
The δ-like DOS allows QDs to accomodate only two carriers of opposite spins on an energy level, which makes them similar to atoms. They are thus often referred to as

---

[1]The solutions are calculated with a finite differences method, using a program written by Dr F. Karlsson, now at Linköping University, Sweden.
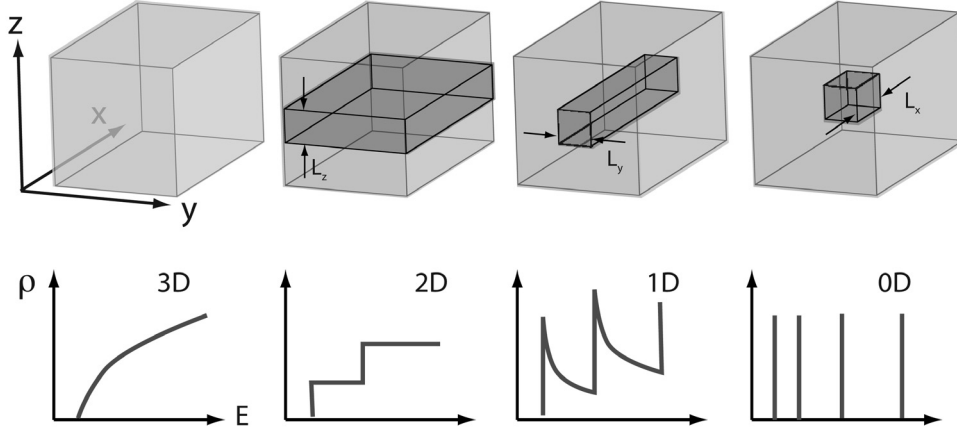
Figure 2.5: Bulk material and heterostructures of different dimensionalities, and the corresponding densities of states.

'artificial atoms'.

At thermal equilibrium, the occupation of the available states is described by a Fermi distribution:

$$f_{Fermi}(E) = \frac{1}{1 + e^{-\frac{E_F - E}{k_B T}}} \tag{2.14}$$

The Fermi level E_F is the energy of the highest occupied level at T = 0. At finite temperatures, the thermal energy allows the occupation (vacancy) of higher (lower) energy states of the CB.

For low carrier densities, the carrier distribution is well described by the sole decaying tail, i.e.: the Boltzman distribution:

$$f_{Boltz}(E) \sim e^{\frac{-E}{k_B T}} \tag{2.15}$$

2.2.2   Coulomb interactions

Considering electrons and holes independently is reductive as it does not account for the Coulomb interaction between the electrons (or between electron and holes). When these correlations are sufficiently strong, electrons and holes are bound and may be considered as a single, composite particle: an *exciton*. It is described by the following Hamiltonian:

$$H_X = H_e + H_h + H_{Coul} \qquad with \qquad H_{Coul} = \frac{-e^2}{4\pi\epsilon|\mathbf{r_e} - \mathbf{r_h}|} \tag{2.16}$$

$H_{e,h}$ are the single-particle hamiltonians as those entering Eq. 2.3, and $|\mathbf{r_e} - \mathbf{r_h}|$ is the relative separation of the electron and the hole. The large value of the dielectric

constant in bulk GaAs ($\epsilon = 12.9$) induces a relatively small binding energy E_B: 4.9 meV [26]. Correspondingly, the exciton Bohr radius a_B, representing the extension of the bound complex, is about 12 nm, therefore larger than the crystal lattice. Such excitons are referred to as Wannier excitons, in contrast to Frenkel excitons, which are found in organic systems and exhibit large ($\sim$1 eV) binding energies.
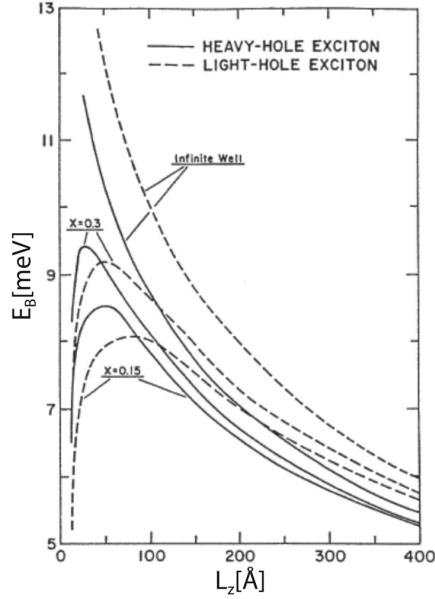
Figure 2.6: Variation of the binding energies of ground states of heavy (solid) and light (dashed) hole excitons as a function of the QW width L_z for different Al concentration x in the barriers. From Ref. [109].

In low-dimensional structures, the confinement constrains the relative positions of electrons and holes. Electrostatic screening is less effective, and the effective dielectric constant is reduced. As a result, the binding energy is increased. Fig. 2.6 gives calculated values of the binding energy E_B as a function of the QW width for heavy and light holes and for different potential barriers. The binding energy increases with the confinement; the lh-excitons have a slightly larger binding energy than hh-excitons and E_B increases also with increasing barrier height [110]. Assuming that the confinement is strong enough, the Coulomb interaction can be neglected in the confinement direction, and the single particle envelope functions $\chi^{e,h}(z_{e,h})$ can be used to decompose the exciton wavefunction:

$$\Phi_X(\mathbf{r_e}, \mathbf{r_h}) = \chi^e(z_e)\,\chi^h(z_h)\,\phi(\boldsymbol{\varrho_e}, \boldsymbol{\varrho_h}) \tag{2.17}$$

The function ϕ describes the in-plane motion of electron and hole in terms of in-plane coordinates $\boldsymbol{\varrho_{e,h}}$. The in-plane wavefunction $\phi(\boldsymbol{\varrho_e}, \boldsymbol{\varrho_h})$ than obeys a single-particle Schrödinger equation with an effective excitonic potential U_X:

$$-\frac{\hbar^2}{2M}\nabla^2\phi(\boldsymbol{\varrho_e}, \boldsymbol{\varrho_h}) + U_X\phi(\boldsymbol{\varrho_e}, \boldsymbol{\varrho_h}) = E_B\phi(\boldsymbol{\varrho_e}, \boldsymbol{\varrho_h}) \tag{2.18}$$

The mass $M = m_e + m_h$ is the exciton mass. The remaining dispersion is written $E_{kin} = \frac{\hbar^2 K^2}{2M}$, with $\mathbf{K}$ the exciton wavevector.

A similar decomposition holds for QWRs. In that case the shape of the confinement potential has no influence on the binding energy. Only the strength of the confinement, characterized by the Bohr radius, is determinant [111]. As a result, the exciton binding energy is larger in QWRs than in QWs [112]. The situation is different for QDs, in which electrons and holes are naturally hold together by the confinement, independently of Coulomb correlation. This latter only modifies the effective confinement and other theoretical approaches have to be used.

Exciton complexes are formed when additional charges are bound to an exciton. A single electron (hole) binding to the initial electron-hole pair forms a negatively (positively) charged exciton X^- (X^+). The binding of another electron-hole pair forms a biexciton (X_2). Thanks to the possibilty of controlling exactly their states occupation, QDs are ideal systems for studying excitonic complexes [60,113].

2.2.3   Optical interactions

The excitation of an electron from the VB to the CB can be triggered by the absorption of a photon. Conversely, the recombination of an electron with a hole can take place via the emission of a photon. The latter has an energy $\hbar\omega = \frac{hc}{\lambda}$ and a momentum $k_\nu = \frac{2\pi}{\lambda}$ negligible compared to that of the electron-hole pair (λ is the photon wavelength and c the light velocity). Transitions therefore imply electrons and holes of equal momentum, which is the reason why direct semiconductor like GaAs are optically so efficient. The spectral distribution of possible transitions is described by the optical density of states [107]:

$$O(\hbar\omega) = \sum_{e,h} \int |M|^2 \delta(E_e(\mathbf{k}) - E_h(\mathbf{k}) - \hbar\omega) d\mathbf{k} \qquad (2.19)$$

The δ function ensures the conservation of energy. Its summation over $\mathbf{k}$ corresponds to a *joint density of states* depending on the system dimensionality. The optical matrix element M calculated in the dipole approximation from the wavefunctions 2.8 is given by:

$$|M| = \langle \psi^e_{m_s} | \boldsymbol{\epsilon} \cdot \mathbf{p} | \psi^h \rangle = \sum_{m_j} \langle \chi^e_{m_s}(\mathbf{r}) | \chi^h_{m_j}(\mathbf{r}) \rangle \cdot \langle u^e_{m_s} | \boldsymbol{\epsilon} \cdot \mathbf{p} | u^h_{m_j} \rangle \qquad (2.20)$$

The oscillator strength is proportional to the overlap of the envelope functions of the recombining holes and electrons. This prevents transitions between levels of opposite parity. The second term evaluates the product of the polarization vector $\boldsymbol{\epsilon}$ and the momentum operator $\mathbf{p}$ between Bloch functions. It is known as the Kane matrix element and it imposes additional selection rules on the polarization of the emitted/absorbed photon in interband transitions. This term is fixed by the m_s and m_j values; the polarization is then determined by the heavy or light character of the hole.
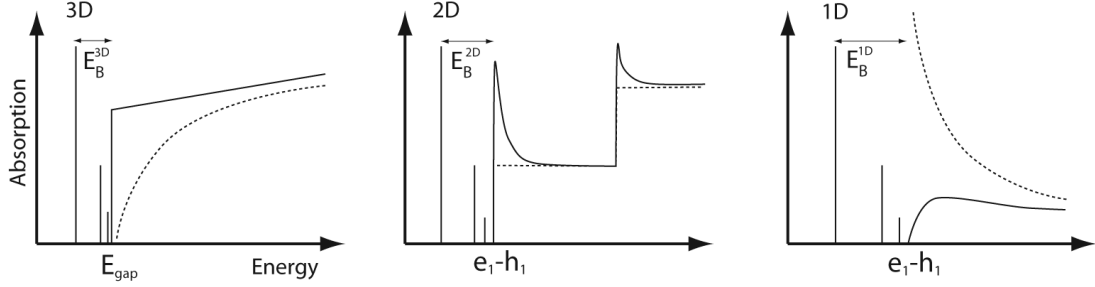
Figure 2.7: Schematic absorption spectra for bulk, 2D and 1D systems. The dotted line corresponds to the free carrier absorption, whereas the continuous line includes Coulomb interaction; i.e.: bound states below the continuum and a modified oscillator strength of the continuum.

Coulomb interactions add complications to this picture. First, the optical transitions associated with bound excitonic states appear below the bandgap. Second, absorption in the continuum states is modified. This is illustrated in Fig. 2.7. Compared to the free carrier case, the oscillator strength is increased at the continuum for bulk and QWs, but decreased for QWRs [114]. This enhancement coefficient (< 1 for QWRs) is known as the Sommerfeld factor. Optical spectra of low-dimensional structures are therefore dominated by excitonic transitions. In particular, in QWRs, the continuum states are barely visible.
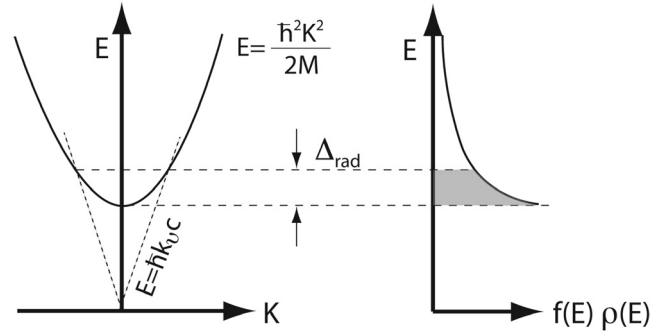
Figure 2.8: Schematic explanation of the temperature dependence of the radiative lifetime. Only those excitons with a wavevector $\mathbf{K} < \mathbf{k}_\nu$ can couple to light (left). Their maximum kinetic energy is Δ_{rad}. These radiative excitons correspond to only a fraction of the total population (shaded area on the right graph). This fraction depends on the occupation function $f(E)$ and the density of states $\rho(E)$. Adapted from Ref. [112].

The excitons with $K < k_\nu$ can undergo radiative recombination. Such excitons have a maximum kinetic energy $\Delta_{rad} = \frac{\hbar^2 k_\nu^2}{2M}$. Their decay is characterized by their *intrinsic* radiative lifetime τ_0. However the average lifetime of the whole exciton population also has to include the 'dark' excitons with $K > k_\nu$. The respective fractions of bright and dark excitons depend on the temperature (through the distribution $f(E)$) and on the DOS (Fig. 2.8). The radiative lifetime is thus written [115, 116]:

$$\tau_{rad} = \tau_0 \frac{\int_0^\infty \rho(E)\ f(E)dE}{\int_0^{\Delta_{rad}} \rho(E)\ f(E)dE} \tag{2.21}$$

which results in (for QWs and QWRs, respectively):

$$\tau_{rad}^{2D}(T) = \tau_0^{2D} \frac{k_B T}{\Delta_{rad}} \qquad (2D) \tag{2.22}$$

$$\tau_{rad}^{1D}(T) = \tau_0^{1D} \sqrt{\frac{\pi k_B T}{4\Delta_{rad}}} \qquad (1D) \tag{2.23}$$

These specific temperature dependence in $\tau_{rad}^{1D}(T) \sim T^{1/2}$ and $\tau_{rad}^{2D}(T) \sim T$ are characteristic of 1D and 2D systems, respectively. The intrinsic radiative lifetime is inversely proportional to the oscillator strength and is ~ 20 ps in QWs and ~ 100 ps in QWRs.

Only parts of the recombinations pathway are radiative. The total lifetime of excitons τ_{tot} is written:

$$\frac{1}{\tau_{tot}} = \frac{1}{\tau_{rad}} + \frac{1}{\tau_{nr}} \tag{2.24}$$

Non-radiative recombinations (for example at crystal defects, which can absorb energy and momentum) are characterized by the rate τ_{nr}^{-1}.

2.2.4   Relaxation and scattering

Under non-resonant excitation conditions, the energy of the photon exciting the electron-hole pairs does not match exactly that of $k = 0$ transitions. Photo-generated electrons (holes) therefore have excess kinetic energy $\Delta_{kin} = \frac{\hbar^2 k^2}{2m_{e,h}}$. Before they recombine, they loose part or all of this energy and electrons (holes) relax toward the bottom (top) of the CB (VB).

Inelastic scattering mechanisms drive this relaxation. Energy can be exchanged with the crystal lattice, through phonons. In the case of GaAs, the most efficient scatterers to carry out the excess energy of electrons are LO-phonons. Their dispersion is almost flat and they have a practically constant energy $\hbar\omega_{LO} = 36$ meV. When $\Delta_{kin} < \hbar\omega_{LO}$, scattering with the less efficient *acoustic phonons* become the dominant relaxation mechanism. At temperatures large enough for a significant phonon population to exist, phonons can also be absorbed and release their energy to the electron (hole).

Nevertheless, many scattering mechanisms are elastic and only contribute to the *thermalization* of the carriers population. By undergoing elastic scattering, particles exchange their kinetic energy. At large carrier densities, collisions between particles have the most important contribution. The scattering rates are different if electrons

and holes are scattered individually or as bound excitons: in QWs, scattering between charged carriers (e-e, h-h, e-h) is the most effective process. The efficiency of the scattering between excitons and charged carriers, or between excitons and excitons, is order of magnitude smaller [117, 118].

The system's dimensionality strongly impacts on the scattering properties. Its relationship with scattering has mainly two origins. The first one is the reduced DOS of 1D systems. Available final states are strongly reduced compared to the 2D case. For elastic events, the conservation of momentum implies that the unique final state available to a particle of wavevector k, is that of opposite sign: $-k$. The second origin lies in the reduced screening of Coulomb interactions. It has been demonstrated that carrier-carrier scattering is reduced in 1D compared to bulk, but that the exciton-phonon scattering is enhanced [119–121]. How the relaxation in 1D compares to the 2D case is then unclear, and reports for faster relaxation [119] coexist along those for slower relaxation [105, 121].

Because they modify the wavevector direction of the particle, scattering events act on its spatial motion. One defines a characteristic time τ_m bewteen scattering events, which change the momentum of a particle of charge e and mass m. For non-degenerate semiconductors, the *mobility* μ is defined by Einstein's relation:

$$\mu = \frac{e\tau_m}{m} = \frac{eD}{k_B T} \qquad (2.25)$$

The *diffusivity* D quantifies the motion of a particle. Another measure often used is the diffusion lenght L_D covered by the particle during its lifetime τ_{tot}, and related to D by:

$$L_D^{2D} = \sqrt{D \ \tau_{tot}} \qquad (2D) \qquad (2.26)$$
$$L_D^{1D} = \sqrt{2D \ \tau_{tot}} \qquad (1D) \qquad (2.27)$$

Analytic approaches to diffusion problems usually calculate the mobility μ_i associated with each scattering mechanism independently, by deriving the scattering rate from Fermi's Golden Rule and using Eq. 2.25. The total mobility is then quantified by the inverse sum, known as Matthiesen rule:

$$\frac{1}{\mu_{tot}} = \frac{1}{\mu_1} + \frac{1}{\mu_2} + ... + \frac{1}{\mu_i} \qquad (2.28)$$

Electron-hole pairs can be scattered as a single particle (excitonic diffusion) or both electron and hole can be scattered independently (ambipolar diffusion). As just mentioned, the scattering rate may be much different in the two cases.

2.3 Disordered quantum nanostructures

The ideal picture of semiconductor nanostructures presented in the previous sections is modified by the inevitable disorder present in real systems. It results in modifications

of the DOS and therefore affects the optical and scattering properties of crystals and nanostructures.

In a crystal, disorder has both extrinsic and intrinsic origins. Impurities are extrinsic atoms incorporating into the crystal. Not only can they release excess charge carriers and induce doping, but they also locally modify the crystal potential, creating states with energy within the bandgap. In the following we concentrate on intrinsic inhomogeneities arising from the materials and fabrication techniques that are used.

2.3.1   Broadening of the density of states

2.3.1.1   Alloy broadening

In an alloy crystal such as AlGaAs, the non-systematic alternance of the Al and Ga atoms creates local perturbations of the potential $U(\mathbf{r})$. The density of states is broadened because of the distribution of the local energy levels (Fig. 2.9(a)). The resulting broadening of the PL line has been investigated by Singh using a statistical approach [122]. The bulk exciton linewidth can be expressed as a function of the alloy concentration and the material properties. In a GaAs/AlGaAs heterostructure, however, only a fraction of the confined excitons probes the alloy in the barriers. The PL linewidth of a QW exciton, σ_{QW}, is then corrected from the bulk value σ_B through the equation:

$$\sigma_{QW} = \sigma_B \frac{\Delta_{QW}}{\Delta_1} \frac{1}{\sqrt{P_0^{ex}}} \tag{2.29}$$

Δ_{QW} is the variation of the confinement energy with the alloy composition and Δ_1 is the alloy bandgap variation with the composition: $\Delta_{QW} = \frac{\delta E^{conf}}{\delta x}$ and $\Delta_1 = \frac{\delta E_g(x)}{\delta x}$. P_0^{ex} is the fraction of the exciton wavefunction extending outside the QW. For very narrow QWs, $\sigma_{QW} \rightarrow \sigma_B$. For wider QWs, the term $\frac{\Delta_{QW}}{\Delta_1}$ is dominant so that σ_{QW} decreases even if P_0^{ex} approaches zero at the denominator.

2.3.1.2   Interface roughness

In practice, the transition from the QW material to the barrier material is neither absolutely abrupt in the growth direction, nor perfectly homogeneous in the interface plane: fluctuations ΔL_z of the QW width result in a broadening $\Delta E \propto \Delta L_z$ of the energy of confined states: the variations of the QW width scatter the energy levels of the confined states and broaden the DOS and consequently the optical linewidth (Fig. 2.9(b)).

An essential feature to consider when addressing the in-plane fluctuations is the ratio between the disorder scale ξ and the extension a_B of the exciton [17]. The value of ξ generally corresponds to the extension of domains at the QW interface that have an atomically flat surface. Such domains are referred to as monolayer (ML) islands. Each
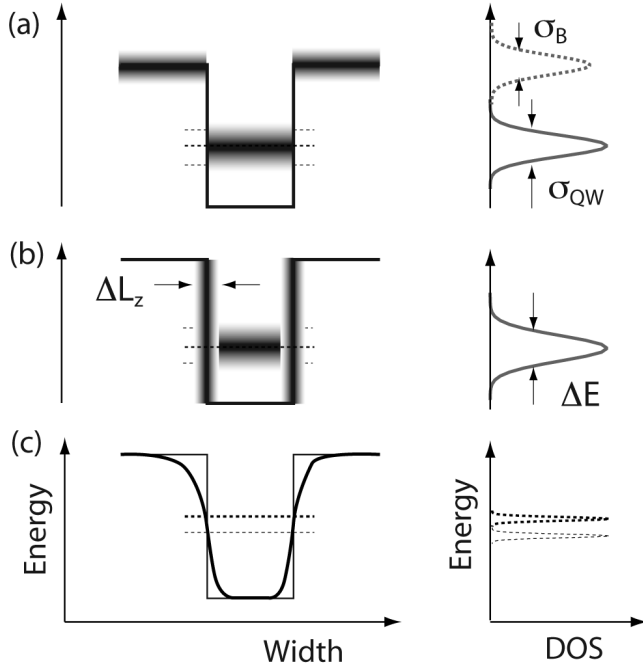
Figure 2.9: Schematic illustration of the effects of (a) alloy broadening, (b) width fluctuations and (c) segregation, on the density of states.

interface often exhibits different characteristics and the correlations between them has to be taken into account [20,123]. Then we more generally define ξ as the characteristic (longitudinal) correlation length of the structure potential.

- For $\xi > a_B$, the exciton 'sees' a homogeneous potential, which translates in optics in a single narrow optical transition line. Sufficiently extended domains of different widths $(L + \Delta L_z)$ thus result in an optical spectra consisting of several narrow lines separated by energies ΔE. The variations ΔL_z correspond to multiples of crystal monolayer (ML) height; they are thus discrete and so are the variations ΔE.

- For $\xi < a_B$, the potential is averaged over the exciton extension. This averaging lifts the discreteness of the exciton energy and results in inhomogeneously broadened optical transitions. Note that very small domains with $\xi < \xi_0 = \frac{\pi \hbar}{\sqrt{2MV_0}}$ cannot confine excitons (V_0 is the potential variation and M the exciton mass) [124].

Beyond the in-plane fluctuations, the interfaces are generally not abrupt along the growth direction. For instance, if one considers the interface AlAs/GaAs, the transition from one material (Al) to another (Ga) usually extends over a few ML, in which both kind of atoms are mixed. This segregation results in a graded variation of the potential (Fig. 2.9(c)). This variation can lead either to an increase or a decrease of the confined states in the QW, depending on which material diffuses preferentially in the other [125]. Nevertheless, in experimental systems, segregation at QW interfaces almost always corresponds to a blueshift of the optical transitions [79,126]. If the effect can be important in some alloys, the interdiffusion does not take place over more than a few ML in the case of AlGaAs alloys and it is considered to result in negligible modifications of the energy levels.

Alloy fluctuations or segregation at the interfaces are of very similar nature. They are often referred to as *micro-roughness* disorder, which is misleading. Therefore we use here the term of *nano-roughness*, which translates better the length-scales involved. Nano-roughness corresponds to fluctuations of the QW width occurring on very short length scales, ultimately, on one lattice period.

2.3.2 Localization

Although the above description explains nicely the broadening of the optical density of disordered structures, more subtle effects on the motion of exciton require a full calculation of the system eigenstates [127,128]. The in-plane part of the exciton wavefunction expressed in Eq. 2.17 can be further decomposed into $\phi(\boldsymbol{\varrho_e}, \boldsymbol{\varrho_h}) = \varphi(\boldsymbol{\rho_{eh}}) \cdot \phi_{COM}(\mathbf{R})$. The first function φ describes the relative motion of the electron and hole with regard to the center of mass (COM), which coordinate is $\mathbf{R} = \frac{m_e \boldsymbol{\varrho_e} + m_h \boldsymbol{\varrho_h}}{M}$. The vectors $\boldsymbol{\rho_{e,h}}$ give the relative electron and hole positions.

In general, the binding energy E_b of the exciton is large compared to the amplitude of the fluctuations of the potential U. It is therefore assumed that the disorder has a negligible influence on the relative motion of the electron and the hole. Instead, only the COM of the exciton is affected by disorder. This situation is described by an effective Schrödinger equation for the COM wavefunction:

$$-\frac{\hbar^2}{2M}\nabla^2\phi_{COM}(\mathbf{R}) + U_X(\mathbf{R})\phi_{COM}(\mathbf{R}) = E_{COM}\ \phi_{COM}(\mathbf{R}) \tag{2.30}$$

The effective excitonic potential entering Eq. 2.30 reads:

$$U_X = \int d\mathbf{R}' \sum_{i=e,h} \eta_i^2 \varphi(\eta_i(\mathbf{R} - \mathbf{R}'))U_i(\mathbf{R}') \tag{2.31}$$

In this equation, $\eta_e = \frac{M}{m_h}$, $\eta_h = \frac{M}{m_e}$ and $U_i(\mathbf{R}')$ describes the fluctuation of the electron (hole) confinement energy in the QW plane. It appears from Eq. 2.31 that the energy fluctuations are averaged by the relative motion of the electron-hole pair.

This phenomena is illustrated in Fig. 2.10. Electrons are subject to a potential U, which fluctuates on a short scale because of nano-roughness and on a longer scale because of interface islands. The nano-roughness component is completely smoothed out by the averaging over the exciton volume and the effective exciton potential U_X mainly follows the long range variations of the potential. Such a potential is well characterized by gaussian-distributed fluctuations of standard deviation Λ and correlation length ξ, in connection with the quantity defined in the previous subsection.

Excitons are localized in the minima of this potential. The disorder also strongly affects the binding energy of exciton, charged excitons and biexcitons [129]. As made clear by the weighting factor η_i in Eq. 2.31, localization confinement has a different
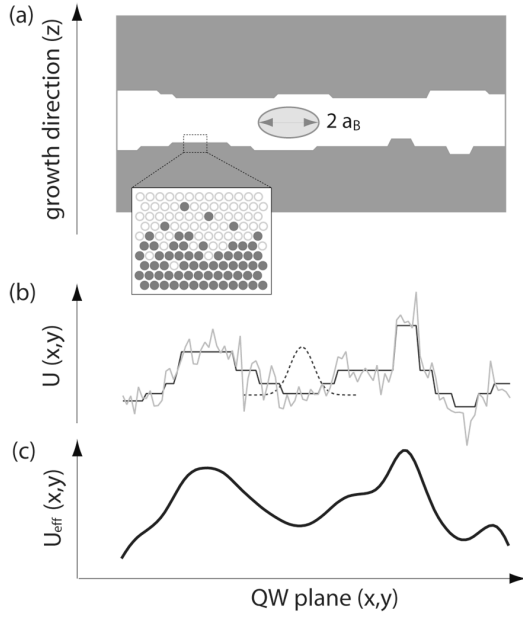
Figure 2.10: (a) Scheme of the interface disorder in a QW: each interface is composed of extended islands, to which is superposed nano-roughness (inset). (b) Resulting potential for a single particle. (c) Effective potential obtained by averaging over the exciton volume (illustrated by the dashed gaussian line in (b)).

influence on the lateral wave functions of electrons and holes: due to its smaller mass, electron is less localized than the hole. The binding energy has a non-monotonous dependence on the size of the localization defect, but is in all case enhanced compared to their binding energy in an ideal structure. Indeed, in QWs, the binding energy of X^- and X^+ are almost similar, but experimental estimates of the binding energy are often larger than the calculated values. Biexcitons [129] and charged excitons [130,131] are more sensitive to potential fluctuations than excitons; this increases their binding energy.

In QWRs, the elongation of the confinement minima has been shown to be determinant for the properties of excitons [98], charged excitons [88,132], biexcitons [57,87]. Their binding energy can span a rather large energy range due to its important dependence on localization along the QWR axis, which has also been thoroughly studied theoretically [87,132–134].

2.3.3 Effects of disorder on carrier dynamics

2.3.3.1 Exciton relaxation and distribution

Because excitons are localized in the minima of the effective potential, the optical lineshape does not reproduce the potential distribution. The optical density is asymmetric and redshifted compared to the gaussian DOS and its linewidth is narrower. This effect is referred to as *motional narrowing* [135].

The *Stokes shift* is defined as the separation between the peak of PL line and that of the absorption line. Its interpretation is actually related to that of the motional narrowing. Whereas the absorption probes the entire collection of *available* states, the

emission is weighted by those that are effectively *occupied*. The latter being preferentially the low-energy localized states, the Stokes shift is considered as a good measure of disorder. At low temperature, without global thermalization, it is indicative of the spectral distribution of the potential minima [135, 136]. No thermal equilibrium can be reached amongst the different minima at low temperature. However, with increasing temperature, as the different minima reach a thermal equilibrium, emission from thermally populated higher-energy states gradually reduces the Stokes shift, which is then proportional to $\frac{\sigma^2}{k_B T}$ (with σ the absorption linewidth) [137, 138].

In between these two regimes, Zimmermann et al. have described the non-monotonous dependence of the Stokes shift and PL linewidth with the temperature [135, 139]. When the thermal energy is large enough for the exciton to overcome a shallow barrier and relax to a deeper minima, it results in an increased Stokes shift and decreased emission linewidth. The thermal behavior is recovered for larger temperatures. Zimmermann and coworkers also pointed out the existence of a *relaxation mobility edge*. Since the spatial overlap is reduced between localized states, their interaction is strongly reduced. As the scattering rate with acoustic phonons depends on the energy separation between the initial and final excitonic state, a threshold energy exists, for which exciton cannot relax to a lower state within their lifetime [140].

2.3.3.2   Exciton motion

Beyond the extreme case of localization, disorder affects the motion of excitons in many ways. Motion between localization sites can take place through tunneling or 'hopping'. The mobility of excitons is however weak through this mechanism [141]. The concept of mobility edge was more generally introduced to refer to the spectral energy separating localized from continuum states [142]. It was identified experimentally in QWs [143, 144] but to our knowledge, there is no clear demonstration of this threshold in QWR.

Nevertheless, delocalized states undergo additional scattering with the interface roughness. The scattering rate between two states, whose energies differ because of interface roughness of a QW, can be expressed via Fermi's golden rule as a function of the potential parameters ξ and Λ defined previously. The resulting mobility μ_{IR} is proportional to $\frac{L_z^6}{\Lambda^2 \xi^2}$ [118]. A similar dependence as R_0^6 holds for (cylindric) QWRs of radius R_0 [145]. The diffusion of excitons is therefore much more affected by disorder in narrow structures.

Other scattering mechanisms include scattering with atomic impurities or with the alloy fluctuations of the system [145, 146]. In the latter case, the determinant factor is the extension of the wavefunction to the barrier material. In GaAs/AlGaAs QWs, the mobility is then found to increase with increasing QW width and Al concentration.

The scattering in 1D systems is particular as the phase space is reduced. A par-

ticle with wavevector k scattering *elastically* can only scatter toward a state with an opposite wavevector $-k$ [38]. A consequence is that the mobility depends importantly on the value of the wavevector. This implies in particular that the scattering efficiency of a rough interface will be non-monotonous with the disorder correlation length and reach a maximum when its Fourier components coincide with the wave vector k_F at the Fermi level [147]. The mobility then depends strongly on the particle density.

2.3.3.3 Exciton recombination

Localized excitons play an important role in the decay time of the photoluminescence over a large temperature range [92, 148, 149]. In particular, the wave function of localized excitons mixes wave vectors, some of which are larger than k_ν and correspond to non-radiative excitons [150]. At low temperatures, it results in an enhanced radiative lifetime.

Several models were proposed to describe the temperature dependence of the radiative lifetime of excitons in disordered systems. In particular, for QWRs, Lomascolo et al. derived a formula in which the radiative recombination rate is expressed as the weighted average between the free and the localized excitons (density N_{free} and N_{loc}, respectively), which are assumed to be thermalized [151]. As a result, the lifetime dependence reads:

$$\tau(T) = \frac{N_{loc} + N_{free}}{\frac{N_{loc}}{\tau_{loc}} + \frac{N_{free}}{\tau_{free}}} \tag{2.32}$$

$$= \frac{N_D \cdot e^{\frac{E_{loc}}{k_B T}} + \sqrt{\frac{2Mk_B T}{\hbar^2 \pi^2}}}{\frac{N_D}{\tau_{loc}} \cdot e^{\frac{E_{loc}}{k_B T}} + \frac{1}{\tau_0}\sqrt{\frac{2M\Delta_{rad}}{\hbar^2 \pi}}} \tag{2.33}$$

In this expression N_D corresponds to the density of localization sites along a QWR, from which localized excitons recombine with a characteristic time τ_{loc}. E_{loc} corresponds to an activation energy for the delocalization.

2.4 Chapter summary

We have presented the basics of the semiconductor physics applied to nanostructures. The peculiarities of GaAs/AlGaAs materials, namely the similarity of the lattice parameter of their crystalline structure and the modifications of the band structure, make them choice systems for the fabrication of low-dimensional structures and offer the possibility to control their properties (*band engineering*).

We have seen how the density of states and the Coulomb interactions are strongly modified in quantum nanostructures and how this affects their optical and motional

properties, either at the spectral or dynamical level.

We underlined some effects stemming from the unavoidable inhomogeneities of practical realizations of nanostructures. Their different origins were reviewed and the emphasis was put on the importance of the length scales of the disorder.

Chapter 3

Samples: growth and characterization techniques

Metalorganic vapor phase epitaxy (MOVPE) allows the fabrication of high-quality quantum wells (QWs). Combined with lithography and micro-processing, it also makes possible to form structures of lower dimensionality, such as quantum wires (QWRs) or quantum dots (QDs). This thesis work deals with QWs and QWRs grown on substrates patterned with V-grooves, whose fabrication techniques are detailed in this chapter (Sec. 3.1).

The demand on reliable characterization techniques has grown in parallel with the quality of nanostructures. Atomic force microscopy (AFM) and electron microscopy allow to determine morphologic features of samples with close to atomic resolution (Sec. 3.2). They usually only give partial information, either on the cross-sectional profile of the structure or on interfaces that are not directly connected to the system properties. The widespread alternative for characterization of nanostructures is to extract indications on their structure from their optical properties (Sec. 3.3). Light absorption and emission provide quantity of information on the energy levels, structure homogeneity and nature of the particles formed inside the system. This chapter details the techniques used in the course of this work. A broader overview of characterization of semiconductor nanostructures can be found in review papers by Stangl [152] or Gustafsson [44].

3.1 MOVPE grown samples

Metalorganic vapor phase epitaxy (MOVPE, also referred to as metalorganic chemical vapor deposition, MOCVD) is nowadays a routine tool for mass production of semiconductor devices such as high mobility electron transistors, light-emitting diodes and lasers. However, although the mechanisms of epitaxial growth have been addressed by many theoretical models [21, 23, 153–156], they are much better understood for molecular beam epitaxy (MBE) than for MOVPE. Whereas for MBE only the adatoms have to be considered, the situation is more complex for MOVPE due to the involvement

of precursor molecules, organic species and hydrogen in the process. Another element explaining the difference in the understanding of the two process is that in the case of MOVPE there is no *standard* tool for in-situ monitoring of the growth process, such as reflective high energy electron diffraction (RHEED) in the case of MBE. Nevertheless, several in situ characterization techniques for MOVPE have been developed, for example by studying the modification of X-ray scattering, sensitive to surface morphology and roughness [157], or by using reflectance-difference spectroscopy (RDS) [158]. Yet, most of the knowledge on the growth has been deduced from the observation of the samples surface after the growth.

3.1.1 Principles of MOVPE

The growth by MOVPE can be described by the following sequence, illustrated in Fig. 3.1:

1. Metal-organic precursors are flown over the substrate, carried by a gas allowing to control the flow and pressure;

2. The precursors penetrate a boundary layer at the interface between the substrate and the gas, and diffuse onto the surface;

3. The precursors decompose and release an adatom, which further diffuses on the surface of the substrate. The organic radical is evacuated by the carrier gas flow.

4. The adatom is finally incorporated into the crystal, typically at a preferable location such as a step edge or a kink.
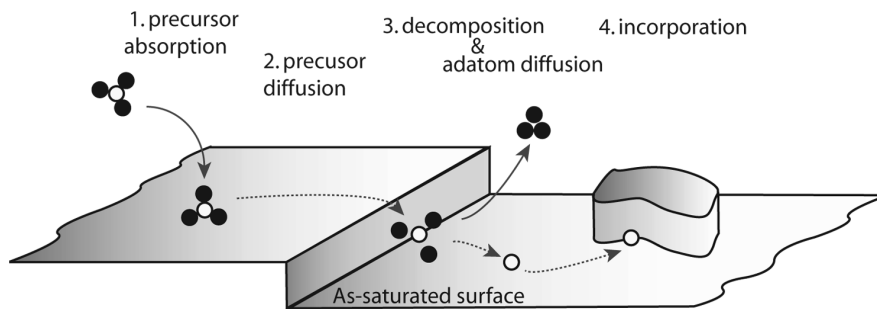
Figure 3.1: Schematic of the main processes of MOVPE growth.

Having in mind this simple model, the successive stages of growth are evidently affected by the following parameters [15, 159]:

(i) The gas *sources* provide the growth materials. Special care has to be taken to ensure their purity and their stability over time. Our samples consist uniquely of GaAs and

AlGaAs layers, for which we used trimethyl-gallium (TMGa) and trimethyl-aluminium (TMAl) as precursors. The As atoms are provided in the form of arsine (AsH_3). In our reactor, the gas are carried by nitrogen N_2 at low-pressure ($\sim$20 mbar).

(ii) The *growth temperature* mainly determines the dissociation rate of the precursors and the mobility of the diffusing species (adatoms and precursors). High growth temperatures enhance the crystal quality [16], but if too high, re-evaporation can occur [160]. Compared to MBE, where the precursor dissociation is not necessary, MOVPE growth temperatures are considerably higher. In our MOVPE apparatus, the substrate is placed on a rotating susceptor and heated by infrared lamps. The liner in which the carrier gas flows is covered with Molybdenum to improve the thermal stability of the system. The susceptor temperature is measured by a thermocouple, from which the temperature of the substrate is estimated. The thermocouple value is quoted in the text; the estimated temperature of the substrate is about 40°C lower. In our studies, the substrate temperature is typically between 650°C and 750°C.

(iii) The *V/III ratio* sets the proportion of the group V elements relatively to the group III ones. We always use high V/III ratio, so that the substrate surface is saturated with As and always provides free bonds to link with Ga or Al atoms. As a result, only the kinetics of the group III elements have to be taken into account when considering the growth dynamics. Later in this section, we will describe the reference growth conditions that we use and discuss in some more details the importance of this parameter.

(iv) The *growth rate* is limited by different factors depending on the regime determined by the growth conditions. The process can be limited by the time necessary for the diffusing specie to reach the site where it is finally adsorbed. Alternatively, it can be governed by the kinetics of the chemical reaction taking place on the surface. This chemical process is synthetized in Eq. 3.1 and involves reactions of dissociation and attachment, which take a finite time to occur and thus can limit the growth rate:

$$[Ga(CH_3)_3]_{gas} + [AsH_3]_{gas} \rightarrow ... \rightarrow [GaAs]_{solid} + [3CH_4]_{gas} \qquad (3.1)$$

In our case, the growth rate was kept at about 1 ML/s, and is probably limited by the decomposition rate of the organometallics [161].

3.1.2 QWs on vicinal substrates

As suggested in Fig. 3.1, atomic steps play a particular role in the growth process: they are believed to have a catalytic effect for precursor dissociation and to favor adatoms incorporation. By definition, *vicinal surfaces* have an orientation $\hat{n}$ close to that of a high symmetry crystallographic plane. The deviation from this direction is referred to as the *miscut* (or misorientation) angle. As explained in the following, growing on vicinal substrates allows to tailor the density of atomic steps and thus to better control the growth.
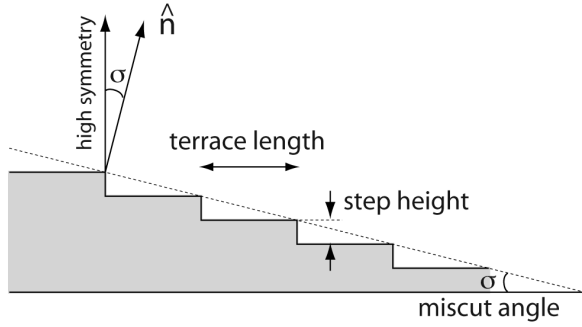
Figure 3.2: Schematic of a vicinal surface.

3.1.2.1 Basics of epitaxial growth

Epitaxial growth is initiated by the arrival of adatoms, which prompts the deposition of additional crystalline layers on the crystal surface. The adatoms have a finite lifetime, during which they diffuse on the surface and are finally incorporated into the crystal. Different growth modes describe the evolution of the surface depending on the initial conditions and experimental parameters. The three main growth modes relevant to the lattice-matched QW structures discussed here are: 2D-island nucleation, step-flow and step-bunching.

Island nucleation occurs when the adatom does not reach a specific site within its lifetime. It is then incorporated at a random location on the surface, and has several dangling bonds available for binding with other adatoms. The adatoms thus conglomerate and form *islands* randomly on the surface. This case is not convenient for growing layers with well defined thicknesses. Therefore, for practical purpose, growth is often initiated on vicinal substrates.

A vicinal surface accommodates its angle by creating *terraces* separated by *steps* (Fig. 3.2). It thus creates many sites favorable for incorporation. Schwoebel first proposed a realistic description of the mechanism regulating growth on vicinal surfaces [162]. He considered the incorporation at a step to be statistical, and assigned it a probability γ. He further took into account the fact that the chemical potential 'felt' by an adatom differs if it approaches the step from one side or the other. This discontinuity is now referred as the (Ehrlich-) Schwoebel (ES) barrier (Fig. 3.3).

Supposing that the diffusion length of an adatom is larger than its distance to a step, and that it has a probability γ^+ (γ^-) to incorporate if coming from the lower (upper) terrace, Schwoebel underlined in particular the two following cases:

⋆ if $\gamma^+ > \gamma^-$, a uniform step separation develops from an arbitrary initial terrace width distribution. Indeed, more adatoms are impinging on a wide terrace and the upper step grows faster, reducing the terrace length. From the point of view of a long-range interaction between steps, it is referred to as a *repulsive* interaction and the growth mode is called **step-flow**.

⋆ if $\gamma^+ < \gamma^-$, steps coalesce as a large terrace grows faster and finally catches up with a lower, smaller one. This is a kind of *attractive* step-step interaction, which leads to **step-bunching**.

These considerations are at the core of all theories and models of crystal growth, which differ by the details they include. The purely 1D point of view of the model above can be extended to consider diffusion along the steps, which explains step meandering [153, 163]. Alternative models for step-bunching are also proposed, as $\gamma^+ < \gamma^-$ corresponds to a negative ES-barrier (as opposed to the positive one sketched in Fig. 3.3(b)), which is hard to justify with atomic configuration arguments [164]. Recently, step-bunching has been nicely reproduced in Monte-Carlo simulations based on a model including two types of diffusing molecules, as it is the case in MOVPE with precursors and adatoms [154, 165, 166].

The kinetic and chemical properties are naturally dependent on the material type. In the case of AlGaAs materials, the mobility of Ga adatoms is larger than that of Al adatoms, as the Ga-As bond is weaker than the the Al-As one. The number of dangling bonds, and thus the γ coefficient, depends on the step orientation [161], therefore introducing growth anisotropies.
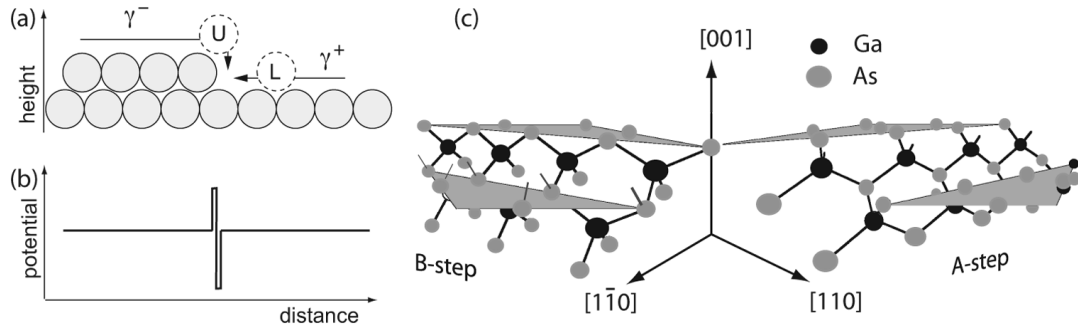
Figure 3.3: (a) Schematic of a surface step illustrating the configuration seen by an atom approaching from the upper (U) or lower (L) terrace, and the attachment coefficient γ. (b) Schwoebel potential barrier, which in that case reflects part of the adatoms approaching the step from the upper terrace (positive ES barrier). (c) Atomic configuration of A and B steps on (001) GaAs.

Fig. 3.3 shows the atomic configuration at steps forming on a (001) GaAs surface when the surface is inclined toward the [110] direction or toward [1$\bar{1}$0]. In the first case, one of the four covalent bonds of Ga is dangling and offers an attachment site. It is referred to as *A-steps*. In the second case, all Ga bounds are saturated but As atoms offer dangling bonds, making thus *B-steps*. A Ga atom binds more tightly at B-steps than at A-steps, which are thus less active. Indeed, it has been observed [24] that the lateral growth rate is faster in the [1$\bar{1}$0] direction. When the growth temperature (and thus the diffusion length) is increased, the transition from 2D growth to step-flow occurs at lower temperatures on B-surfaces than on A-surfaces, as islands coalesce more rapidly with a

B-step. For the same reasons, A-steps are generally smoother than B-steps, which show kinks and undulations. Note that this picture of step chemistry makes abstraction of the rearrangement of dangling bonds at equilibrium, which is known as surface reconstruction.

3.1.2.2 QW samples

Growth of quantum wells is used in our laboratory as a routine characterization of the status of our MOVPE reactor. We use the PL properties of a standard triple quantum wells structure (TQW - 15, 5 and 2 nm QWs embedded in thick $Al_{0.3}Ga_{0.7}As$ barriers, see Annex A) to check the quality of the sources and ensure that the impurity level in the system is low. Deviations from routine values allow us to detect leaks or contaminations in the system. However, fluctuations from a growth run to another initially used to be important and did not allow a fine optimization of the growth conditions and a reliable reproducibility.

Two factors allow to considerably improve the optical properties of TQW and to use these samples as real indicators for the MOVPE system conditions. The first factor is the use of slightly misoriented substrates, which allows to control the interface quality as it will be explained in detail in Ch. 4. The second is a significant increase of the V/III ratio during growth of the AlGaAs layers.

The V/III ratio is known to influence the impurity content in compound layers [159, 167]. Whereas a low V/III ratio gives rise to p-type background doping, increasing the V/III ratio gradually reduces it and eventually yields n-type layers. The range in which background doping is small enough ($\lesssim 10^{14} cm^{-3}$) is known as the compensation point. As schematized in Fig. 3.4, an increase in growth temperature shifts the compensation point toward lower V/III values. For $Al_x Ga_{1-x} As$ alloys, it moves to lower V/III values for smaller x.
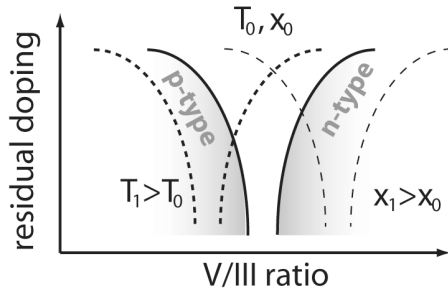
Figure 3.4: Schematic dependence on the V/III ratio of the residual doping and of the compensation point, for different growth temperatures T and aluminium concentrations x.

This behavior can be understood when considering the competition between the nominal species (here Al, Ga and As atoms) and impurities (typically C, Si, O) [167,168]. In our case, the main residual impurity is the carbon from the methyl groups of the sources. As the V/III ratio increases, the number of As vacancies decreases and prevents C incorporation. Other improvements have been reported when using large V/III ratio,

like increase in the adatom diffusion length (triggered by H-passivation) [169, 170] or modified surface morphologies [163, 171, 172].

With these considerations in mind, we achieved growth showing a dramatic improvement in the material quality. In Fig. 3.5 we show the chronological evolution of the FWHM of TQW samples (except for the 4 first samples, which excluded the 2 nm QW), grown on 0.2°-off substrates at standard conditions (see Table 3.1). We clearly see that increasing the AlGaAs V/III ratio by a factor close to 3 reduced the linewidth of the 15 and 5 nm QW PL from about 3 meV for both to typically 0.8 and 1.8 meV, respectively. Deviations from these values are visible and indicate either problems within the reactor or modification of the sources (for example, bottle replacements). It is interesting to note that the thinnest QW is essentially unaffected by the V/III change, suggesting that the dominant broadening is not linked to impurities (see Sec. 4.3).
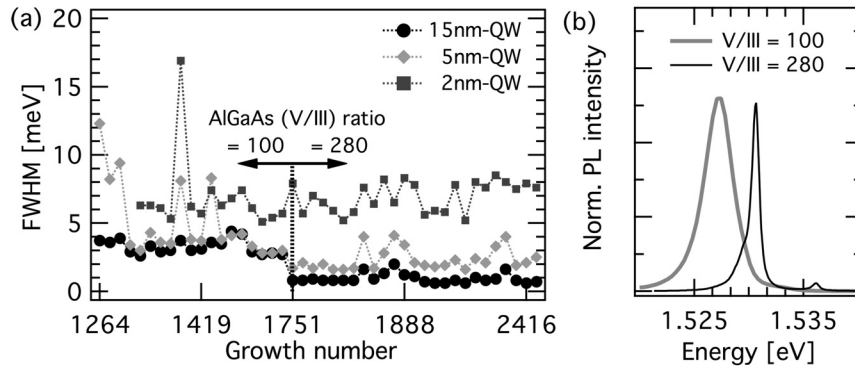
Figure 3.5: (a) FWHM of the PL of three QWs grown in TQW structures, displayed according to the chronological order of the growth. (b) PL spectra of the 15nm thick QW of samples with low and high V/III ratio.

In Table 3.1, we summarize the principal characteristics of our MOVPE reactor, together with the growth parameters and quality indicator (photoluminescence linewidth) for the TQW structure.

3.1.3 V-groove QWRs

The fabrication of V-groove QWRs evolved continuously throughout this thesis project, as new tools became available and growth quality became better controlled. We present below the fabrication procedure that we used, and discuss some of its crucial steps.

3.1.3.1 Substrate patterning

The preparation of V-groove patterns on a GaAs substrate is sketched in Fig. 3.6. First, a 50 nm SiO_2 layer is deposited on the substrate surface (a). A line pattern is writ-

Substrates	2" GaAs
Metalorganic sources	TMGa, TMAl
As source	AsH_3
Carrier gas	N_2
Growth T	730°C
$V/III(Al_{0.3}Ga_{0.7}As)$	280
$V/III(GaAs)$	130
15 nm QW linewidth	0.5 meV
5 nm QW linewidth	1.6 meV
2 nm QW linewidth	5.2 meV

Table 3.1: Main characteristics and standard growth conditions of our Aixtron MOVPE reactor and record PL linewidth values obtained for reference QWs.

ten along the $[1\bar{1}0]$ direction, either by standard optical lithography in photoresist, or by electron beam (e-beam) lithography in a polymethylmethacrylate (PMMA) resist deposited on the oxide layer (b). The resist serves as a mask to open apertures in the SiO_2 layer. We used either buffered hydrofluoric acid (BHF) wet etching or reactive ion etching (RIE) to etch the SiO_2 (c-d). The grooves are etched in a solution of bromic acid, bromine and methanol (HBr:Br:Meth), which etches anisotropically GaAs, exposing {111}A facets (e). The SiO_2 mask is finally removed in BHF (f).
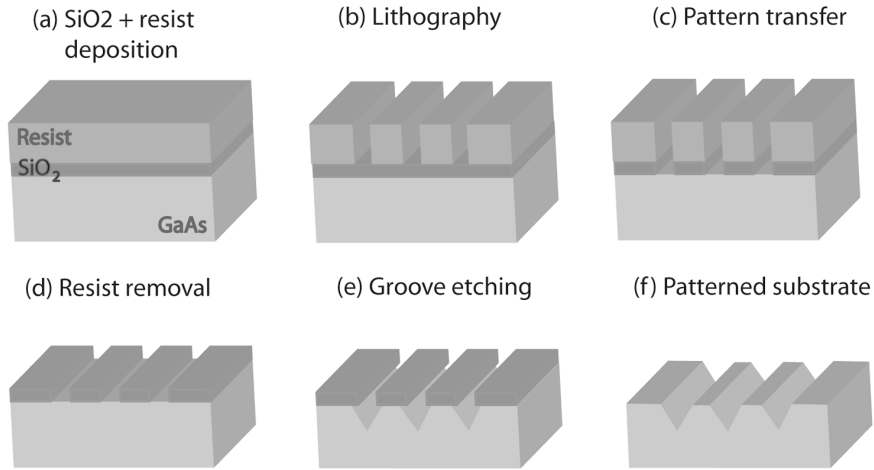
Figure 3.6: Schematics of the main steps for substrate patterning.

Smooth groove boundaries are crucial for the quality of the grown QWR structures [173]. The roughness of the line pattern is better controlled when e-beam lithography, rather than standard optical lithography, is used. Low writing speed allows to produce smooth patterns, although covering a smaller substrate area (typically 500 by 500 μm^2). We noticed no difference between wet BHF etching and dry RIE when transfering the

pattern to the SiO_2 layer. As BHF is more hazardous, the RIE was preferentially used as it became available in our facilities.
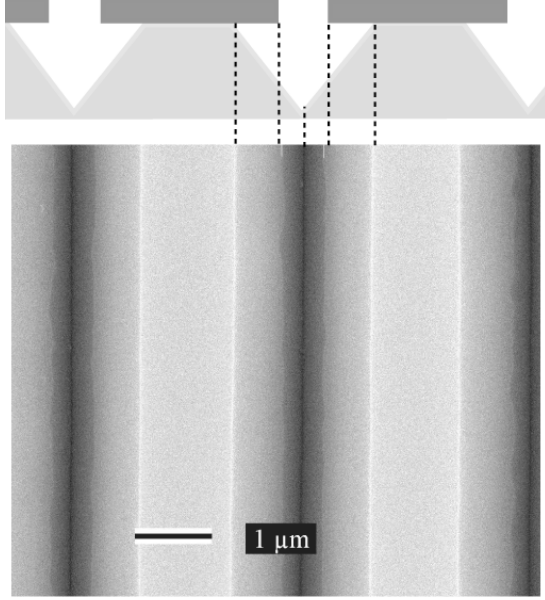
Figure 3.7: Top view SEM image of V-grooves etched in GaAs, still covered with the SiO_2 mask, as schematized in the cross-section scheme above.

The pattern has then to be transfered properly to the GaAs. Br:Meth solution allows a fidel imprint of the SiO_2 mask geometry to GaAs. However, adding HBr in the solution induces a slow under-etching below the mask, and smoothes possible imperfections. This is illustrated in Fig. 3.7. The lines correspond to the etched groove and SiO_2 boundaries, as sketched above the SEM image. In this particular case, the SiO_2 mask exhibited important roughness (amplitude up to 100 nm) but the etched GaAs has much smoother edges (amplitude < 20 nm).

Note that alternative methods can be used to etch GaAs V-grooves. For example, the mixture $NH_4OH : H_2O_2 : H_2O$ (1:3:50) can be used directly by using resist as a mask and thus eliminating the SiO_2 patterning steps. A post-etching procedure consisting in a further dip of the grooves to the etching solution after mask removal has been proposed to further smooth the grooves sidewalls [174]. However, when applied to our samples, we found no improvement justifying its systematic use.

Fig. 3.8(a) shows a typical V-groove grating just before the removal of the SiO_2 layer. Grooves are formed with their center every 3 μm, which ensures a sufficient density for subsequent QWR ensemble measurements but also a sufficient separation to address them individually (Sec. 3.3). The initial opening in the mask is around 800 nm, but the final groove width is around 1.5 μm due to the under-etching. Part (b) are AFM images of a 10 μm long groove segment. Height (top) and amplitude (center) images (see Sec. 3.2) evidence long scale ($\sim$2 μm) fluctuations, as well as a shorter
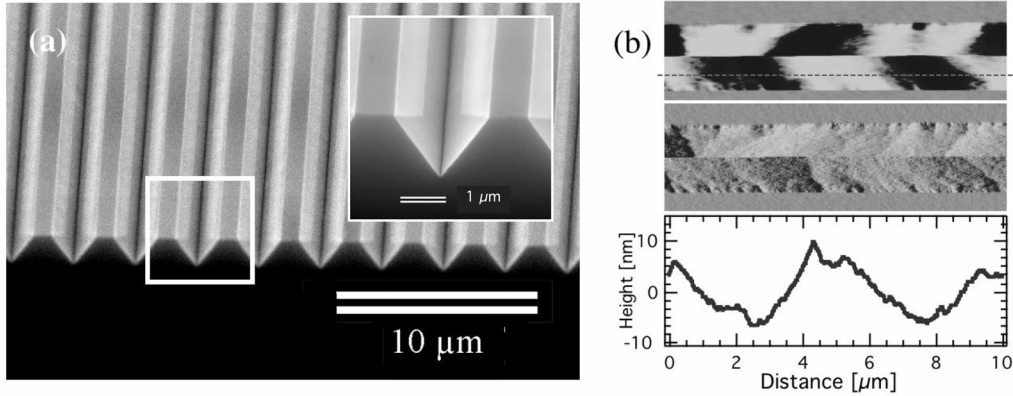
Figure 3.8: (a) Cross-sectional SEM images of a 3 μm pitch V-grooved substrate. The magnified view in inset clearly shows the remaining SiO_2 mask, and the under-etching below it. (b) AFM images (top: height; middle: amplitude (see Sec. 3.2)) and cross-section (bottom, along the dashed-line) of a V-groove.

scale roughness. The lower panel is a line scan in the middle of the groove sidewall. The amplitude of the fluctuations (15-20 nm) is typical of all the substrates that we prepared. We note that the edges of the groove are rougher, but the fluctuations are identical over the rest of the sidewalls. In most case, the fluctuations of one sidewall are not correlated with those of the other, although correlated or anti-correlated domains exist.

In addition to the morphological aspects of the sample, special care has to be taken to keep its surfaces clean and free of contamination. The process thus involves several cleaning steps, the last one being a desoxidation in HCl just before growth. The detailed processing sequence is given in the Annex A.

3.1.3.2 Growth on non-planar surfaces

Compared to the description of MOVPE given in Sec. 3.1.1, the growth on non-planar, patterned substrates involves additional mechanisms that can be used to control the composition and structure of epitaxial layers in other directions than the growth axis. This is owing to the fact that the chemical potential $\mu(x,y)$ of the surface can be locally modified. Example modifications are those induced at surface steps or island edges, as described in Sec. 3.1.2. Even more important are the effects of corrugations or facets, as those of V-grooves.

These effects can be well understood from the simplified model sketched in Fig. 3.9(a), with two types of facets [176]. The growth rate of each facet can be expressed in terms of the adatom flux by the continuity equation $\frac{\partial z}{\partial t} \sim \frac{\partial j}{\partial x}$, in which the flux j is the sum of a lateral flux j_l and the impinging flux from the gas phase. The lateral flux obeys Fick's law:
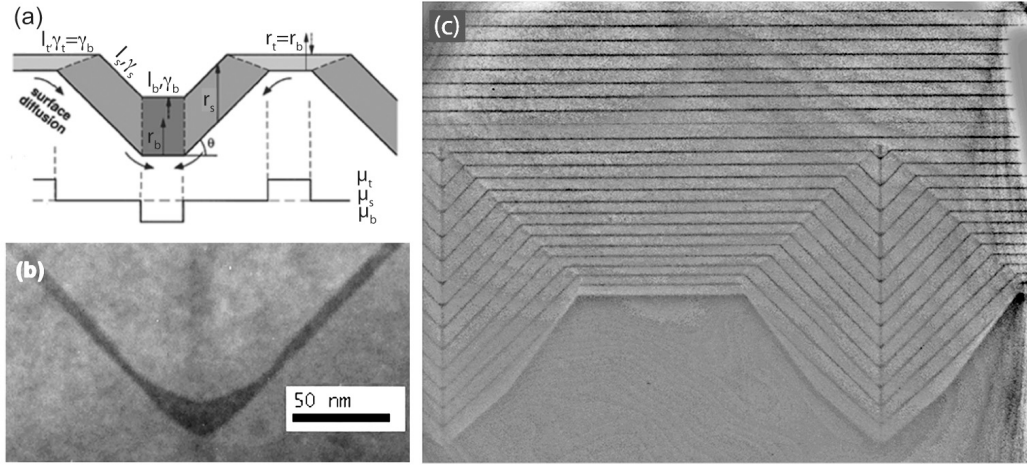
Figure 3.9: (a) Schematic illustration of the growth rate and diffusion flux in a model structure, indicating the local variations of the chemical potential below (from Ref. [175]). (b) Detailed view of the profile of a nominally 10 nm thick GaAs layer, showing the different faceting of the AlGaAs and GaAs layers. (c) TEM image of a thick $Al_{0.3}Ga_{0.7}As$ layer grown with GaAs (dark) marker. Each period corresponds to a nominal 100 nm thickness and the separation between the grooves is 3 μm.

$$j_l = -\frac{nD}{k_B T}\frac{\partial \mu}{\partial s} \tag{3.2}$$

where n is the surface density of adatoms, D is their diffusion coefficient and s is the curvilinear abscissa along the surface. The *growth rate* of a facet α of length l_α is then dependent on the flux from and to the neighbouring facets, β and δ:

$$\frac{\partial z_\alpha}{\partial t} = R_\alpha(x) + \frac{\Omega_0}{l_\alpha}(j_{\beta\alpha} - j_{\delta\alpha}) \tag{3.3}$$

The term R_α is the direct deposition, from the gas phase, of adatoms on the facet α and for MOVPE depends on the catalytic properties of each crystallographic plane. Ω_0 is the atomic volume. For corrugations with {111}A sidewalls, the decomposition rate is larger on these than on the (001) surfaces, and these facets expand. However, this is counterbalanced by the lateral flux.

The variation of the chemical potential has several origins [175], but only two are relevant for unstrained materials like AlGaAs:

$$\mu = \mu_0 + \mu_{cap}(\gamma, \kappa) + \mu_{mix}(x) \tag{3.4}$$

The component μ_{cap} describes the *capillarity effect*, dependent on the local surface energy γ and curvature κ. Concave surfaces with high curvatures yield an increased flux resulting in a larger local growth rate. Therefore, as the bottom facet gets narrower as a result of growth rate anisotropy, the lateral flux increases due to capillarity and finally both effects compensate to yield a steady state at the center of the groove. This results in a *self-limited profile*, with the width of the central facet given by:

$$l_b^{self-limited} = \left(\frac{2\Omega_0 L_s^2 \gamma}{k_B T} \cdot \frac{r_s}{r_s - r_b} \right)^{1/3} \tag{3.5}$$

The r_i are the growth rates on the different facets (i = s: sidewalls, b: bottom-(001)) and L_s is the diffusion length on the sidewalls. This length is much larger for Ga adatoms than for Al (L_s^{Ga} is of the order of 150-200 nm on {111}A at 700 °C and L_s^{Al} is around 5 nm [177]), and thus AlGaAs layers have a much sharper profile than that of GaAs.

The initial V-groove profile usually does not have a (001) facet at its bottom. But a thick (∼200 nm) GaAs buffer is always grown prior to other layers so that AlGaAs growth proceeds on a self-limited GaAs template. The AlGaAs layer has itself a sharper profile, which forms the lower boundary of the QWR. A thin GaAs layer grown above, although not reaching a self-limited profile, has a larger bottom facet. This results in a *crescent-shaped* GaAs QWR region (Fig. 3.9(b)), which confines carriers in the two directions of the plane of Fig. 3.9 [178, 179].

The capillarity effect also participates to the gradual narrowing of the groove opening: at the top (001) facet, the convex surface triggers adatom diffusion toward the groove and thus further reduces the growth rate of the ridge compared to that of the sidewalls. Together with the growth rate anisotropy, this leads to the planarization of the surface when sufficiently thick layers are grown. This is illustrated by Fig. 3.9(c): GaAs marker layers grown every 100 nm allow to follow the growth front of a thick $Al_{0.3}Ga_{0.7}As$ layer. The sidewalls gradually shrink and finally vanish, leaving a flat (001) surface.

The different diffusion lengths of Ga and Al adatoms lead to the formation of an additional structure in the center of the groove during the growth of an alloy [180]. Due to their larger diffusivity, Ga adatoms are more effectively driven to the groove center by the capillarity. This results in a Ga-enriched region extending vertically in the groove center, with a lower effective bandgap compared to the surrounding material. This 2D structure forms a vertical quantum well (VQW) region and plays an important role in the confinement and capture of carriers in the QWR. The effective Al concentration x_{eff} of the VQW is empirically given by the relation [175]:

$$x_{eff} = \frac{x}{x(1 - K) + K} \tag{3.6}$$

where the parameter K accounts for the enhanced fluxes of Ga compared to Al, and is of the order of 2 for our growth conditions.

The last term of Eq. 3.4 has a corrective effect in the case of alloy growth. A non-uniform alloy composition on the substrate induces also a modification of the chemical potential. For the case of an AlGaAs layer, a local increase in the concentration of Ga raises the chemical potential of this species, which induces counter-fluxes to balance the

inhomogeneity.

Although giving a good description of the experimental growth profile, the model described above is simplistic as it accounts only for two types of planes: (001) and {111}A. Real growth actually develops other facets along {113} planes, both at the top and bottom of the groove. These facets actually grow in the step-bunching mode, the amplitude of which is correlated with the appearance of the self-limited profile [178]. This relation between the growth rates of the different facets is also evidenced by atomic patterns forming on the (001) ridges between the grooves. They were also explained as resulting from the fluxes between the groove facets and the ridge [181].

As we understand from the mechanisms explained above, the growth parameters have important effects on the crescent shape of the QWR and its confining properties. Otterburg [182] has studied systematically the optical properties of QWRs, whose barrier composition and growth temperature were varied. Our typical growth temperature for QWRs was 650°C and the V/III ratio were kept at 220 and 133 for $Al_{0.3}Ga_{0.7}As$ and GaAs, respectively. The residual doping in non-planar structures is much more complexe to control than in QWs, as surface kinetics play an important role in impurity incorporation [183, 184] and the best growth conditions are different for distinct crystal orientations.

The main characteristics of the QWR structures that we have grown are detailed in the Annex A.

3.1.3.3   Post-growth processing

Ridge removal

In addition to QWRs, several other nanostructures form during the growth in V-grooves (Sec. 5.1.1). In some cases, the emission from QWs spectrally overlaps excessively with the QWR emission and hides it. It is the case in particular for samples with low potential barriers (Sec. 5.2). Therefore, it is sometimes necessary to remove sections of the QWs by post-growth processing.

The method is depicted in Fig. 3.10. We first cover the non-planarized sample (a) with a thick layer of photoresist (b). This layer is then partially etched by O_2-plasma, which leaves only the resist that has accumulated in the grooves (c), thus protecting the structures grown in their center. The other parts can be etched for example with a solution of sulfuric acid (d) [185]. The ensuing PL modification is shown in Fig. 3.10(f) for a sample with 11% aluminum. One can see that the PL spectral parts that overlap with the QWR lines are largely removed. The detailed recipe is given in the Annex A.
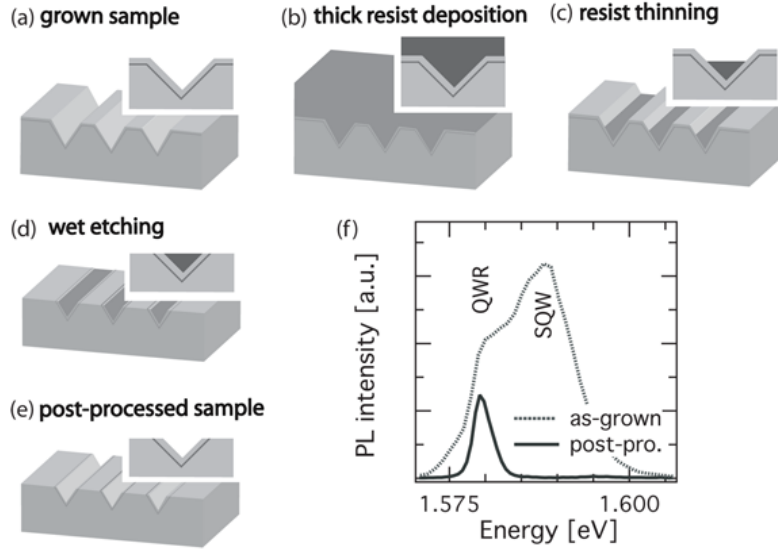
Figure 3.10: (a)-(e) Post-processing steps for edge removal. (f) PL spectra of a QWR sample, before and after post-processing.

Mask deposition

For the time-of-flight measurements of carrier diffusion that will be described in Ch. 6, optically opaque metal masks with narrow apertures are necessary. First attempts to prepare such masks were implemented by etching openings in the metal, but we finally used a lift-off process to create the desired pattern. Both methods are illustrated in Fig. 3.11.

In the first case, 700 Å Al were first uniformly evaporated on the sample surface. The apertures were then written using e-beam lithography, developed, and the Al layer was locally etched in a KOH (0.1 N, ~ 60 s) solution. As visible in Fig. 3.11, the resulting mask leads to important modifications of the PL spectra measured through the aperture (in that particular case a high-quality 15 nm QW). We identified these modifications to be due to strains induced by the large Al coverage on the samples surface. The mask design was therefore modified to keep the Al only on a reduced area around the apertures. This area was made large enough to fullfill its optical masking function (typically 20 μm margins around the apertures), but sufficiently narrow so that strain effects get negligeable.

To process this mask with a reduced Al coverage, we used a lift-off approach. The masking area were written by e-beam lithography, and developed before the Al layer was evaporated on top of the resist layer. It was then removed by lift-off, leaving Al only on the written areas. This allowed to fabricate sufficiently narrow apertures (down to ~ 1 μm). Their effective sizes slightly differed from the nominal ones, but could be easily measured by SEM. The effect of strain is strongly reduced because of the reduced area covered by Al. A small resdhift is still visible (lower right panel of Fig. 3.11), but its amplitude (~ 0.5 meV) is much smaller than the inhomogeneous broadening of the samples studied in Ch. 6 and can thus be neglected.
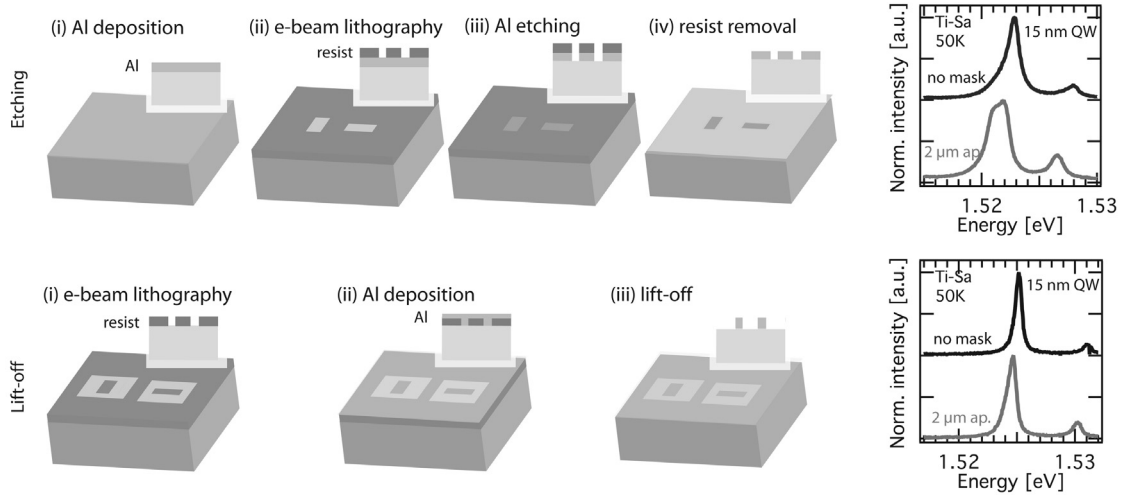
Figure 3.11: Etching (up) and lift-off (bottom) processes for mask deposition. The right panel shows in each case the resulting PL of a 15 nm thick QW measured through a 2 μm aperture in the mask and compared to that measured on the bare surface. (The two samples are different in the two cases).

Note also that on some sample, we deposited a Ti-Au (25-50 Å) coating, before depositing the opaque Al-mask, as it was (erroneously) believed to be necessary for the Al adhesion. This also changes significantly the optical properties of the samples, as it is described in Annex C. However this layer was not necessary and thus not added in the samples for which diffusion measurements will be presented.

Backetching

Finally, let us mention that we checked the possibility to apply a substrate removal procedure to our QWR samples. This *backetching* process is regularly applied to pyramidal QDs in order to improve the PL extraction efficiency [186] and as it can be seen in Annex A, it is efficient for QWRs as well. However, such samples need a different structure that requires design and growth optimization, and therefore we did not use this approach in the experiments presented later.

3.2 Structural characterization

The morphological aspects of our samples provide useful information, either to assess the quality of a patterned substrate, check the growth mode of layers or extract the dimensions of a particular structure of interest. We used information obtained from three types of microscopies during this work. If transmission electron microscopy (TEM) has been used only on few occasions, scanning electron microscopy (SEM) and atomic force microscopy (AFM) were routinely used prior to growth to control the quality of the patterned substrates and to check the samples after growth.

It is not the purpose of this section to explain in great detail these techniques. For this, we refer the reader to the review of Stangl et al. [152]. We will just give some information on AFM, as important results of this thesis were acquired with this tool, which may be subject to misleading artefacts.

The second part of this section gives some details on the method that has been used to selectively remove sacrificial AlAs layers in order to image by AFM the interior interfaces of heterostructures.

3.2.1   Atomic force microscopy

In our experiments, we used commercial AFM instruments made by Veeco (Digital Instrument, Nanoscope III) or PSIA (XE-100). AFM is now a routine tool in nanotechnology labs and we just briefly remind its principle. In this technique, a sharp ($\sim$10 nm radius of curvature) tip emerging from a Silicium cantilever is scanned over the surface of the sample. In the non-contact mode that we used, the tip is oscillating with a frequency that is modulated by interactions with atoms close to the surface. A feedback mechanism is employed to correct the tip height in order to keep it at a constant distance from the surface. An image of the surface is then reconstructed from the z-movement of the tip, which reproduces the fluctuations at the surface.
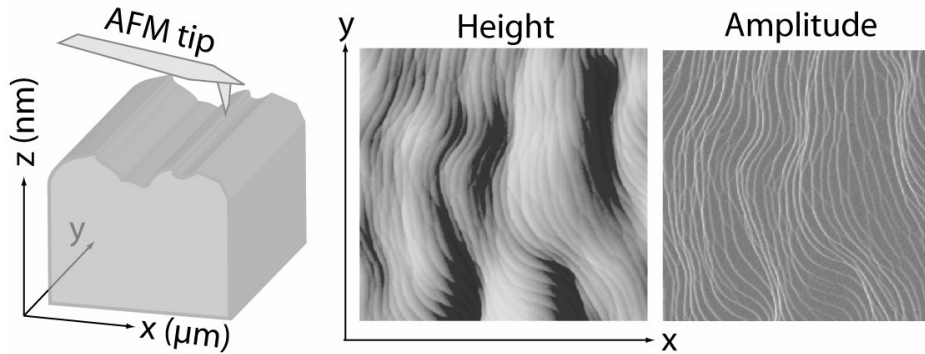
Figure 3.12: Sample AFM images of a GaAs surface, in the height or amplitude representation.

To correct non-linearities from the piezo-actuators, or a possible tilt of the sample, corrections of the AFM image have to be applied. We typically used third order flattening corrections, consisting in fitting the low frequency height modulation by a polynominal function and to substract it to enhance the short scale contrast. This has to be kept in mind when the images show certain kind of undulation, that in fact correspond to relative deviations from a regular slope.

To determine the average periodicity of the image features, we used 2D Fourier transforms, as illustrated in Fig. 3.13. It gives a direct measure of the average terrace width of planar surfaces, and allows to display clearly anisotropic patterns.
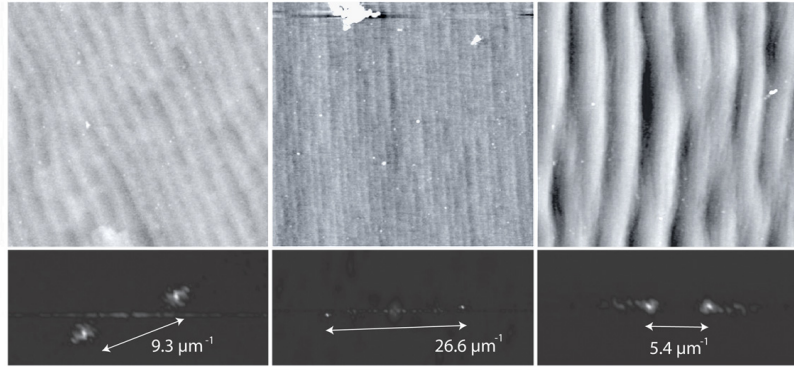
Figure 3.13: 3x3 μm^2 AFM images of different surfaces (top), and their 2D Fourier transform (bottom) allowing the determination of the surface periodicity, i.e. 216 nm, 75 nm and 370 nm. Note that the reciprocal space images have different scales.

Alternatively, the height contrast is sometimes better rendered by showing the *amplitude images*. The 'amplitude' corresponds to the feedback signal from the photo-diode monitoring the deflection of the cantilever. Thus, the quantitative information on height is lost, but boundaries at which the surface is abruptly changed (such as mono-layer steps) is better evidenced. It is particularly convenient for images of V-groove structures, for which the height fluctuations have very different scales depending on the different facets probed.

In the latter case of V-grooved substrates, the scan orientation is always set precisely parallel to the groove, so that the flattening correction is done on a fixed relative height of the surface. The ridge edges and groove bottom are regions particularly sensitive to artefact, as the part of the tip interacting with the surface abruptly changes when moving from one zone to another. For the same reason, it is not relevant to compare the roughness of surfaces that have different orientations, as their relative orientation to the tip is different. The occurrence of most of these artefacts can be checked by modifying the scan direction or using tips with different radius of curvature. In particular, ultra-sharp tips, with radius of curvature smaller than 5 nm, allow to minimize these effects.

3.2.2 Selective etching

The morphology observed on a sample surface is different from that representing the growth front during epitaxy. In particular, buried hetero-interfaces do not have the same morphology as that of a fully relaxed capping layer. A technique was developed

to uncover the interior interfaces without altering them [187]. AlGaAs layers with high Al concentration can be etched by diluted hydrofluoric acid (HF). The etching rate is highly dependent on the Al concentration in the barrier, and decreases so much with x that HF has no effect on GaAs. As a result, even large HF concentration (40%) cannot etch the 30% Al barriers of our standard TQW samples. Specific samples with high Al barriers have thus to be used. To limit hazard and reduce etching time, and to ensure an optimal selectivity between the materials, we used samples with a pure AlAs sacrificial layer. By using 10% diluted HF the etching of 300 nm AlAs is almost instantaneous, and the selectivity on GaAs is virtually perfect.

This perfect selectivity has been demonstrated in Ref. [187] and we further checked it on our samples. Even by dipping the sample for several seconds in HF, the etch systematically stops at the QW depth and the uncovered surface morphology is independent of the etching time. The surface then remains stable over days, signaling that the surface is purely GaAs as no oxid forms. As it was checked by imaging the GaAs cap before and after etching, the GaAs morphology is preserved at the atomic level, thus ensuring that the imaged surface is exactly the one forming the QW. In spite of precautions and clean environment, dusts and etch residual may still locally contaminate the surface.

The inverse (AlGaAs) interfaces can be studied in the same way. We proceed similarly by covering the $Al_{0.3}Ga_{0.7}As$ layer, whose surface we want to image, by an AlAs sacrificial layer. The selectivity is still extremely good when using a slightly more diluted (1.5%) HF solution during 5 s.

As AlGaAs layers oxidizes rapidly, all samples are covered with a GaAs cap (10-30 nm). It is removed prior to the HF etch by a solution of $NH_3(30\%)$ strongly diluted in $H_2O_2(25\%)$ (1:150) so that the pH is neutral. For a 30 nm cap the etching time was 60 s, the surface turning violet once the GaAs has been removed. The AlAs layer has to be removed immediately afterwards, to prevent oxide formation.

In Annex B we briefly report the application of this sacrificial etching technique to non-planar samples. Its validity for non-(001) orientations has however not been checked, thus interpretation is reserved to the ridge facets.

3.3   Photoluminescence spectroscopy

We performed essentially four types of optical experiments: standard (macro) photoluminescence (PL), photoluminescence excitation (PLE), micro-photoluminescence (μPL) spectroscopy, and time-resolved micro-photoluminescence (TR-μPL) measurements. Whereas PL and PLE give general spectral informations, μPL provides spatially resolved spectra at the micron level, allowing to investigate specific locations or structures on the sample. TR-μPL additionally delivers information on carrier dynamics. Unless specifically stated, all measurements are performed at 10 K.

The physical mechanism linked to light-matter interactions have been described in Ch. 2. In this section, we describe the experimental setups used for the optical characterization.
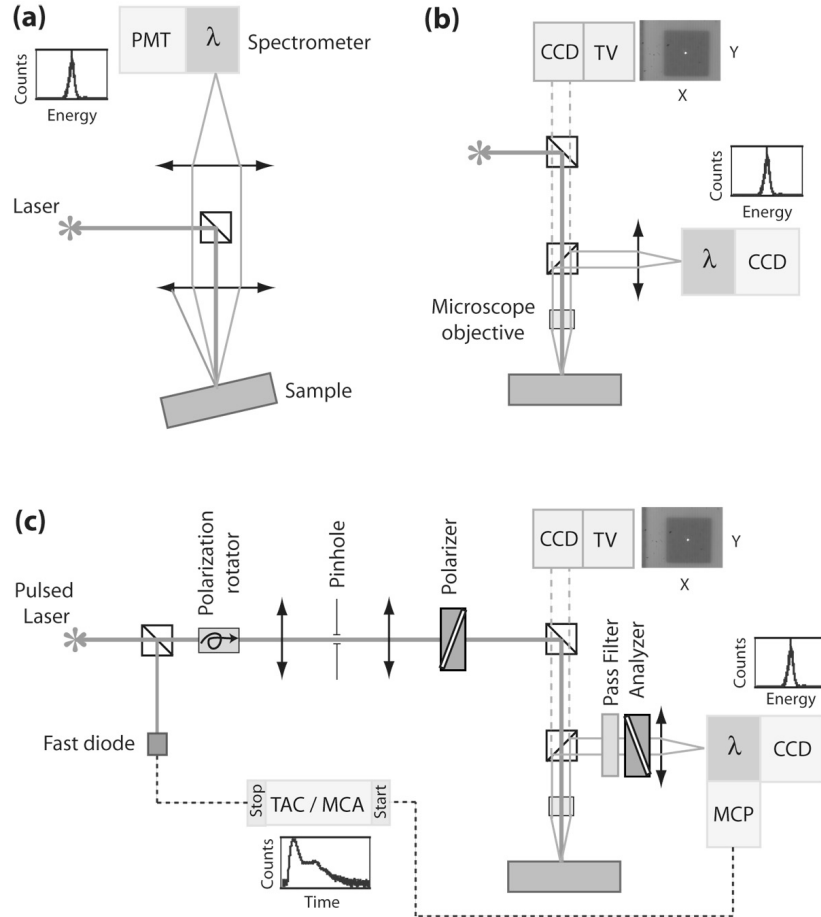
Figure 3.14: Schematics of the optical setups for (a) PL/PLE (b) μPL and (c) TR-μPL.

3.3.1 Standard photoluminescence

The setup used for standard PL characterization is shown in Fig. 3.14(a). The light is excited with either the green (514 nm) line of an argon laser (Ar+, Coherent Innova 400) or that of a titanium-sapphire laser (Ti-Sa, Coherent MIRA 900) tunable in the range 690 nm - 840 nm in CW operation. In the second case, the Ar+ laser is used to pump the Ti-Sa crystal.

The beam is focused to a $\sim$30 μm diameter spot on the sample surface by using an f = 80 mm lens, which in turn is used to collect and collimate the luminescence. It is then focused on the entrance slit of a double spectrometer (Spex 1404) by an f = 30

cm lens, and dispersed towards a Peltier-cooled photomultiplier tube for detection. The best spectral resolution achieved is about 150 μeV.

Several samples can be mounted in a helium-flow cryostat (Janis Research Corp.) and their temperature can be varied in the range 5 K - 300 K. To avoid reflection of the exciting beam entering the spectrometer, the samples are slightly tilted ($\sim$10°). Excitation powers quoted in PL experiments are measured just before the focusing lense. A typically employed 50 μW nominal power corresponds to an excitation density of the order of 5 W/cm^2. An example PL spectra from a triple QW sample is shown in Fig. 3.16(a).

3.3.2 Photoluminescence excitation

The setup for the PLE experiments is the same as for the PL measurements, but in this case the spectral resolution is determined by the laser linewidth; the typical resolution is thus $\sim$500 μeV. PLE allows to probe the higher energy levels of a structure, in analogy to absorption measurements. Assuming an ideal relaxation of carriers to their ground state, from which they recombine radiatively, the measure of the lowest transition PL intensity is equal to the absorption at the excitation energy (Fig. 3.15). This hypothesis is mostly verified. At low temperature, however, relaxation effects may have non-negligible effects, for example on the intensity of the first PLE peak, which depends on the detection energy [139, 188].

Practically, the spectrometer is set to measure the intensity at a fixed energy, while the excitation wavelength is scanned. As the output power of the laser is varying with wavelength, as represented in Fig. 3.16(b), one needs to renormalize the experimental PLE curve to account for these variations, in order to analyze it in analogy to an absorption spectra. An example of such a renomalization is shown in Fig. 3.16, but unless specified, this procedure will not be systematically applied to the PLE spectra presented in this thesis. Indeed, we will mainly be interested in identifying resonances, for which no renormalization is needed.

3.3.3 Micro-photoluminescence

The experimental arrangement for μPL spectroscopy is schematized in Fig. 3.14(b). The exciting laser beam is here focused with a microscope objective (Zeiss, x50, NA = 0.5) allowing a spatial resolution of about 1 μm for the Ar+ spot and 1.5 μm for the Ti-Sa one. The emitted PL is collected by the same objective lens and directed toward a spectrometer (Jobin Yvon HR460), at the entrance of which the PL is focused by a f = 40 mm lens. The spectra are recorded on a CCD array after dispersion by a 1200 l/mm grating, corresponding to a maximal spectral resolution of 150 μeV.
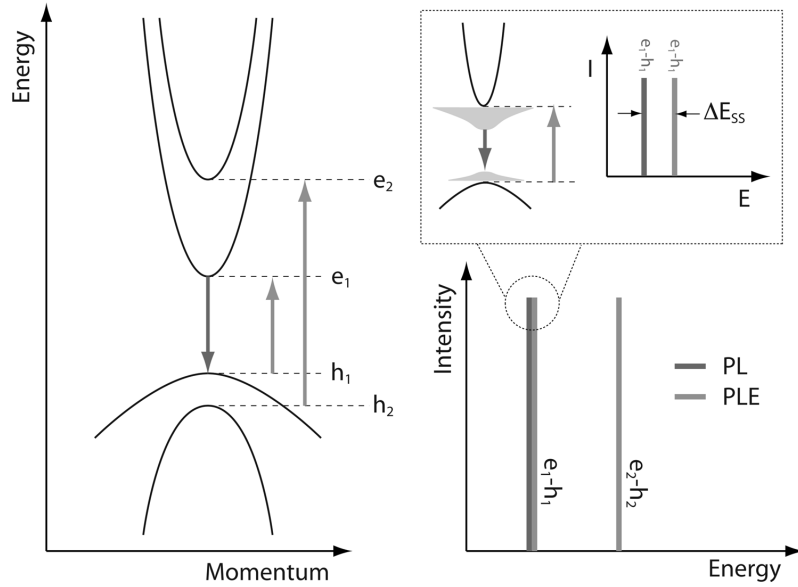
Figure 3.15: Principle of PLE measurement: the detection energy is fixed to measure the ground states transition ($e_1 - h_1$). The excitation energy is scanned through the higher index transitions. The PL intensity is proportional to the absorption, especially strong at resonances. The inset illustrates the Stokes shift ΔE_{SS} (see Sec. 2.3.3): it corresponds to the energy difference between the emission from localized states and the absorption at the band bottom.

The samples are fixed with silver glue on the cold finger of a He-cooled cryostat (Cryovac), fixed on a x-y piezo-stage for precise positioning. The microscope image is monitored on a screen to correctly position the excitation spot on the sample.

3.3.4   Time-resolved micro-photoluminescence

The temporal decay of the photoluminescence is determined by measuring the time interval between an exciting pulse and the emission of a photon. When set to the picosecond configuration, the MIRA laser delivers short pulses at a frequency of 78 MHz. Its spectral tuning range is then slightly reduced: the smallest wavelength at which it was operated in this mode-locked mode was 710 nm. Several optical elements have to be added to the setup (Fig. 3.14(c)) in order to: (i) controle the spot shape; (ii) reject laser reflections from the measured signal.

The mode-locking mechanism of the MIRA laser uses narrow slits in the laser cavity, which also induce a diffraction of the beam. To obtain a clean gaussian shaped spot on the sample, the beam is spatially filtered by a 50 μm pinhole inserted between two f = 120 mm lenses. The pinhole acts as a new source and the second lens allows to correct the beam divergence for focusing the laser in the same image plane as the sample surface.

In the μPL cryostat the sample cannot be tilted without losing imaging contrast on
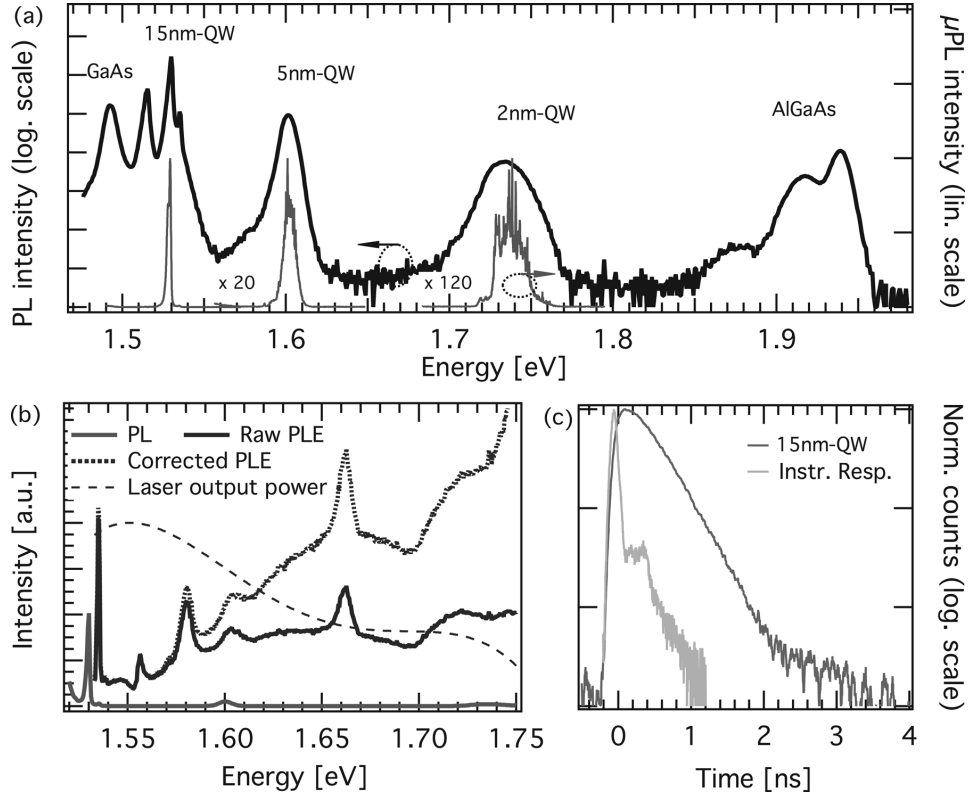
Figure 3.16: Example of the different optical measurements performed on a TQW sample: (a) Ar+ PL; (b) Ti-Sa PL and PLE with an example (c) of intensity correction to account for the variation of the laser output; (d) μPL and (e) TR-μPL where the instrumental response is also displayed.

the microscope CCD, which makes the spatial positioning difficult. To attenuate laser reflections at the spectrometer entrance, we used a polarizer in the excitation path (which removes unpolarized fluorescence) and a cross-polarized analyzer before focusing on the spectrometer slits. In addition, we used different beam splitters and low-pass filters to optimize rejection according to the PL energy.

For time-resolved acquisition, we use a Peltier-cooled multi-channel plate (MCP, Hamamatsu). The spectral range over which the signal is integrated is determined by slits in the focal plane of the spectrometer. The MCP signal (after noise discrimination) provides the stop pulse on a time to amplitude converter (TAC, Tennelec). The start signal is delivered by a fast photodiode triggered by a fraction of the exciting pulse. The TAC signals are sorted in a multi-channel analyzer (MCA, Oxford), which after time calibration displays the photon arrival time distribution. Accounting for the instrumental response depicted in Fig. 3.16(c), we estimate the time-resolution of the setup to about 20 ps.

Chapter 4

Quantum well heterostructures: disorder at vicinal interfaces

The homogeneity of quantum wells (QWs) has benefited from constant progress since the first structures were grown in the 1970's. Amongst the indicators of QW quality, the broadening of the PL line has always been the most widely used, because it is the most straightforward. Yet, the relationship between the interfaces of QWs and the resulting PL has been at the center of rich debates. A paper from 1990 resumed the main interrogation in its title: "Does luminescence show semiconductor interfaces to be atomically smooth ?" [189]. Since then, investigations evidenced interfaces, whose roughness covers different length scales and stems from various phenomena occuring during growth [11, 12, 99].

The growth of high-quality samples by MBE often relies on growth interruptions at the interfaces, but this technique is less efficient in the case of MOVPE [16]. Instead, attempts were made to control the growth by using vicinal substrates. Growth on substrates with a large miscut angle off the (001) crystal planes are known to reduce the incorporation of impurities into the crystal [201]. But smaller miscuts have attracted considerable interest, because they allow to impose on the system a length scale different than its 'natural' one, set by the diffusion length of adatoms. Different morphologies were observed on vicinal surfaces [170, 171, 202, 203] and many efforts were devoted to understand how they could affect the physical properties of the samples [199, 204–208]. The interpretations were often ambiguous, either because of the contribution of other phenomena, or because the surface morphology of the samples was used to interpret the results.

Recently, our group reported a striking reduction of the PL linewidth of GaAs/AlGaAs QWs grown by MOVPE [209]. The values obtained are comparable to those of the best structures grown by MBE (Fig. 4.1). This improvement was made possible by the combined use of high V/III ratio and of vicinal substrates. In this chapter, we present a detailed study of the dependence of the optical properties on the miscut angle of the substrate. We show that, for given growth conditions, small variations in the sub-
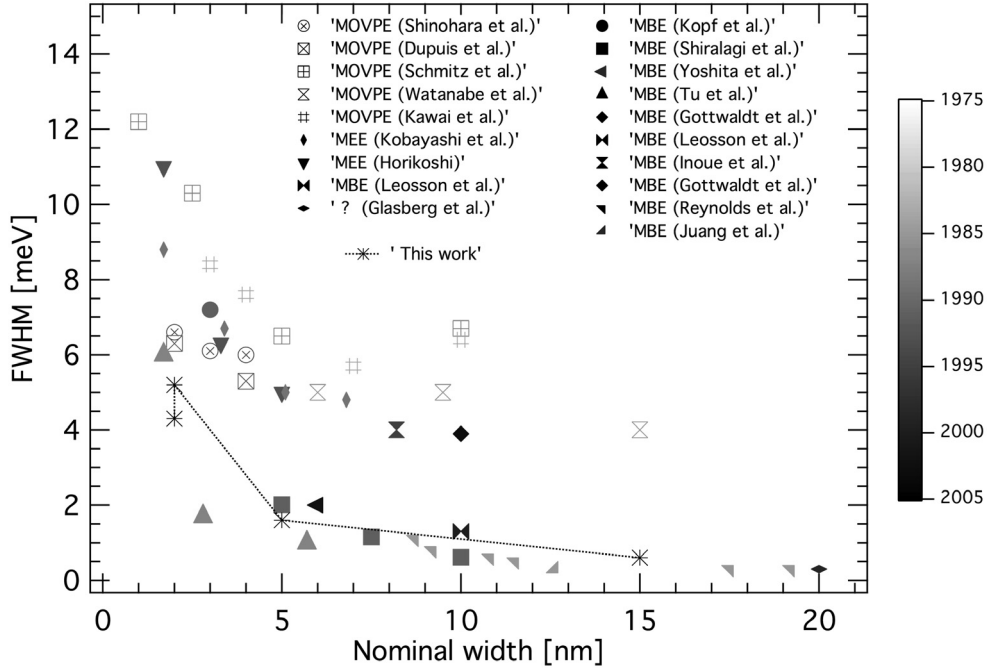
Figure 4.1: Overview of the PL linewidth of GaAs/Al$_x$Ga$_{(1-x)}$As QWs of different widths (and various x) grown by MBE or MOVPE over the years. Full (empty) symbols correspond to MBE (MOVPE) grown samples and their grey level indicates the year of publication, from the older ones (light grey) to the more recent ones. Compiled from Ref. [16, 17, 19, 24, 79, 190–200]

strate misorientation infer large changes in the optical properties of QWs grown by MOVPE (Sec. 4.1). We establish that they can only be explained by changes in the interface structure, which we observe by atomic force microscopy (Sec. 4.2). We make a direct correlation between the interfaces morphology and the optical properties of QWs grown on vicinal substrates, and explain why so good optical results can be obtained with MOVPE. Finally, we also discuss some aspects of MOVPE growth revealed by AFM images, in light of the existing growth models (Sec. 4.3).

4.1 Dependence of the optical properties on the substrate miscut

We investigated samples containing three QWs of 15, 5 and 2 nm thickness grown between Al$_{0.3}$Ga$_{0.7}$As barriers on (001) vicinal substrates (TQW structures, see Annex A). Due to the large number of samples, several runs were necessary, but an identical reference substrate was systematically used to check the reproducibility of the growth. The nominal misorientation of the substrates spanned the range between 0°('exact' (001)) and 8° toward [110], thus leading to the formation of A-steps on the surface. We have already mentioned that A-steps are usually smoother than B-steps, and they are therefore expected to result in better-defined QW interfaces.

4.1.1 Optical properties

The low-temperature (10 K) PL spectra of the grown samples are displayed in Fig. 4.2(a) on logarithmic scale, as the emission intensity of the deeper, narrow well is about two orders of magnitude weaker than that of the top 15 nm QW. Three emission lines, emanating from the 15, 5 and 2 nm thick QWs and flanked by features from the bulk GaAs (buffer and substrate) and AlGaAs (barriers), can be observed. The PL was excited with the Ar+ laser at a power of 50 μW.

There are significant differences between the spectra of the samples: if most QWs emit around the expected energy (1.53, 1.61 and 1.74 eV for the 15, 5 and 2 nm QW, respectively), with minor fluctuations, the samples grown on substrates with a miscut between 0.6° and 1.2° show QWs emission that are shifted toward lower energies, while at the same time their lineshape changes completely. Oppositely, there is a narrow range of angles, around 0.2°, for which the QW PL line is slightly blueshifted and is much narrower compared to the other miscuts.
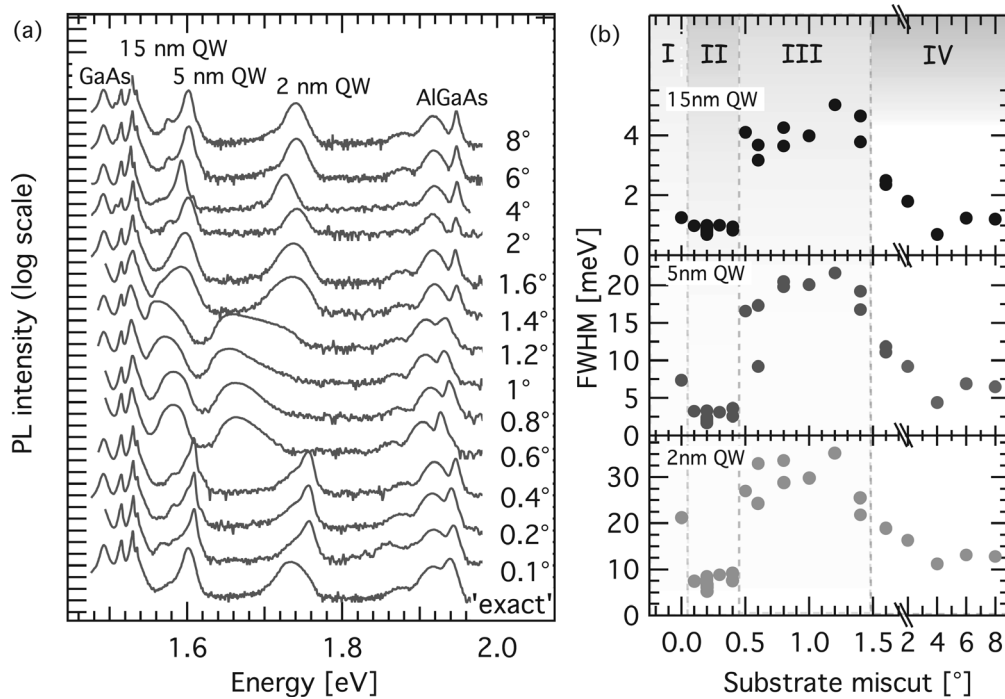
Figure 4.2: (a) Low temperature (10 K) PL spectra of TQW structures grown on substrates with different miscuts. (b) Variation of the QW FWHM as a function of substrate miscut. All miscuts are relative to the (001) plane toward [110].

The FWHM of the PL of the QWs is displayed as a function of the miscut angle in Fig. 4.2(b) for QWs of different thicknesses. All three kinds of QWs show the same

behavior: for nominally exact samples, the linewidth is moderate and decreases with increasing miscut angle to reach a minimum around 0.2°, for which the best values are 0.6, 1.6 and 5.2 meV for the 15, 5 and 2 nm QWs, respectively. For intermediate angles (∼0.4° - 1.4°), the lines broaden importantly to reach values more than twice those obtained on 'exact' substrates. Above about 1.4°, the FWHM decreases again and is then more or less constant for larger miscut angles, setting at values between those of 'exact' and 0.2°-off samples. Accordingly, we divided the angle range into four domains I to IV delimited in Fig. 4.2(b).

The features of the bulk materials are also affected by the substrate miscut. Weak differences are seen between the GaAs emission of the different samples, but the Al-GaAs PL lineshape shows significant variations, reported in Fig. 4.3. The AlGaAs emission consists of spectral features due to recombination of bound excitons (BX), donor-acceptor pairs (D-A) and phonon replica ($\phi_{replica}$). The FWHM of the bound exciton line follows a non-monotonous dependence on the substrate miscut. From about 9 meV on 'exact' substrates, it reduces down to 5 meV before increasing again to more than 12 meV for the 1.2°-off sample and finally decreasing abruptly to reach its smallest value (3 meV) for larger miscuts. Although the behavior is similar to that of the QWs, we note that: (i) the local minimum for small miscut is extended over a larger angle range than for the QWs; (ii) large FWHM values are obtained only within a narrow angle range as compared to QWs; (iii) the narrowest linewidths are obtained for large miscut angles.
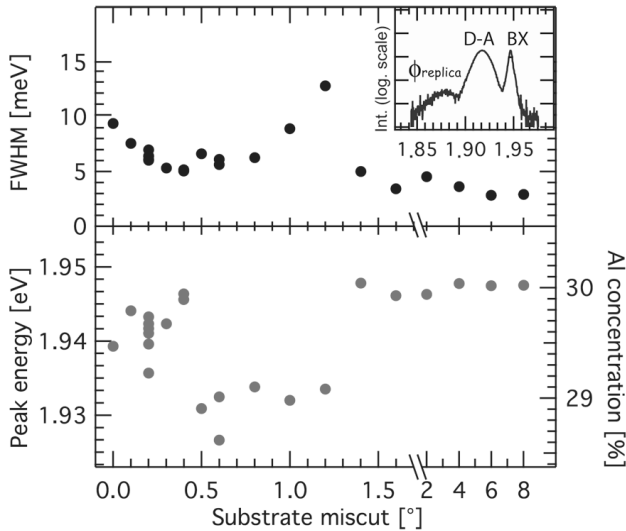
Figure 4.3: Linewidth and peak energy of the PL line of the exciton bound to impurity in the nominally 30% AlGaAs barriers. The inset shows the AlGaAs emission lineshape: bound exciton BX, donor-acceptor (D-A) and the phonon replica.

In the lowest panel of Fig. 4.3, it is seen that the peak energy of the AlGaAs is also strongly modified by the substrate miscut. In the range between 0.5° and 1.2°-off, it is about 10 meV lower than for other angles. This corresponds to fluctuations close to 1% in the Al-content of the barrier. Nevertheless, the variations from growth to growth can be rather large (the 0.2°-off samples are distributed within 8 meV). Also, we underline that the fluctuations of the FWHM and of the energy are not exactly correlated. Still,

the FWHM of the lines emitting at the highest energy (for samples with miscut $> 1.5°$) are the narrowest ones. This can be interpreted as a result of the competition between Al atoms and impurities to incorporate into the crystal.

PLE measurements of the 15 and 5 nm QWs on a typical sample from each angle domain are shown in Fig. 4.4. The first heavy (hh) and light hole (lh) excitonic transitions are well resolved and their broadening mimics that of the PL lines.

The ratio between the intensity of the hh and lh transitions of the 15 nm QWs is comparable for all samples. In the case of the 5 nm QW, there are differences. The ratio is larger for the 0.2°-off sample. Inversely, the $e_1 - h_1$ transition disappears for the 0.6°-off sample. In that case, two PLE spectra are shown, corresponding to different detection energies: one at the peak and the other 15 meV below, in the low-energy tail of the PL spectra. No other transition is detected in the latter case.

We note that the low-energy PL tail of all 5 nm QWs exhibit shoulders at 1.58 eV, actually corresponding to the PL peak energy of the 0.6°-off sample. We attribute these shoulders to impurities and the correspondance of energies to a pure coincidence. Under this assumption, all PLE resonances remarkably appear at the same energy. The shift of the PL energy between the samples thus corresponds to a Stokes shift.
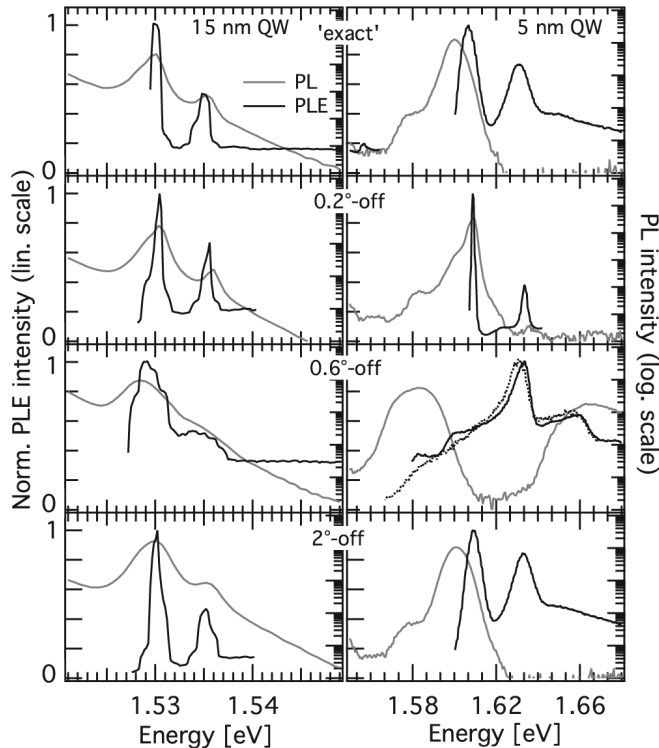
Figure 4.4: 10 K PL ($\lambda_{exc} = 700$ nm, 200 μW) and PLE spectra of four samples with different miscuts, for the 15 nm and 5 nm wide QWs.

4.1.1.1 Dependence on the excitation conditions

The systematic investigation of the optical spectra requires the definition of standard conditions. All the PL measurements reported above were made at 10 K with an Ar+

laser photoexcitation creating carriers in the barriers at an excitation density of about 2.5 W/cm^2 (corresponding to a 50 μW beam intensity). In Fig. 4.5(a), we present the FWHM of the three QWs of a 0.3°-off sample as a function of the excitation power, varied over 5 orders of magnitude. We observe slight variations of the FWHM with excitation density for the two thinnest wells, mainly due to variations in the low energy tail. The dependence for the 15 nm QW is much more pronounced. The PL spectra are shown in panel (b). At low power, the main excitonic line does not change. The dotted line, corresponding to a gaussian line, fits nicely the high-energy side of all spectra up to 50 μW excitation. However, at very low excitation power, the emission displays an additional low energy peak, separated by 1 meV. This peak is broader than the exciton line and exhibits some additional unresolved features. Its relative intensity decreases with increasing power and gets minimal in the 50 μW spectra. Upon further increase of excitation, another low-energy shoulder develops, with a slightly larger energy separation. At the same time, the exciton line also broadens on the high energy side, and emission from the light hole state becomes visible at 1.536 eV.
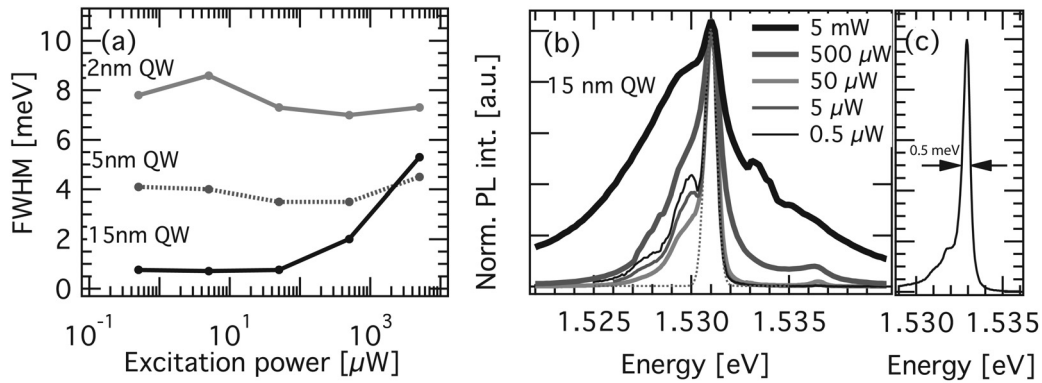
Figure 4.5: (a) Power dependence of the FWHM of the PL of QWs grown on a 0.3°-off substrate. (b) Spectra at different excitation power for the corresponding 15 nm QW. (c) Record low-linewidth PL spectra, measured with an excitation power of 5 μW, at 10 K, on a 0.2°-off sample.

The temperature dependence of the PL spectra is shown in Fig. 4.6(a), for all three QWs grown on a 0.2°-off sample. The spectra are here displayed in logarithmic scale and clearly exhibit a thermal exponential high-energy tail, and a low energy tail, indicating effects of impurities and localized states. The lineshape asymmetry reduces with increasing temperature: at 10 K, the PL spectra of the 5 nm QW exhibits a shoulder similar to that reported for the 15 nm QW. It saturates with increasing excitation and temperature and has an energy separation of about 2 meV. A similar but not completely resolved feature can be distinguished on the 2 nm QW PL line at 10 K. These complex lineshapes and the rapid change in the relative intensity between the peaks induce a non-monotonous dependence of the FWHM with temperature, as reported in Fig. 4.6(b). The saturation of the low-energy component first leads to a decrease in the apparent FWHM, before it increases above 20 K, because of the thermal occupation of the higher

energy states. At 25 K, the emission from the low-energy states is completely quenched.
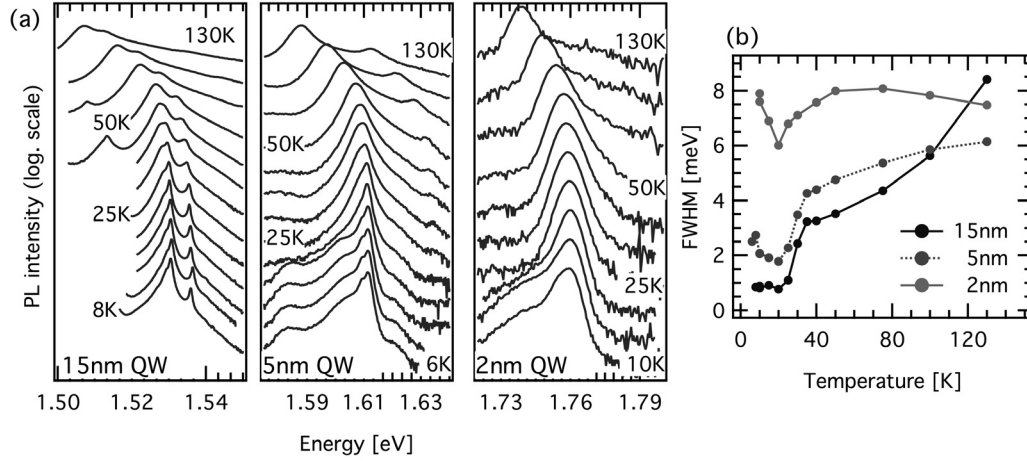
Figure 4.6: (a) Temperature dependence of the PL spectra of the three QWs grown on a 0.2°off substrate. (b) FWHM as a function of the temperature.

These effects are best evidenced on samples of the miscut domain II, with narrow linewidth, and do not affect as much QWs with broader linewidths. The choice of 50 μW excitation at 10 K corresponds to the minimization of the low-energy tail of the best 15 nm QW, but is somehow arbitrary. The narrowest linewidth reported in these conditions is 0.6 meV but the absolute minimum of 0.5 meV was obtained at 5 μeV excitation on a 0.2°-off sample (Fig. 4.5(c)). Note that we did not systematically fitted the data to extract the linewidths, as the lineshape is clearly non-gaussian at low-temperature. We thus point out that the values reported throughout this study are a good characterization of the sample optical properties, but should be considered with care when their absolute values are discussed.

4.1.1.2 Observation of exciton complexes

The importance of the excitation energy has also to be stressed, as it is related to the appearence of a charged excitonic complexe. Fig. 4.7(a and b) shows the μPL spectra of a 15 nm QW grown on a 0.2°-off substrate, with different excitation conditions. In the panel (a), the thick lines correspond to excitation below the barriers. The dotted-line spectra were obtained by additionally shining light with a large spectrum lamp ('white light'), thus generating carriers in the barriers. The difference is striking: for below-barrier excitation, the μPL is strongly (>1 meV) redshifted and rather broad (1.8 meV FWHM). With increasing power, the line slightly blueshifts and a shoulder appears at higher energy. This shoulder corresponds to the narrow exciton line, as evidence by Fig. 4.7(b), in which spectra obtained with 'white light' excitation of increasing intensity are superposed to spectra obtained with Ar+ laser excitation. For weak 'white light'

excitation, the spectra is comparable to that obtained with Ti-Sa excitation. With additional excitation intensity, the situation is similar to that described in standard PL, in which a large low-energy shoulder increases with excitation power.
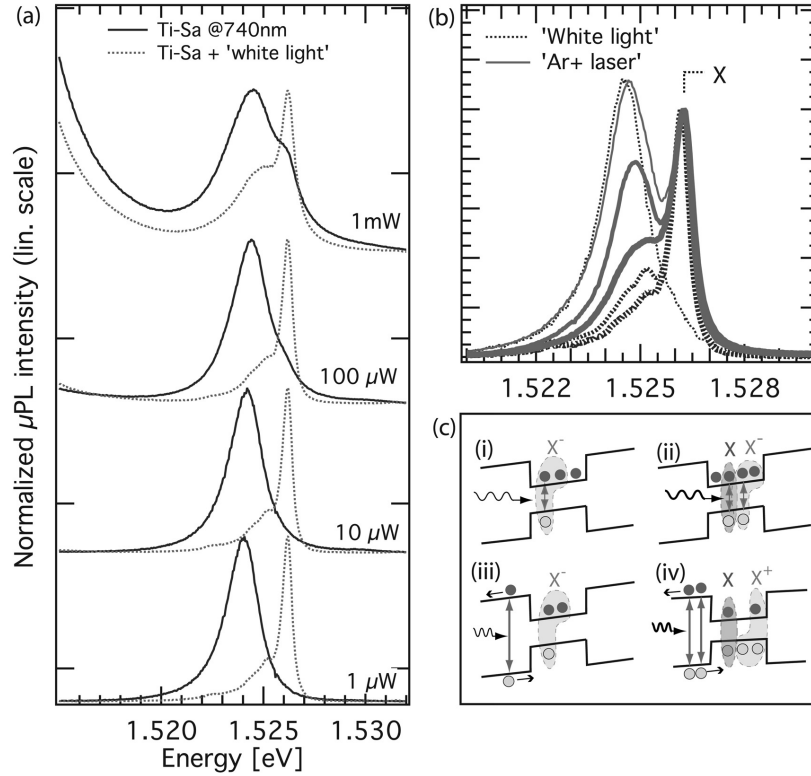
Figure 4.7: (a)μPL spectra of a 15 nm QW (0.2°-off) excited below the barrier (740 nm) with increasing power. The dotted line shows the effect of an additional excitation above the barriers. (b) The same QW excited above barrier at different densities. Dotted lines stands for excitation of a large area with a 'white light', continuous lines are for localized excitation with the Ar+ laser. Increasing line thickness corresponds to increasing intensity. (c) Illustration of the charged excitons formation mechanism discussed in the text, with two initial excess electrons.

Spectral lines appearing on the low-energy side of excitons have been reported in several systems, and were attributed to diverse origins. They could correspond to emission from QW area of different thickness, excitons localized by potential fluctuations [210–212], excitons bound to impurities [213], or excitons complexes [131, 214, 215]. In our samples, the energy separation ($\sim$1.2 and 2 meV for the 15 and 5 nm QWs) rules out thickness differences. Localized excitons can be rejected in regard of the discussions later in this chapter. The particular behavior that we observe when varying the excitation conditions (first the saturation of the low-energy component and then the increase of another line) suggests the formation of two types of excitonic complex.

If electron-hole pairs bind to excess charges in the QW, they form a charged exciton.

As the number of excess charges is fixed by the residual doping, the charged exciton line saturates at increasing excitation power. A further increase in intensity may lead to the formation of biexcitons. A biexciton is yet expected to have a larger binding energy than a charged exciton [129]. This fact does not fit our observations. One may therefore consider the saturation of one type of charged exciton (say negatively charged), before the other type (positively charged) gets dominant. The binding energy of negatively charged excitons is known to be larger than that of positively charged excitons in QWs and disorder induced QDs [129, 131], although the values are very close to each other [194].

In order that this interpretation fits our observations, it requires the assumption of an initial excess density of electrons in the QW, and an increasing number of holes with increasing excitation density. Two mechanisms can be imagined to provide excess charges to the QW. First, the charges can be due to the residual background doping, independently of the excitation conditions. Second, one-type of charge can be preferentially captured due to a built-in electric field.

The first mechanism does play a role in our structures, as we observe the low-energy line when we excite below the barriers. The second mechanism is also probably active, as proved by the strong effect of the above-barriers excitation power. The small shifts visible with increasing excitation power also support this affirmation.

This mechanism is illustrated in Fig.4.7(c): weak excitation leads to the formation of negatively charged excitons due to the presence of excess electrons (i and iii). Additional holes created by increased excitation bind to form neutral excitons, coexisting either with negatively (ii) or positively (iv) charged excitons depending on the band bending and excitation wavelength.

Fig. 4.8 displays the temperature dependence of the PL spectra of the 15 and 5 nm QWs, both grown on a 0.2°-off substrate. The excitation dependences of the spectra at 10 K are also shown. These particular samples were coated by thin Ti / Au layers to screen out the internal electric fields formed due to charges around the QW layers (cf. Annex.C). The samples were excited with a Ti-Sa laser at 735 nm, creating carriers directly in the QWs. As a result, at 10 K, even in this below-barrier excitation condition, the exciton line has an intensity almost comparable to that of the charged exciton. The non-monotonous evolution of the low-energy component with excitation density is evident. Also, the disappearance of the low-energy line with temperature corresponds to an ionization of the bound complexes, consistent with the binding energy.

Yet, similar behavior might be expected for excitons bound to impurities. A definite attribution of the PL lines that we observe would require more sophisticated measurements. Impurity-related transitions could be investigated by intentionally doping the samples. Distinguishing between positively and negatively charged excitons or even biexcitons could also be attempted by measuring the PL under a magnetic field
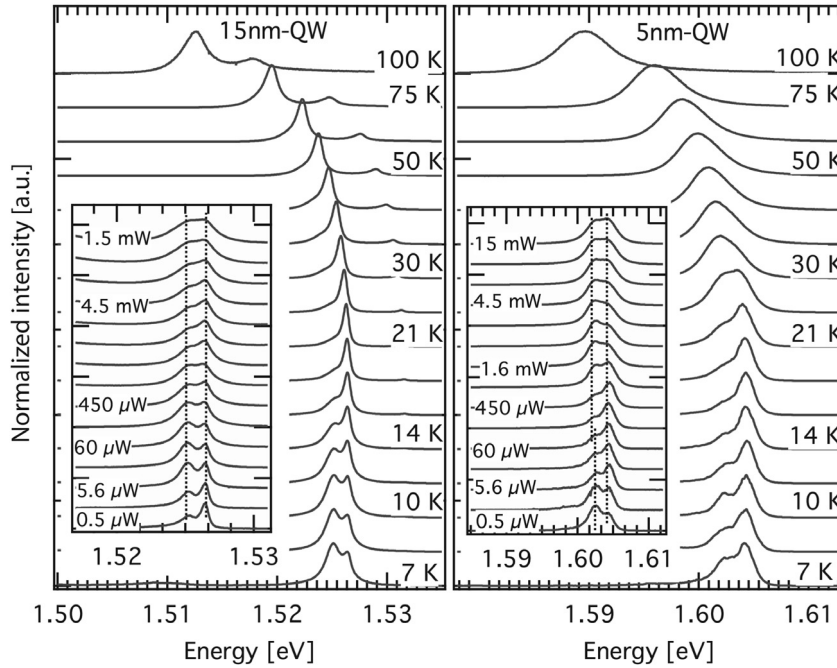
Figure 4.8: Temperature dependence of the μPL spectra of two QWs of different thickness, grown on 0.2°-off susbstrates, and excited below barriers at 1.687 eV. On these particular samples, additional metallic coating has been deposited, which screens internal electric fields (see Annex C). The insets exhibit the power dependence for similar excitation conditions, measured at 10 K.

[194, 216]. Still, the larger linewidth of the low-energy line is more consistent with exciton complexes than with bound excitons [217].

4.1.2   Origins of the minimal linewidth for 0.2°-off samples

The data presented above show specific trends compared to existing reports on the PL spectra of QWs grown on vicinal substrates:
    - the variation in the features that we described is not monotonous with vicinality;
    - the trend in variation is similar for QWs of very different width;
    - the amplitude of the spectral variations, both in linewidth and energy, is very large.

We now adress the possible contributions to the inhomogeneous broadening, and how they could be affected by the surface miscut. We discuss residual doping, alloy quality and interface roughness.

4.1.2.1   Doping

Doping depends on the surface miscut [184, 218] as a result of the competition between the crystal adatoms and the impurities for incorporation at the steps. Large background

doping results in linewidth broadening and possibly in a redshift due to bandgap renormalization. But the amplitude of the shift (the 2 nm QW PL covers a 100 meV energy range) makes this hypothesis very unlikely. Indeed, on the PLE spectra of Fig. 4.4, the hh- and lh-excitonic transitions of the 15 nm QWs have similar intensity ratio for the different samples. This indicates that the residual doping in all these structures is small and cannot be responsible for the large differences in linewidth observed between samples. Also, the miscut-dependent variations in the optical properties were also observed for samples grown at smaller V/III ratio, which is assumed to lead to higher residual doping concentration [219].

Small differences of the doping according to the miscut cannot be completely ruled out. It might be a reason for which the intensity ratio of the heavy and light hole transitions vary slightly for the 5 nm QW. Nevertheless, this effect is marginal and doping is unlikely to be the cause of the differences bewteen the samples.

4.1.2.2   Alloy quality

For the same reasons as those just mentioned, alloy crystals grow differently, depending on the substrate orientation [44]. The alloy quality of the barrier may have an important contribution to the inhomogeneous broadening of the QW PL. We reported in Eq. 2.29 a result of Singh [122] allowing to evaluate the alloy disorder contribution to the total broadening of a QW PL. According to this, from the worst value of AlGaAs linewidth that we measured ($\sigma_B = 13$ meV), the alloy related contribution is 0.7, 3.3 and 7.8 meV for 15, 5 and 2 nm wide QWs, respectively. This is much smaller than the differences that we observe between the best and the worst samples linewidth (4.9, 20.4 and 30 meV, respectively).

Also, comparing the miscut angle dependence of the AlGaAs linewidth (Fig. 4.3) and of the QWs (Fig. 4.2(b)), it is clear that they are not correlated. We thus reject the alloy broadening as the source of the linewidth fluctuations with miscut angle.

4.1.2.3   Interfaces roughness

We now consider the influence of the interfaces roughness on the linewidth. Monolayer fluctuations of the width of the 15, 5 and 2 nm QWs correspond respectively to 0.5, 6 and 22 meV. These values are similar to (for the 15 nm QW) or larger than (for the 5 and 2 nm QWs) the FWHM of the best QWs, but much smaller than those of the worst ones. Such differences should manifest in the topology of the QW interfaces.

Several authors [199, 204, 206] presented studies of roughness effects on QW optical properties, based on the sample surface morphology. However, it has been shown that surface morphology differs from the real hetero-interfaces of the QWs [187]. We therefore have to investigate the morphology of the real interfaces of QWs, by using modified samples.

4.1.3   Optical properties of double-QW structures for morphology investigations

In order to image the real hetero-interfaces of the QWs, we used the method described in Sec. 3.2.2 to remove the barriers. To ensure a perfect selectivity of the etch, we used a modified design of the samples, consisting of double QWs (DQWs, with 15 and 5 nm thick QWs), the upper one (QW1) being caped by a 300 nm AlAs barrier and a 30 nm GaAs cap. The upper QW was devoted to morphology characterization, whereas the deeper one (QW2) was used to investigate the optical properties. To guarantee similar interfaces for both QWs, we added 5 ML AlAs on the top of QW2; this reproduces interfacial effects such as segregation, and saves a lengthy optimization of the AlAs growth, while maintaining a good optical quality. Except for this layer, the Al content in the AlGaAs barriers was kept at 30% and other growth parameters were kept similar to those of TQW structures.
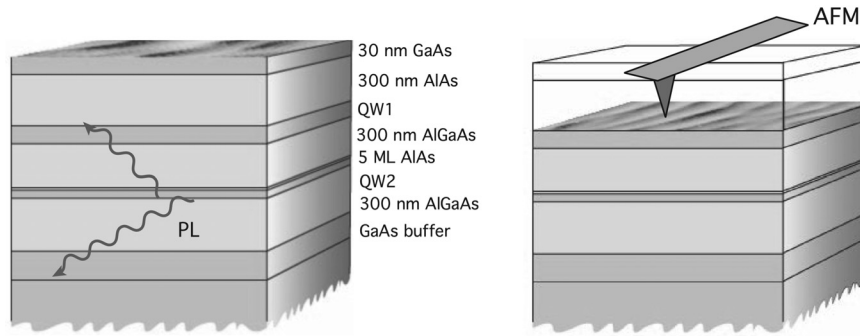
Figure 4.9: DQW sample structure. QW2 is used for optical studies while the upper barrier of QW1 is removed to allow imaging the hetero-interface.

The sample structure and the method are illustrated in Fig. 4.9. We grew these DQW structures simultaneously on four types of substrates corresponding to the four miscut angle domains identified previously. Similar samples were made to study the QW lower interfaces, in which the $Al_{0.3}Ga_{0.7}As$ was directly covered with AlAs.

On panel (a) of Fig. 4.10 we display the PL spectra of the 5 nm QW2 of the DQW structure. The FWHM is compared in panel (b) to the typical values of 5 nm QWs grown in TQW samples. The tendency observed for the PL linewidth of TQW is also found for DQWs, with the 0.2°-off samples exhibiting systematically narrower emission lines. The redshift of broader lines is also systematically reproduced. Slightly broader and shifted lines compared to those of the optimized TQW samples are attributed to the thick AlAs layer grown on top of QW2. The growth of this AlAs layer is not optimized; this layer may be doped and internal fields may also modify the carrier confinement. For the same reason, the PL of the upper 15 nm QWs (QW1) with asymmetric barriers is strongly redshifted and broad, almost merging with the GaAs emission. On QW2, these are minor effects in regard of the general trend that is of interest to us.
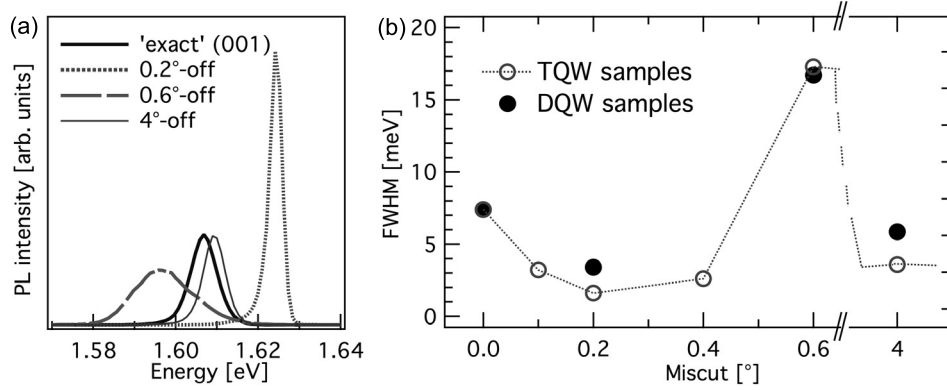
Figure 4.10: (a) PL spectra of the 5 nm QW (QW2) of the DQW structure grown on different substrates. (b) FWHM of the 5 nm thick QW2 as a function of substrate miscut, compared to the linewidth of similar QWs grown in TQW samples.

Growth run #	QW2	G.I. [s]	QW2 PL FWHM [meV]			
			'exact'	0.2°	0.6°	4°
2021	5 nm	-	7.4	3.4	16.7	6.2
2018	5 nm	20	7.9	3	18.7	6.4
2079	5 nm	-	10.9	5.7	21.5	8.8
2080	5 nm	120	9.3	4.4	17.8	8.8
2082	5 nm*	-	8.2	3.7	17.2	6.8
2081	15 nm	-	3.2	3.2	4.4	1.3

* without 5ML AlAs at interface

Table 4.1: List of DQW structures, indicating the linewidth of the burried QW2 for each substrate.

As visible from the results summarized in Table 4.1, the 5ML AlAs at the interface of the investigated QW2 do not have a significant influence on its optical properties. They were excluded in growth #2082, without changing the PL results. Variations observed are at least smaller than the growth to growth fluctuations, which are quite important (of the order of 20% if comparing growth #2021 and #2079). Again, we attribute these fluctuations to the presence of AlAs, or possibly to a degraded purity in the reactor chamber, but they do not question the validity of the trend that we discuss.

The FWHM values for the samples having a 15 nm QW2 emission do not follow the trend with miscut observed for the TQW samples. The corresponding PL spectra are shown in Fig. 4.11. There is no reduction between the nominally exact and the 0.2°-off samples, and the 4°-off sample has the narrowest linewidth. The power dependence of PL shown for the 4°-off sample reveals that in the standard excitation conditions, the low-energy line is already largely saturated. By contrast, in the 'exact' sample the low-energy component of the doublet has an intensity almost equal to that of the exciton, and dominates the PL at 5 μW. This indicates that here the residual doping varies between samples with different miscut, and is smaller for the 4°-off sample. The presence

of impurities is visible as small satellite peaks in the low energy tail of the 5 nm QWs. Their energy separation with respect to the exciton line is 33 and 45 meV. They are thus likely to be transitions involving the hole from C and Si impurities, respectively. The binding energy of an exciton bound to an impurity increases with decreasing QW width down to about 5 nm [100], and is therefore larger than the bulk values of 26 and 34 meV. This residual doping blurs the linewidth tendency observed in the case of the 15 nm QW, which is more sensitive to the presence of impurities. Nevertheless, we note that the trend is well visible even in the 5 nm QW1 having asymmetric barriers.
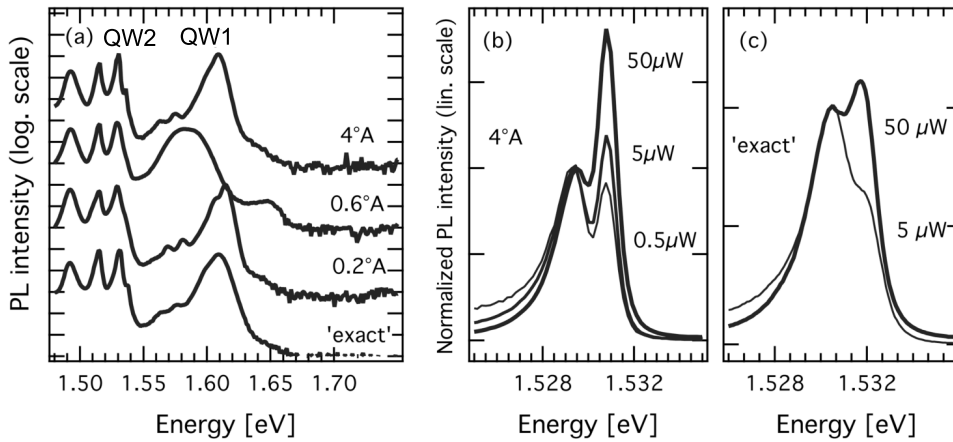
Figure 4.11: PL spectra of the samples grown in growth #2081: DQW with 15 nm QW2 and 5 nm QW1(a). Power dependence of the PL emission line of the 15 nm QW of sample 4°-off (b) and nominally exact (c).

Early experiments on samples grown at a lower V/III ratio generally showed a detrimental effect of growth interruption (G.I.) at any or both interfaces. In general, G.I. during MOVPE does not improve the optical properties [16]. Consistently, as visible in Table 4.1, we did not observe a significant effect on the PL linewidth of the G.I. at the upper GaAs interface (of QW1 and QW2) of our DQW structure. The variations that we observe are small with respect to the growth to growth fluctuations measured in that type of sample.

We have highlighted so far important variations of the inhomogeneous linewidth of the PL of QWs grown on misoriented substrates. We finally investigate the local properties of the emission using μPL spectroscopy. The μPL spectra in Fig. 4.12 were taken at about 1 μm distance intervals, on samples with different miscuts and a growth interruption of 2 min at the GaAs upper interface. Spectra of the 'exact' and 4°-off samples both exhibit sharp lines attributed to localized excitons. These lines are distributed slighty more homogeneously on the 4°-off sample. On the 0.2°-off sample, the emission is very uniform and has a slightly asymmetric lineshape due to a low energy tail, as observed in standard PL. Finally, μPL allows to decompose the emission of the 0.6°-off sample, which exhibits a broad and redshifted PL spectrum, into several peaks widely distributed in space and energy.
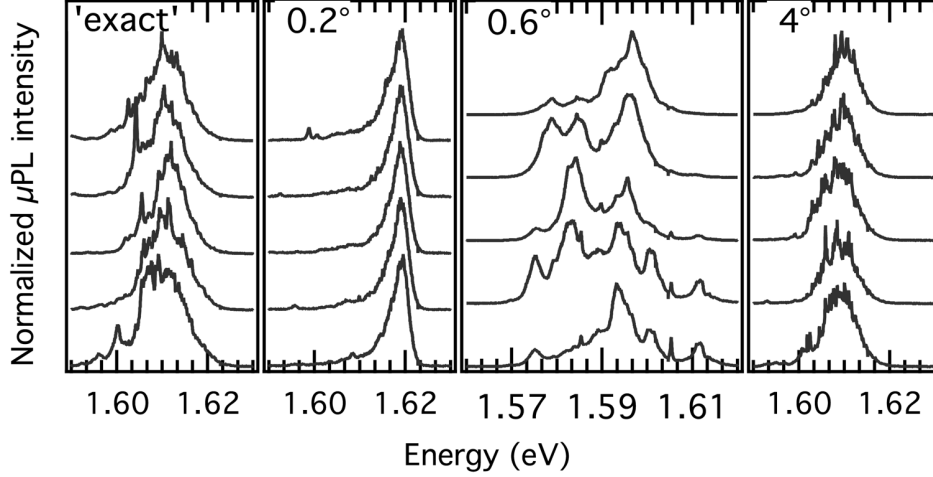
Figure 4.12: μPL spectra of the 5 nm wide QW2 grown on substrates with different miscuts. The growth was interrupted for 2 min at the upper interface. They are taken at about 1 μm distance intervals.

4.2 Probing the morphology of quantum well interfaces

We demonstrated in the previous section that DQW (QW2) and TQW structures display similar optical properties and should therefore be structurally comparable. The AlGaAs barrier of TQW does not allow its chemical etching and thus the imaging of the real QW interfaces. Conversely, the AlAs sacrificial layer of the DQW structure modifies the growth morphology observed on the sample surface. In this section, we discuss the morphology of the GaAs and $Al_{0.3}Ga_{0.7}As$ layers. We therefore investigate separately the surface of the TQW and the interfaces of the DQW samples.

4.2.1 Surface morphology

Fig. 4.13 shows AFM images of the *annealed*[1] GaAs surface of the TQW samples that are representative of each substrate miscut domain I-IV. We observe very different types of morphologies. The surface of the 'exact' samples shows *step-flow*: there are ML high terraces, which width depends on the local miscut angle. We observed that this angle changes considerably within a single wafer and sometimes exceeds the nominal specification of $\pm 0.02°$.

---

[1]These surfaces are *annealed* in the sense that they can evolve during the cooling of the sample at the end of the growth.

There are no clearly defined terraces on 0.2°-off surfaces. For step-flow growth, we would expect 80 nm wide terraces. Instead, the steps merge locally, creating 1-2 ML height fluctuations. We will refer to this morphology as *coalescent step-bunching* (CSB).

The sample representing the third miscut angle domain (here: 0.6°-off) shows a different type of step-bunching: the length of the terraces progressively reduces and the steps merge to create multisteps at more or less regular interval. We call this morphology *periodic step-bunching* (PSB). The height variations are here on the nm scale. The steps are rather straight although they still mix together locally.

Samples with larger miscut angles (domain IV) also exhibit coalescent step-bunching, although with a larger amplitude and more closely separated steps.
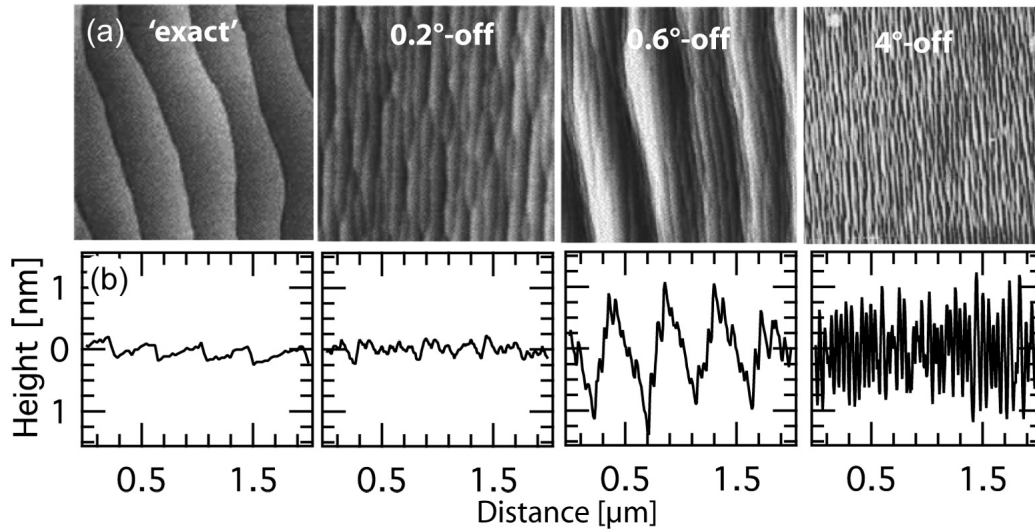
Figure 4.13: (a) 2x2 μm^2 AFM images of the GaAs surface of TQW samples grown on misoriented substrates. The respective height scales are 2, 2, 5 and 4 nm. (b) Representative sections of the surfaces.

It is obvious that the fluctuations observed in the optical properties correspond to important changes in the surface morphology. It is however not clear how these changes are correlated, in particular for the best optical results, which are obtained on samples showing coalescent step-bunched surfaces. As already mentioned, it is essential to image the real QW interfaces, in order to elucidate the reasons leading to these optical differences.

4.2.2   Hetero-interfaces morphology

The hetero-interfaces obtained after selective etching of the DQW barriers (Sec.3.2.2) are displayed in Fig. 4.14. As for the surfaces, we find that very different morphologies are associated with the various miscuts. Remarkably, the GaAs and AlGaAs interfaces look very similar. Less details are visible on the AlGaAs, which is probably related to

a native oxide forming between the growth and the AFM measurement.
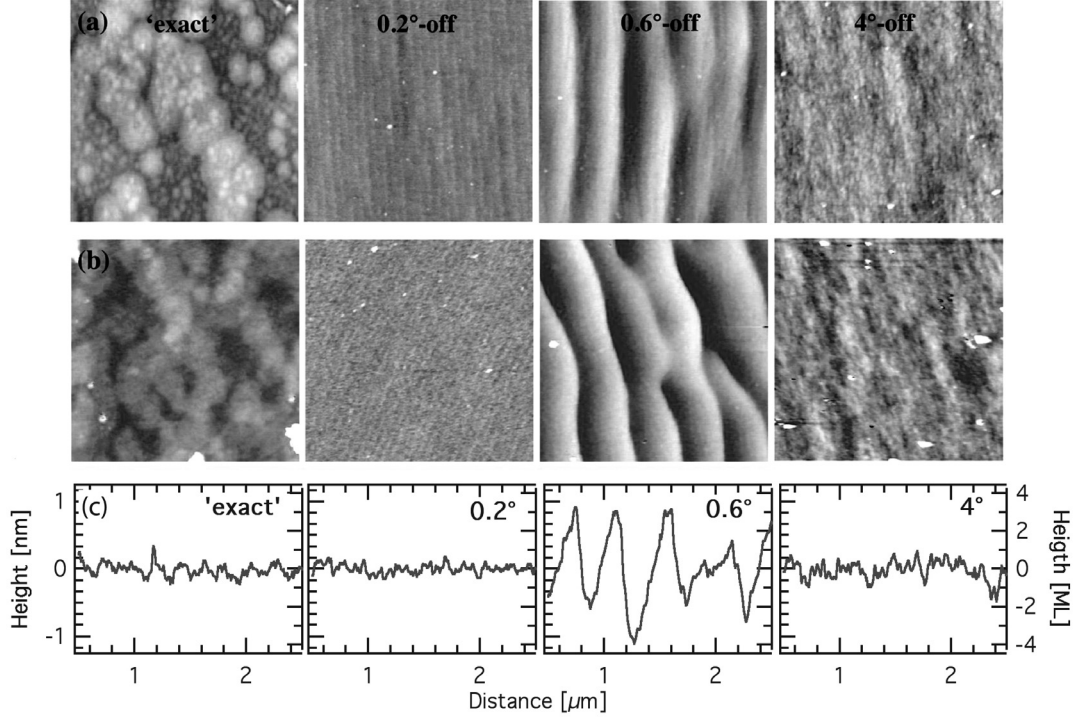
Figure 4.14: 2x2 μm^2 AFM images of the (a) GaAs and (b) AlGaAs interfaces of the 15 nm QWs (QW1) grown on substrates with 4 different miscuts, after selective etching of the AlAs layer. (c) Cross-sectional profiles of the GaAs interfaces in (a). The respective height scales are 2.5, 3, 6 and 3 nm.

The 'exact' samples interfaces consist of islands dispersed on the surface. Their diameters range between a few nanometers and several hundreds of nanometers and their geometry is roughly isotropic. Most islands are monolayer high, but as small ones are distributed over larger ones, the global height variation may reach several monolayers.

In contrast, the 0.2°-off interfaces are well ordered, with neatly arranged parallel steps separated by about 75 nm. Although some surface effects due to the etching blurs the height resolution, we can confidently state that the steps are ML high, as this terrace width is close to the value expected for step-flow on a 0.2°-off surface (80 nm).

There is a vertical stripe pattern on the images of 4°-off samples, but we cannot identify clearly the growth mode; in this case, step-flow would lead to 4 nm wide terraces, well below our imaging resolution here. For simplicity, we will refer to this morphology as *unresolved step-flow* (uSF). Still, as attested to by the cross-sectional profile, the height fluctuations of the 4°-off interfaces have an amplitude comparable to those of the 'exact' sample.

The 0.6°-off interfaces stand out from the other ones. They show the same periodic step-bunching of large amplitude, as that observed on the annealed surface of the TQW

samples (Fig. 4.13).
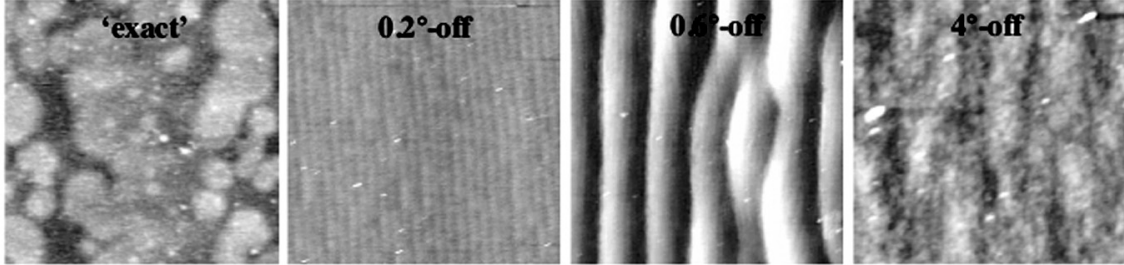
Figure 4.15: 2x2 μm^2 AFM images of the GaAs interfaces of 5 nm QWs grown on substrates with 4 different miscuts. The respective height scales are 3 nm, except for the 0.6°-off for which it is 6 nm.

We checked with a separate growth that the 5 ML of AlAs above QW2 do not modify the growth mode of the layers grown above. We also measured the GaAs interface of a 5 nm QW. As visible in Fig. 4.15, the morphology of the GaAs surface is independent of the thickness of the GaAs layer, at least in the 5-15 nm range. We observe the same 2D-SF-PSB-uSF evolution with miscut as for that on 15 nm QWs.

To summarize, we have observed that the morphology of the real hetero-interfaces of the QWs are different from those of the annealed surface. However, to a change in the morphology of the interfaces, corresponds systematically a characteristic change of the surface. From this point of view, the annealed surface morphology is indicative of that of the real hetero-interface. We have checked that the AlGaAs and GaAs layers have a similar morphology, independently of the thickness of the QW. As a result, we can safely state that the interfaces in the DQW structures are representative of those in TQWs.

4.2.2.1   Effect of growth interruption

We investigated the effect of a growth interruption (G.I.) on the morphology of the hetero-interfaces. The flux of group III elements precursors was stopped while the samples were still under AsH_3 flow. Several series on the same four different types of substrates were grown, with interruption either at the GaAs interface (20 s or 2 min) or at the AlGaAs interface (20 s).

The resulting interface morphology of these vicinal samples is similar to those without G.I. discussed above. We observe SF, PSB and uSF for the 0.2°, 0.6°, and 4°-off samples, respectively. There is nonetheless a striking difference for nominally exact samples: while the continuously grown interface displays islands distributed over the surface, steps appear at the growth interrupted GaAs interface. Moreover, the islands still subsist on the terraces between the steps.
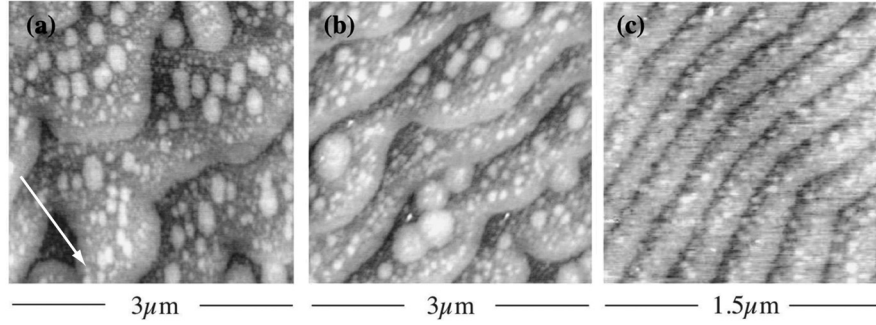
Figure 4.16: AFM images showing 3 examples of exposed GaAs interfaces after a growth interruption of 20 s on nominally exact substrates. The local misorientations are (a) < 0.02° (b) 0.02°(c) 0.08°. The arrow shows the descending direction. The height scale is 2 nm.

Several images are presented in Fig. 4.16 for 20 s growth interruption at the GaAs interface of three nominally exact samples. The respective step separation is approximately 1 μm, 700 nm and 200 nm, corresponding to miscut angles smaller than 0.02°, 0.02°, and 0.08° for images (a),(b) and (c) respectively. A reference growth, without G.I. at the interface, was done on three substrates cut in the same wafers, for comparison. All the interfaces displayed 2D islands, without step formation. Although the local fluctuations of the miscut angle on a wafer can be important, this is a good indication that the step formation is really induced by the G.I.
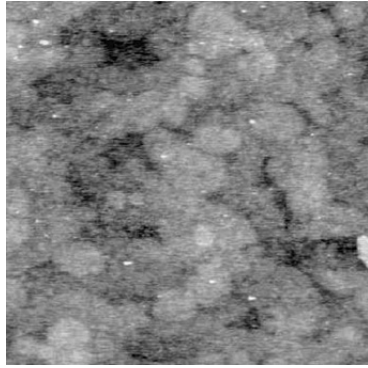
Figure 4.17: 2x2 μm^2 AFM image of the AlGaAs interface of a nominally exact sample after 20 s growth interruption.

We attribute these differences to slightly different effective miscut angles. For the nearly exactly oriented surface, the steps are strongly curved and do not have a well defined direction. Large islands appear where the terraces are broader. The largest undulations at step edge can thus be regarded as islands collapsing with, or detaching from, the upper terrace. The roughness of the step edge decreases with decreasing terrace width and the steps parallelism improves. On narrow terraces, only small islands subsist on the upper side of the terrace. Indeed, in all these images, we observe that a narrow band, about 100 nm wide, remains free from islands close to the descending step edge. Increasing the growth interruption time to 2 min does not modify these features.

In particular, we see no difference on the island size and distribution.

In the case of 20 s G. I. at the AlGaAs interfaces, we do not observe any change as compared with continuous growth. The vicinal interfaces are similar to those reported in Fig. 4.14(b). As for the 'exact' sample, in contrast to the GaAs interface, we do not see step formation. Such a surface is shown in Fig. 4.17; one can see that the growth mode is still clearly two dimensional.

4.3 Correlations between optical properties and interfaces morphology

We now analyze both the optical and topological results, and discuss them in the frame of the disorder model presented in Sec. 2.3.

4.3.1 Tuning the optical properties by controlling the growth mode

We identified four miscut angle domains, amongst which the QWs PL linewidth varies in a significant way. To each of these domains correspond specific surface and interface morphologies, the latter being identical for GaAs and AlGaAs. In this section, we examine how the optical properties can be correlated to the interfaces morphologies.

In domain I, corresponding to nominally 'exact' samples, the numerous islands at the interfaces correspond to a broad PL linewidth and sharp lines in μPL spectra. These sharp lines originate from the recombination of excitons localized in minima of an inhomogeneous potential. These minima are created by the width fluctuations induced by the islands, which extension ξ is larger than, or of the order of, the exciton Bohr radius a_B. Interrupting the growth up to 2 minutes does not change the optical properties significantly, since islands subsist in between steps.

In domain II, the QW interfaces are characterized by narrow terraces, free of 2D islands. The corresponding PL spectra are very narrow, and spatially very homogenous even at the micron level. Indeed, these terraces are larger than the exciton Bohr radius, and excitons are subject to a potential modulated mainly by the nano-roughness of the terraces. This latter modulation is much smaller than that induced by islands, and in addition occurs on a length scale inferior to a_B and is thus averaged over the exciton spatial extension. In particular, it is not large enough to localize the excitons.

Domain III is determined by a dramatic change of the morphology of both the surface and interfaces, which display periodic step-bunching. The PL and μPL spectra are radically different than those in the other domains. The PL displays a very broad

| Miscut | Morphology | | Length | Optics | |
domain	Surface	Interface	Scale	PL FWHM*	μPL
I	SF	2D	$\xi \geq a_B$	1.3 meV	sharp lines
II	CSB	SF	$\xi < \xi_0$	0.7 meV	homogeneous line
III	PSB	PSB	$\xi \gg a_B$	3.9 meV	broad, distributed lines
IV	CSB	uSF	$\xi < a_B$	1.2 meV	sharp lines

* Representative value for a 15 nm QW

Table 4.2: Synthesis of the correlations observed between the optical properties and the morphology of the samples.

and redshifted spectra, which corresponds to the inhomogeneous emission from several well-separated local minima, as it can be decomposed in the μPL spectra.

Domain IV is distinguished by the disappearance of PSB, and the recovery of flatter interfaces, the growth mode of which cannot be resolved properly. The interfaces exhibit amplitude fluctuations comparable to those of 'exact' samples, and larger than those of 0.2°-off ones. A small PL linewidth is recovered in this miscut domain, and does not change much up to the highest miscut investigated (8°). Its value is smaller than that of QWs grown on 'exact' sample, but slightly larger than that obtained on 0.2°-off samples. The μPL also shows features due to localized excitons, but more densely distributed (spectrally) than in the case of the 'exact' sample. For this larger miscut, the topological fluctuations are separated by a distance much smaller than the exciton Bohr radius. Fluctuations are thus expected to be averaged by the exciton. The resulting effective potential is smoother and leads to a spatially more uniform emission than for 'exact' samples. The observation of localized excitons however implies deep enough minima, and therefore a deviation of the growth mode from pure step-flow. This is consistent with the larger height fluctuations observed locally at the interfaces.

As summarized in Table 4.2, the imaging of the hetero-interfaces allows a consistent description of the linewidth of the PL and μPL spectra for four different types of disorder. Particularly determinant is the length scale over which height fluctuations take place, and its relation to the exciton extension.

4.3.2 Relation between broadening and emission energy

Four types of interface disorder result from the same growth conditions but are determined by slight differences in the substrate miscut, with respect to the exact (001) orientation. The samples being grown together, with the same nominal QW thickness, they are expected to emit at the same energy. It is not the case: the broader PL lines systematically appear at a lower energy than the narrower lines. Although there are small deviations from this behavior, the general trend is made clear in Fig. 4.18. The amplitude of the energy shift is much larger for the thinner QWs. Whereas for the 15

nm QW the maximum redshift of 4 meV is of the order of the largest FWHM, the shift for the 5 nm QWs is as big as 47 meV, and reaches 110 meV for the 2 nm QWs, which show a FWHM of 33 meV in the worst case. For these latter QWs, we observe that an ensemble of points, corresponding to the step-bunched samples, are well separated at lower energy and with larger broadening, while in the remaining cases, all points align along a line with a slope of the order of 0.8 meV (FWHM) / meV (peak energy).
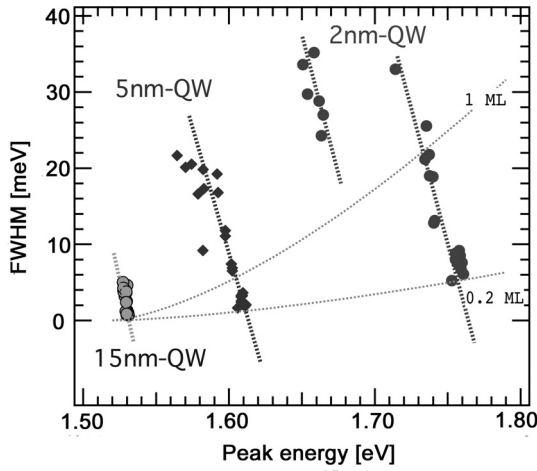
Figure 4.18: PL linewidth as a function of the peak energy, for the samples which spectra are displayed in Fig. 4.2. Oblique lines are are guide to the eye. The dotted curves are calculated from Eq. 2.5.

This distribution seems at first sight anomalous. For the same degree of interface roughness, the linewidth is expected to be broader for narrower QW, emitting at higher energy. This is the tendency we observe for the best samples, which exhibit a FWHM equivalent to fluctuations of a fraction of ML, as shown by the dotted curves in Fig. 4.18, calculated for an infinite barrier model from Eq. 2.5, and width fluctuations of 1 and 0.2 ML. However, within the points obtained for a given nominal thickness, the broader lines are redshifted, indicating a more complexe relation to interface roughness.

To understand it, one has to take into account the occupation factor of the carrier states. If large fluctuations occur at the interfaces, it induces important variations of the well width. However, at low excitation and low temperature, only the minima of the resulting potential landscape are occupied, thus shifting the emission toward lower energies. The low-temperature PL broadening is a measure of the distribution of these minima, and not of the overall potential fluctuations. This is schematized in Fig. 4.19 for two extreme situations. The amplitude of the potentials are calculated from the height variations measured by AFM at the interfaces, reported to an average 5 nm thick QW. The local width is converted into the single particle confinement potential, by using a simple model of a rectangular QW with finite barrier height. For the 0.2°-off sample, the minima are distributed over a few meV, homogeneously across the sample. In the case of the large interface fluctuations observed in 0.6°-off samples, for a cross-section taken along the miscut direction, the local minima are much deeper and widely distributed, both in space and energy.

This corresponds well to the spectra observed in μPL: over the about 1 μm large spot,
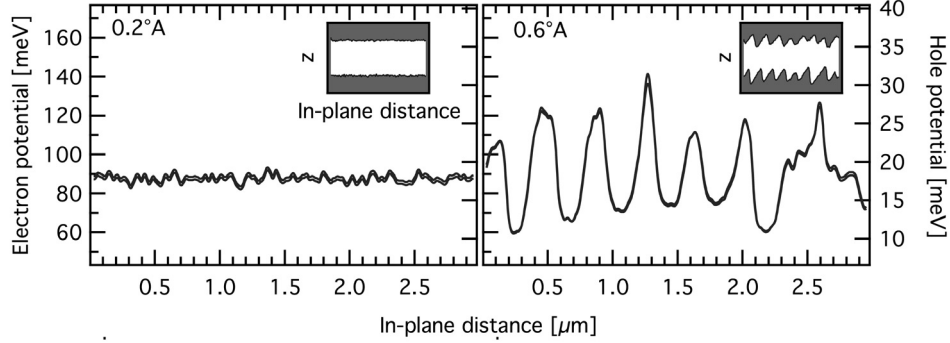
Figure 4.19: Representative potential landscape extracted from the interfaces morphology of 0.2°and 0.6°-off samples. Insets: schematic QW cross-section

typically two or three local minima are visible for the 0.6°-off sample. This picture also describes the various PL lineshapes that we observe. The more deeply localized states rapidly saturate for the smoothest samples, which therefore have a smooth low-energy tail [123].

Conversely, an extended high-energy PL tail arises from more disordered samples. It is directly related to the large distribution of potential minima. The large barriers between these minima prevent thermalization of the excitons confined at different positions, and this tail does not correspond to a global thermal distribution. It reflects instead the distribution of local minima and their concentration at energies much lower than that corresponding to the average QW width.

We cannot totally exclude a different origin to the redshift that we observed. Shifts of the QW PL lines are often attributed to graded interfaces resulting from segregation [12, 79, 125]. Even if smaller than in other systems, interdiffusion of Al and Ga atoms over a few ML takes place in GaAs/AlGaAs QWs. Its dependence on the substrate miscut should however be very large to explain the dramatic amplitude of the measured shift. The consistency of the explanation above with all our experimental observations strongly supports that the optical properties are determined by the interfaces morphology.

4.3.2.1 Correlation between the hetero-interfaces

The large amplitude of the height variations observed on PSB samples, comparable to the width of the 2 nm QWs, raises the question of the correlation of these variations between the two interfaces. The importance of interface correlation has been recently underlined in several publications [20, 123, 220], but was long overlooked in the discussion of the relations between interface roughness and optical properties. Ponomarev et al. recently demonstrated that narrow lines can be obtained even with rough QW interfaces, if their fluctuations are correlated [20]. Indeed, in the framework of a model of local variations of the QW width, a perfect correlation would lead to a constant

width. It has been shown by X-ray diffraction that step-bunched interfaces grown by MBE were correlated [164] and that growth interruption could actually be detrimental as, even though the correlation length of the disorder is increased in the QW plane, the correlation between the two interfaces, in the growth direction, is reduced [19].

Usually the AlGaAs interfaces are considered rougher than the GaAs ones, due to the smaller diffusion length of the Al atoms. In our study, except in the case of growth interrupted QWs grown on 'exact' substrates, all samples exhibit top and bottom interfaces having the same morphology. We can anticipate that the different growth modes observed affect differently the correlation between the two hetero-interfaces. In the case of step-flow, the interfaces are obviously correlated in the sense that width fluctuations are periodic and have a maximum amplitude of 1 ML. If the step edge moves by a distance κ across the QW layer (cf. Fig. 4.20), it creates potential minima having an extension of length κ. Assuming that the step cannot advance more than one lattice period per deposited layer, κ cannot exceed the QW thickness. As these values are comparable (15 nm QW) to or smaller (5 and 2 nm QW) than the exciton Bohr radius, excitons average these fluctuations and are only weakly localized.

For 2D growth, for which islands are growing one on top of another, fluctuations may reach several monolayers. The observation of sharp lines points toward localized excitons; it implies that interfaces are not correlated.
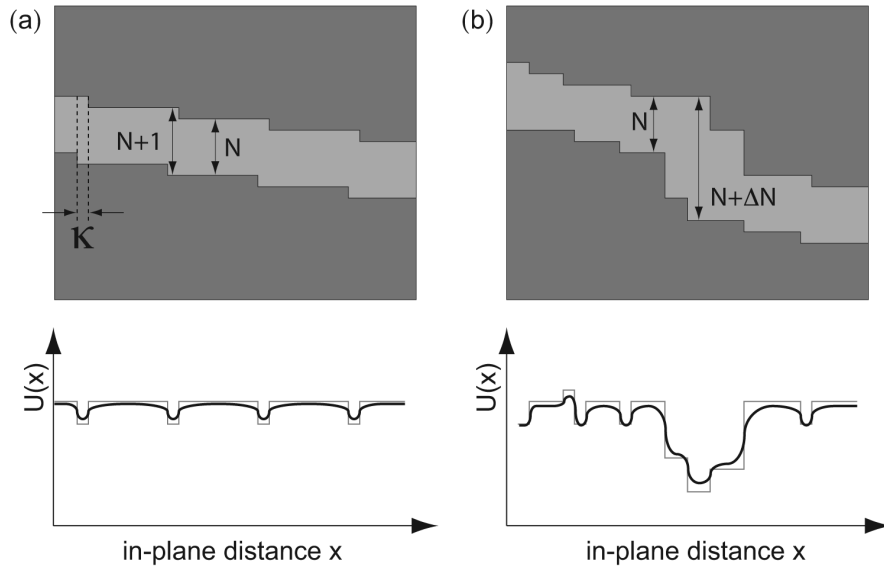
Figure 4.20: Schematic of the effect of (non)-correlations between the interfaces in the case of (a) step-flow, and (b) step-bunching. Variations in the QW width correspond to the variation of the effective potential sketched below.

The occurence of step-bunching is particularly interesting in the case of the thinnest QW. The redshift of the PL of the 0.6°-off samples is close to 100 meV compared to the others. Its PL energy corresponds to a QW of effective thickness around 4 nm.

This is consistent with uncorrelated interfaces creating deep potential minima (Fig. 4.20(b)). The carriers relax toward the wider regions, where they recombine. A small fraction still recombines in the thinner parts, which gives rise to the extended high-energy tail of the PL, up to the energy actually corresponding to the nominal QW thickness.

4.3.3 Versatility of MOVPE growth modes

From an epitaxial point of view, the striking features of our study is the observation of several growth modes within a short range of substrate miscut angle. Also remarkable is the fact that both the GaAs and the AlGaAs layers have similar morphologies, at least on a few nanometers scale. AlGaAs surfaces are known to be rougher than GaAs ones, due to the shorter diffusion length of Al adatoms. This is not in contradiction with our results, as here we are discussing the formation of meso-structures (islands, terraces). We do not directly consider the nano-roughness on top of these, which could have a residual effect on the optical properties.

The observation that the GaAs interface morphology does not depend on the QW thickness is a natural consequence of this similarity between GaAs and AlGaAs. Indeed, theoretical studies show that often several hundreds of ML have to be grown before reaching a steady state of the growth front [221]. This condition is always satisfied in our growths as we grew a thick buffer prior to depositing the structures.

Let us now discuss the formation of the different morphologies that we observed. For almost flat substrates (domain I), the evolution of the interface with growth interruption shows that the morphology is determined by the finite migration velocity: steps form only during G.I. A similar evolution of macrosteps with G.I. time was already reported for MOVPE [222]. In that study, growth was performed at a lower temperature (625°C) and with a different As source (TBA), which may explain differences in growth kinetics. Nevertheless, they observe a continuous evolution of the steps up to 2 minutes of G.I. and remaining islands on the annealed surface. We surprisingly do not observe any evolution between 20 s and 2 min growth interruption; we still observe islands in between the steps. The flat terraces, which were obtained on annealed surface, in contrast to the apparently steady-state islands between steps obtained during growth, raise the question of the possible occurrence of atom detachment from steps, at our rather high growth temperature. Indeed, an increased roughness due to islands has been observed on samples grown at larger temperature [223]. Yet, because large differences can be created by small, uncontrolled, variations of the local miscut for nearly exact substrates, many growth experiments would be required to distinguish real kinetic effects from purely geometric ones.

Similar considerations can be made for the morphology of the domain-II sample, which shows step-flow during growth, but coalescent step-bunching at the relaxed surface. The pure step-flow that we observed at the interface is obtained when the migra-

tion length of adatoms is larger than the step separation. The migration length is given by the island-free (*denuded*) zone at step-edge ($\sim$100 nm). The evolution to a CSB morphology on the surface is less intuitive. Shinohara et al. studied experimentally the occurrence of step-bunching at the surface of GaAs layers grown by MOVPE on slightly misoriented substrates [204, 224]. They observed step-flow for small miscuts, and coalescent step-bunching above a critical transition angle. At a lower growth temperature and using B-misoriented substrates, they obtained step-flow on 0.5°-off surfaces [205]. They found that the critical angle decreases with increasing temperature and proposed a model based on the saturation of the Ga atoms at steps by the adatoms, and on the desorption of atoms from the surface. According to this model and their experiments, step-bunching occurs at a smaller angle during annealing than during growth. Our observation that the step-flow taking place at the QW interfaces corresponds to a step-bunched surface is consistent. The exact formation mechanism of CSB is still unclear, although a model, which relies on desorption and exchange of adatoms between steps, has been proposed to describe the formation of step-branching during annealing [225].

The denuded zone observed at the lower terrace edge is at first sight indicative of a negative Schwoebel (ES) barrier. This is however inconsistent with the step-flow observed for small terrace width. Instead, it is an evidence of the preferential precursor decomposition at the steps, from where the released adatoms diffuse.

The inclusion of precursors indeed allows to mimic the effect of a negative ES barrier. The precise morphology of periodic step-bunching that we observed has been modeled by Pimpinelli et al., who considered both precursors and adatoms kinetics [165,166,221]. They calculated that a thick layer (of the order of 100 ML) has to be grown before the instability sets in. They also predict that once the growing surface has evolved to the bunched state, no coarsening of the bunches happen and the morphology remains stable. Indeed, the morphology that we observed on the TQW surface, thus several hundreds of ML grown above the QW, is still identical.

The reason why step-bunching sets in when increasing the miscut angle (decreasing the terrace length) and disappears upon further increase might possibly be found in the model of ref. [166]. The step-bunching instability is described as a function of the product ζl, where ζ is an increasing function of the dissociation rate of the precursors (ν_p) and decreases with the precursors diffusivity (D_p): $\zeta = \sqrt{\frac{\nu_p}{D_p}}$. l is the average terrace width. The instability shows up for large enough ζl. Although it is not accounted for by the model, the cracking ν_p of the precursors should increase with increasing miscut, as the steps play a catalytic role. As at the same time l decreases, the product behavior might be therefore non-monotonous with the miscut. Quantification of the kinetics variables would be however necessary to check this mechanism.

4.3.4   Is further optimization possible ?

All the results describing the surface and interface morphology presented in this chapter correspond to specific growth conditions: a growth temperature of 730°C and a high V/III ratio. These values were selected as a result of a systematic optimization of the optical properties, mainly regarding growth temperature and V/III ratio, and by sporadicaly checking some other parameters like growth rate. This optimization was done by varying one parameter and keeping the other fixed. The optimum that we obtained may not be absolute, but only local in the {T,V/III}-parameter space. With the understanding of disorder effects that we gained through this study, the question arises whether it is possible to further improve the optical properties of the QWs.

Usually, the observation of record low linewidth of QW PL are explained through extended ML flat terraces [197]. Extended islands can also lead to the appearance of doublet in the PL spectra, corresponding to recombination from regions, which thickness varies by ML integer. We introduced in Sec. 2.3 the characteristic length ξ_0 giving the minimal size of an island necessary to confine an exciton [124]. For 15 / 5 / 2 nm QWs we evaluate it to be $\sim$30 / 10 / 5 nm. In Fig. 4.20 we defined the length κ as the extension of a potential minima in the case of SF growth. For all three QWs, $\kappa < \xi_0$, thus preventing localization and therefore peak splitting. Except for the 15 nm QW, we also have the relation $a_B > \kappa$, therefore this contributes further to smoothing the potential and reducing V_0. For that reason, we believe that the interface roughness only has a residual effect on the broadening; this is linked to the nano-roughness inherent to an alloy interface.

Beyond the interface, it is interesting to examine the value of broadening expected from the alloy disorder in the barrier. Using the formulation of Singh [122], and the measured linewidth of the bulk AlGaAs PL, we calculate a broadening of approximately 0.3 / 1.5 / 3.6 meV for the 15 / 5 / 2 nm QWs, respectively. For the 15 nm and in particular for the 5 nm QW, these values are very close to the record values that we measured (0.6 / 1.6 meV). Alloy quality could therefore be the limiting factor in this case.

Remarkably, the FWHM of the 2 nm QW did not improve like for the other QWs when we increased the V/III ratio, and even slightly increased in average. It also has a much larger variability compared to the linewidth of the other QWs (cf. Fig. 3.5). Due to the large penetration of the wavefunction into the barriers, the properties of narrow QWs are expected to be determined principally by the barrier material, more than by interface fluctuations. The calculated value of the alloy influence is still however much smaller than the measured linewidth. We cannot exclude for example an effect of the V/III ratio on the nano-roughness. More likely, the extension of the carrier wavefunction deep in the barriers of a narrow well favors the formation of excitons bound to impurities in the barriers. Indeed, we observed an even narrower linewidth for a 2 nm thick QW, for which 5 ML AlAs were deposited before the second $Al_{0.3}Ga_{0.7}As$ bar-

riers. We measured a record low value of 4.3 meV, although the growth of AlAs was not optimized. This indicates that the extension of the wavefunction in the barriers is likely to play an important role for the 2 nm QW linewidth. At the moment however, we have not clearly identified the limiting factor for the FWHM of this QW.

Further optimization of the optical properties of narrow QWs requires more experimentation over the parameter space to, first, identify the origin of the broadening. The miscut angle range in which we obtain narrow linewidth is small under our growth conditions. It is limited by island formation for small miscuts and initiation of step-bunching for larger ones. This angle range can certainly be extended. Still, an improvement of the absolute values obtained from thicker QWs is more speculative and has to address crystal properties which were neglected up to now, for example alloy quality.

In general, an optimization of growth for devices will require a more global approach including optical properties, morphology (ex. for multilayer mirrors) and electrical transport. Transport measurements on structures grown on vicinal substrates were also performed [209]. They allowed to obtain high mobilities in QWs grown on vicinal substrates. The properties of these samples proved to be less dependent on the growth temperature. The optimal miscut angle and growth conditions were however different than those presented here for optics, as the origins of PL broadening and carrier scattering are different.

4.4   Chapter summary

In this chapter, we reported a systematic study of the optical properties of QWs of different thicknesses, as a function of the miscut of the substrate on which they were grown. We observed large and non-monotonous variations of the optical spectra with the miscut angle, and we were able to explain them with respect to the QW interfaces morphologies.

These morphologies indicate several transitions of the growth mode in a small range ($\sim 2°$) of the substrate miscut angle. Whereas the annealed surface of the samples also shows significant variations of morphology, and are therefore indicative of a change in the buried layers, their morphology is not representative of the effective QW interfaces.

These two features (rapid and non-monotonous variations, and discrepencies between the morphologies of surfaces and interfaces) have probably prevented a better control of the growth conditions in MOVPE up to now. The understanding of these phenomena allowed us to better control the QW interfaces and to reach record values of the PL FWHM of QWs grown by MOVPE. These values are comparable to those reported for MBE growth, and allow to resolve exciton complexes formed in the larger QWs.

In addition, the data that we present are important indicators to test or further refine the numerous theoretical models proposed for epitaxial growth. In particular, the morphologies that we observed are consistent with existing model accounting for the presence of two types of diffusing species.

Chapter 5

Quantum wires: disorder and localization

One dimensional (1D) systems are more susceptible to disorder than 2D systems [226]. In the previous chapter, we have seen that the main origins of inhomogeneities in quantum wells (QWs) are alloy disorder, crystalline impurities and interface roughness. Quantum wire (QWR) systems are subject to the same sources of disorder, but are particularly sensitive to interface roughness, due to the increased number of interfaces and the more complexe procedures required to form them.

Excitons localized by the local fluctuations of the confinement potential usually dominate the physical properties of QWRs and prevent the observation of pure one-dimensional effects. This is particularly true for V-groove QWRs: their structure and their specific disorder characteristics are described in the first part of this chapter together with their impact on the optical properties (Sec. 5.1). In the second part, modifications of the structure are implemented and characterized, in an attempt to bring V-groove QWRs closer to real 1D systems. First, samples with lower potential barriers are investigated (Sec. 5.2). Second, we study samples grown on vicinal substrates (Sec. 5.3).

5.1   State of the art V-groove QWRs

V-groove QWRs are very attractive systems for fundamental studies and for integration into devices [45]. Very early on, they were shown to be suitable as laser devices [77]. Recent investigations aimed at integrating them into cavities or waveguides [66, 67, 227, 228]. Meanwhile, studies on dynamical optical properties [90, 148, 151, 229], relaxation [230–232], optical anisotropy [76, 233], excitons [91, 234–236], many-body effects [81, 84, 237], or transport [64, 96, 229, 238–240], were conducted.

Many of these studies evidenced the crucial role of disorder on the physical properties of V-groove QWRs [89, 98, 148, 164]. The disorder can damp or even suppress some

of the attributes of 1D systems, by localizing carriers along the wire axis, by broadening the density of states, by modifying the band mixing, or by hampering the carrier thermalization. Improvements of the uniformity of the system are thus highly desired for addressing pure 1D properties.

5.1.1   The V-groove QWR structure

The fabrication method of V-groove QWRs was detailed in Sec. 3.1.3. Their structure is represented in Fig. 5.1(a). In this system, the confinement along the growth direction is provided by the hetero-interfaces, as for a QW. The confinement in the second (lateral) direction follows from the bending of these interfaces, which results in the faceted crescent represented in the TEM image of Fig. 5.1(b); the lateral barriers are formed due to the thinning of the side-QWs (SQWs) formed on the near-{111}A sidewalls (referred to as {111}A for simplicity in the following). In addition, the segregation of Ga and Al at the center of the groove forms a vertical-QW (VQW), which lowers the potential in the groove center. Although the ground state energy is lower in the SQW than in the VQW, a thinning of the GaAs layer at the crescent's sides creates a high potential barrier, which prevents the transfer of carriers to the QWR. Therefore, the VQW is the lowest energy barrier, and sets a large value of the effective 1D confinement potential (typically larger than 100 meV).
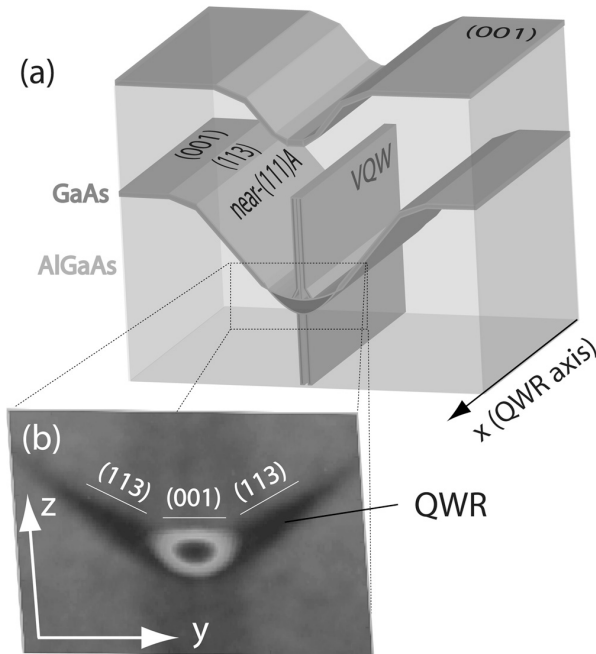
Figure 5.1: (a) Schematic illustration of a V-groove QWR structure, with QWs forming on different facets and at the center of the groove. (b) TEM cross-sectional micrograph of a crescent-shaped QWR, over which the contour plot of the calculated wavefunction of the confined electronic ground state is superposed. The faceted geometry of the groove is also underlined.

To introduce in detail the main characteristics of V-groove QWRs, we present here the optical properties and the surface morphologies of two QWR samples grown with the following layer structure: a nominally 2 nm thick GaAs layer embedded in $Al_{0.3}Ga_{0.7}As$ barriers, grown at a temperature of 690°C on a 3 μm pitch groove array, which was

defined by optical lithography on a nominally exact (001) substrate. The two samples differ by the thickness of the bottom barrier, which is 200 nm in one case and 1 μm in the other. The top barrier is in both cases 100 nm $Al_{0.3}Ga_{0.7}As$; it is capped by a 10 nm GaAs layer. These samples are representative of the state of the art samples fabricated up to now in our group.

5.1.2 Surface morphology: steps and corrugations

The very different total thicknesses of the two samples importantly modify the aspect of their surfaces. As described in Sec. 3.1.3, a thick buffer grown below the QWR leads to a progressive reduction of the groove's width and depth. In the present case, the total thickness is not sufficient to planarize the surface and the grooves are still visible. The surface morphology of the two samples are imaged in Fig. 5.2(b). A simplified schema in (a) allows the identification of the facets.
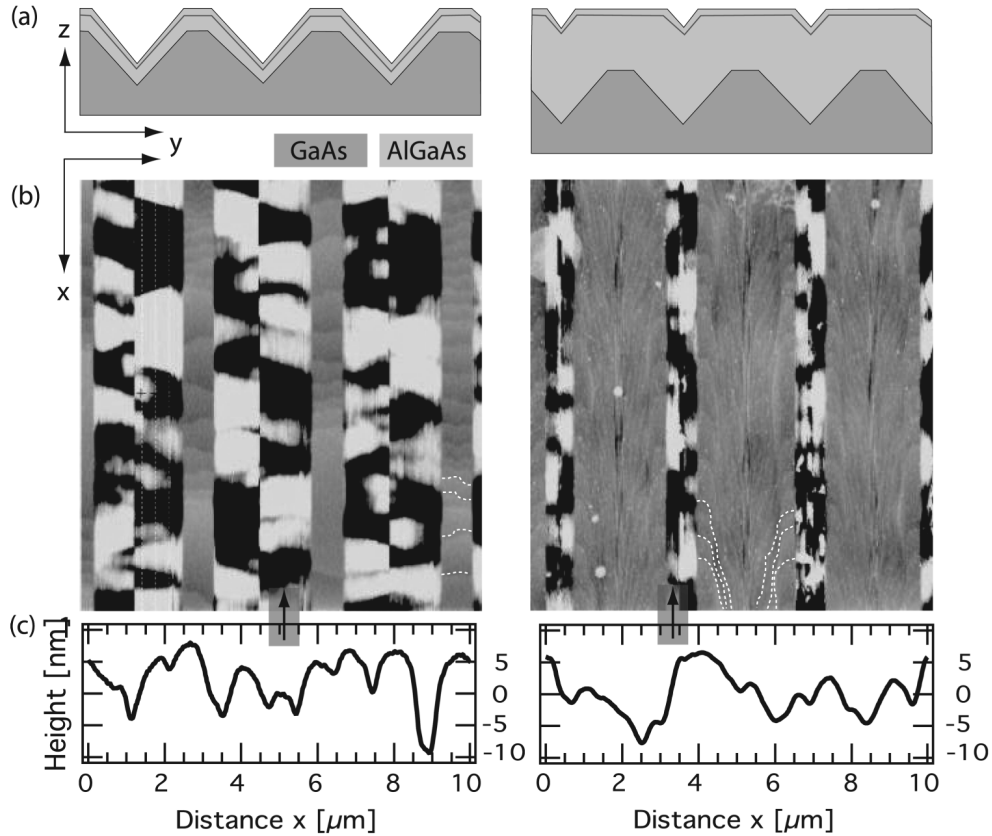
Figure 5.2: (a) Schematic cross-sections of the two QWR samples grown either with a thin (left) or with a thick (right) buffer. (b) 10 x 10 μm^2 flattened AFM images of the surface. The full z-scale is 5 nm. A few step edges are retraced for clarity. (c) Measured profiles of the sidewalls along the QWR-axis direction.

The surface of the thin buffer sample has deep ($\sim$1 μm) and wide ($\sim$2.1 μm) grooves. The black and white alternance on the groove sidewalls in the AFM images corresponds to large (around 15 nm) height variations, as evidenced in the cross-sections shown in Fig. 5.2(c). These fluctuations are comparable to those resulting from the groove etching (Fig. 3.8(c)). The facets essentially fluctuate along the groove direction; the facets profile is rather constant across the sidewall width (in the (y-z) plane). There is no *systematic* correlation between the two sidewalls, but locally correlated domains exist. On the sample grown with a thick buffer, only narrow ($\sim$700 nm) and shallow ($\sim$300 nm) grooves remain. The sidewalls fluctuations are similar to those of the sample having a thin buffer.

The step pattern formed on the ridge strongly depends on the width of the (001) top facet [181, 241]. For narrow ridges, ML steps form perpendicularly to the grooves (B-steps), and define terraces, the width of which varies between 250 nm and about 2 μm (corresponding to local angles ranging from 0.06° to less than 0.01°). We find no correlation between the step pattern and the sidewalls fluctuations.

The surface pattern is drastically different when the ridge width increases. In Fig. 5.2, we see that the steps near the groove arrange perpendicularly to its edge. Then, about 400 nm away from the groove edge, they curve to align parallel to it, becoming A-steps. As a result, a dimpled ridge is formed. However, the morphology observed on these wide ridges depends strongly on the position on the surface. This is probably caused by fluctuations of the local miscut: Fig. 5.3 is a composite of several AFM images taken close to a defect on the surface. This extreme arrangement allows to observe a whole range of different step patterns on the ridge. The common features observed are: (i) an alignement of the steps perpendicular to the groove, within a distance of a few hundreds of nanometers away from the groove edge, and (ii) a curvature of the steps.

5.1.3   Optical properties: recombination of localized excitons

The PL spectra of the two samples are displayed in Fig. 5.4. The excited area contains about 15 QWRs. Several spectra are presented in order to illustrate the slight variations, which are found at positions a few millimeters apart. All the system components give rise to specific optical transitions, which result in a rich optical spectrum.

The thickness of the crescent at its center is larger than that of the QWs that form on the various facets of the substrate; the QWR emission thus corresponds to the lowest energy line above the GaAs PL energy and is around 1.6 eV. The average linewidth is 5.3 and 5.6 meV for the thick and thin samples, respectively. The intensities of the QWR PL of the two samples differ by a factor of nearly 2. The absorption length is about 150 nm for the excitation at 2.41 eV and therefore many carriers are created below the QWR. In the case where the AlGaAs bottom barrier is thin enough, some of the photons are directly absorbed in the GaAs buffer. A significant fraction of the carriers generated in the barrier might also be captured in the buffer instead of diffusing
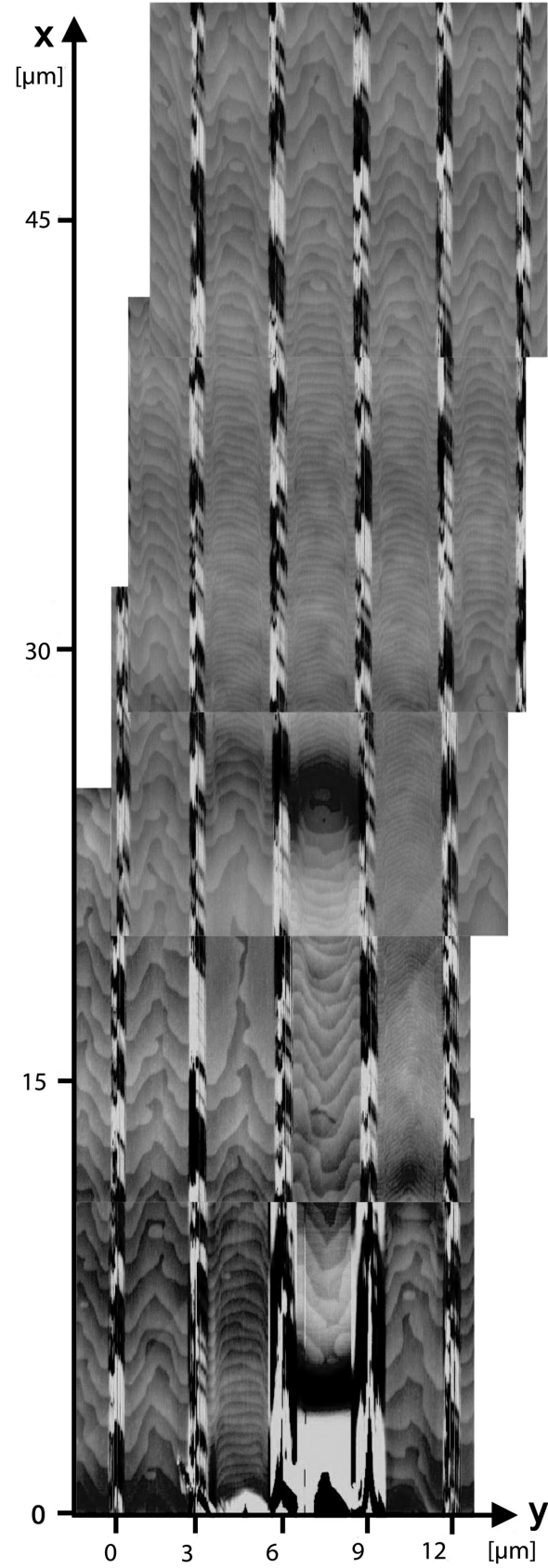
Figure 5.3: AFM composite images of the surface of the sample grown with a thick buffer, illustrating different types of surface morphologies. In that case, they are induced by a defect at (x=0, y=7.5).

toward the QWR. This results in a weaker intensity of the QWR PL for the sample grown with the thin buffer. The reduced area of the VQW can also be responsible for the weaker intensity, as it is known to be an efficient pathway to guide carriers to the QWR [242].

The emission energies of the QWRs on the two samples are also different: the sample with the thin buffer emits at a significantly higher energy (1.612 eV $\pm$ 4 meV) than the one with the thick buffer (1.594 eV $\pm$ 3 meV). It indicates that a thinner buffer leads to a thinner QWR. This might be directly related to the growing surface area at the time of the QWR layer deposition: when a thin buffer is grown, the surface of the sample has a larger area. Assuming that the deposition rate is not modified and that a fixed amount of material is deposited, the larger is the surface area, the thinner is the deposited layer.
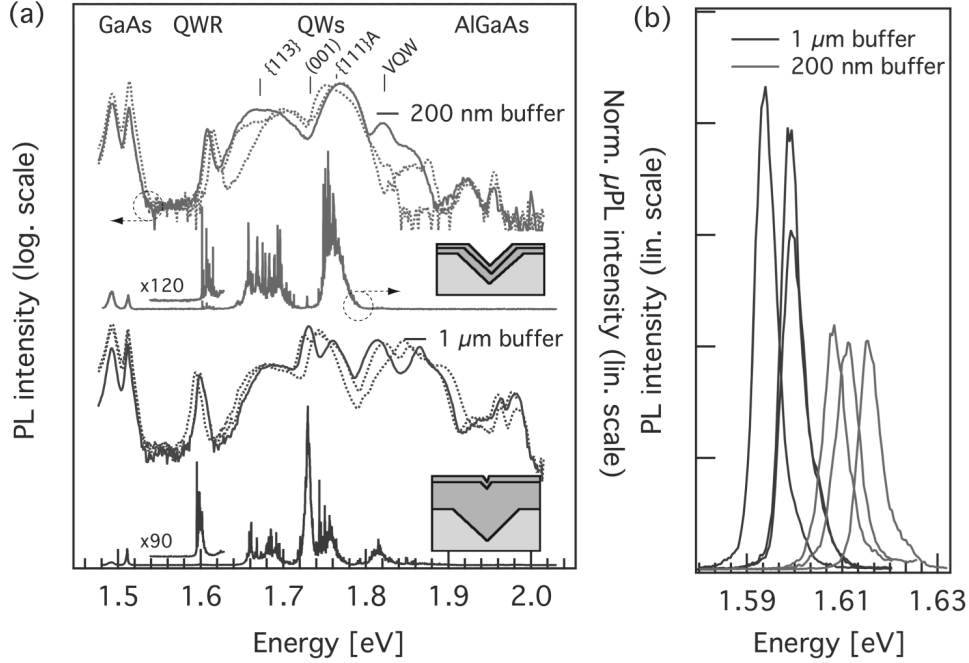
Figure 5.4: (a) PL (in log scale) and μPL (in lin. scale) spectra of the two samples. The multiple PL spectra are measured at different positions on the samples and show the good reproducibility of the spectra. (b) Sets of PL spectra of the QWR, measured at different positions with a higher spectral resolution.

The attribution of the other spectral lines is less straightforward as several QW structures are formed on the various facets. With regard to the different facet areas in both samples, (001) (resp. {111}, see insets in Fig. 5.4) QW emission should dominate in the thick (resp. thin) sample. We thus attribute the emissions at 1.73 eV and 1.75 eV to the (001) ridge and {111} sidewalls QWs, respectively.

Similarly, the VQW extends across the whole AlGaAs layer, and therefore has a larger area in the thick sample. Thus, it should correspond to the lines around 1.81 eV, consistently with the energy expected from Eq. 3.6. Finally, the broad emission between

1.65 eV and 1.7 eV probably comes from small and strongly disordered {113} facets separating the ridges and the sidewalls. These facets will be discussed later.

An analogue reasoning can be made to identify the PL of AlGaAs layers grown on the different facets. AlGaAs emits at a lower energy (1.959 eV) in the sample with the thin buffer, where it is mainly grown on {111}A facets. As the top (001) facet expands when a thick buffer is grown, the part of AlGaAs growing along that orientation dominates and is seen to emit at 1.985 eV. We deduce that the effective aluminum concentration is about 3% smaller when grown on {111}A instead on (001) planes. This is in contradiction with other reports [243], which concluded that $x^{eff}_{\{113\}} < x^{eff}_{(001)} < x^{eff}_{\{111\}A}$; this different behavior might be due to different growth conditions.
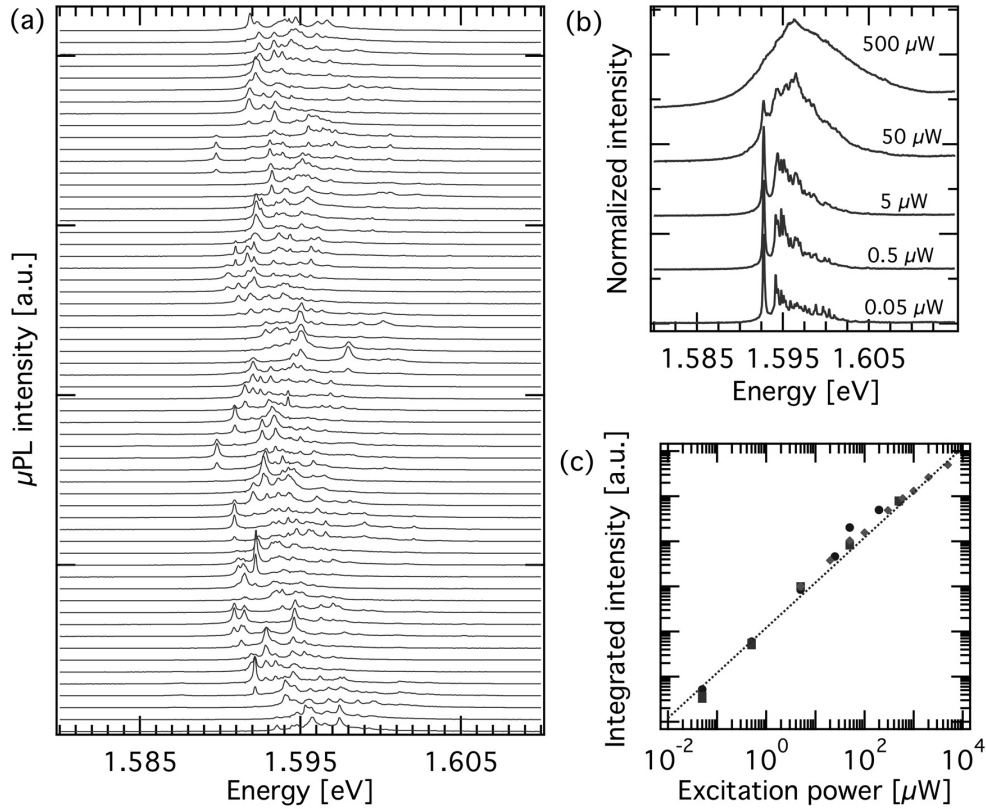
Figure 5.5: (a) 10 K μPL spectra measured at $\sim$1 μm intervals along a QWR (b) Excitation power dependence measured at a single position. (a) and (b) are measured on a QWR grown above a thick buffer. (c) Integrated intensity of QWR PL excited with a power spanning more than 5 orders of magnitude. Different symbols represents measurements at different positions of either the thin- or the thick-buffer sample.

In μPL measurements, only a single QWR is probed over a length of $\sim$1 μm. In addition, a smaller area of the ridge and sidewall regions is probed in this case. The broad PL lines decompose into dense groups of sharp lines corresponding to localized excitons (see Fig. 5.4(a)). In particular, the QWR spectra consist of multiple narrow

lines, as evidenced in Fig. 5.5(a). This figure shows μPL spectra acquired at $\sim$1 μm intervals along the QWR axis. We note spectral variations along the QWR of two types: (i) a shift of the PL 'center of gravity' (mean energy), between spectra measured over a few microns, and (ii) a variation of the number and energy of the narrow lines between individual spectra. The linewidth of isolated lines is typically 200-300 μeV. The number of peaks varies significantly from spot to spot; it is indicative of the number of deep potential minima within the probed area.

Often, a single line dominates the spectra at low energy, and higher energy peaks are weaker and spectrally less separated, as shown in Fig. 5.5(b). This situation corresponds to an efficient relaxation into the lowest minima of the potential. As the excitation density is increased, the lowest energy line saturates, and the spectral weight shifts toward higher energies as more and more states become occupied [244]. A high energy tail develops with increasing excitation power and hides the fine structure at increased density. The intensity integrated over the whole QWR spectral width (and from which the overlapping background emission from the QW PL tail has been substracted) increases linearly over the whole range of excitation density used in the measurements (Fig. 5.5(c)): this indicates that QWR states are further filled without saturation.

Finally, polarization resolved μPL spectra are shown in Fig. 5.6. In the usual measurement geometry, the luminescence is collected from the top of the sample, and hence one cannot access the light polarized along the growth axis. In order to probe such polarization states, we cleaved the sample and mounted it on its edge. Fig. 5.6(a) displays the spectra obtained in the y- and z-polarization sketched in panel (d). The z-polarized intensity is almost completely quenched as a result of the anisotropy of the QWR cross-section. The polarization degree PD is displayed as a function of energy on the upper panel of the graph; it is close to unity.

In the top view geometry (Fig. 5.6(b) and (c)), the light is also polarized mainly along the y-direction. In that case, it is not a quantum mechanical effect, but an electomagnetic phenomena related to the non-planarized surface of the sample [245]. Still, these measurements evidence a fine splitting ΔE_{int} of the individual μPL lines. This splitting is here of the order of 100 μeV, at the limit of the system resolution. It was shown to be due to the effect of exchange interaction on the localized states [246]. The lowest energy component of the split doublet is polarized along the QWR axis. This sign of ΔE_{int} is characteristic of the extension of the exciton wavefunction in the weakest confinement direction.

5.1.4   Origin of disorder in V-groove samples

The observations reported above are typical of V-groove QWRs, and have been the topic of several reports that appeared in the literature in recent years. The spectral fluctuations are due to spatial variations of the excitonic potential along the QWR, which take place over two length scales. The variation of the PL mean energy corre-
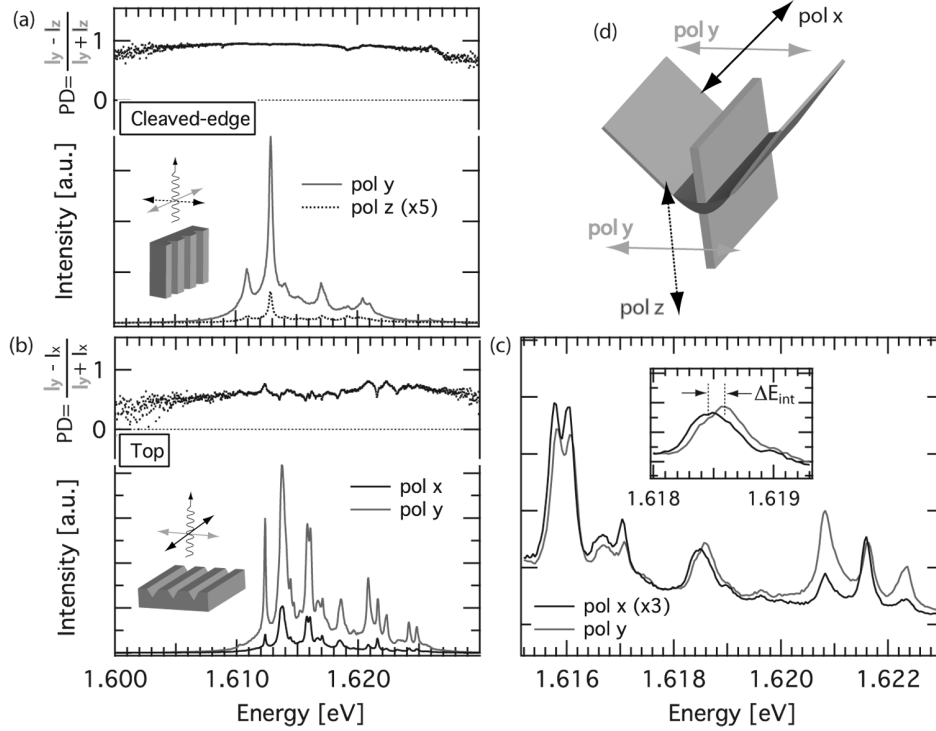
Figure 5.6: Polarization resolved μPL spectra of the QWR grown over a thin buffer, measured (a) in a cleaved-edge geometry, (b,c) in the usual top-view geometry. Graph (c) is an expansion of graph (b). (d) Schema of the polarization axis.

sponds to variation of the QWR thickness, which is related to the fluctuations along the groove over μm-scale distances. Indeed, these large scale fluctuations have been directly correlated to the spatial variation of the luminescence energy along a QWR and have been attributed to a modified QWR shape and thickness [173]. It is noteworthy that these results were obtained on a segment along which both sidewalls fluctuations were correlated, even though we have observed that these correlations are often non-systematic across samples. The second type of disorder relates to exciton localization. In V-groove QWRs, short-scale disorder is often attributed to step-bunched {113} facets that form the side of the crescent (see Fig. 5.7(a)) [247, 248]. Such a growth mode is indeed observed on the {113} facets forming at the bottom of the groove on the sample surface, as will be shown later.

5.1.4.1 Comparison to the 'best' samples

As excitons are localized in shallow potential minima, disordered 1D systems can often be considered as a chain of QDs randomly distributed along the 'wire' [249]. In typical V-groove samples, the extension of the potential minima is evaluated to be in the range of a few tens of nanometers [88]. The best results toward a reduction of these inhomogeneities were presented by Guillet et al. [98]. Their studies revealed a mean localization
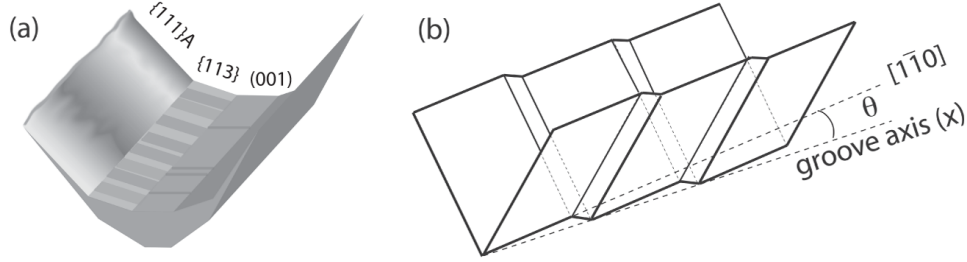
Figure 5.7: (a) Schematic illustration of V-groove QWR disorder features: ML steps on the central (001) and step-bunched {113} facets. (b) Scheme of the ML steps induced laterally by a deviation of the groove axis from the $[1\bar{1}0]$ direction.

length ξ of 400 nm, i.e. one order of magnitude larger than that of our standard samples. They attributed this improvement to three factors: (i) the smoothing of the patterned substrate using chemical etching [174]; (ii) the use of TBA (another arsenic source) during growth, which reduces the impurity incorporation [250, 251]; (iii) the improvement of the alignement of the groove direction with the $[1\bar{1}0]$ crystallographic direction.

(i) We checked the effect of an additional etching with a solution of $NH_3 : H_2O_2 : H_2O$ (1:3:50) after the groove formation and SiO_2 mask removal. The roughness was not significantly modified and the amplitude of the fluctuations was of the order of 20 nm over a few microns length. Actually, as seen in Sec. 3.1.3, the under-etching below the SiO_2 mask already contributes to the smoothing of the facets edge in our fabrication procedure. This additional processing step is thus not necessary.

(ii) The use of TBA as a gaseous source of As was previously investigated in our group for the growth of QWs, but did not lead to substantial improvements. Further tests would be difficult to implement, as they would affect all the structures grown in our MOVPE reactor.

(iii) We finally checked the importance of the groove alignement (Fig. 5.7(b)), which is presented by Guillet et al. to be the most sensitive parameter. For that purpose, we prepared patterned samples written by e-beam lithography. Several patterned areas were written, in which the groove direction was intentionally deviating from the $[1\bar{1}0]$ direction in the (001) plane. The grooves were prepared with a *nominal* angle between -0.05° and 0.4°. The 0.05° value corresponds to the evaluated precision of the alignement in the e-beam: it is based on the parallelism between a cleaved edge of the substrate and the line pattern and it is limited by the translation range of the e-beam stage. This is one order of magnitude larger than the precision attained by Guillet and coworkers (0.004°), who do not explicit their alignement procedure.

We grew 2 nm (nominal) thick QWRs in $Al_{0.3}Ga_{0.7}As$ barriers and measured the PL linewidth of the QWR emission from each area having a different misalignement (Fig. 5.8). PL lines exhibited a comparable linewidth around 6 meV and their μPL spectra

revealed many narrow lines in all cases.
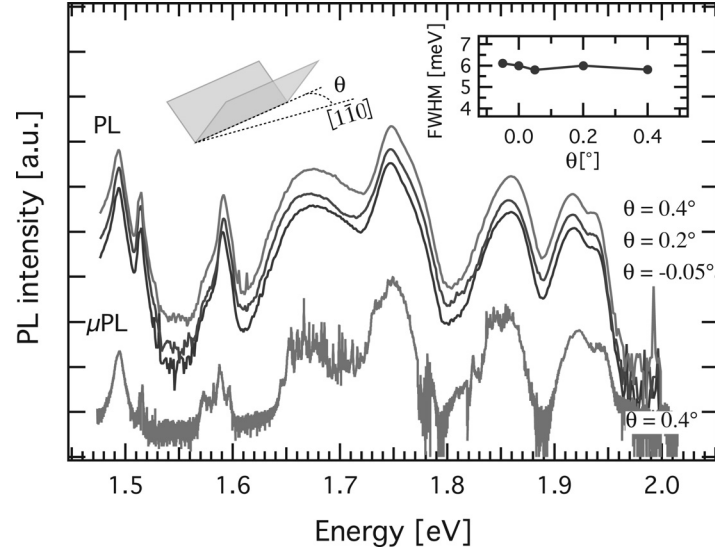
Figure 5.8: PL spectra for QWRs grown on groove nominally misaligned by an angle θ with respect to the [1$\bar{1}$0] direction. The inset shows the almost constant FWHM with θ.

It thus appears that, in our case, the factor limiting the QWR homogeneity is not the lateral alignement with respect to the [1$\bar{1}$0] direction. The 0.004° angle precision attained by Guillet et al. would allow about 4 μm long segment before a ML step forms laterally. In our case, the alignement precision still corresponds to ∼300 nm long segments. Nonetheless, it has to be underlined that the lithography and etching processing steps obviously do not reach a ML precision. Therefore we believe that the effect of misalignement is negligible as compared with the effect of etching [173].

In spite of the progress reported, the picture of disorder and of its formation are far from being as clear for V-groove QWRs as for QWs. The growth model explaining the self-limited profile presented in Sec. 3.1.3 only addresses growth mechanisms in the (y,z) plane, but not those along the groove. Yet, specific growth phenomena take place in the x direction on non-planar substrates. They are manifested in the particular patterns on the ridge facets. Although they are apparently not related directly to the QWR morphology, they attest to the existence of material flux (adatoms, precursors) along the groove direction.

The challenge that one faces is then to reduce the fluctuations along the groove, or at least their effect. The next sections investigate two approaches toward the fabrication of improved 1D systems: first, reducing the barrier potential, which makes the carriers less sensitive to interface fluctuations; second, growing QWRs on vicinal substrates, which proved so successful for QWs.

5.2   V-groove QWRs with low confinement barriers

The first approach, which we present below, aims at reducing the influence of interface disorder on the optical properties by lowering the barriers potential around the QWR, i.e. reducing the Al content x of the $Al_xGa_{1-x}As$ barriers. We expect mainly two effects arising from such a modification. First, the amplitude of the potential fluctuations related to the disorder should be reduced. Second, the exciton wavefunction should extend deeper into the barriers and across the fluctuations, and further smooth out the effective potential (Fig. 5.9). A systematic study for QWs [252] showed that the localization of excitons increases with increasing Al content x, as the standard deviation of the potential fluctuations increases.
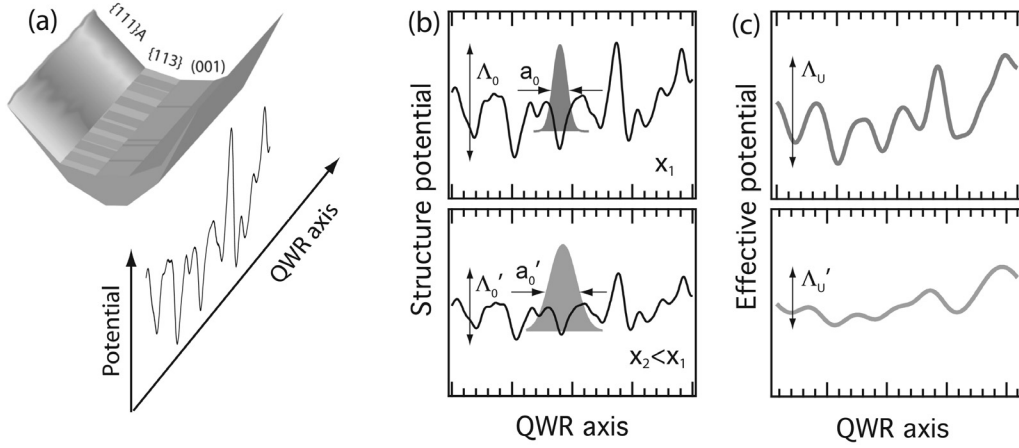
Figure 5.9: (a) Schematic illustration of the structural fluctuations of the potential along the QWR axis. (b) Schematic illustration of the exciton wavefunction in a potential determined by 'high' (top) or 'low' (bottom) barriers. (c) Corresponding effective potential resulting from the averaging by the exciton.

To quantify the effect of a reduced barrier height, we calculated the confined states for different barrier compositions using the model described in Sec. 2.2.1. The QWR profile that we used was obtained from the TEM image of a nominally 3 nm thick QWR, grown between $Al_{0.3}Ga_{0.7}As$ layers, but we scaled it down to a nominal 2 nm thick layer. It resulted in a height of $\sim$5.6 nm at the center. The profile is known to change with the Al content, but to isolate the effect of barrier height we kept it constant and modified only the Al content in the barrier. The barrier bandgap was calculated from the expression in Table 2.1 and the VQW concentration was calculated from Eq. 3.6 with K = 1.85.

The results are reported in Fig. 5.10(a). The transition energy gradually decreases with decreasing Al concentration. For sufficiently small Al contents, the wavefunction of the ground state electron extends importantly into the VQW, but the lowest energy states remain confined in the QWR [108]. Our model cannot calculate those extended states properly because of the finite length of the calculation gride. In panel (b), we report the variation of the ground state energy E_{ML} arising from a slightly different
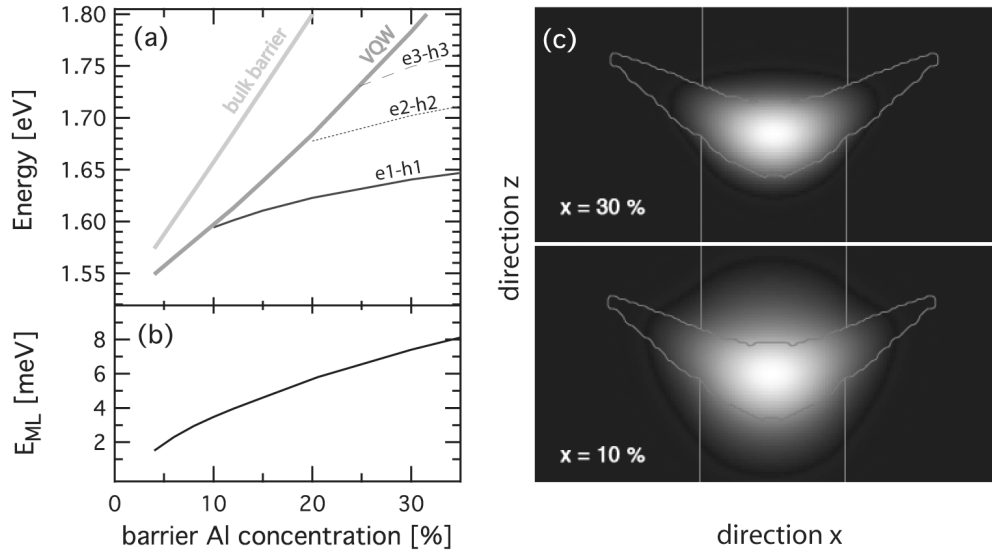
Figure 5.10: (a) Calculated transition energies for a 2 nm QWR as a function of the Al concentration x in the barriers. The VQW and bulk barrier energies are also shown. (b) Calculated variation of the ground state energy for a difference of one ML in the QWR thickness. (c) Density of probability of the ground electronic state, for two different barrier compositions. The crescent thickness at the center is 5.6 nm.

profile, which thickness differs by 1 ML over the whole width of the crescent. A reduction from x=30% to x=10% reduces E_{ML} by a factor close to 2. In panel (c), we display the normalized density of probability of the ground electronic state for these two cases. For x=10%, the extension of the wavefunction is much larger than for the higher barriers case. It extends particularly vertically toward the VQW, which corresponds to the lowest barrier region.

5.2.1 Samples and growth conditions

Several QWR samples with a low Al content x in the barriers were grown. The structure consisted in: a 2 nm QWR layer grown on top of a 200 nm $Al_xGa_{1-x}As$ lower barrier, covered by a 100 nm $Al_xGa_{1-x}As$ upper barrier and a 10 nm GaAs cap, deposited on a 3 μm pitch substrate prepared by standard photo-lithography and wet chemical etching. When the Al concentration is reduced, the self-limited profile has a larger central facet (or, equivalently, a wider crescent) [176, 177]. As a result, the lateral confinement decreases when x is reduced. This was compensated by using a lower growth temperature, which reduces the crescent width. In turn, the V/III ratio had to be adjusted to these new parameters. This was implemented on the basis of the trend shown in Fig. 3.4 and our experience with shallow-barrier QWs.

As all these factors are tightly inter-linked, several iterations were necessary to optimize the parameters for a given Al nominal concentration. Planar QW structures with

Sample	x_{nom} (%)	T_{Growth} (°C)	V/III (GaAs/AlGaAs)	x_{act}
2085	30	690	133/220	30.5
2114	15	650	80/150	17.7
2424	12	650	80/150	12.3
2422	12	650	80/80	12.0
2351	11	675	80/115	11.9
2272	7	675	80/115	10.9
2271	7	650	80/115	10.8
2177	7	650	80/115	9.8
2331	7	675	80/100	7.6
2329	7	675	80/140	7.5
2232b	4	650	80/100	5
2242	4	600	80/100	5
2243	4*	650	80/100	4.3

*different buffer: 10 nm GaAs and 300 nm $Al_{0.1}Ga_{0.9}As$ below the 4% barrier.

Table 5.1: List of the QWR samples grown with different nominal Al concentrations x in the barriers and their main growth parameters. The actual Al concentration x_{act} is deduced from optical measurements.

the same layer sequence grown on 0.2°-off (001) (toward [110]) substrates were systematically grown at the same time, serving as references. The list of samples is given in Table 5.1. Because of calibration discrepencies, the actual Al content differs from the nominal one. It was deduced from the PL energy of the AlGaAs material using the relation given in Table 2.1: as illustrated in panel (a) of Fig. 5.11, AlGaAs emission in the QWR samples is visible under high excitation. When available, PLE spectra also gave a good evaluation of the barrier energy, as it corresponds to a strong resonance. As previously mentioned, the AlGaAs layers grown on the planar reference emit at a different energy. Nevertheless, for simplicity, we use the actual Al concentration deduced from the QWR sample to refer to the concentration of its planar references as well. In some cases, the samples were post-processed, as described in Sec. 3.1.3.3, to remove part of the QWs, which emission overlaps strongly with the PL of the QWRs.

5.2.2 Dependence of the PL spectra on Al content

A common feature of the PL spectra of the samples grown with a low Al content is a relatively intense and broad emission around 1.55 eV. It is more pronounced for low barriers, and slightly redshifts with decreasing Al content. Fig. 5.11(b) displays a PLE spectra of this shoulder, for a sample with $x_{act} \simeq 12\%$. It exhibits a large Stokes shift and an important PLE resonance at the barrier energy, but only a very weak modulation at the QWR energy. Also, it shows no VQW resonance and no polarisation anisotropy. It is thus clearly not related to the QWR. It is however linked to the growth on the
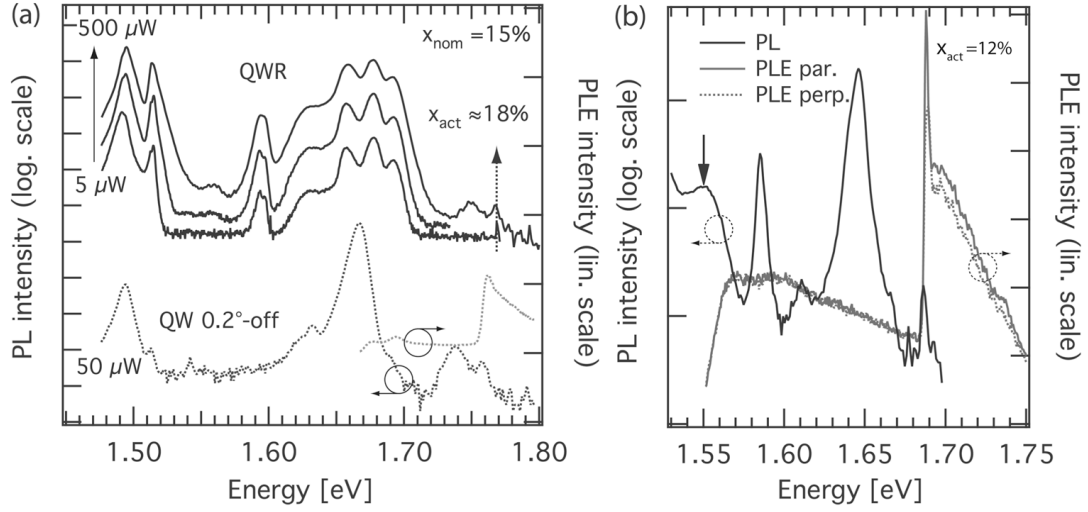
Figure 5.11: (a) Power dependence of the PL spectra of the QWR sample #2114 (upper part); PL of the reference QW and PLE evidencing the barrier energy (lower part). (b) PL and PLE spectra of the 1.55 eV shoulder on sample #2351. The PLE is measured with excitation polarized parallel and perpendicular to the QWR.

grating, as it is not present on the spectra measured in the planar parts. Its origin is nonetheless unclear.
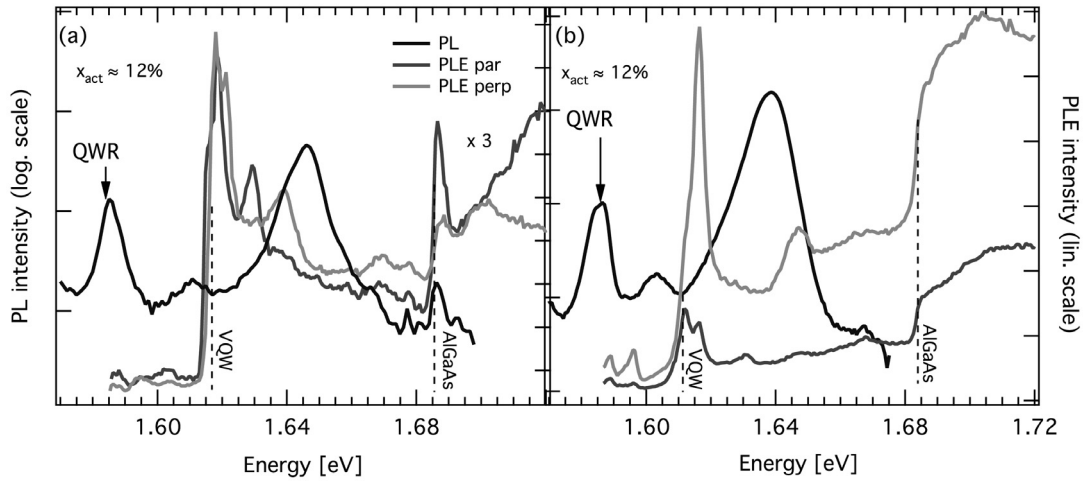
Figure 5.12: (a) PL and PLE spectra of two samples with x_{act}=12%.((a) #2351 and (b) and #2422). The arrows point to the detection energies.

The identification of the QWR line is clear from its characteristic lineshape, and is further confirmed by PLE spectra. Two examples are presented in Fig. 5.12. Both samples were grown with about 12% Al content in the barriers, as visible from the strong absorption at $\sim$1.686 eV. Sample #2422 (b), which was grown at a slightly lower temperature and lower V/III ratio, has no excitonic resonance at the barrier energy, which possibly indicates a stronger residual doping. The VQW absorption is visible around

1.617 eV (consistently corresponding to K $\sim$ 1.8 in Eq. 3.6). We note the heavy and
light hole splitting of the VQW absorption line: the ratio between the intensity of the
two peaks depends on the polarization [243]. Below these strong resonances, the QWR
transitions are very weak, but their intensities still allow a measurement of the Stokes
shift ($<$ 3 meV) and of the energy separation between the first two transitions ($\sim$7meV).
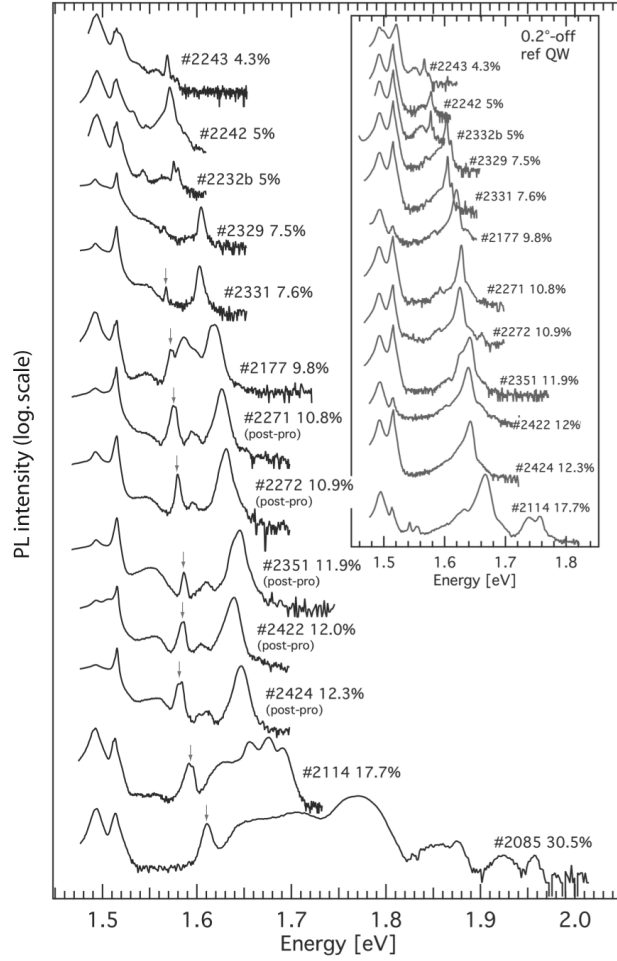
Figure 5.13: 10 K PL spectra of QWR samples grown with different AlGaAs barriers com-
position, as detailed in Table 5.1. The QWRs emission is marked by arrows. Some samples
were post-processed to remove part of the QWs, as indicated. Inset: PL spectra of reference
QW samples grown simultaneously on planar 0.2°-off substrates.

The PL spectra of all QWR samples are shown in Fig. 5.13. There is a global redshift
of the PL lines with decreasing x (except for that of the GaAs). The QWR emission
is indicated by an arrow. For the post-processed samples, it is well resolved from the
other PL lines. The lines of the different QWs and of the AlGaAs gradually merge as x
is reduced. The GaAs emission also changes from sample to sample, probably because
of the variation of the growth conditions. The inset of Fig. 5.13 shows the PL spectra
for the QW reference samples.

The peak energy is reported as a function of the Al content in Fig. 5.14(a). The

QWR emission shifts toward lower energies, from 1.612 eV for $x = 31\%$ to 1.567 eV for $x \simeq 8\%$. In the latter case, the QWR signal is very weak, and for even lower barriers, the QWR emission is no more visible; the signal is probably merged with the low-energy tail of the QW PL. In comparison, the emission of the reference QWs redshifts much more. For the QWR, the decrease of the transition energy with decreasing barrier height follows nicely the trend calculated in Fig. 5.10, which is reported as a dashed line in Fig. 5.14(a). The difference in absolute energy is at least partly due to the QWR profile that we used for the model calculations. The good agreement indicates that the QWR shape was roughly kept constant in all grown samples, thanks to the adjustments of the growth parameters. The exciton binding energy might also change between samples, but this effect is probably negligible [110].
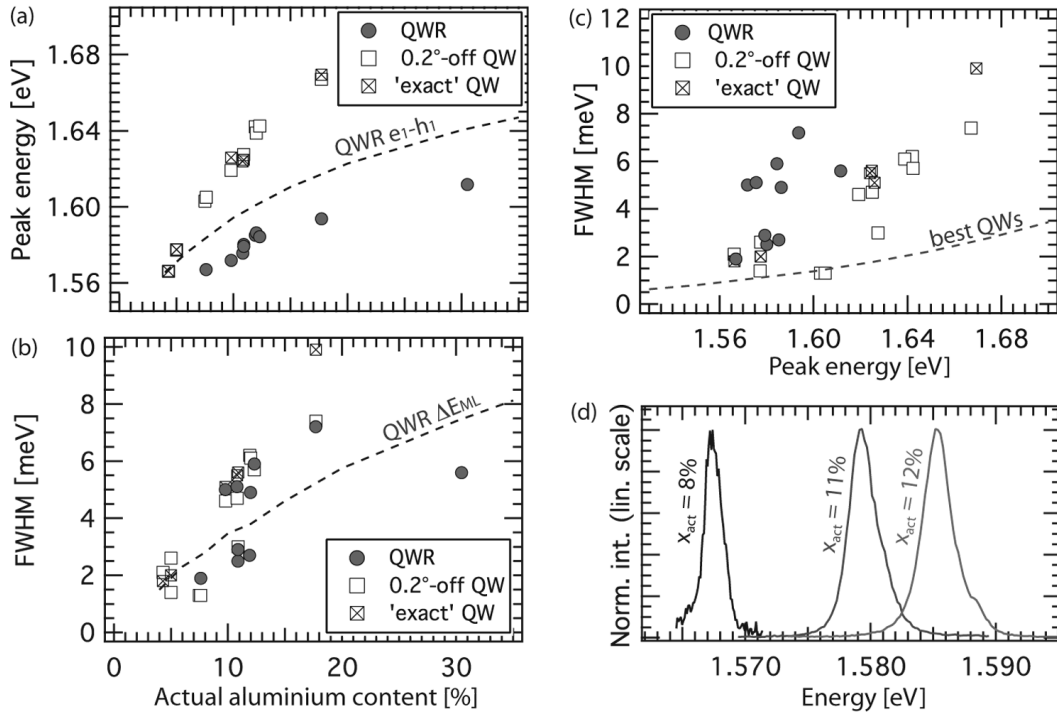
Figure 5.14: (a) Peak energy and (b) measured FWHM of the PL line of the QWRs and reference QWs as a function of the actual aluminium content. (c) FWHM as a function of the peak energy for the same samples as in part (b). Note that x_{act} was measured only for the QWRs and that this value is used to present the data for the reference QWs grown together. Dashed lines are defined in the text. (d) PL spectra of QWRs grown with low barriers and exhibiting narrow linewidth.

Fig. 5.14(b) displays the FWHM of the QWR and QW lines. There is quite a large dispersion of points around $x_{act} = 10\%$ as a result of the successive growths carried out for optimization. Nevertheless, it is seen that the FWHM is strongly reduced when the barriers height is lowered. Very narrow (2-3 meV) linewidth are obtained for the lowest Al concentrations, although the smallest one (1.9 meV) corresponds to a very weak line. For comparison, the dashed line shows the expected trend, calculated for fluctuations

corresponding to a ML thickness variation of the QWR profile. The panel (c) of Fig. 5.14 compares the FWHM of QWRs and QWs as a function of the peak PL energy, which serves as an indication for the strength of confinement in the structure. For a given emission energy, the QWR linewidth is in general larger than that of the QWs, even though the latter were not optimized at all. Still, without any optimization, 2 nm wide QWs with low barriers reach PL linewidths that are comparable to those of wider QWs grown in TQW structures with 30 % barriers and exhibiting similar confinement energies. Those linewidths are represented in the graph by the dashed line that joins the best data of Fig. 4.18. Nevertheless, the best QWR linewidth are close to those of the QWs, in spite of their much more intricate interfaces. Some of the corresponding spectra are shown in Fig. 5.14(d).

5.2.3   Doublet splitting of the QWR PL line
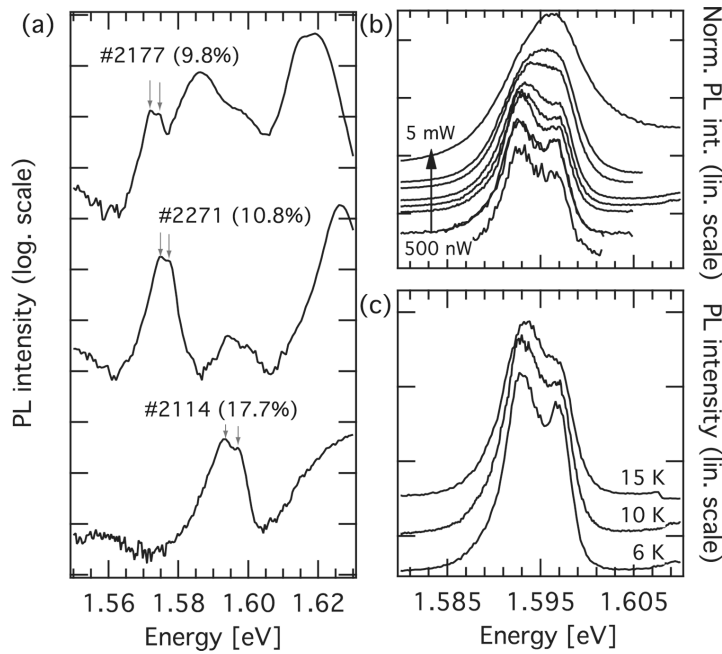
Figure 5.15: (a) Close-up on three PL spectra featuring a doublet splitting of the QWR line (10 K, 50 μW excitation power). Power (b) and temperature (c) dependence of the PL spectra of sample #2114 ($x_{act} \simeq 18\%$).

In the sample series discussed here, one of the origins of the dispersion of the FWHM is that several samples exhibit a barely resolved doublet in the PL line of the QWR. Three representative spectra are shown in Fig. 5.15(a). Panels (b) and (c) display the dependence of the PL on the excitation power and temperature, respectively, for a sample grown with ~18% Al in the barriers. The low energy component dominates at low excitation power and low temperature. At very high excitation, the two components broaden and merge, and only a broad, blue-shifted line subsists. The energy separation

Sample	x_{act} [%]	$\Delta_{doublet}$ [meV]
2114	17.7	3.5
2424	12.3	3.3
2422	12.0	2
2271	10.8	2.2
2177	9.8	2

Table 5.2: Doublet separation measured in the PL spectra as a function of the effective Al content in the barrier.

of the doublet mostly decreases with decreasing aluminium content, as reported in Table 5.2.
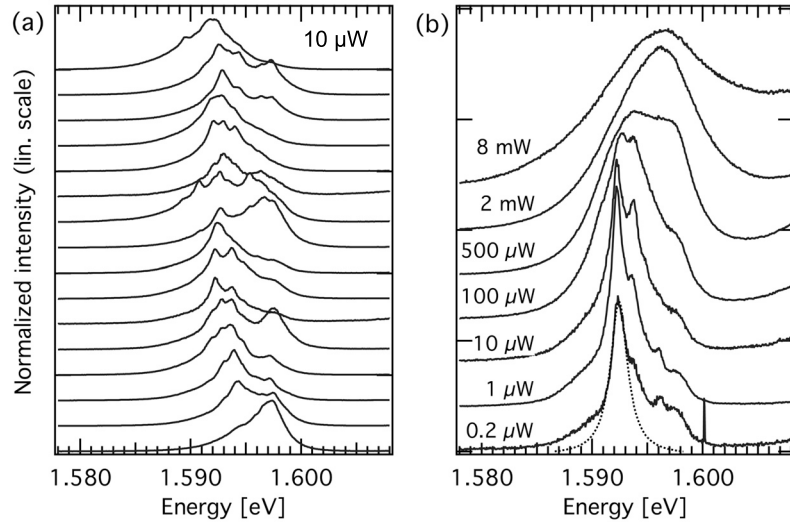
Figure 5.16: (a) Low temperature (10 K) μPL spectra of sample #2114 (x_{act}= 18%) taken at $\sim$1 μm distance along a QWR segment (a). Spectra measured at a given position with different excitation powers (b). The dotted line is a lorentzian fit of the dominant line at the lowest excitation density. Its FWHM is 1.7 meV.

The doublet is not systematically present in μPL spectra: this is seen in Fig. 5.16(a) for the same sample as in Fig. 5.15. Instead, the emission consists of several peaks, which are all rather broad. Here again, we observe fluctuations of both the mean energy and of the fine structure of the PL line. Even at the lowest excitation power the dominant line has a linewidth much larger than 1 meV (panel (b)). With increasing excitation intensity, the broadening and blue shift are clearly due to occupation of higher energy states. At intermediate intensity (500 μW), the lineshape indeed exhibit an unresolved doublet. No new emission line appears at higher energy with increasing excitation density, but only the intensity of the highest energy feature visible at low-excitation is increasing. Local saturation of the low-energy states may then explain the occurrence of doublet-like emission in some spectra of Fig. 5.16(a), which has an energy separation of the order of that measured in μPL. The possible origins of the low-energy states will

be discussed later in Sec. 5.4.1.

5.3   V-groove QWRs grown on vicinal substrates

In Ch. 4, we showed how the growth on vicinal substrates can efficiently modify the optical properties of QWs as a result of a change of the growth mode. In this section, we investigate the same approach for improving V-groove QWRs. The situation is, however, much more complicated in this case because several crystallographic facets are involved. It is known that, under given growth conditions, each of these facets displays a different growth mode. An optimization of the growth conditions is hence necessary, in order to find the best compromise for the QWR structure.

The situation is further complicated by the initial groove disorder: the growth takes place on an inhomogeneous template. We have observed in Sec. 5.1 that even the growth of a thick buffer layer before growing the QWR does not allow to smooth out these fluctuations. The self-limited growth described in Ch. 3 takes place in the groove sectional plane. It would be desirable to have a comparable mechanism along the QWR direction. In the following, we investigate the effect of a small misorientation of the (001) substrate toward the $[1\bar{1}0]$ direction on the optical and morphological properties of V-groove QWRs samples (Fig. 5.17(a)). We expect the miscut to influence the growth mode along the groove.
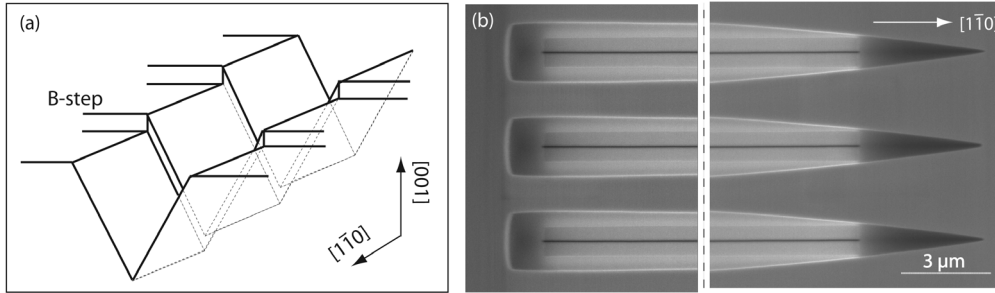
Figure 5.17: (a) Schema of B-steps close to a V-groove etched in a substrate misoriented toward $[1\bar{1}0]$. (b) SEM images of the two extremities of V-groove patterns etched in a 8°-off substrate. The SiO_2 layer is still present.

A first effect of the miscut occurs already at the stage of the groove processing. The lateral etching rate of the HBr:Br:Methanol solution increases with the miscut angle. The etching time is therefore adapted to ensure similar grooves dimensions on all substrates. As illustrated in Fig. 5.17(b), the extremities of the grooves also exhibit different shapes, which indicates an anisotropic etching rate in the $[1\bar{1}0]$ direction. However, the resulting sidewalls all display a roughness similar to that described in Sec. 3.1.3.

5.3.1 Dependence of the PL spectra on the miscut angle

The PL spectra of V-groove samples grown on patterned substrates with various miscut angles are shown in Fig. 5.18(a). The samples consist of a 2 nm (nominal) QWR layer, embedded in 500 nm and 300 nm $Al_{0.3}Ga_{0.7}As$ barriers, and covered by a 30 nm GaAs cap. For all samples, the QWR PL is clearly identified around 1.6 eV, whereas that of the QWs and AlGaAs consist of several lines, the energy and shape of which depend strongly on the miscut angle. The FWHM and peak energy are reported in panel (b) as a function of the substrate miscut angle. For each angle value, several points are reported, corresponding to different locations on the substrate surface and thus probing the overall homogeneity, which is found to be rather good. An exception is the sample grown on a 2°-off substrate, which displays rather large PL linewidths due to an unresolved fine structure. This fine structure is not always observed; when it is not observed a rather narrow linewidth is measured. We will disregard this anomalous feature in the following discussion.
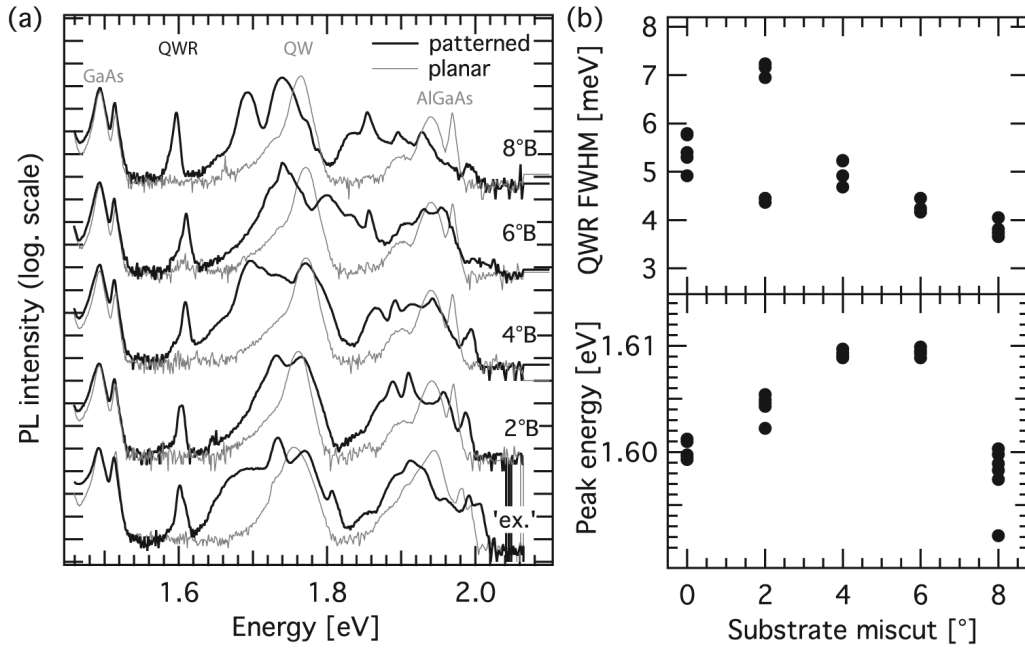
Figure 5.18: (a) 10 K PL spectra of 2 nm QWRs samples grown (simultaneously) on substrates with different miscuts. The light gray lines correspond to non-patterned parts of the substrates. (b) Linewidth and peak energy as a function of the miscut.

The FWHM of the QWR PL decreases with increasing miscut angle particularly for angles larger than ∼4 °. For an 8°-off miscut angle, the FWHM is as narrow as 3.7 meV. The peak energy of the QWR PL from this sample is significantly redshifted. This is in contrast to the trend showing an increase of the emission energy with increasing miscut angles between 0° and 6°. Another characteristic feature of these spectra is the change of the QWR PL lineshape, which is well visible in the logarithmic scale representation of Fig. 5.18. The sample grown on the 'exact' substrate shows a QWR PL with a tail

on the high-energy side. In contrast, the samples with a larger substrate miscut angle exhibit a stronger spectral weight on the low-energy side of the line.

In Fig. 5.18(a), the light grey lines correspond to the PL measured on a non-patterned area of the same samples. The GaAs, 2 nm thick QW and AlGaAs emissions are clearly identified. We note the important difference in the AlGaAs quality between the sample grown on an 'exact' substrate and the vicinal ones: whereas donor-acceptor recombination dominates the PL of the 'exact' sample, the relative intensity of the bound exciton emission increases with increasing miscut angle and its lineshape gets narrower. Also, we observe that AlGaAs grows with a higher Al content on the patterned parts. In the PL corresponding to the patterned area, the QW and AlGaAs lines split into several components corresponding to the growth on the different facets. Discussing the PL lines from these structures is difficult, because we cannot identify them more precisely.

The QWR emission of the samples grown on the 'exact' and 8°-off substrates are further compared in Fig. 5.19(a). This figure displays μPL spectra measured at random positions on the samples. At first sight, the local disorder is important and similar in both cases. For both samples, the mean energy of the spectra and the number of sharp lines fluctuate over the sample. Yet, we note that the tails of spectra are smoother, on average, for the 8°-off sample than for the 'exact' one. In the latter case, several small features are visible, both on the low- and high-energy sides, generally of weak intensity. On the contrary, spectra acquired from the 8°-off sample often display a smoother low-energy onset of the PL. Similarly, the high-energy tail generally decreases more smoothly than for spectra measured on the sample grown on an 'exact' substrate.

Important deviations from this general behavior are, however, worth commenting on. Several spectra obtained on the 8°-off sample are shifted by a few meV toward higher energies. Their intensity is systematically weaker than those emitting closer to 1.6 eV, as indicated by the larger relative contribution of noise to these spectra. This is better evidenced in Fig. 5.19(d), which displays the integrated intensity of the QWR PL as a function of its mean energy (the 'center of gravity' of the emission). The data dispersion in intensity is important and is partly due to slight misalignments of the laser spot relatively to the groove axis. Still, a trend is visible, showing that emission at low energy is weaker. For the 8°-off sample, however, several points deviate from this trend. Although they span a higher energy range than the data relative to the 'exact' sample, they do not influence the overall PL lineshape because of their low intensity.

Panels (b) and (c) of Fig. 5.19 display the sum of each individual spectrum of part (a), for the two samples. The non-normalized spectra were summed, and the background signal corresponding to the emission tail of QWs was subtracted. The lineshape that is obtained through this procedure closely resembles that obtained in standard PL measurements. The emission of QWRs grown on the 8°-off substrate is well fitted by a Gaussian over one order of magnitude. The low-energy side of the spectra is slightly
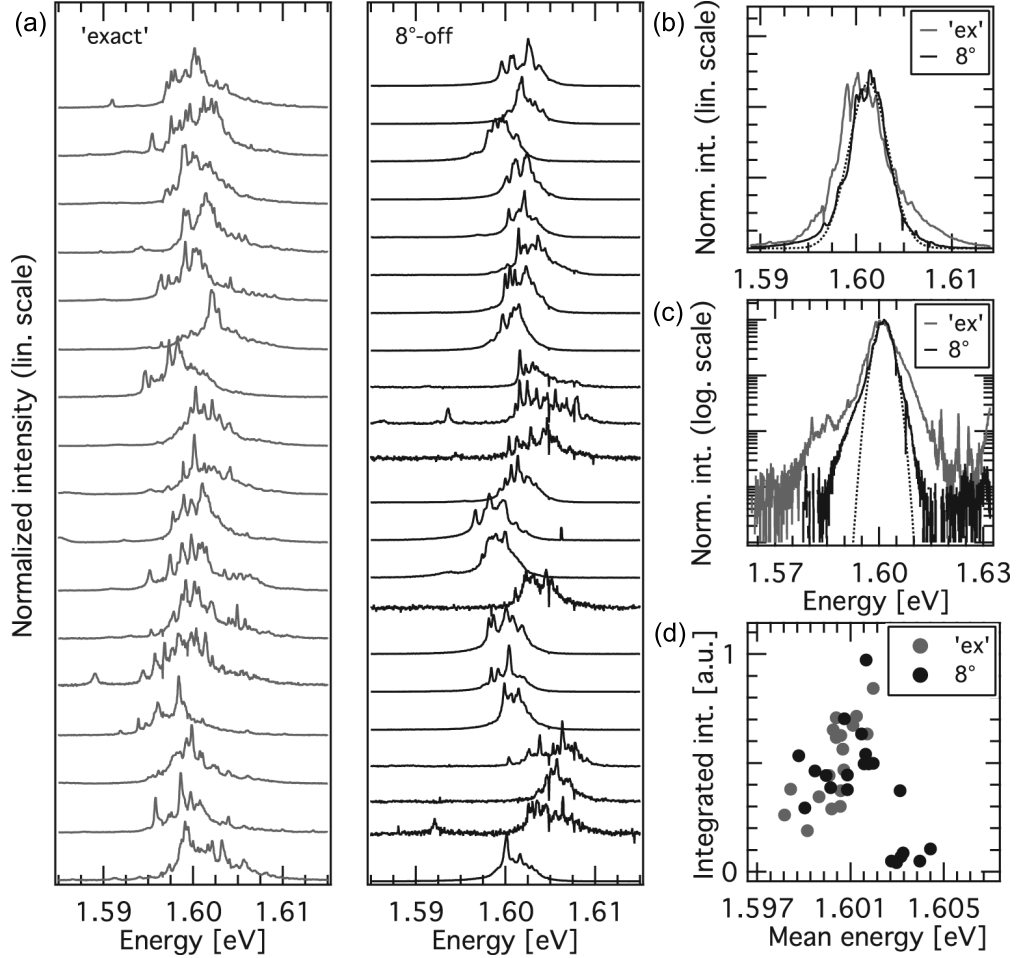
Figure 5.19: (a) 10 K μPL spectra of QWRs grown on 'exactly' oriented and 8°-off substrates. The spectra are taken at random locations on the patterned area. (b) Linear and (c) logarithmic scale spectra of the two samples, obtained by summing the individual spectra (without normalization) of panel (a). In both panels, the dashed line is a gaussian fit to the 8°-off sample spectra. (d) Distribution of the integrated intensity of the spectra of panel (a) as a function of their mean energy ('center of gravity').

broader and decays exponentially. In contrast, the numerous peaks visible on the individual spectra of the 'exactly' oriented sample form an important shoulder on the low-energy side of the ensemble lineshape. On the high-energy side, another shoulder is present, about 6 meV above the peak.

The broadening of the PL line for the two samples is further discussed through the power and temperature dependence of the μPL lineshape (Fig. 5.20). The global effect is the same for an increasing excitation power (panel (a)) or temperature (panel (b)). At a low temperature ($T = 10$ K) and a low excitation power ($P \simeq 1$ μW), the PL of the QWR grown on the 'exact' substrate exhibits the characteristic sharp lines discussed above. The background from which they emerge increases with increasing P (or T). The sharp lines gradually merge with this background and finally become a single broad line, although with some fine structure still visible at the extremal measurement conditions used here ($P = 1$ mW or $T = 50$ K). Most importantly, in both cases, the PL lineshape of the 'exact' sample develops a strong asymmetry with increasing P (or T), as more states are occupied by state filling (or thermal redistribution).
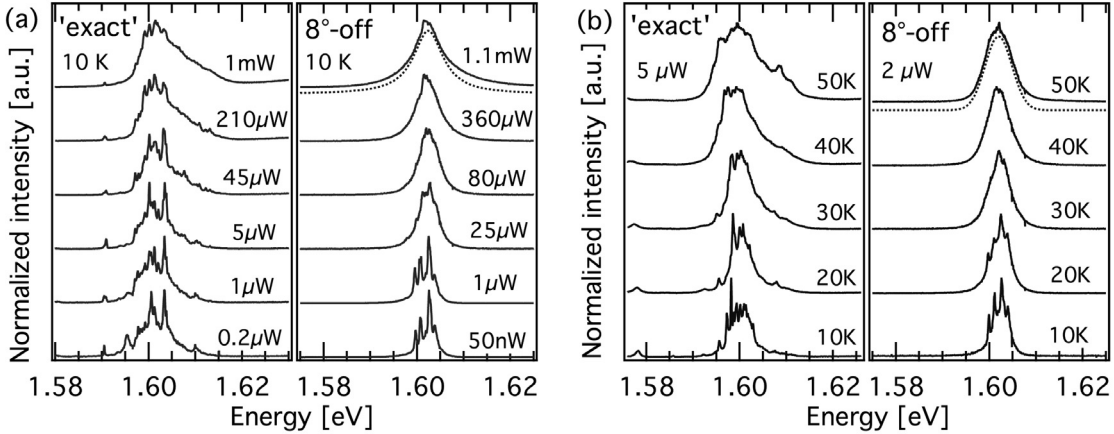
Figure 5.20: (a) Excitation power and (b) temperature dependence of the μPL spectra of two samples grown either on an 'exactly' oriented substrate, or on a 8°-off substrate. The dashed lines are Lorentzian (a) and Gaussian (b) fits to the upper spectra of the 8°-off sample, vertically shifted for clarity.

Strikingly, the data relative to the sample grown on the 8°-off substrate indicate a totally different behavior. The increase of background and disappearance of sharp lines are also observed, but the overall lineshape symmetry is conserved up to 1.1 mW or 50 K, and no high energy tail appears. This is illustrated by the two fits that are displayed on the 1.1 mW and 50 K spectra of the 8°-off sample. Interestingly, the lineshape is lorentzian at high excitation power, but it is Gaussian at high temperature (in both cases with a linewidth of $\sim$7 meV).

To further characterize the specific behavior of the 8°-off sample, we performed PLE measurements. Representative spectra measured at 10 K with the laser polarization pa-
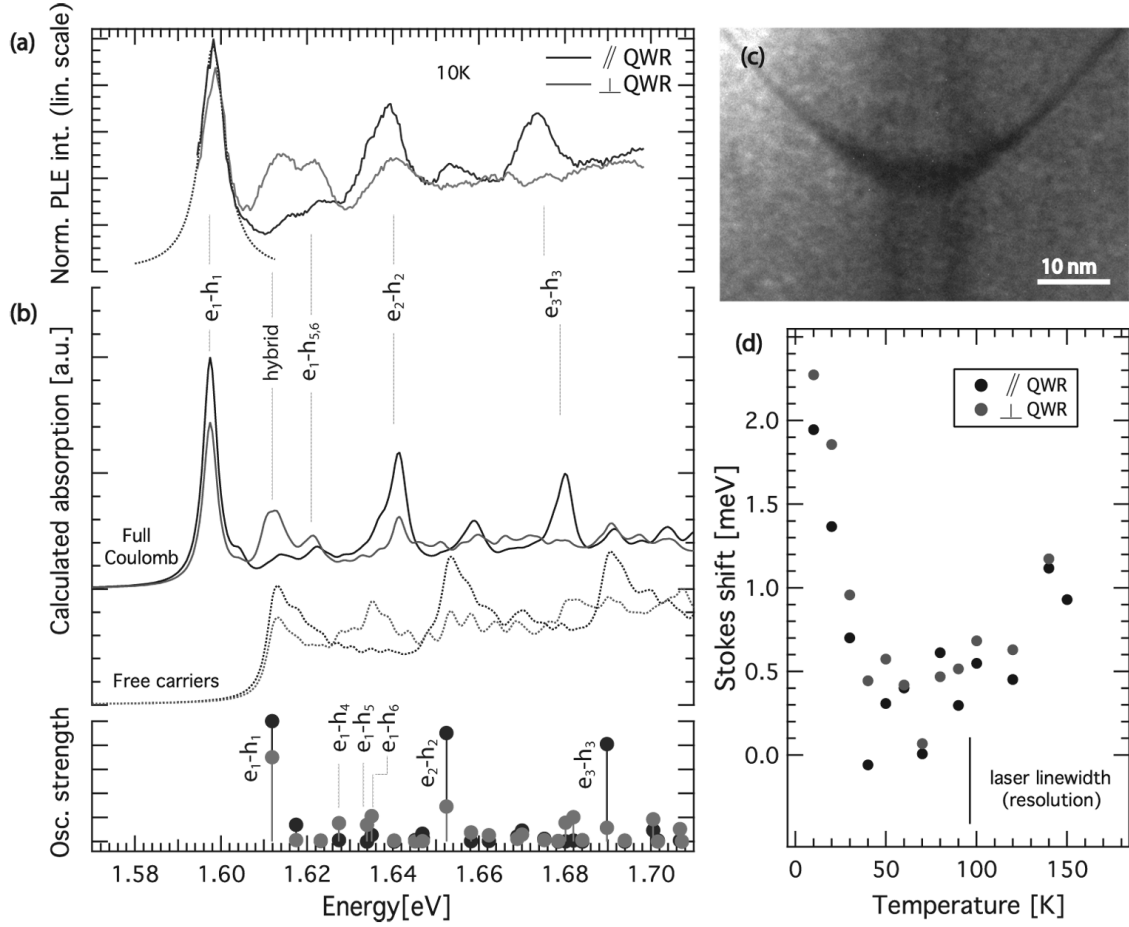
Figure 5.21: (a) PLE spectra measured at 10 K on the 8°-off sample. (b) Absorption spectra calculated with and without accounting for Coulomb interactions and oscillator strength of the transitions. (c) TEM image of the 8°-off sample used to determine the potential of the model calculations. (d) Stokes shift as a function of the temperature, deduced from PLE spectra polarized either parallel or perpendicular to the QWR.

rallel and perpendicular to the QWRs are displayed in Fig. 5.21(a). First, we note that in spite of the redshifted emission of the QWR for this sample, a strong subband separation is maintained (41 meV between $e_1 - h_1$ and $e_2 - h_2$). Second, the linewidth of the first transition (fitted by a Lorentzian in the figure) is as narrow as 6 meV. Third, a very rich fine structure is visible in the spectra.

This fine structure has been predicted a few years ago [253], but this sample is the first one, in which it can be resolved experimentally. Part (b) of Fig. 5.21 displays absorption spectra and the elements of the transition matrix (Eq. 2.20) calculated from the TEM profile shown in panel (c). The matrix elements and the dashed lines, corresponding to free carrier absorption, are obtained with the method described in Sec. 2.2. The full lines are obtained with a more sophisticated method, which includes Coulomb

correlation between all the subbands considered (here 8 for electrons and 9 for holes)[1]. Once the potential and material parameters are determined, there is *no free parameter* left in this model.

The agreement between the experimental and calculated spectra is outstanding. Not only the calculated energy and polarization anisotropy of the main transitions fit extremely well the experimental data, but the fine structure, in particular the doublet around 1.62 eV, is very well reproduced. Usually, a single transition polarized perpendicularly to the QWR is found at this energy in the absorption spectra of QWR and is ascribed to an excitonic transition involving the ground state electron and excited holes with a dominant light-hole character [254]. However, a sizable oscillator strengths in the perpendicular direction can be distributed over two or three nearby hole transitions (here h_4, h_5 and h_6 as can be seen in the matrix element spectra) depending on the exact wire geometry.

The intensity ratio of the two components of the doublet appearing in the perpendicular free carrier absorption spectrum is reversed: indeed the intensity of the low energy line is enhanced in the perpendicular polarization. We may notice that the spectral position of the first excited state (2s) of the $e_1 - h_1$ exciton (that we can guess from the continuum band-edge of $e_1 - h_1$ in the free carrier spectrum) is indeed very close to the lower component of the doublet. Therefore we are led to ascribe the modified absorption to an hybridization resulting from the coupling of the $e_1 - h_1$ 2s-exciton with the $e_1 - h_4$ light-hole-like exciton. This hybrid state gives the dominant contribution to the optical anisotropy in this energy range. Nevertheless, further theoretical investigations are required to fully support this conclusion.

Overall, these data indicate an exceptional quality of the 8°-off sample. This is confirmed by the very small Stokes shift, whose temperature dependence is displayed in Fig. 5.21(d). The 10 K value is around 2 meV. It decreases very rapidly with increasing temperature to reach zero around 40 K. At temperatures above, and considering the limited resolution of the measurement ($\sim$0.5 meV), the Stokes shift has practically vanished. The slight increase, especially at 150 K, is not explained.

In summary, these measurements demonstrate the superior quality of QWR samples grown on substrates with a large miscut and the possibilities that they offer for the experimental observation of subtle physical phenomena.

5.3.1.1   QWRs of different thicknesses

To confirm the systematic occurence of the improvement obtained with vicinal samples, we discuss in this section the optical properties of a series of samples with different QWR thicknesses, grown in pairs on patterned substrates having either a small (0.6°) or large (6°) miscut towards [1$\bar{1}$0]. Their measured PL spectra are displayed in Fig. 5.22(a). A general blueshift with decreasing layer thickness is very clear. The QWR PL is well

---

[1]These calculations are made by Dr M.-A. Dupertuis, from the IPEQ, EPFL.

separated from the QWs emission, except in the case of the narrowest QWRs, for which the QWR PL line overlaps with that of the QWs. The QWR peak energy and FWHM are displayed in Fig. 5.22(b) and (c), respectively. For a given sample, the measured values of the FWHM depend on the position on the sample where the measurement was carried out and are distributed within about 1 meV. As these positions may be centimeters apart, the overall uniformity is very good.
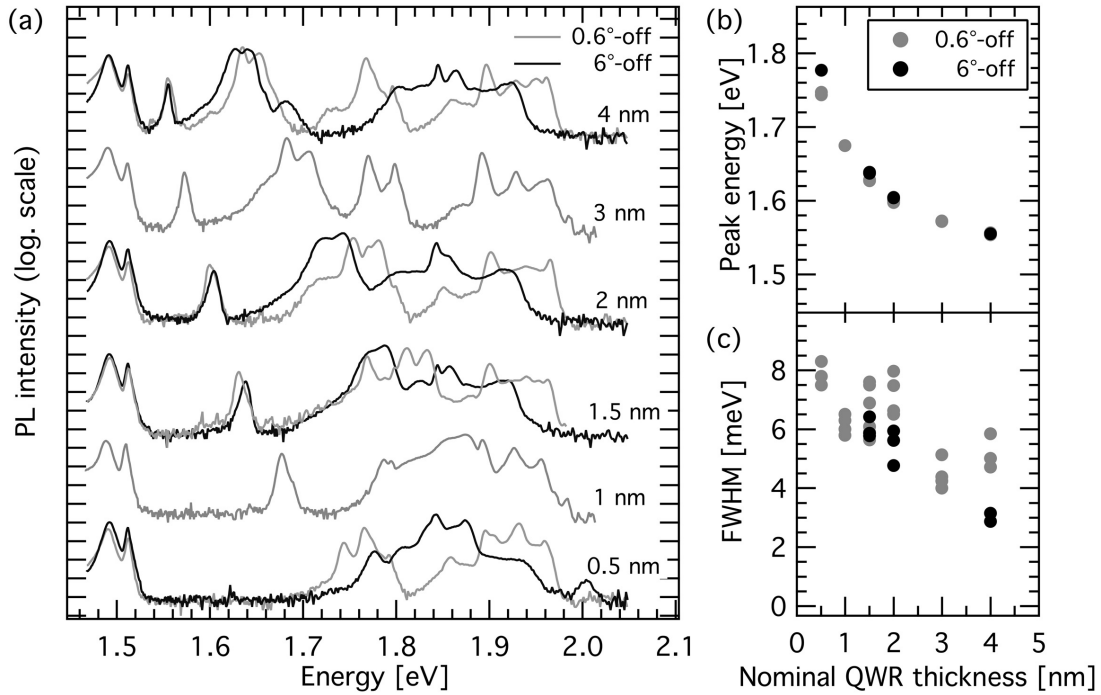
Figure 5.22: (a) PL spectra of samples grown with nominal QWR layer thicknesses of 4, 3, 2, 1.5, 1 and 0.5 nm, on substrates with miscut angle of 0.6° or 6°-off (001). (b) Peak energy and (c) FWHM dependence on the nominal QWR thickness. The dispersion of points corresponds to measurements at random positions on the samples.

The trends highlighted with the previous series of samples are confirmed: (i) the peak energy of the PL of 6°-off samples is slightly larger than that of 0.6°-off samples. Their energy separation increases with decreasing QWR thickness; (ii) the PL FWHM is smaller for the 6°-off samples; (iii) the lineshape is modified with the miscut.

The latter point is better evidenced in Fig. 5.23, in which the spectra of three pairs of samples are superposed. The spectra of the 6°-off samples are fitted with a Lorentzian, which nicely reproduces the low-energy tail. There is however a deviation at high energy. The spectra of the 0.6°-off samples exhibit a shoulder, separated from the main line by 2, 3 and 5.6 meV for the 4, 2 and 1.5 nm thick QWRs, respectively. In addition to the shoulder, the spectral PL decay is slower at high energy, resulting in the modified lineshape asymmetry underlined before. The overall lineshape is perfectly fitted with two Gaussians.

The spectra of the 1 and 3 nm thick 0.6°-off samples in Fig. 5.22 also display such an asymmetric PL lineshape. These two samples were grown at several months interval with respect to the other ones. Compared to the trend set by the other 0.6°-off samples, they exhibit lower FWHM values, which could be related to better conditions in the MOVPE reactor at the time of the growth. Hence, the asymmetry of the PL lineshape is not directly related to the linewidth of the sample, but is an intrinsic characteristic of the substrate miscut angle.
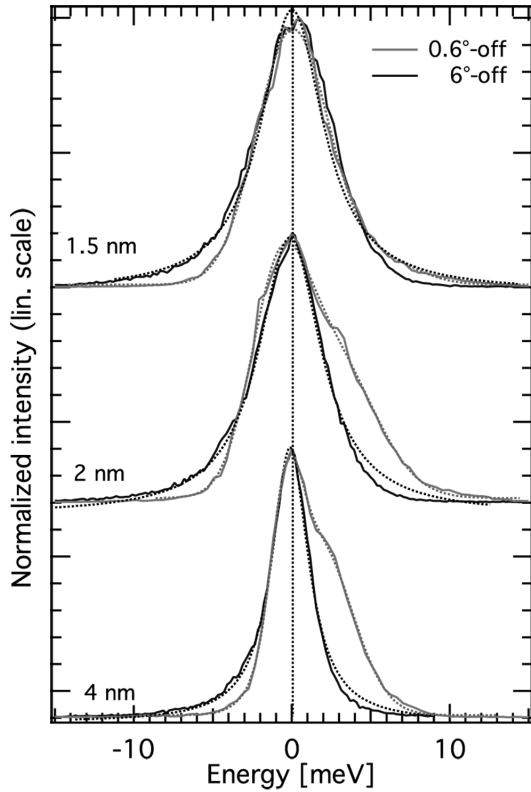
Figure 5.23: 10 K PL spectra of three pairs of QWR samples grown on 0.6° or 6°-off substrates, superposed according to their peak energy. The dashed lines correspond to fits with a Lorentzian for the 6°-off samples, and with two Gaussians for the 0.6°-off sample.

PLE measurements were performed on each pair of samples. The comparison of the spectra of Fig. 5.24 indicates that the confinement is similar for both the slightly and largely misoriented samples. All the spectra exhibit strong resonnances, which are attributed to the direct e_i-h_i excitonic transitions and to the e_1-h_x line that is perpendicularly polarized (h_x is the lowest lh-like level). The energy separation between the first subbands is reported in the Fig. 5.24(b). The subband separation increases with increasing confinement and then saturates. It even decreases for the narrower wire due to the penetration of the wavefunction in the barriers. The energy separation between the major subbands is large: around 30 or 40 meV between e_1-h_1 and e_1-h_2; the separation between the nearest transitions (e_1-h_1 and e_1-h_x) is between 10 and 20 meV.

The Stokes shift measured at 10 K is reported in panel (c). It decreases with increasing QWR thickness, again with the exception of the 0.5 nm thick sample. We note that the values obtained for the 6°-off samples are systematically slightly lower than those
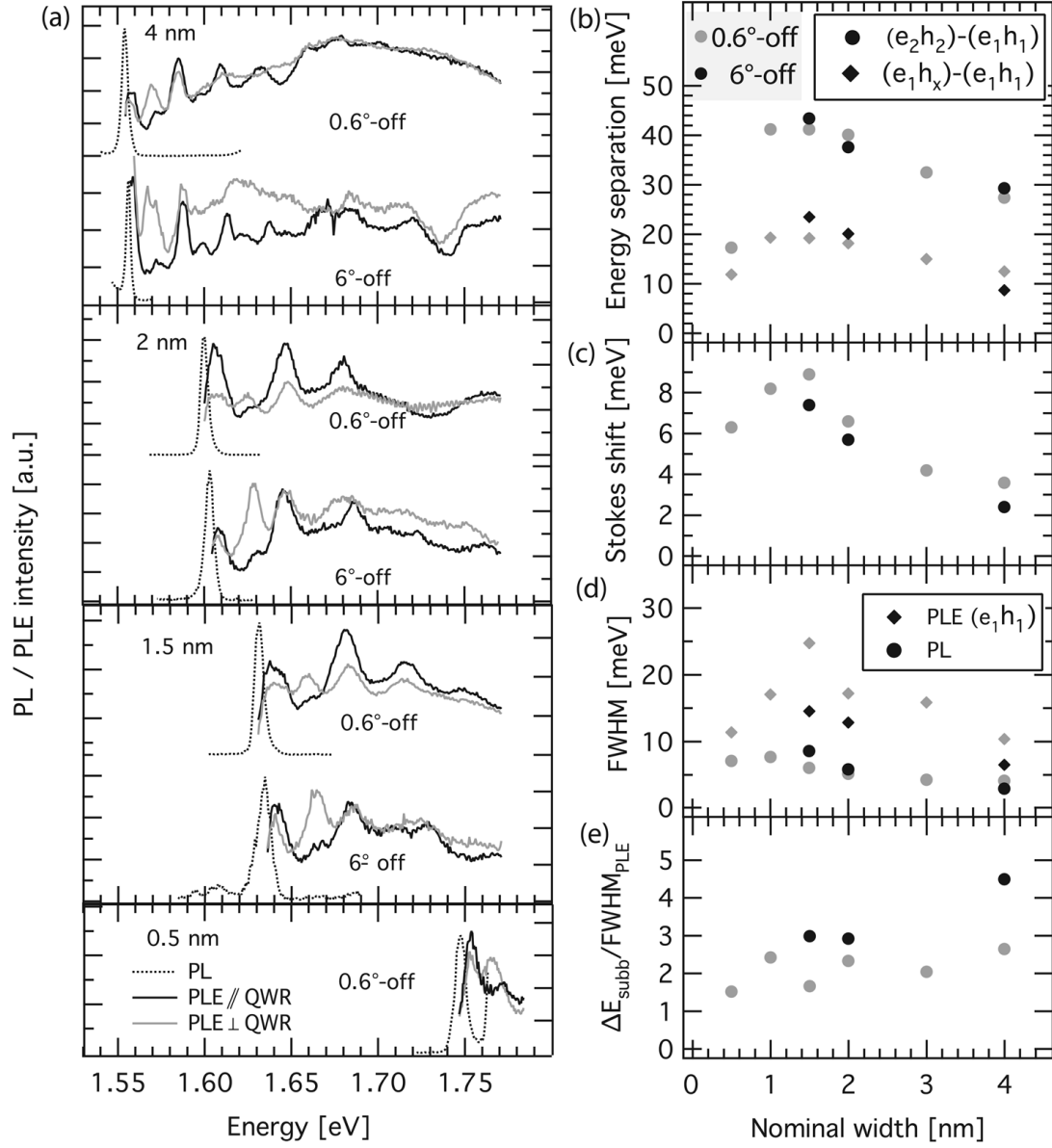
Figure 5.24: (a) PL and PLE spectra of samples grown with a QWR thickness of 4, 2, 1.5 and 0.5 nm (nominal), on substrates with miscut angles of 0.6° or 6°. The PL is excited at 1.77 eV. (b) Energy separation between the lowest energy transitions. (c) Stokes shift at 10 K. (d) FWHM of the PL excited at 1.77 eV and 1 mW, and of the lowest energy transition of the PLE spectra. (e) Figure of merit (see text). All parameters are displayed as a function of the nominal width of the QWRs.

of the 0.6°-off samples. Because of the good quality of the PLE spectra, one can fit the first transitions with a gaussian and extract their FWHM. These values are reported in the panel (d): they are systematically larger than those of the PL line (although they were measured with a rather large excitation density (1 mW at 1.77 eV)). Again, the broadening increases with decreasing QWR thickness and then reduces for the narrower samples. The broadening of the transition for the 6°-off sample is significantly narrower than that of the 0.6°-off one.

The last panel (e) of Fig. 5.24 shows the values of a figure of merit proposed by Otterburg et al. [182] to characterize the quality of the QWR samples: the ratio between the subband separation ΔE_{subb} and the PLE linewidth. The values of this figure of merit are larger for the 6°-off sample than for the 0.6°-off sample.

In summary, all these indicators confirm the higher quality of QWRs grown on substrates with a large miscut.

5.3.1.2 Identification of the other PL lines

We noticed in Fig. 5.22 that the QWs and AlGaAs emission give rise to very different spectra depending on the miscut angle of the substrate on which they were grown. We discuss here in more details the example of the 2 nm QWR samples, which μPL spectra are displayed in Fig. 5.25 with a logarithmic scale. Spectra measured on a non-patterned, planar (001) area are superposed for comparison.
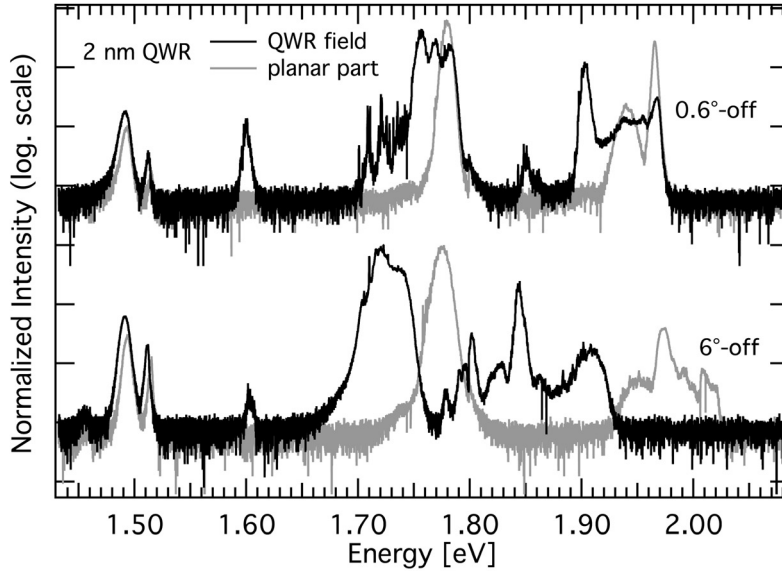
Figure 5.25: μPL spectra of the 2 nm thick samples grown on substrates with miscut angle of 0.6° or 6°-off. The black lines are measured on the patterned areas, whereas the grey lines correspond to PL spectra measured on non-patterned parts of the respective samples.

As previously noticed, we find an important redshift of the emission of AlGaAs grown on patterned substrates. The prominent feature of the spectra of the 6°-off sam-

ple is that there is almost no spectral overlap between the PL measured on the planar part and that emitted by the patterned area, either for the AlGaAs emission, or for that of the QWs. In contrast, for the 0.6°-off sample, the patterned area spectra clearly has a component coinciding with that of (001) surfaces.

In Sec. 5.1.3 (for an 'exactly' oriented substrate), we attributed the broad and densely peaked emission appearing here around 1.7 eV to {113} facets. It thus seems likely that on large miscut samples, the {113} structures are favored with respect to the (001) ones. In the next section, we turn to the morphological aspect of the samples, which confirms this hypothesis.

5.3.2   Modification of the V-groove facets

An inspection of the surface of two of the V-groove samples having significantly different miscut angles immediately demonstrates a major change in the geometry of the structure. The cross-section SEM images of the two samples that were used for the μPL spectra presented in Fig. 5.25 are shown in Fig. 5.26. In that particular case, a thick barrier was grown in order to planarize the surface. Indeed, for the 0.6°-off sample, the initial grooves (that are still visible in the lower part of the image) are completely filled, and the surface is planarized. In contrast, the growth on 6°-off substrates results in a corrugated surface, although the initial grooves were identical in depth and width to those of the other sample. These corrugations make an angle of about 25° with the (001) surface, and therefore correspond to {113} facets. This observation is therefore consistent with the attribution of the PL lines of Fig. 5.25 to structures grown on {113} facets.
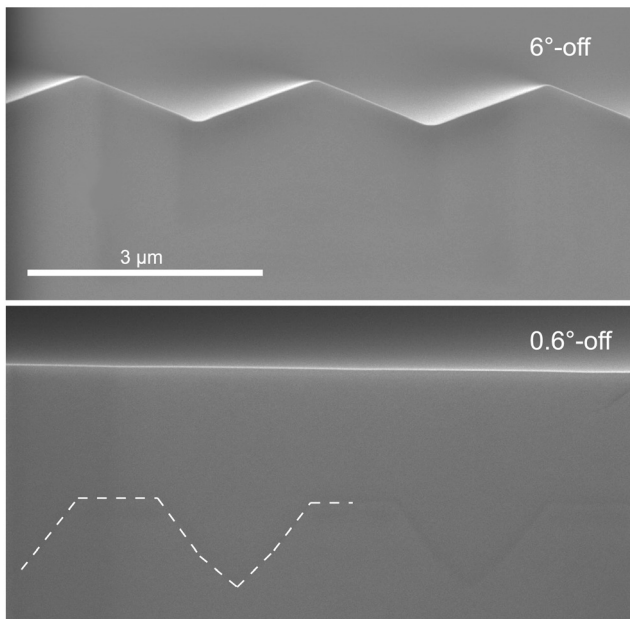
Figure 5.26: Cross-sectional SEM images of samples grown on 0.6° and 6°-off substrates. In the bottom part of the 0.6°-off sample image, the GaAs V-grooves are barely visible and their profile is retraced by the dashed line on the left part.

To further characterize the growth evolution with the miscut angle, the surface of samples grown with thinner barriers were imaged by AFM. The results are shown in Fig. 5.27. The optical spectra of these samples were presented in Fig. 5.18. The GaAs cap, which surface is imaged, is 30 nm thick. Amplitude AFM images are displayed in order to enhance the contrast of the observed features. The surface of the nominally exactly oriented sample is very similar to that described in Sec. 5.1.2: monolayer steps cross the ridge, making a large and wavy curve between the grooves and joining their edges perpendicularly. Shallow (∼300 nm deep) grooves subsist. The groove profile is displayed in the left column; the groove angle corresponds to the usual near-{111}A sidewalls. Nevertheless, on the surface image, a narrow band follows the groove edge and exhibits fluctuations on a short distance. It corresponds to the narrow {113} facets at the intersection of the (001) ridges and sidewalls.

The 2°-off sample is almost completely planarized. Narrow terraces are separated by bunched steps forming a kind of 'arrow' pattern on the ridge. We do not discuss this sample in more details, because it does not follow the trend of the other samples, as we have already noticed with regard to its optical properties (see Fig. 5.18).

The sample grown on a 4°-off substrate exhibits a similar 'arrow pattern' on the ridge. As visible from the cross-section, a shallow depression in the center of the ridge results from the high density of steps and their curvature across the ridge. The {113} facets are slightly wider than on the 'exactly' oriented sample and the grooves are deeper.

All these features are further accentuated on the 6°-off sample. The ridge width is strongly reduced, and the sidewalls are predominantly defined by {113} facets. The groove angle only reduces at the bottom and closes with {111}A planes. A slanted stripe pattern is visible on these planes. Remarkably, the characteristic short-scale step-bunching that is usually observed on {113} planes occurs only in the vicinity of the boundary with {111}A sidewalls.

Finally, the {111}A facets have completely disappeared from the surface of the sample grown on the 8°-off substrate. Only the {113} facets remain, displaying much more pronounced undulations that appear as the oblique pattern on the image. The amplitude of this undulation is depicted in the right panel of Fig. 5.27, where the profile along the groove direction is represented. It ranges between 2-4 nm; this is much smaller than the fluctuations observed on {111}A sidewalls, which are in the 10 nm range. Its period is however short, on the order of a few hundreds of nanometers.

5.3.3   Morphology of the bottom of the groove

The data presented in the last section clearly demonstrate a major change of the growth front for samples grown on vicinal substrates. However, they do not provide direct information about the facets that form the interface of the QWR. Whereas we clearly observe major effects of the miscut on the ridge and groove sidewalls, the QWR is formed by narrow (001) and {113} facets formed at the *bottom* of the groove, which may show different behavior. These QWR facets are difficult to image on the samples
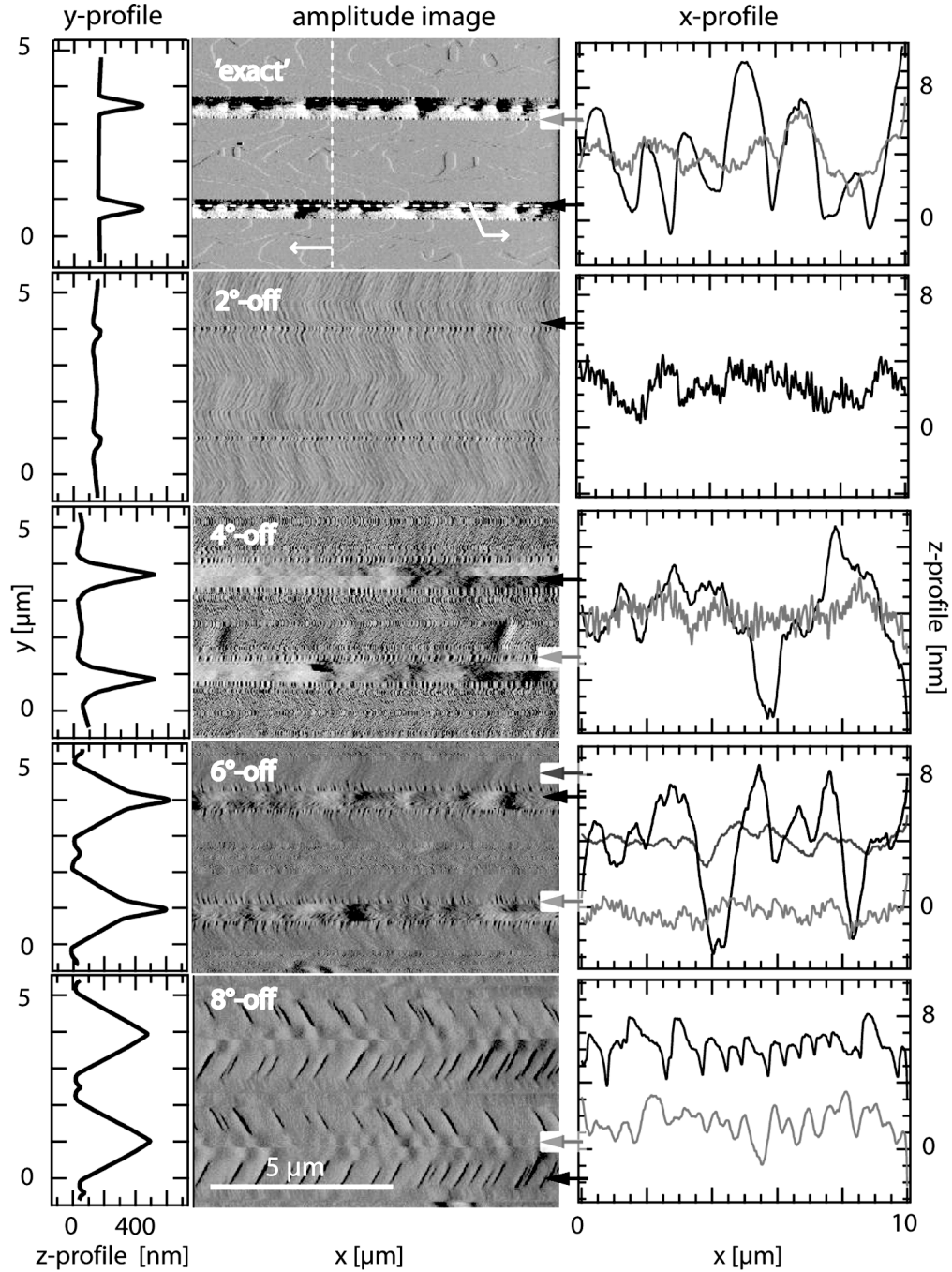
Figure 5.27: AFM amplitude images of the surface of five samples with different miscut angles. The left panels are the measured profiles of the surface, measured perpendicularly to the grooves. The right panels are profiles measured along a groove facet, at the y-coordinates indicated by arrows.

dedicated to optical studies because of the rather narrow groove opening.
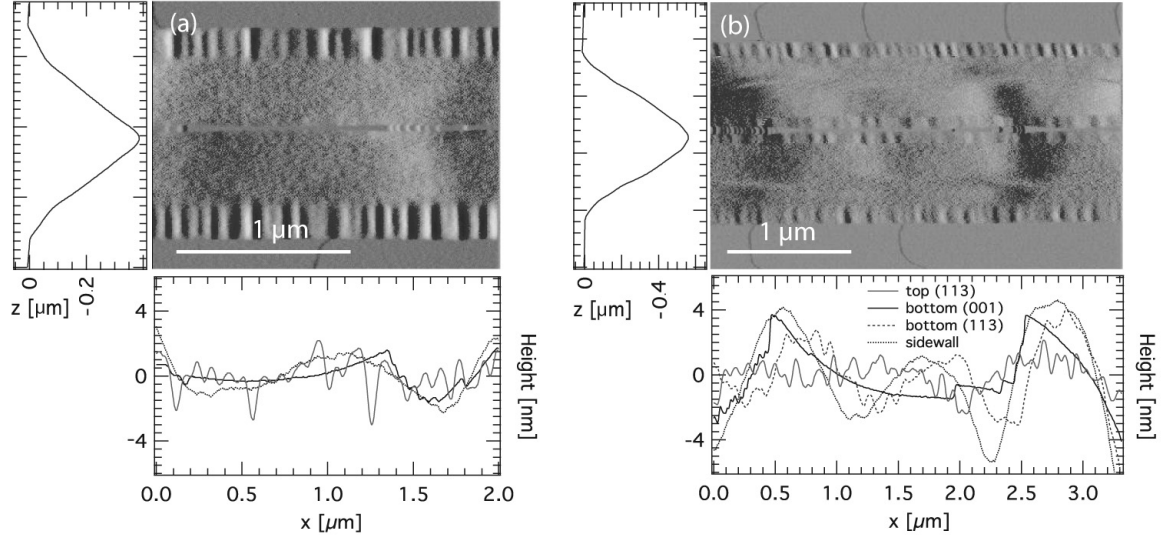
Figure 5.28: AFM images of samples grown at 780°C on nominally exact substrates. (a) 10 nm GaAs cap (b) 200 nm GaAs cap.

To check wether the bottom facets are also affected by the substrate miscut, we grew samples at a higher temperature (780°C, starting with a thick AlGaAs buffer at 690°C), that resulted in a wider groove opening [176]. We know (Sec. 3.1.3) that facets form differently for GaAs and AlGaAs layers. As a consequence, GaAs morphology has to evolve from the one set by AlGaAs growth [177]. We evidence this evolution in the two images of Fig. 5.28. The two samples differ by the thickness of the GaAs cap. If this layer is too thin (10 nm, (a)), no step-bunched {113} facet is observed at the bottom of the groove. The (001) facet is however well visible, with bunches of steps at positions where the sidewalls fluctuates importantly. When growing a much thicker GaAs layer (200 nm, (b)), the GaAs profile is self-limited and the bottom {113} facets get really apparent, with step-bunching amplitude comparable to that of the top {113} facets.

This last growth sequence with a 200 nm GaAs cap was also used to grow samples on substrates with a small miscut (∼0°, 0.2° and 0.6°) and a sample grown on a substrate with a larger miscut angle (4°). The AFM images of the surfaces are shown in Fig. 5.29. The observations made in the previous section are valid also here: in particular the increasing width of the {113} facets with increasing miscut angle and the appearence of oblique stripes on the sidewalls. Wide near-{111}A sidewalls subsist however in all cases. Also, the angle range over which the transformation takes place is different due to the different growth conditions.

The Fig. 5.30 shows more details at the bottom of the groove of the latter samples. The image in (a) is an example from the 0.2°-off sample. In the bottom of the groove, we distinguish clearly the {113} facets, for which the amplitude of the step-bunching is
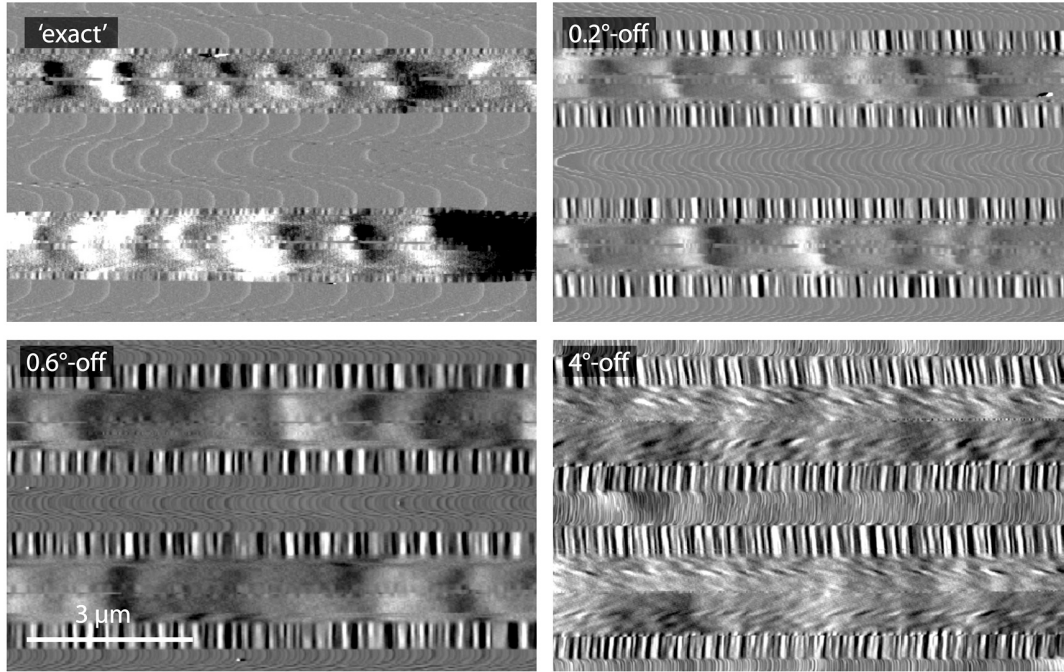
Figure 5.29: AFM amplitude images of the surface of 4 samples with different miscuts, grown at 780°C with a thick (200 nm) GaAs layer as cap.
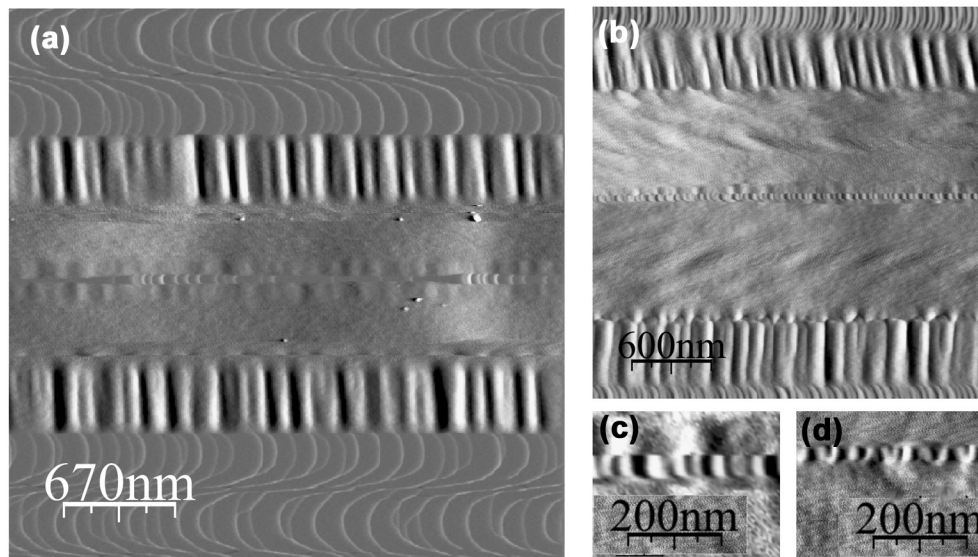
Figure 5.30: AFM amplitude images showing details of the groove bottom on the 0.2°-off sample (a) and 4°-off sample (b,c,d).

strongly reduced (< 1 nm) compared to the top $\{113\}$ facets (~ 3 nm). We also see the narrow (~ 50 nm wide) (001) central facet; its width varies slightly along the groove. Curved steps are visible, and have a height from 1 to 3 ML in this case, i.e. much smaller than the nm-high corrugations of the groove. Indeed, the large fluctuations of the sidewalls also induce slight changes of the width of the (001) facet. In between the steps, rather long (μm-scale) segment are atomically flat.

This is no more the case for the 4°-off sample (Fig. 5.30(b,c,d)) for which the steps are very closely spaced (separation of the order of 40 nm). We note (d) that the steps seem to merge at one extremity when the central (001) facet is very narrow. Also, the bottom $\{113\}$ facets are barely visible. The image (b) also details the structured morphology of the sidewalls, which show stripes starting from the top-$\{113\}$ corrugations toward the center of the groove.

5.3.4   Evolution of the growth front

We observed that a tilt of the patterned substrate in the groove direction modifies the growth front of the layers grown on it. It is however not a true change of growth *mode*, as the transition is continuous with increasing substrate miscut angle. The observed trend is an increasing width of the $\{113\}$ facets with increasing miscut angle. It leads to a reduction of both the (001) ridge and the $\{111\}$A sidewalls. The latter ones disappear after the growth of a sufficiently thick layer, while the ridge deepens in its center. The growth fronts are schematized in Fig. 5.31 and illustrated by TEM images of two structures grown on nominally exact (001) and 6°-off substrates. These particular samples consist of a thick $Al_{0.3}Ga_{0.7}As$ layer, in which 10 nm thick GaAs markers are inserted every 90 nm. We note a small asymmetry of the growth on the 6°-off sample, but it does not perturb the self-limited profile at the groove center.

A significant difference is already observed before the onset of the AlGaAs growth: the darker region in the TEM images (c,d) (and in the schemes (a,b)) corresponds to the ~ 200 nm GaAs buffer systematically grown underneath any of our structures. This layer already shows strong $\{113\}$ faceting, and the subsequent expansion of these facets through the AlGaAs growth seems to originate from this initial pattern.

In fact, the $\{113\}$ facets are formed prior to any growth, as we show in Fig. 5.32. This AFM image represents the surface of patterned 0.2° and 4°-off substrates, that have undergone the desoxidation procedure inside the MOVPE reactor without any subsequent deposition. This procedure consists in heating the substrate up to 800°C before cooling it down to the growth temperature. It is systematically applied at the beginning of each growth run. In that particular case, the process was stopped after the desoxidation, and no material was deposited. Nevertheless, we observe that the main features that we have previously described on the surface of the grown samples are already present at this stage: in particular, the curved pattern on the ridge, with steps aligning perpendicularly to the grooves, and the narrow and step-bunched $\{113\}$
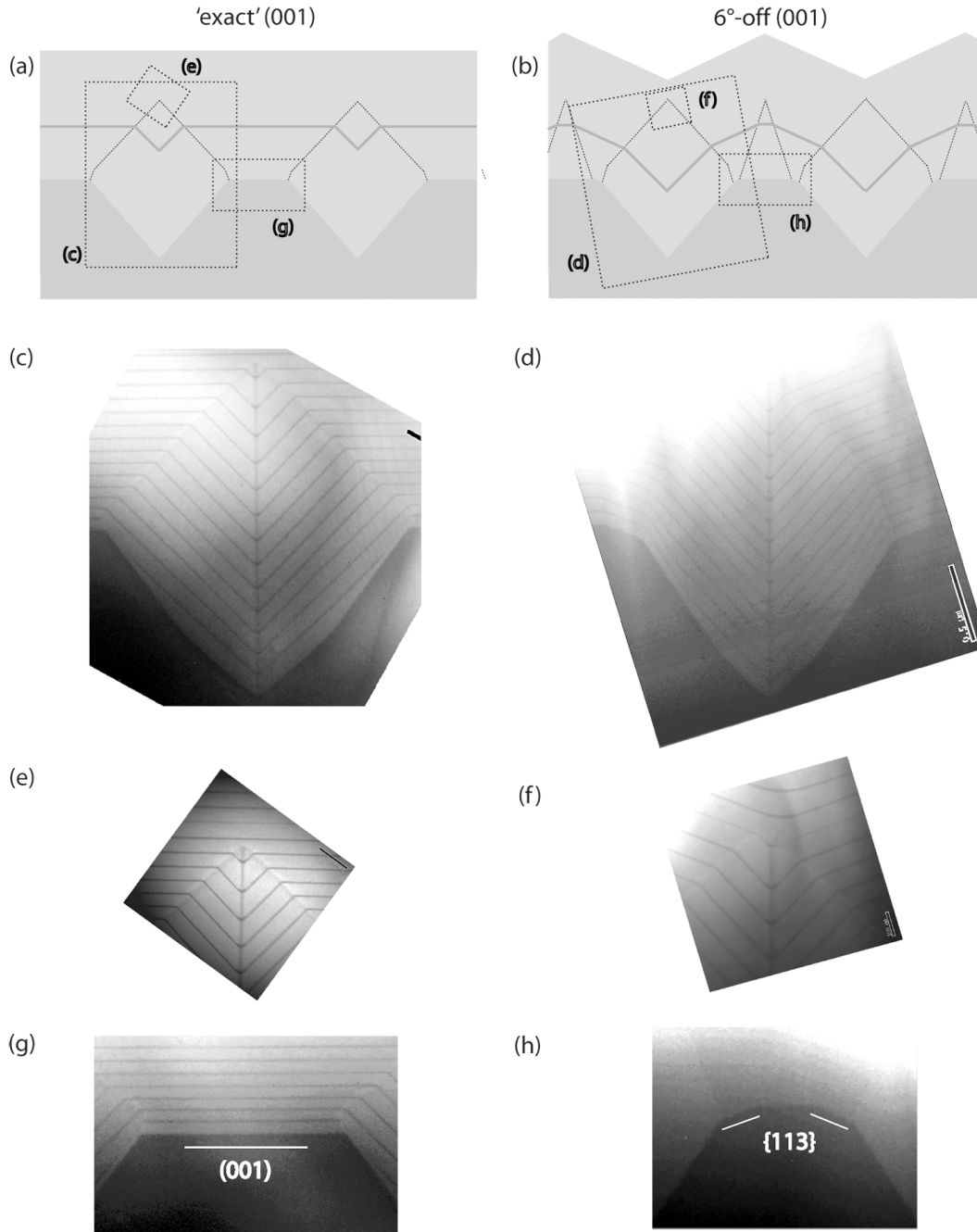
Figure 5.31: Schematic illustrations of the growth front on a substrate with (a) no (or small) miscut and with (b) a large miscut. (c-h) TEM images illustrating the framed areas in (a) and (b); (c-g) are measured on an AlGaAs sample in which GaAs markers were deposited with a period of 100 nm (see text), whereas (h) is measured on a sample with a single 4 nm thick (nominal) QWR. (c,e,g) correspond to an 'exact' (001) substrate and (d,f,h) to a 6°-off substrate.
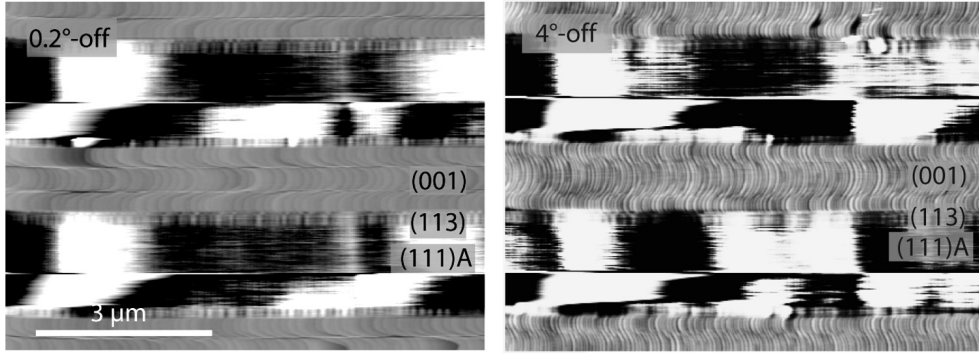
Figure 5.32: AFM images of 0.2°-off (left) and 4°-off (right) patterned substrates annealed at 800°C in the MOVPE reactor, without any subsequet layer deposition.

facets at the intersection of the grooves and the ridges. As expected, the ridge pattern changed importantly with the miscut angle in the 0°- 6° angle range that we have investigated. However, the width of the {113} facet was comparable for all the samples that we checked. The amplitude of the height fluctuations (2-3 nm) is also similar in each case.

From these observations, we infer that the *formation* of the {113} facets is due to annealing and is independent of the substrate miscut angle. Its *expansion* during growth, however, is clearly related to the miscut angle. This indicates that the former phenomena is related to adatom diffusion, whereas the expansion of the {113} facets results from a modified decomposition rate of the precursors on vicinal substrates.

5.4   Discussion

5.4.1   Interplay between confinement and disorder

For a given structural disorder, a stronger confinement obviously leads to larger fluctuations of the potential and, thus, to broader spectral linewidths. In the experiments reported in this chapter, we modified the confinement in two ways: first, by reducing the barriers height (for QWRs of constant thickness) and second, by modifying the QWR thickness (for constant $Al_{0.3}Ga_{0.7}As$ barriers).

The first approach proved very effective. We obtained a strong reduction of the PL linewidth of QWRs grown in between highly diluted AlGaAs alloy layers. Yet, there is still much disorder at the micron scale, as evidenced by the μPL spectra; however, the power dependence of the μPL spectra indicates that the minima of the potential are shallow. Indeed, when increasing the number of carriers in the QWR, we did not observed emission from new states, on the high-energy side of the QWR emission. Instead, the highest energy line has an increasing intensity and decays smoothly at high-energy. This leads to the occurrence of a doublet in the PL lineshape, which energy separation

decreases with increasing barrier height.
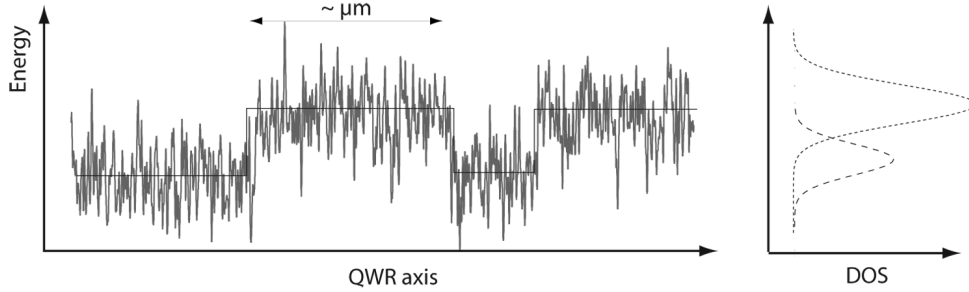
Figure 5.33: Schematic illustration of the QWR potential, which fluctuations are due to a superposition of the nano-roughness and sidewalls fluctuations.

We could possibly attribute the high energy line to the 1D continuum and the lower lines to localized states. The former attribution is supported by the constancy of its emission energy and the fact that no localized states seem to be present at higher energy. However, the non-vanishing Stokes shift indicates that it corresponds more likely to shallow localized sites. The lower energy lines, which appear in the μPL spectra would then correspond to deeper minima. Their depth consistently decreases as the barrier height is reduced. Such an interpretation of local variations of the potential is consistent with a previous report of cathodo- and photo-luminescence measurements performed on GaAs/Al$_x$Ga$_{1-x}$As V-groove QWRs, which demonstrated quasi-periodic spatial oscillations of the luminescence intensity along the QWR axis [173]. This was interpreted as resulting from fluctuations of the QWR thickness along the groove axis (Fig. 5.33). Our measurements show that the density of low-energy states is much reduced compared to the shallow minima, as indicated by their saturation at higher excitation power. Reducing the Al content minimizes the fluctuations induced by the nano-roughness (which is superposed on the larger variations) and hence smoothes the spectra, therefore ensuring the constant energy of the high-energy line.

We cannot completely exclude that the lowest component of the doublet corresponds to impurity-bound excitons or excitonic complexes. In GaAs/Al$_{0.3}$Ga$_{0.7}$As QWRs of comparable thickness, their binding energy was found to be around 4 meV for X^- and 3 meV for X^+. These values should decrease with a decreasing confinement, which is consistent with our observations. However, the *local* existence/absence of excess charges could be only explained by local fluctuations of the type described above.

We noticed that single spectral lines observed in μPL spectra have a broad individual linewidth, larger than 1 meV. Such a feature was observed in 1D V-groove samples [98]; the linewidth obtained on the best T-shape QWRs is also of this order [73]. Guillet et al. attributed it to an increased effect of the piezo-electric field on extended domains. However, in our case, the AlGaAs alloy is very diluted. Consequently, we do not expect a strong piezo-electric effect. Instead, the continuous adaptation of the growth conditions

to maintain a sufficiently sharp QWR profile did not allow a rigorous characterization of the residual doping. We therefore keep residual doping as a possible origin of the large broadening of individual lines in μPL spectra. Indeed, scattering of excess electrons has been observed to broaden significantly the linewidth of charged excitons in comparable QWRs, when the electron density is increased [235]. This could also explain the larger linewidth that we measured. Yet, the reduction of the disorder amplitude is clear in the sample with reduced Al content.

Increasing the QWR thickness also proved effective in reducing the PL linewidth. Indeed, the figure of merit calculated in Fig. 5.24 is maximum for the thickest QWR that we have investigated, as a good subband separation was maintained in that sample. Nevertheless, even if the reduction of the confinement strength reduces the amplitude of the fluctuations of the confining potential, a further control of the *structural* disorder is desired to improve the homogeneity of V-groove QWRs.

5.4.2 Improvement of V-groove QWRs grown on patterned vicinal substrates

The different values characterizing the disorder of V-groove QWRs, which we reported in this chapter, indicate the high quality of our samples. In Fig. 5.24(e), we reported the calculated figure of merit $\rho_{PLE} = \frac{\Delta E_{subb}}{FWHM_{PLE}}$ for our wires. We routinely obtained values of ρ_{PLE} between 3 and 5 for the best samples, which is comparable to the values obtained on samples of the previous generation [235]. On the 8°-off sample, the ratio ρ_{PLE} reaches 6.8, which is equal to the value recently reported for pyramidal QDs [255]. An alternative figure of merit is also often used; the linewidth of the PLE line is replaced by that of the PL: $\rho_{PL} = \frac{\Delta E_{subb}}{FWHM_{PL}}$. Compared to ρ_{PLE}, ρ_{PL} incorporates effects of carrier relaxation and thermalization. Using that indicator, all the values that we obtain for QWRs grown on 6°-off substrates are systematically above the value of 7 obtained by Otterburg et al. as a result of an optimization of the structure grown on 'exact' (001) substrates [182]. The value $\rho_{PL} = 11$ is obtained for the QWRs grown on 8°-off substrate, attesting of the superior quality of that structure.

The major improvement obtained with the samples presented in this chapter is obtained on the PL linewidth. For comparable confinement, all the samples that we presented exhibit narrower PL linewidths (between 4 and 6 meV) than those of other V-groove samples: for the samples presented by Otterburg et al. in Ref. [182], a FWHM of 7.5 meV is quoted for an emission around 1.588 eV. Even the samples studied by Guillet et al., which were discussed in Sec. 5.1.4, are characterized by a linewidth around 8 meV for an emission at 1.635 eV. Representative values collected in the literature are reported in Fig. 5.34. This figure shows the PL FWHM as a function of the emission energy, taken as a measure of the confinement. Although they are not as good as those obtained on T-shaped QWRs, the values obtained in this work represent significant improvement compared to previous V-groove QWRs.
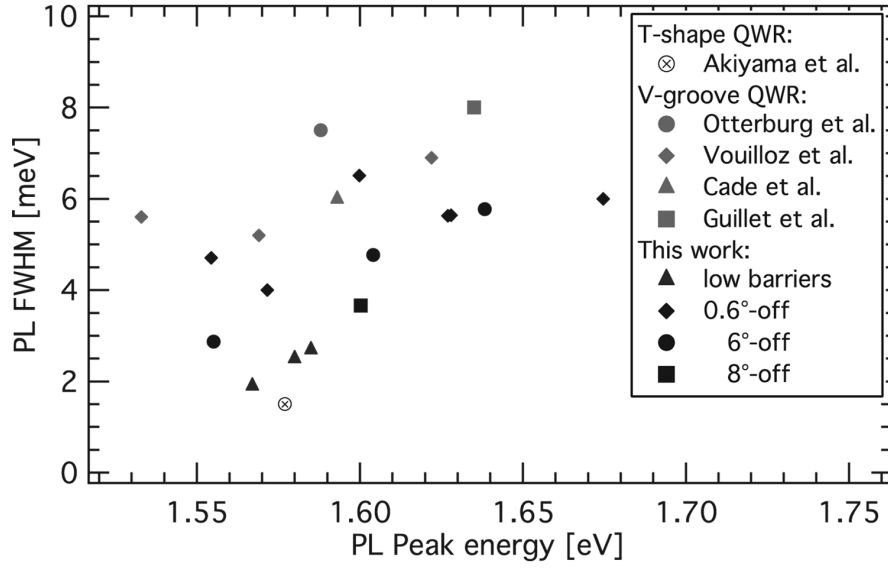
Figure 5.34: PL FWHM as a function of the PL peak energy, for representative samples grown on vicinal substrates or in between low barriers and compared to QWRs samples described in Ref. [57, 98, 182, 188, 230].

The origins of these improvements are twofold. Progress has been made on the control of the MOVPE conditions, mostly thanks to the better reproducibility obtained on vicinal QWs, which allows to characterize the reactor condition prior to the growth of QWR samples. Even the QWRs grown on nominally exact (001) substrates exhibit improved linewidth compared to five years ago. In addition, we achieved further advances through the use of patterned vicinal substrates.

We underlined three systematic features when comparing samples with small and large miscuts. (i) We reported a systematic reduction of the PL and PLE linewidth of the QWRs, as well as a reduced Stokes shift, for samples grown on substrates with a large miscut. It indicates a reduced amplitude of disorder.

(ii) High quality samples systematically emit at a slightly higher energy. This is consistent with the observations that we discussed in Ch. 4 for QWs, in terms of occupation of the potential minima. A significant exception is the 8°-off sample, which emission energy does not follow the trend determined by the other samples. From the cross-section visible in TEM images, the crescent seems to be wider than for other QWR samples. This has however to be checked more carefully. In any case, this underlines that additional elements have to be taken into consideration, as compared to QWs.

(iii) Another striking change is the inversion of the PL lineshape asymmetry for samples grown on vicinal substrates: whereas the PL line of QWRs grown on substrates with a small (at least up to 0.6°) miscut is broadened on the high energy side, that of

the samples grown on substrate with a miscut of a few degrees exhibit a pronounced low-energy tail.

The high-energy shoulder might be due, at least partly, to substantial residual doping in the barriers, which results in an increased density of carriers in the QWR. As discussed in the case of QWs (Sec. 4.1.2), a modification of the background impurity concentration with the substrate miscut is likely, in particular when considering the variety of crystallographic orientation involved in the growth. Indeed, we noted important variations of the PL of the AlGaAs. In contrast to our observation on QWs, the variations of the QWR PL linewidth with the miscut angle are small and monotonous. Also, the PLE spectra do not provide valuable information on doping, as there is no systematic tendency in the intensity ratio of the first transitions. Therefore, for QWRs, we cannot completely reject a dependence on miscut of the residual doping to be responsible for the change of linewidth.

Nevertheless, two facts indicate that different background impurity incorporations are unlikely. First, the broadening of individual lines in μPL spectra is similar for samples that exhibit a high-energy tail and those which do not. Scattering with impurities would be expected to broaden these lines. Second, samples grown on 0.6°-off substrates and that exhibit a narrow linewidth (see Fig. 5.22) also display a high-energy tail.

The origin of the high-energy shoulder is more likely linked to a larger density of localized states. Indeed, the high-energy tail of μPL spectra often includes several individual lines corresponding to localized excitons. The relative intensity of these transitions increases with both excitation power and temperature without saturation. This indicates that a large number of localized states is available. The PLE linewidth supports this interpretation. This also relates to the observation of the doublet discussed in the previous section and supports the existence of domains with important potential fluctuations.

Fewer localized states are visible in the μPL spectra of QWRs grown on substrates with a large miscut. Independently of the density of sharp lines in the spectra, their high-energy threshold is smooth, indicating that no localized states exist above this value. With increasing excitation power and temperature, the initial transitions broaden, but no new transitions appear. We underlined particular lineshapes in Fig. 5.20. The Lorentzian lineshape at high excitation power suggests a reduced dephasing time due to carrier-carrier scattering. The characteristic time obtained from the linewidth Γ equals $\tau = \frac{\hbar}{\Gamma} \simeq 0.1$ ps. This is somewhat less than a value (0.7 ps) reported for similar QWRs, but consistent with the much larger excitation density used here [98]. The Gaussian lineshape obtained at 50 K would more likely be associated to a redistribution of carriers over distant *shallow* potential minima, i.e. diffusion.

Exceptions to those observations were found in some μPL spectra of the 8°-off sample shown in Fig. 5.19. We noted that some segments of the QWRs grown on a substrate with a large miscut deviated significantly from the average PL emission energy. Nevertheless, their weak intensity did not contribute significantly to the ensemble PL lineshape. They indicate that domains with higher potential exist in that sample,
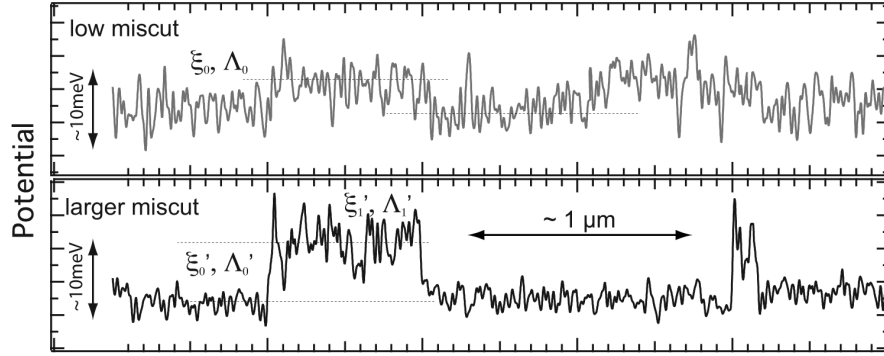
Figure 5.35: Schematic of the potential corresponding to the optical measurements for samples grown on 'exact' or 8°-off substrates (Fig. 5.19).

too. These segments are more disordered than the ones at lower energy. Their extension is larger than the exciton diffusion length, or systematically bound by larger barriers, because no emission is observed from lower states. Except for these sections, the amplitude of disorder Λ_0' is smaller than that found in substrates with a low miscut (Λ_0). The picture of the excitonic potential that we extract from these observations is sketched in Fig. 5.35. The reason for the lower intensity of the emission appearing at higher energy is not clear but might be related to the capture by the VQW, which might also be affected by the increased disorder at those specific locations.

In synthesis, we evidenced a clear influence of the substrate miscut on the optical properties of V-groove QWRs, and we have sketched the major characteristics of the confinement potential along the QWR axis. We discuss in the next section how this could be related to the morphologic changes that occur for growth on patterned vicinal substrates.

5.4.3 Modification of the growth mechanisms on patterned vicinal substrates

There are clear effects of the substrate miscut angle on the morphology of the sample surface. The first one is the modification of the monolayer step pattern on the ridge. The curved aspect of the terrace is maintained independently of the step-height, which is one monolayer for the small miscuts but larger when the steps start to bunch. In other words, the lateral growth mode (in the y-direction) is independent of the longitudinal growth mode (step-flow or step-bunching along the groove direction). The specific curvature of the steps on the ridge, with their typical alignement perpendicular to the grooves, was modelled by introducing interactions between the ridge and sidewalls facets, in terms of adatoms flux from the sidewalls to the ridge and reflecting barriers preventing the transport in the other direction [181]. We demonstrated that this arrangement of the steps takes place even in the absence of layer deposition and are therefore due to transport of adatoms.

The formation of narrow, step-bunched {113} facets at the intersection of the sidewalls and of the ridge, also occurs during annealing, independently of the substrate miscut. During growth, however, the relative growth rate on the (001) and {113} planes are modified significantly by the miscut angle. We observed that, with increasing misorientation, the growth of the {113} facets at the top of the groove takes over that of the (001), which results in wide {113} facets and a reduced ridge width. Interestingly, the {113} facets grow in the short-period step-bunched mode only in the vicinity of near-{111}A sidewalls. When they are large enough, the upper part exhibits fluctuations with a lower spatial frequency and a much reduced amplitude in comparison with the fluctuations on the sidewalls. This amplitude tends however to increase with increasing miscut angle.

This could possibly explain the longitudinal potential that we sketched in Fig. 5.35, if we assume that the morphology of the top-{113} facets are *representative* of the bottom-{113} facets (which form the QWR interfaces). The periodicity of these fluctuations is of the order of a micron, thus consistent with the rather long segments expected for high-quality QWRs. Because of the large amplitude of the fluctuations (several nm), they are likely to *cut* the QWR and create high potential barriers between the segments. In addition, because growth rate anisotropy has opposite effects at the top and at the bottom of the groove, extended {113} facets at the top are indicative of reduced {113} facets at the QWR interface. Their reduction could then explain the reduced short-scale disorder, as step-bunched {113} facets have a significant contribution to this effect.

However, in the absence of a detailed knowledge of the *real* QWR interfaces, alternative explanations can be proposed. In spite of the above-mentioned features, the substrate misorientation appears to have no effect on the large fluctuations systematically observed on the {111}A sidewalls. We observed that these fluctuations trigger the formation of steps and modify the width of the bottom (001) facet. We also observed that, when the miscut is large enough (4° for growth at 780°C, Fig. 5.30), there are no more step-bunched {113} facets at the bottom of the groove and that the central (001) facet displays continuous bunches of steps, with about 1 nm amplitude, and 40 nm periodicity.

A possible interpretation is therefore to attribute the smoother excitonic potential observed with increasing miscut to (i) the disappearance of step-bunching on the {113} surfaces of the groove and/or (ii) the reduced length scale of the fluctuations along the QWR axis. A few words of caution are nonetheless necessary with regard to this interpretation.

First, we underline that all the observations of the morphology reported in this chapter adress the sample *surface*. Yet, it is clear from Ch. 4 that it can be misleading to correlate directly the optical properties to the surface morphology. We unsuccessfully tried to apply to our QWRs the same selective etching technique used for QWs (see Annex B). We could however evidence on an 'exactly' oriented substrate that 2D islands

formed instead of the usual step-flow pattern observed on the ridge. This highlights once more the role of kinetics on the growth front. As a matter of fact, the standard model of the QWR disorder, which was depicted in Fig. 5.7(a), and the picture of short-range step-bunched {113} facets relies only on observations made on the surface of samples. In favor of this picture, we can argue in view of our experience for planar growths that periodically bunched steps at the surface always correspond to the same morphology of the buried layers. Yet, there is no proof of a similar behavior on non-planar samples.

Second, the observations that we made on the morphology of the bottom facets were based on samples grown in different conditions, since the narrow facets formed at the standard growth temperature are too narrow to be properly imaged. Importantly, and in connection to the above objection to the usual model of step-bunched {113} facets, the step-bunching is visible only when sufficiently thick layers are grown. The existence of these facets on the arms of the QWR crescent is clearly attested by TEM cross-section images. But their morphology along the QWR direction cannot be probed in that way and has not been established.

In addition, the correlation length of the step-bunched (001) facet that is observed on the substrates with large misorientations is around 40 nm. It is similar to the localization length determined for standard samples grown on 'exact' substrates [88]. Smoothening of the excitonic potential, by averaging the fluctuation over the exciton extension, would require a further reduction of this length. We have no hint of structural features on a shorter length scale.

To conclude, we have evidenced important changes of the surface morphology of samples grown on patterned substrates with large angle miscut, compared to structures grown on 'exact' substrates generally used for the fabrication of V-groove QWRs. The growth on misoriented substrates favors the growth of {113} facets, which have potentially smoother fluctuations when they do not develop close to a {111} surface. However, several reasons prevent us from identifying directly these facets to those forming the QWR, and as a consequence, from correlating the change of morphology to the improved optical properties of the QWRs.

5.5 Chapter summary

In this chapter, we investigated two approaches for smoothing the effective potential of excitons in V-groove QWRs. The first one aimed at reducing the *effect* of interface disorder by decreasing the effective confinement potential through a reduction of the Al concentration in the AlGaAs barriers. We observed a significant narrowing of the PL linewidth of the QWR. Values of the FWHM smaller then 3 meV were obtained on samples with $Al_{0.11}Ga_{0.89}As$ barriers and even lower values were obtained at the expense of an important drop in PL intensity.

We also conducted experiments to reduce the structural disorder of QWRs embedded into $Al_{0.3}Ga_{0.7}As$ barriers, which strongly confines carriers and results in large 1D subband separation. We significantly improved the quality of V-groove QWRs by a better control on the fabrication process, and we demonstrated that the optical linewidth can be further reduced by growing the structures on substrates misoriented by several degrees toward the groove direction. In particular, the specificities of the optical properties of QWRs grown on 8°-off substrates were presented in detail. We described how the growth was modified on such substrates and discussed the implications on the disorder at the QWR level.

The effect of the growth on misoriented substrates is more significant on the PL properties of the QWRs. This may indicate specific relaxation and diffusion properties in these samples. In the next chapter, we address these questions by studying the effect of carrier delocalization in V-groove QWRs.

Chapter 6

Quantum wires: delocalized excitons

The diffusion and drift of charge carriers in one-dimensional systems has attracted attention since the prediction of a large electron mobility due to the reduced phase space for scattering in 1D [38]. Up to now, however, experimental investigations failed to demonstrate such an enhancement of the transport. Compared to the many studies reported on unipolar transport in quantum wires (QWRs), only few reports address experimentally the transport properties of electron-hole pairs in QWRs and even less reports describe systematic investigations of this phenomenon.

The diffusion of electron-hole pairs in QWRs has been investigated with different techniques, including pump and probe experiments [256], cathodoluminescence [257] or imaging of the PL spot extension (either time-resolved [258] or in a steady-state [259]). Previous studies mainly concentrated on GaAs systems. The diffusion length was studied at 15 K in triangular-shaped QWRs of different sizes [259]. Rather long (up to 4 μm) diffusion lengths were measured, although the experiment did not completely separated possible contributions from the 2D structures involved. Near-field investigations concluded that an enhancement of the mobility in QWRs grown on patterned (113) substrates occurs compared to QWs and evidenced a transient non-equilibrium transport over short time- and length-scales [256]. In QWRs grown in pyramidal recess, a value of the diffusion coefficient D of 11 cm^2/s was measured at 92 K [260]. In V-groove QWRs, isolated estimation of the diffusivity led to values of $D \simeq 10$ cm^2/s in InGaAs QWR at 100 K. In GaAs QWR samples comparable to ours, no diffusion was observed at temperature below 70 K [81].

All these values of the diffusion coefficient are small compared to expectations; but the lack of systematic experiments prevented the analysis of the reasons for this discrepancy with the theoretical predictions. This chapter presents the measurement of electron-hole pair diffusion in several V-groove QWR samples that were discussed in Ch. 5. We will discuss our results in view of the sample disorder, which is further characterized by the evolution of the Stokes shift as a function of the lattice temperature.

6.1 The time-of-flight method

For the investigations presented in this chapter, we used a time-of-flight method first proposed by Hillmer to study exciton diffusion in QWs [261]. The principle was reproduced and adapted in several experiments [117, 262–264]. Here, we present it in detail for the study of diffusion in QWRs.

6.1.1 Principle

The time-of-flight (TOF) method consists in measuring the temporal decay of the luminescence through apertures in an opaque mask deposited on the sample and comparing it to the decay obtained without mask. The principle is illustrated in Fig. 6.1.
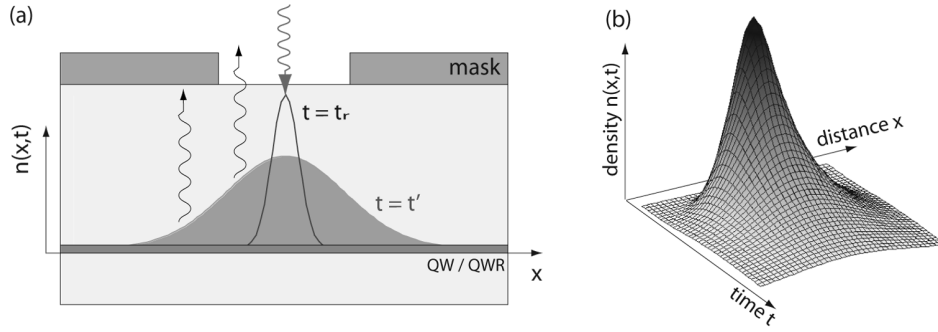
Figure 6.1: Principle of the TOF method: (a) Carrier density profile under the opaque mask at different times; τ_r: soon after the creation of carriers in the QWR, t': after they have diffused along the QWR. (b) Spatio-temporal dependence of the carrier density in the QWR ground state.

In this method, a short laser pulse creates electron-hole pairs in the QWR. The carriers then relax toward lower energy levels, where they recombine. Meanwhile, if they move along the QWR, the carrier distribution spreads along the axis of the QWR. In the TOF measurement, the electron-hole pairs are excited at the center of an aperture in an opaque mask. The carriers that diffuse outside the aperture before recombining do not contribute photons to the PL signal. The temporal decay Υ_w of the PL therefore contains information about both the radiative decay and the motion of the carriers.

Quantitatively, we tentatively model this system with single one-dimensional particles (excitons) in a three-level system (inset of Fig. 6.3). The excitons are created in an excited state m and emit from a ground state n. Their motion is described by a constant diffusion coefficient D related to 1D motion, independently of the energy level. The exciton distribution in both levels, $m(x,t)$ and $n(x,t)$, obey the following rate equations:

$$\frac{\partial m(x,t)}{\partial t} = D\frac{\partial^2 m(x,t)}{\partial x^2} - \frac{m(x,t)}{\tau_r} \tag{6.1}$$

$$\frac{\partial n(x,t)}{\partial t} = D\frac{\partial^2 n(x,t)}{\partial x^2} + \frac{m(x,t)}{\tau_r} - \frac{n(x,t)}{\tau_d} \tag{6.2}$$

τ_r^{-1} is the relaxation rate from level m to level n and τ_d^{-1} is the decay rate from level n. Assuming a gaussian distribution of excitons at t = 0 in the excited state, $m(x,0) = A \cdot e^{-\frac{x^2}{\sigma_0^2}}$, the solution for the ground state is:

$$n(x,t) = \frac{\sigma_0 A}{\sqrt{4Dt+\sigma_0^2}}\frac{\tau_d}{(\tau_r - \tau_d)}e^{\left(-\frac{x^2}{4Dt+\sigma_0^2}\right)}\left(-e^{\left(\frac{-t}{\tau_d}\right)} + e^{\left(\frac{-t}{\tau_r}\right)}\right) \tag{6.3}$$

Then, if we assume that the PL intensity $I(t)$ is directly proportional to the exciton density, we obtain as a function of time:

$$I(t) \propto \int_{-a}^{a} n(x,t)dx \tag{6.4}$$

In standard time-resolved experiments, the signal is collected from the complete space ($a = \infty$), whereas for excitation through a mask, the integration is limited to the aperture area ($a = w/2$). As a result, the PL decay is faster in the second case.
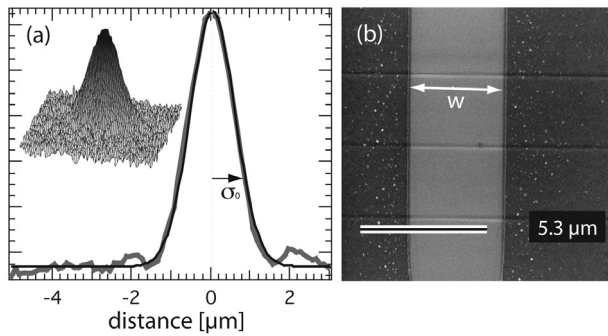
Figure 6.2: (a) Exciting spot line-shape (inset) and cross-section fitted with a gaussian. (b) SEM image of an aperture in an opaque mask (dark parts). In this case the V-groove positions are indicated by the shallow corrugations.

This method allows to quantify directly the diffusion coefficient D. Indeed, most of the parameters appearing in equations 6.3 and 6.4 are measured independently:

- The gaussian width σ_0 of the initial exciton population is determined by the extension of the exciting beam. It is measured from the image of the laser spot formed on the microscope CCD camera and is typically 0.9 μm (corresponding to a FWHM of 1.5 μm, see Fig.6.2(a));

- The size w of the apertures in the mask is measured by SEM (Fig. 6.2(b));

- The rise and decay times, τ_r and τ_d, are obtained from time-resolved measurement

without shadow mask.

The only remaining unknown terms are the coefficient A and the diffusivity D, which can be extracted by a fit to the PL decay curve. In principle, the coefficient A should be consistently determined as well. The ratio of the area delimited by the decay curves obtained with and without mask must be the same as that of the integrated PL intensities. However, extracting A from this procedure proved fastidious and inconsistent. The reason lies probably in the interpolations that have to be done to isolate the PL signal from the background. Yet, in most cases this coefficient can be eliminated by a normalization of the model and experimental decay curves. However, in some cases, it prevents us from quantitatively analyzing the data, which deviate from the model at short delay time, as will be discussed later.
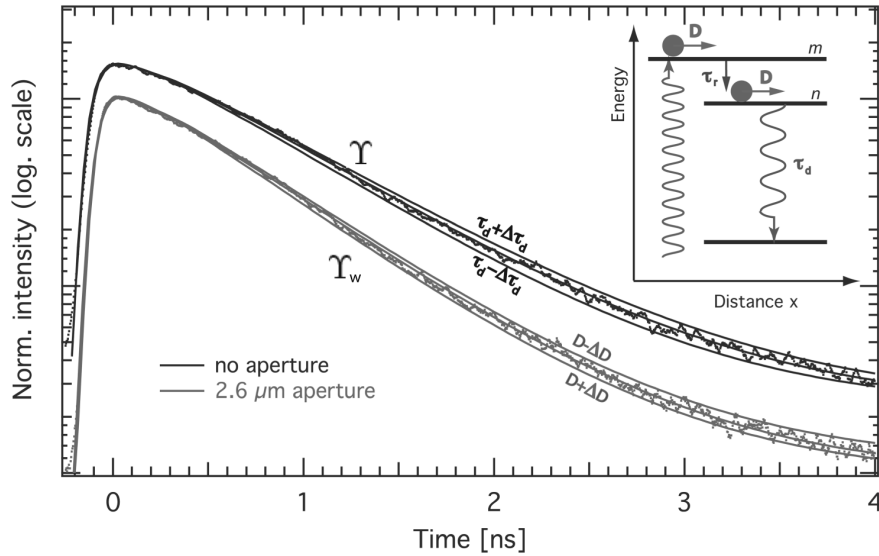
Figure 6.3: (a) Example of experimental temporal decays of the PL measured either on a bare QWR sample (Υ), or through a narrow aperture in a mask deposited on its surface (Υ_w). In each case, the central continuous line is the best fit to the data with the model sketched in the inset and described in the text. The continuous bordering lines correspond to the decay curves obtained with coefficient varying by one standard deviation, as determined from the fit.

The fitting procedure includes a convolution of Eq. 6.4 with the instrumental response of the TR setup (see Fig. 3.16(c)); it is performed over about 2 orders of magnitude of the intensity. This results in an excellent agreement between the fit and the experimental data, as visible in Fig. 6.3.

6.1.2 Sensitivity and reliability

For the measurements aiming either at determining the lifetime or the diffusion coefficient, we quantified the quality of the fit by the standard deviation Δ of the coefficients τ_r, τ_d or D obtained through our procedure. The external lines in Fig. 6.3 correspond to values of $\tau_d \pm \Delta_{\tau_d}$ and $D \pm \Delta_D$. Yet, in addition to the intrinsic uncertainty given by the fit, other possible sources of systematic error were quantified to assess the sensitivity and precision of the method. We discuss below the influence of the various parameters entering the measurement procedure and the data analysis.

(i) The maximum error in the determination of the *extension of the exciting beam*, characterized by σ_0, is estimated to be around 15%. σ_0 was measured only once for each measurement session, and a constant value was used throughout the analysis. However, it may fluctuate sligthly, due to the need to adjust the focus at different positions on the samples. Such variations affect significantly the value of D only when it is measured through narrow slits. Misevaluating the value of σ_0 by 15 % results in a maximal error of the order of 10% in the value of D.

(ii) A deviation from an initial *gaussian distribution* of excitons, as used in the model, may occur for the narrowest apertures. First, if the aperture is too narrow, the mask may cut the tail of the laser beam, creating a truncated gaussian distribution of carriers. The missing fraction of carriers (corresponding to the tails of the gaussian distribution) that is inappropriately accounted for by the model, could (virtually) diffuse back below the aperture and contribute to the signal. This over-evaluation of $I(t)$ would result in an over-estimation of the value of D by the fit. For the narrowest aperture that we used (1.9 μm wide), the cut signal amounts up to about 10% and is negligible for the experimental curves that we present later. Second, diffraction through the aperture may occur. However, in view of the actual dimensions of our samples, its effect on the initial exciton profile would be within the error in σ_0 calculated in (i), even for the narrowest aperture that we used.
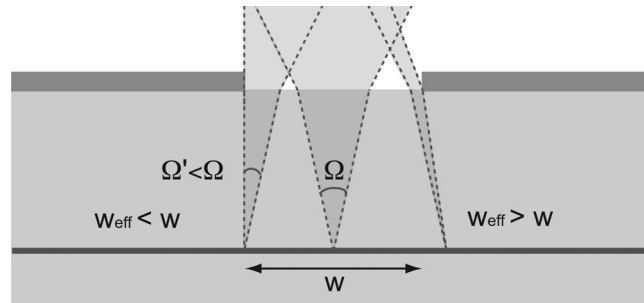
Figure 6.4: Scheme of the light extraction from an aperture of width w. The collection angle is Ω in the center of the aperture. Close to the aperture boundary (but still below it) the collection angle is reduced, which leads to a reduced effective width (left). Oppositely, a fraction of the light emitted from below the mask is also collected, which increases the effective width of the aperture (right).

(iii) The *aperture width w* is measured by SEM with a precision of a few tens of nanometers. However, as the carriers are confined a few hundreds of nanometers deep below the mask, some 'shadow effect' might modify the *effective* width of the aperture. As illustrated in Fig. 6.4, the PL is collected within a solid angle Ω, set by the numerical aperture of the objective. In the vicinity of the mask, this angle is reduced. The effective width of the aperture is therefore reduced compared to its value measured on the surface. This effect is partially compensated by the fraction of PL, which is collected even though it is emitted from a position below the mask. For a 2 μm wide aperture that is 1 μm above the QWR, we estimate the maximum variation of the effective width to be 300 nm. Without accounting for the partial compensation of the effect, and for the most unfavorable parameters, this would imply a 20 % difference with respect to the value of D calculated with the aperture width measured from the SEM.
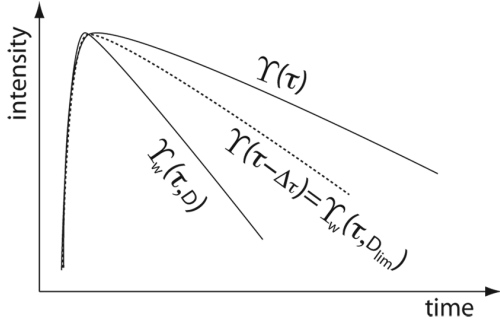
Figure 6.5: Illustration of the criterion used to define the aperture sensitivity (see text).

The width of the aperture also sets minimum values for which the diffusivity can be detected. As a criterion, we defined D_{lim} as the minimum value of the diffusivity, for which the corresponding decay curve $\Upsilon_w(\tau_d, D)$ is distinguishable from that (obtained without mask) corresponding to the lower limit of the decay time: $\Upsilon_w(\tau_d, D_{lim}) = \Upsilon(\tau_d - \Delta_{\tau_d})$ (Fig. 6.5). Again, this value depends on the excitonic lifetime: the diffusion of long-living particles is easier to detect than that of short-living ones. As an example, the diffusivity of a particle for which the characteristic PL decay time is 300 ps needs to be above ~ 2.6 cm^2/s to be reliably measurable through a 2 μm aperture. For a 3 μm aperture, this value increases to 5.1 cm^2/s.

(iv) An error in the integration of Eq. 6.4 may arise from a deviation ϵ of the *alignment* of the exciting spot with respect to the center of the aperture. Here also, the influence would be the largest for narrow apertures. We control the positioning of the laser beam on the surface with a precision of the order of 100 nm. We verified that a deviation of the alignment of this order results in a negligible error compared to the factors already cited.

(v) Once the *time constants* τ_r and τ_d are extracted from the time-resolved PL profiles measured without mask (or through apertures sufficiently large to not affect the PL), they become fixed parameters of the fitting function for the curve measured through the narrow aperture. For example, when using a 2 μm wide aperture, a 20 ps uncertainty on a τ_d value of 300 ps results in an uncertainty on D of 3 cm^2/s (4 cm^2/s) if its central value is $D = 2$ cm^2/s (5 cm^2/s). The influence is less pronounced for longer

decay times.

(vi) As the use of masks requires to measure Υ and Υ_w at different positions of the sample, it is also necessary to check the *homogeneity of the sample*: when measuring the decay time at different positions (without apertures), at some fixed conditions, the values of τ_d were distributed within about 20 ps around the mean value. Within the precision that we claim, the use of such parameters deduced at different positions is thus adequate.
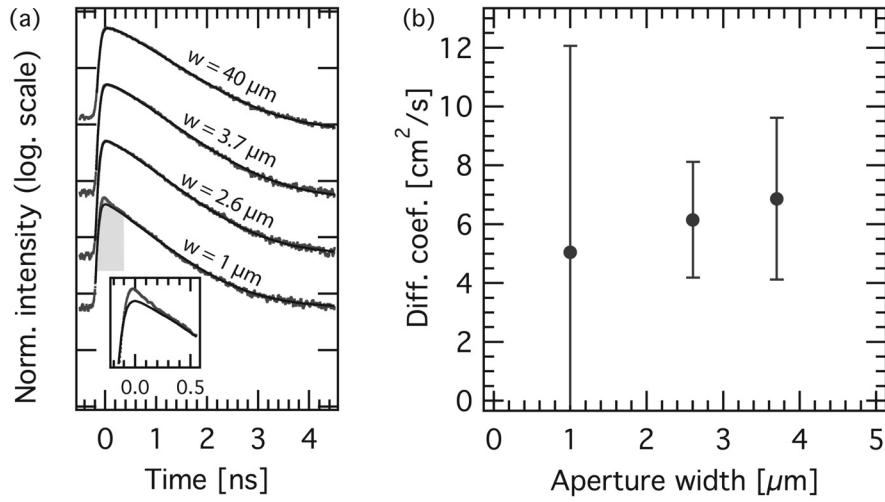
Figure 6.6: (a) TR-μPL decay curves measured through apertures of different sizes, with their best fits. The inset zooms in on the t = 0 peak for the data measured through the narrowest aperture, which is not accounted for by the model and prevents a reliable determination of D. The values obtained are shown in (b) with the error bars corresponding to the standard deviation obtained through the fit.

Among the previous factors, the possible error in the determination of the decay time is by far the most important. However, the standard deviation of the coefficient D obtained through the fit is systematically larger than the possible errors that we have estimated above. Therefore, the values reported as error bars in the following are the standard deviation of the fit coefficient; the interval they define includes the possible contribution of the factors enumerated above. As shown in Fig. 6.6 for illustrative conditions, we obtain consistent values when using apertures of different sizes. This confirms that the possible deviations, to which the narrow apertures could be particularly sensitive, are not relevant compared to the error in the fit coefficient. An important exception is very narrow apertures such as the 1 μm wide one, the corresponding decay curve of which is shown in Fig. 6.6. In that particular case, the experimental data cannot be reproduced by the model at short time (close to $t = 0$). This is due to an important participation to the signal of short lived contributions spectrally overlapping with the QWR signal (see Sec. 6.1.3). The fit can be done by rejecting the data at short time (in the shaded area in Fig. 6.6), but as it is no more possible to precisely

normalize the model, it results in a larger uncertainty in the determination of the value of D. Such narrow apertures were not used to extract the diffusivity, but masking part of the data as described here was necessary on a couple of measurements making use of larger apertures, for which the exponential decay profile exhibited a similar deviation at short delay.

6.1.3   Samples and experimental conditions

The fast decay component at short delays is an important issue of the TOF measurements. In the case of a temporal profile corresponding to the carrier lifetime, the fit can be done over a reduced range of the signal as the function is usually mono-exponential. However, the decay profile corresponding to measurements through apertures is not a decaying exponential function, but has a changing logarithmic slope. As explained above, a clear determination of the maximum of the curve is important to allow the normalization of the model curve and its comparison to the normalized experimental data: it allows to compare only the shapes of the two data sets and to get rid of the amplitude coefficient. If an additional component contributes to the detected signal and prevents this normalization, a precise determination of the diffusion coefficient is no more possible.

We identified three origins to signals that can overlap with the PL of the QWR. First, reflection of the laser light from the cryostat window or from the sample surface (in particular at the metallic mask) can be detected. To reduce it, we used filters and crossed-polarizers, but the laser light could not be systematically completely rejected.

Second, the requirement to excite only 1D states imposes excitation below the barriers and in particular below the VQW. The carrier population in the QWR is formed only by the weak absorption in 1D states and thus demands rather large excitation power to observe sufficiently intense PL. This not only increases the laser reflection intensity, but it also strongly increases the relative PL intensity of the GaAs substrate, which absorbs the remaining photons. The tail of the GaAs emission then overlaps with the QWR PL, especially at high temperatures, and leads to a rather fast decay component (< 100 ps).

Third, emission from the SQWs can be close (in energy) to that of the QWR. Although their emission energy is lower than that of the VQW, the layer necking at the lower boundary prevents the transfer of the carrier to the QWR (at sufficiently low temperatures). Therefore, if the excitation of electron-hole pairs in that 2D structure does not spoil the 1D character of the measurements, it may still impair its detection.

These observations impose constraints on the samples and experimental conditions that can be used. On one hand, we chose samples with a miscut angle of 0.6°-off (toward [1$\bar{1}$0]) in order to limit the spectral overlap of the SQW PL. These samples present the largest energy separation bewteen the PL of the two structures. To investigate the larger miscut angle range, we chose a QWR sample grown on a 6°-off sample, which

benefits also from a PL line well-separated from the other emissions (see Fig. 5.18). On the other hand, the overlap with the GaAs emission forced us to work with rather narrow QWRs, emitting at sufficiently high energies.
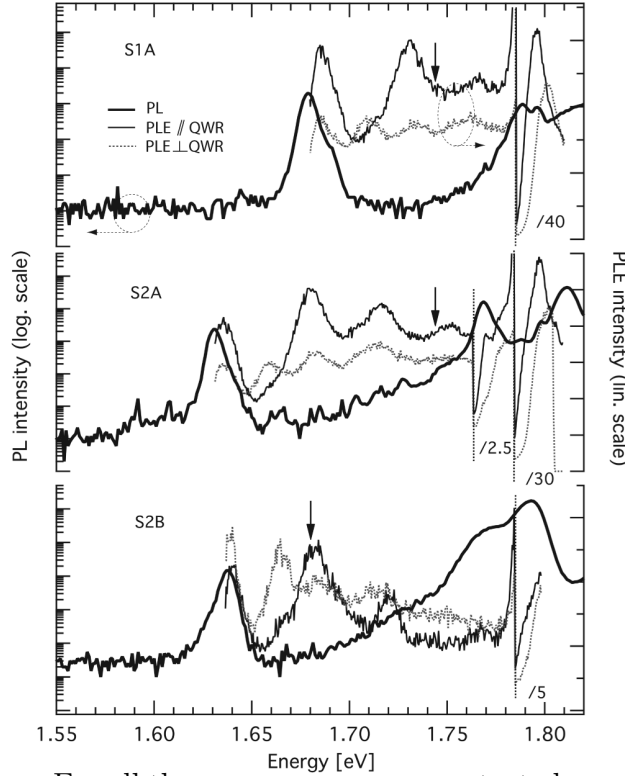
Figure 6.7: 10 K PL (logarithmic scale, left) and 100 K PLE (linear scale, right) spectra of three QWR samples with different nominal QWR thicknesses. The PLE spectra are shifted in energy to account for the bandgap reduction at 100 K. The arrows indicate the excitation energy for time-resolved measurements.

For all these reasons, we concentrated our efforts on the measurements of three samples. They were all previously discussed in Ch. 5 and, for the sake of clarity, we will refer to them as S1A, S2A and S2B in the following. S1A has a 1 nm thick (nominal) QWR, and S2 (A and B) contained 1.5 nm thick wires. Samples 'A' are grown on 0.6°-off substrates and sample 'B' is grown on a 6°-off substrate. Their surface is almost planarized, except that of S2B, which exhibits {113}-corrugations. Their PL and PLE spectra are presented in Fig. 6.7. In that particular case, the PL is excited above the barriers, at 10 K. The PLE spectra are measured at 100 K, so that they are expected to be free of relaxation effects. They are shifted in energy to account for the bandgap reduction at that temperature. The $e_1 - h_1$ transitions are well resolved for all these samples[1].

The excitation energies used in the TR-measurements are in each case indicated by an arrow. In general, they are set out of resonance with higher subbands and coincide with rather constant regions of the PLE spectra. As the spectra shifts toward red with increasing temperatures, the excitation takes place slightly higher in the subbands, but the excited density is not significantly modified. Sample S2B makes exception to this rule because we had to excite on a resonance to get sufficient PL intensity for the mea-

---

[1]In other QWR samples, we observed a strong quenching of the absorption in the first subband. Some measurements on those samples are reported in Annex C.

surements. In all cases, the laser excites electron-hole pairs below the VQW energy, which strong absorption is visible around 1.8 eV; this ensures that only 1D phenomena are probed.

6.2   Exciton dynamics

6.2.1   Exciton lifetime

The temporal PL profiles for all three samples are displayed in Fig. 6.8 for different measurement temperatures. The measurements were performed at the center of a 40 μm wide aperture, large enough to prevent any effect due to diffusion, but allowing a precise positioning of the excitation spot and thus a good reproducibility. The PL decay is mono-exponential over about two orders of magnitude, which allows a precise extraction of the decay time constant τ_d. We checked under specific conditions that the decay time was not modified when the laser power was varied by a factor of 4 at least (see Fig. 6.13). We note the appearance of a fast decay component on the transient of sample S2B at the highest temperatures. This corresponds to residual laser light and is rejected in the analysis here.
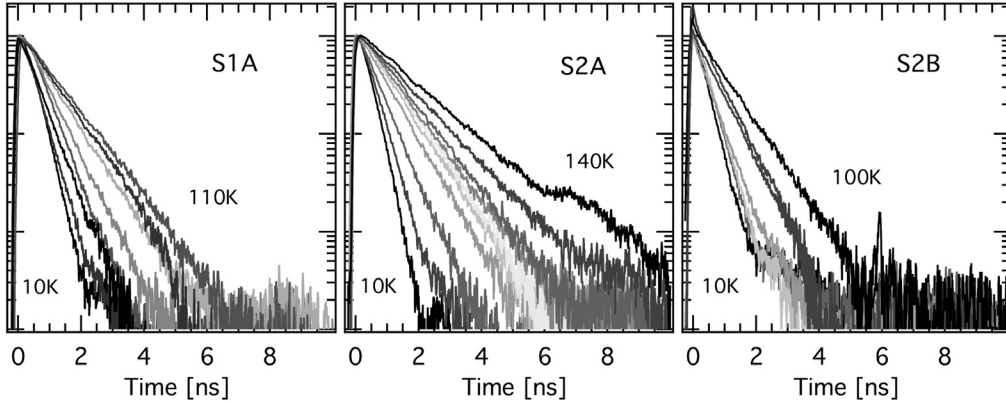
Figure 6.8: Profiles of the PL temporal decay measured at different temperatures, for the different QWR samples. The bump in the 140 K spectra of sample S2A is a noise artefact.

The decay time constants τ_d extracted from the fits are summarized as a function of temperature in Fig. 6.9 for the three samples. Up to about 100 K, the trend is the same for all the samples: their lifetimes at 10 K are all comparable, ranging from 260 ps (for S2A) to 290 ps (for S2B). τ_d first increases slightly up to about 40 K and then the slope increases to reach lifetimes of the order of 1 ns at 100 K. The time constant for sample S1A reaches a maximum at 110 K and then decreases down to 450 ps at 150 K. In that case, it is correlated with a significant decrease of the PL intensity, connected to the activation of non-radiative recombinations. The radiative lifetime is linked to the integrated PL intensity through the radiative efficiency $\eta(T) = \frac{\tau_{decay}}{\tau_{radiative}} = \frac{I(T)}{I_0}$, in which

I_0 is the PL intensity at low temperature. According to this expression, the radiative lifetime is increasing monotonically also for sample S1A.
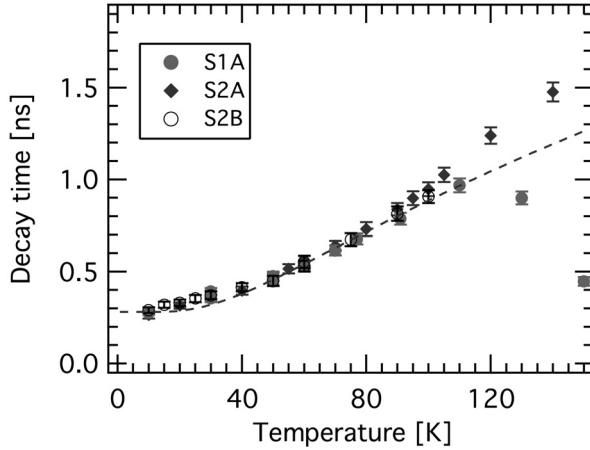
Figure 6.9: Decay time for the three samples as a function of the temperature. The dashed line, based on expression 2.32 (see text), is a guide to the eye.

The trend of $\tau_d(T)$ does not follow at all the $\sqrt{T}$ dependence that is predicted theoretically for 1D systems (Eq. 2.22). In fact, there have been few observations of such a dependence, whatever the system considered [98, 116, 265, 266]. Instead, behavior of the radiative lifetime with the temperature that is similar to the one in Fig. 6.9 has been reported for many QWR structures [148, 151, 267]. In particular, Oberli et al. studied V-groove QWRs of different thicknesses and found that the radiative lifetime of the thickest QWRs increases more rapidly with temperature than that of the thinner QWRs. For delocalized excitons, this is explained by the smaller oscillator strength of particles that are less confined. For localized excitons, the radiative lifetime increases because of disorder [150]. The radiative recombination rate was even found experimentally to vary linearly with the length of the localization minima [92].

The dashed line in Fig. 6.9 is drawn from the relation given by Eq. 2.32, with a density of localized sites of $N_D = 1.5 \cdot 10^5 cm^{-1}$, a localization energy $E_{loc} = 8 meV$, the localized exciton lifetime $\tau_{loc} = 290$ ps and the intrinsic lifetime $\tau_0 = 110$ ps. This model fails in the description of the data on two domains. At low temperature, it predicts a complete saturation of the lifetime, whereas we observed a weak dependence on temperature, although the slope of $\tau_d(T)$ is smaller than above 40 K. Second, at high temperatures, we would expect to see the lifetime approaching the $\sqrt{T}$ dependence followed by the model. Instead, our experimental data continue to increase linearly with temperature. This discrepancy is maybe due to a slight variation of the radiative efficiency, which we are unable to detect in the intensity of the integrated PL.

6.2.2 Carrier relaxation

The rise time values of the PL signal obtained from the fit are displayed in Fig. 6.10. The panel (a) separates the values for S1A, S2A and S2B to evidence their individual tendency. For all three samples the rise time decreases with increasing temperature and

assumes values close to our detection limit above about 50 K. The 10 K value is around 93 ps for samples S1A and S2A and 67 ps for S2B. As made clear in panel (b), in which all data are superposed, the values for the sample S2B are systematically smaller than those of the other samples. Also, the decrease of τ_r with the temperature is slightly slower for S1A.
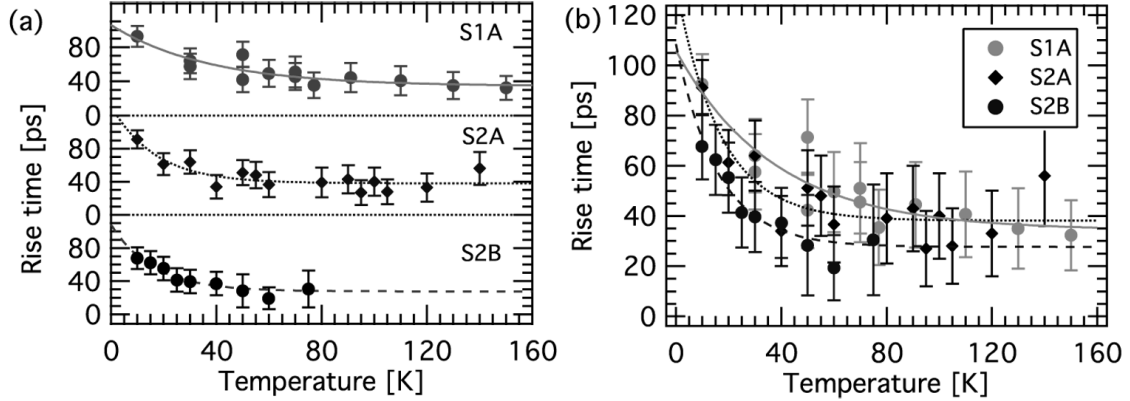
Figure 6.10: Rise time of the three samples as a function of the temperature. They are displayed on separate vertical scales in (a) and together on the same scale in (b). The lines are guides to the eye.

We observe a rather fast rise time of the signal. This rise time likely includes: (i) the initial relaxation of electrons and holes; (ii) the exciton formation; (iii) further relaxation of the exciton. For QWs, Takahashi calculated that the relaxation is slower for excitons than for electron-hole pairs [118]. The electron-electron (hole-hole) scattering is more efficient than electron (hole)-excitons or exciton-exciton scattering. He underlined that excitons only relax by exciton-exciton and exciton-phonon scattering, which are rather inefficient. However he only considered excitons created with an initially small kinetic energy, which can relax only through acoustic phonons. In addition, in 1D systems, the exciton-acoustic phonon scattering is enhanced and the exciton-carrier scattering is reduced [119]. In our experiments, the initial excess energy is always larger than that of optical phonons, the scattering rate of which is larger than that of acoustic phonons. The initial relaxation of electron and holes is therefore likely to proceed through the emission of optical phonons.

In other studies, the exciton formation time was predicted to depend strongly on the initial excess energy of the e-h pairs [268]. Nevertheless, it takes place within a few picoseconds, as was verified for instance in crescent-shape QWRs [90].

The rise time of the PL signal is ultimately determined by the fraction of excitons effectively coupling to light. At low temperature, the relaxation into a thermal distribution peaked at $k = 0$ is slow. As the thermal population spreads out at increasing temperature, the excitons with initially large momentum reach this distribution more rapidly [269]. Note, however, that at low temperature the short exciton lifetime does not permit to reach a thermalized distribution [270].

6.2.3 Exciton diffusion

The investigation on exciton diffusion was performed under the same experimental conditions as described above, using narrow apertures in the opaque masks. A typical set of measurements performed at different temperatures on samples S1A, S2A and S2B is shown in Fig. 6.11. Each graph displays two sets of data. The first one corresponds to the PL decay measured without any mask (lifetime) and the second one measured through a narrow aperture. The curves representing the best fit by our model are also shown and attest to a very good correspondence.
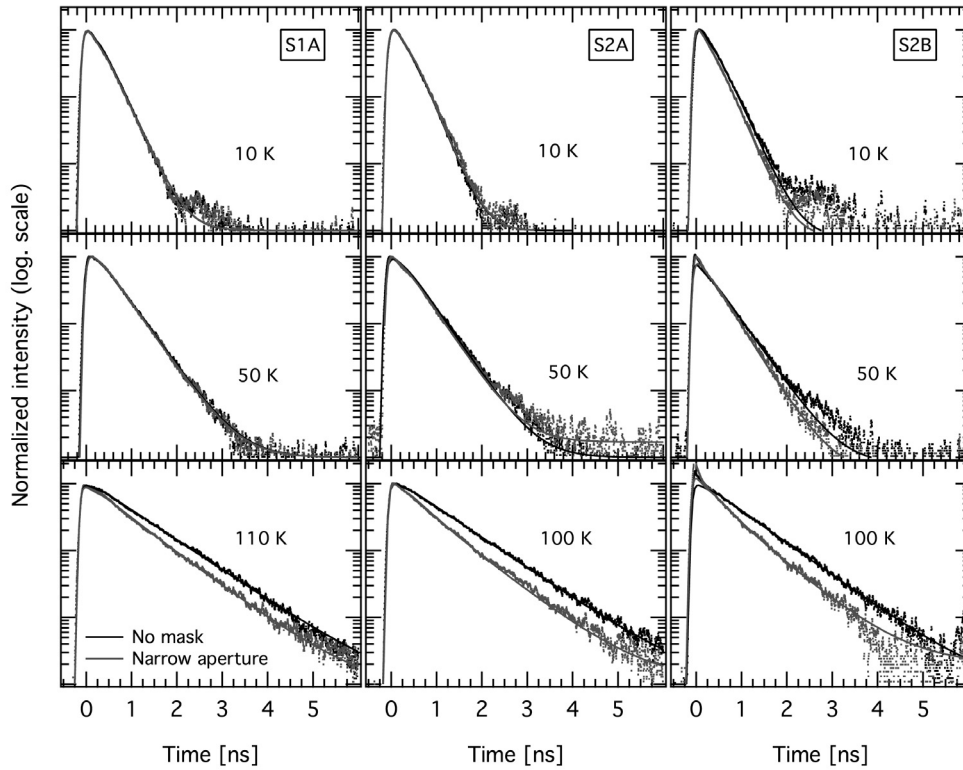
Figure 6.11: Example TR-μPL decay curves for samples S1A, S2A and S2B, measured both without mask and through 3.7, 2.4 and 1.9 μm wide apertures, respectively.

At 10 K, the two curves are superposed for both samples S1A and S2A. This indicates that no diffusion takes place at that low temperature. The curve measured through the aperture for sample S2B decays slightly faster than that measured on the bare surface. We deduce a small value of the diffusion constant of $D = 3.2\ cm^2/s$ with a significant uncertainty ($\pm\ 2.6\ cm^2/s$). To illustrate the sensitivity of the method that we detailed in Sec. 6.1.2, the value of D that we obtain if we use the lower value of τ_d in the fitting equation is $D = 1.2 \pm 2\ cm^2/s$; this value is within the interval determined by the best fit coefficients.

The same situation prevails up to a temperature of about 50 K: both curves are

superposed, indicating a diffusion constant close to zero. As shown in Fig. 6.11, from and above this temperature the fit does not reproduce correctly the peak of the time profile measured on sample S2B. The error on the normalization gradually adds up with the error on the coefficient D, which eventually looses significance at larger temperatures. Yet, the steeper slope of the temporal profile at longer delay time is indicative of diffusion taking place in that sample. At temperatures above 50 K, effect of diffusion is clearly visible for all samples and, for samples S1A and S2A, the data are nicely fitted by our model.
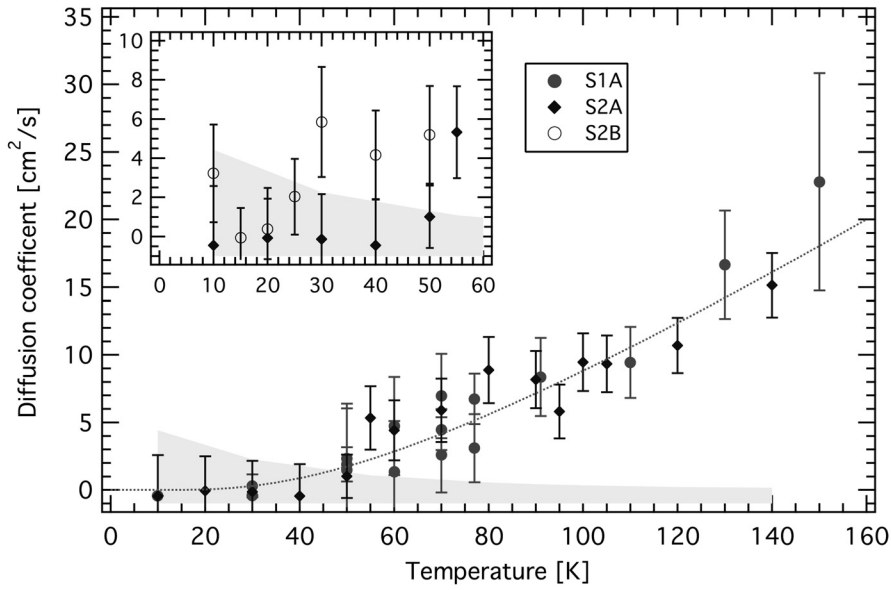
Figure 6.12: Diffusion coefficients measured on three QWR samples as a function of temperature. The main panel compares samples of different confinement grown on substrates with the same miscut. The inset compares samples of identical confinement, but grown on 0.6° and 6°-off vicinal substrates. The dashed line is an eye guide; it is proportional to the fraction of delocalized excitons (see Sec. 6.4.1). The shaded area indicates the detection limit for sample S2A.

The diffusion coefficients obtained by the best fits are summarized in Fig. 6.12. The main panel demonstrates that samples S1A and S2A behave similarly. The diffusion is close to zero below 50 K. As we mentioned in Sec. 6.1.2, the short decay times at low temperature reduces the sensitivity of the measurement through the aperture. The shaded area represents the detection limit for the 2.4 μm wide aperture used for sample S2A. (For sample S1A, apertures of different widths, 2.6 and 3.7 μm were used). We note that we cannot exclude that some diffusion takes place at 10 K in sample S1A and S2A, because the apertures that we used have a limited sensitivity for the short lifetime at low-temperature. However, if non-zero, the diffusivity remains small (below $\sim 4~cm^2/s$ at 10 K).

Above about 50 K, the values of D start rising and then increase regularly up to

the highest temperatures that we could measure. We obtain a highest value of about 23 cm^2/s at 150 K for sample S1A. The rather large error bars ($\pm$ 8.5 cm^2/s) are due to the significantly shorter lifetime measured on this sample at this temperature. It corresponds to a diffusion length (Eq. 2.26) of about 1.4 $\pm$ 0.3 μm. The maximum diffusion length that we determined (2.1 $\pm$ 0.2 μm) was however obtained for the sample S2A at 140 K.

In the inset of Fig. 6.12 the values obtained for samples S2A and S2B are compared. A larger diffusivity is systematically found on sample S2B for T > 30 K. Extracting confident enough values for sample S2B from the measurement at T > 50 K is prevented by the short time signal overlap. Nevertheless, significant diffusion in that sample is still visible at larger temperatures.
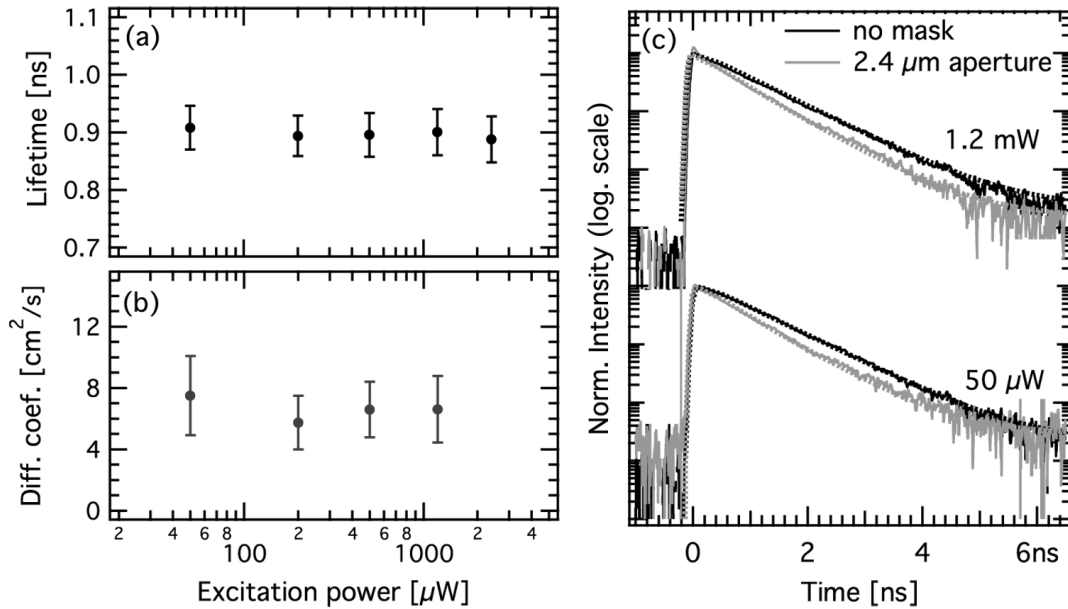
Figure 6.13: Power dependence measured at 95 K on sample S2A of the decay time (a) and diffusion constant (b), with example decay curves (c) without mask and through a 2.4 μm aperture.

For a typical set of experimental conditions, we checked the effect of the excitation density on the value of the diffusion coefficient. As for the measurement of the lifetime, the laser power could be changed by a factor of at least 4 (either up or down) without observation of a substantial change in the determined value of D (i.e. without a deviation from the uncertainty range that is obtained at standard conditions). This is illustrated for sample S2A at 95 K, for which we could change the excitation power over more than one order of magnitude: the Fig. 6.13 shows the constancy of both the lifetime (a) and the diffusion coefficient (b) for a laser power between 50 μW and 1.2 mW. The experimental temporal profiles for these two extreme cases are also displayed together with their best fits (c).

6.2.3.1   Evaluation of the exciton density

Although the excitation power does not seem to be determinant in the range that we investigated, it is interesting to evaluate the exciton density that is created in the QWR. A rough estimation based on the (crude) assumption that 1% of photons are absorbed in the QWR leads to an order of magnitude of 10^6 cm^{-1}.
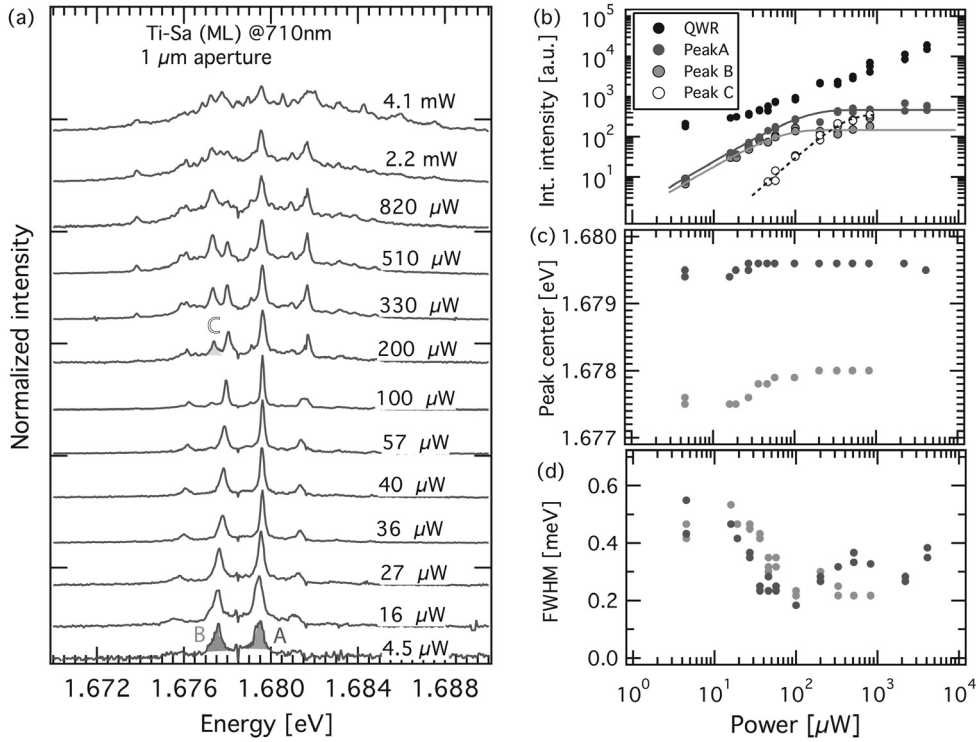
Figure 6.14: (a) Power dependence of the μPL spectra of sample S1A, measured through a 1 μm aperture (Ti-Sa excitation at 710 nm) at 10 K. (b) Intensity (c) Energy and (d) FWHM of the dominant lines, as a function of excitation power.

We checked this value by using a procedure described in Ref. [271]. We measured the 10 K μPL spectra of sample S1A as a function of the excitation power, through a narrow aperture (1 μm wide). These spectra are displayed in Fig. 6.14(a). Two single peaks are isolated at the lowest excitation density. With increasing power, new transitions appear both on the high and low energy sides of the two initial peaks. In the panel (b) of the figure, we report the integrated intensity of the whole QWR PL line, as well as the integrated intensity of the main individual lines. The latter integration was done by means of a lorentzian fit and accounted for the important background. The overall intensity increases almost linearly ($I \propto P^{0.9}$), but the individual lines saturate at an intermediate excitation density. The saturation power P_0 is extracted from a fit with the function $I(P) = A \cdot (1 - e^{(-\frac{P}{P_0})^\alpha})$, in which α accounts for the slight non-linearity in

the low-excitation range. The value P_0 corresponds to the existence of (on average) one exciton in the localized site corresponding to the sharp PL line. For the line labeled A (B) in Fig. 6.14(a), we find $P_0 \simeq 220\ \mu W (60\ \mu W)$. As its line intensity corresponds to 5% (4%) of the total intensity, we estimate by a simple rule of thumb that one exciton in the QWR (along the 1 μm segment) would correspond to an excitation power of 10 μW (2.5 μW). Therefore, the 200 μW power used in the time resolved measurements corresponds to an exciton density of $2 \cdot 10^5\ cm^{-1}$ ($8 \cdot 10^5\ cm^{-1}$). The difference between the two values is large and illustrates the limits of this method. Yet, it gives the order of magnitude of the density, consistent with our initial estimate.

Fig. 6.14(c) and (d) present the energy and the linewidth of peaks A and B. We see that above about 20 μW both peaks slightly shift toward higher energies and that their FWHM decreases. The first phenomena was already identified as a many-body effect [85, 272]. The reduction of the linewidth is usually attributed to the neutralization of charged impurities in the vicinity of the localized exciton. At low excitation densities, their states fluctuate as they capture free carriers, thus slightly modifying the electric field at the localization site. As the intensity increases, the impurity is saturated and the potential does not fluctuates anymore.

Most importantly, we note that effects of exciton interaction are clearly visible at the density at which the time-resolved measurements were performed. First, the intensity of localized sites is saturated. In addition, a new line, labeled C, appears above this excitation power. The supra-linear dependence of its integrated intensity with increasing power and its energy separation to the line A (-2.3 meV) suggest that it corresponds to a biexciton. A similar new line also appears at 1.674 eV and may tentatively be associated with a biexciton stemming from exciton B. All these observations therefore indicate that the system under study is an *interacting* exciton gas.

6.3 Temperature dependence of the optical spectra

The results presented in the previous section indicate that diffusion is a thermally activated process. It is then noteworthy to check if an increase of the temperature also affects the optical properties of the QWR. In particular, changes in the scattering rates (i.e. broadening), as well as spatial and spectral redistribution of the carriers are expected. In this section, we address this issue by looking at the evolution of the μPL and PLE spectra of the QWR as a function of the temperature.

6.3.1 Modification of the PL lineshape

In Ch. 5, we have already noticed that the lineshape of the PL spectra broadens when the temperature increases. In Fig. 6.15 we report the PL spectra measured through a narrow ($\sim$1 μm wide) aperture on sample S1A. First, the spectra redshifts, correspon-

ding to the bandgap reduction with increasing temperature, particularly pronounced above 50 K. Second, each line broadens individually, already starting from the lowest temperatures. In parallel, a broad inhomogeneous background appears progressively, which dominates over the individual lines from about 30 K. Above this temperature, the initial fine structure of the emission is completely hidden and only a broad emission line subsists. As the temperature is further increased, a high energy tail expands, indicating occupation of higher energy states.
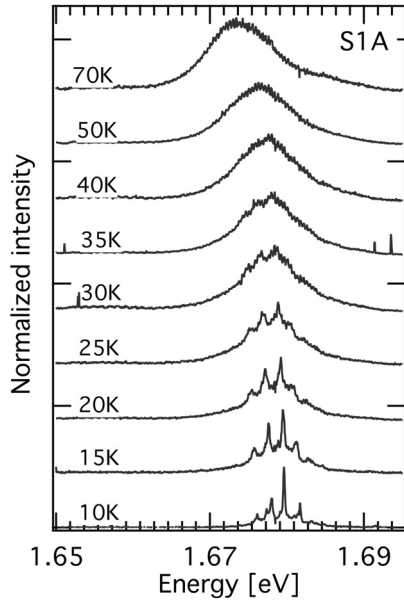
Figure 6.15: μPL spectra of sample S1A as a function of temperature. These spectra were taken through a 1 μm wide aperture.

A systematic background in near-field optical spectra of a QWR at low temperature was reported [273]. It was attributed to the emission from delocalized states. Like in our case, the background was spanning a spectral range wider than that on which the localized lines appear. This result was thus suggesting that there was no abrupt spectral separation between localized and delocalized states, i.e. no 'mobility edge' in QWRs. Nevertheless, we see here that the relative intensity between the emission from the narrow lines and that of the background is strongly modified between 10 K and 50 K, whereas no (or weak) diffusion is observed in that temperature range. Actually, the broadening of individual lines and the appearance of a dominant background with increasing temperature has been shown to arise from scattering with acoustic phonons [91, 123].

The latter explanation keeps open the existence of a mobility edge in QWRs. Yet we should then expect signs of spectral diffusion when measuring the integrated PL spectra through apertures: the emission on the high energy side of the PL line, corresponding to delocalized states, would be expected to vanish when diffusion occurs. We found no clear evidence of such a spectral narrowing in our data: the fluctuations observed between the linewidth of spectra measured through aperture and without an aperture are within the variations due to the sample inhomogeneities. Therefore, there is no indication of

delocalization in the modification of the spectral lineshape with increasing temperature.

6.3.2   Reduction of the Stokes shift

The Stokes shift is a widely used indicator of the degree of disorder in heterostructures. As it is related to the emission from localized states, it is sensitive to the delocalization of the carriers. We measured the Stokes shift for the three samples S1A, S2A and S2B as a function of the temperature. The spectra of the first PLE transition are displayed in Fig. 6.16 according to a relative energy scale, the zero of which corresponds to the energy of the PL peak at the same temperature. These values were measured with the polarization of the laser set parallel to the QWRs. As already noticed in Sec. 5.3.1, the transitions are rather broad and exhibit some sub-structure, the origin of which is not clearly understood. This is true in particular for the samples grown on 0.6°-off substrates.
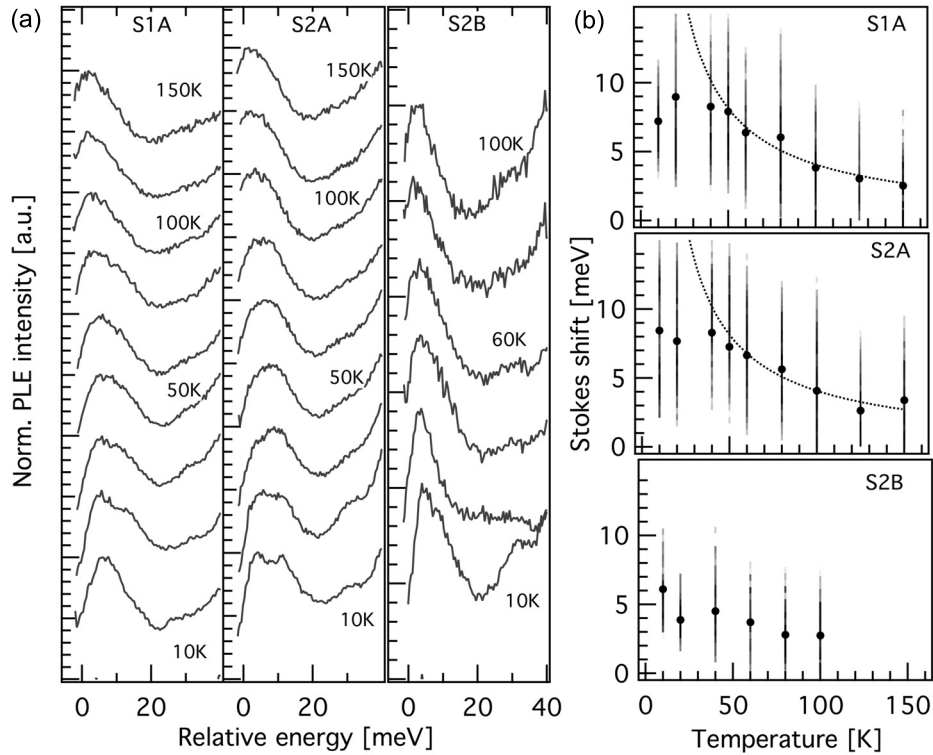
Figure 6.16: (a) PLE spectra (laser polarized parallel to the QWRs) of samples S1A, S2A and S2B measured at different temperatures. The zero of the energy scales corresponds to the peak energy of the PL spectra. (b) Stokes shift as a function of temperature. The vertical lines (plotted with changing grey levels) indicate the intensity of the $e_1 - h_1$ transition with the grey scale spanning the range $[0.8 \cdot I_{max}$ (light grey) ; I_{max} (black)]. The dots correspond to the mean energy of the line, which is measured in the same interval.

The large broadening and the sub-structure of the PLE transition make it difficult

to characterize the Stokes shift. For instance, we observe clearly that in the case of sample S2A the spectral weight is displaced toward the high-energy side of the line as the temperature increases. In Fig. 6.16(b) we make use of two criteria, which allow to quantify and compare the temperature-dependent Stokes shift for the three samples. The first one accounts for the broadening of the line: each spectrum is represented on a gray scale starting from $0.8 \cdot I_{max}$ (in light gray) and ending at the maximum intensity I_{max} (in black) of the $e_1 - h_1$ transition. A global decrease of the relative energy with increasing temperature is clearly found for all three samples, although it is occurring only above around 50 K for samples S1A and S2A. In the same figure, we also propose a quantitative determination of the Stokes shift that is obtained from the mean energy of the transition in the range where its intensity is larger than 80% of its maximum: $< E_m > = \frac{\int_{E_b}^{E_a} I(E) \cdot E \ dE}{\int_{E_b}^{E_a} I(E) \ dE}$ (with $I(E_a) = I(E_b) = 0.8 \cdot I_{max}$ and $E_a < E_b$). The trend in temperature that we observe is the same as the one just described with the previous criterion.

The difference in inhomogeneous broadening between samples 'A' and 'B' is clearly evidenced in Fig. 6.16(b). The low temperature values of the Stokes shift obtained by the mean energy criterion (7.2 / 8.4 / 6.1 meV for the S1A, S2A and S2B, respectively) further attest of the higher homogeneity of the sample S2B.

6.4   Discussion: delocalized excitons

6.4.1   Thermal activation of the excitonic diffusion

The measurements that we performed allowed to directly quantify the exciton diffusion in QWRs. We first discuss the behavior observed for samples S1A and S2A. The TOF measurements show that the diffusion is almost null at low temperatures. At an intermediate temperature, around 50 K, we observed a clear activation of the exciton diffusion and then a monotonous increase of the diffusion with increasing temperature. We found comparable values for S1A and S2A, which have different nominal thicknesses. There is therefore no effect of the confinement strength in our data.

This activation coincides with a strong reduction of the Stokes shift. In spite of the relative dispersion of the experimental data and of the difficulty in identifying a sharp absorption peak, the two methods that we used to quantify the Stokes shift clearly demonstrate its reduction with increasing temperature, which gets truly important above around 50 K.

We observed significant differences in the diffusion and PLE measurements performed on the sample S2B, grown on a 6°-off substrate. First, the diffusion is significantly larger than that of the sample S2A in the range 30 K - 50 K. It was unfortunately not possible to compare the diffusion at temperatures above 50 K because of the weak

signal of the PL. Second, the Stokes shift is smaller in this temperature range and appears to decrease, without initial saturation, with increasing temperature. These observations are consistent with the results of Ch. 5 pointing toward a reduced disorder in QWRs grown on substrates with a large miscut.

Gurioli et al. proposed a model [137] that explains such a reduction, under the sole assumption that the carriers are in thermal equilibrium at a temperature T_c. The Stokes shift can then be expressed as a function of the temperature as $\Delta E_{SS} \propto \frac{\delta^2}{k_B T_c}$, in which δ is the FWHM of the absorption line. For a gaussian absorption lineshape, they determined the proportionality coefficient to be equal to 0.18. Such a model gives an approximative description of the trend that we observe: the dashed line in Fig. 6.16(b) corresponds to $\delta = 14$ meV, which is much smaller than the FWHM of the PLE that we measure (25 meV). This value is arbitrary as we do not measure a gaussian absorption line and the unidentified substructure in the PLE line contributes to the broadening. Yet the $1/k_B T$ dependence describes reasonably our data above 50 K. The bad agreement of the model below 50 K originates in the non-validity of the thermalization hypothesis at low temperature. It has been shown in comparable QWRs that no thermal equilibrium was reached by the carriers at temperatures below 60 K [89]. This value is consistent with the threshold temperature at which the Stokes shift reduces significantly.

In a similar framework, we can describe the increase of the diffusivity as being proportional to the fraction of excitons, whose energy is above a value E_{loc}. Such a threshold could be identified as a mobility edge: in Fig. 6.12, the dotted line corresponds to $f(T) \propto \int_{E_{loc}}^{\infty} \alpha(E) \cdot e^{-E/k_B T} dE$. Within such a description, the localization energy is independent of the broadening of the absorption line $\alpha(E)$, although it is likely that they are actually linked in reality. For the model curve of Fig. 6.12 we used a 1D density of states convoluted with a gaussian (FWHM = 5 meV, which results in a total FWHM of the DOS comparable to the experimental one) to describe the absorption lineshape. E_{loc} was chosen to correspond to the maximum of this line.

Let us note finally that we surprisingly did not observe a shorter lifetime for sample S2B at low temperature, as we would have expected for a sample displaying a smaller disorder. The value at 10 K is 290 ps for the sample S2B, whereas it is slightly smaller (265 ps) for S1A. These values are comparable with those obtained previously on V-groove QWRs (350-400 ps in Ref. [148], 150-480 ps in Ref. [92]). The similarity of the temperature dependence of the lifetime between samples apparently exhibiting such a different disorder is not understood.

6.4.2 Scattering mechanisms

The model above is too simplified in the sense that it does not account for the mechanisms underlying the diffusion and for their own dependence on temperature. In QWs the diffusion at low temperature was described by tunneling and/or phonon mediated

transitions [141, 274]. In the first case, an exciton migrates by hopping between nearby localization sites, over which exciton wavefunctions overlap. Possible energy mismatch are then compensated by acoustic phonons. The absorption of a phonon can also promote an exciton to a delocalized state.

Phonon interactions are evident in the broadening of the μPL spectra of our samples, which evidence their increasing importance with increasing temperature. However, acoustic phonons do not explain the rather abrupt onset of diffusion around 50 K. Instead, previous studies on QWs allowed a quantification of the various scattering mechanisms. An increase of mobility with temperature was observed in GaAs/AlGaAs QWs with width ranging from 4 nm to 74 nm [261]. The thinner was the QW, the smaller was the diffusivity. Moreover, for the 4 nm QW (emitting around 1.65 eV, thus with a confinement energy similar to our samples) the diffusion was activated only above a temperature around 50 K and reached values of about 15 cm^2/s at 150 K. These results are very similar to those obtained in our QWRs.

An increase of the diffusivity (or equivalently of the mobility) with increasing temperature in the low temperature range is expected from reduced interactions with ionized impurities. However, observations in QWs did not supported the prediction of a larger diffusivity for narrower QWs and emphasized the role of interface roughness at low temperatures [275]. The latter was calculated for QWRs in Ref. [147] and Ref. [276]. The second reference adresses specifically V-shaped QWRs with a geometry close to our system. Both predict an initial decrease of the mobility with increasing correlation length ξ of the disorder along the QWR. The mobility reaches a minimum and then increases with ξ. This behavior is due to the fact that the scattering is more effective when the correlation length approaches the Fermi wavelength. The carrier density is thus determinant for the value of the mobility, although contradictory results exist depending on the screening approximations that are used [147, 277]. Actually, because of the larger efficiency of the carrier-carrier scattering compared to the exciton-exciton scattering, the electronic transport is expected to depend on density, while the excitonic transport does not [118].

Our measurements as a function of the excitation power did not show a density dependence. This supports an interpretation in terms of excitonic diffusion consistent with the model that we used. For excitons, scattering with the interface roughness is predicted to be the dominant phenomenon limiting the mobility. Yet, we noticed that, in our experimental conditions, excitons are interacting; this would require a more proper modeling than the single particle picture, on which our model relies.

6.4.3   Comments on the model hypothesis

We described our system in terms of a single type of particles (excitons) and a unique and time-independent diffusion coefficient. This model allowed a good description of the results, as attested to by the good agreement of our fits to the experimental data. Ne-

vertheless, some assumptions of the model are worth discussing in view of other studies. In particular, Monte Carlo simulations allow to address non-equilibrium situations. For example, Takahashi performed simulations of the relaxation and transport of excitons in a QW [118]. He included most of the relevant scattering mechanisms and compared their efficiency for excitons and electron-hole pairs. Several of his findings addressed phenomena relevant to our study.

First, he demonstrated that the diffusion coefficient is not constant, but decreases over time. As the spread of the exciton population is directly linked to the velocity of the exciton, a hotter initial distribution expands more rapidly. Takahashi found that it is however correct to consider a time-independent value of the diffusivity to characterize the exciton motion. Indeed, the curves that we obtained with a time-independent diffusion coefficient are in good agreement with the experimental data and do not indicate significant variations of D with time.
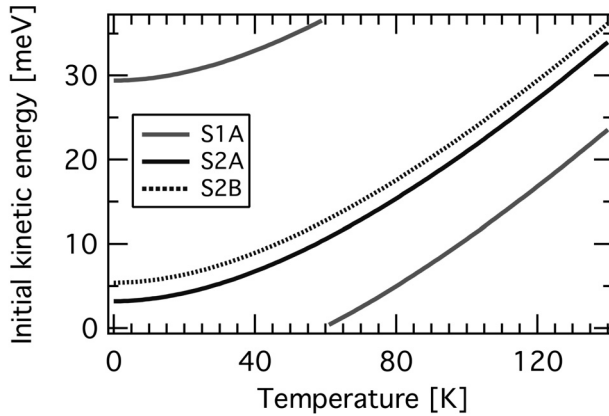
Figure 6.17: Initial kinetic energy after the fast emission of one or two optical phonons. The increase with the temperature is calculated from the redshift of the bandgap (Eq. 2.2) and the low temperature value is set by the energy of the laser, relatively to the PL energy.

The role of the initial kinetic energy was underlined in several studies [268, 278, 279]. The diffusion is directly linked to the velocity of the excitons, hence to their kinetic energy. As the relaxation process through optical phonons is very fast, the initial kinetic energy E_{kin} is defined as the remaining energy after such a (or several, n) process: $E_{kin} = E_{las} - E_{PL} - n \cdot E_{LO}$. In our study the diffusion is clearly not related directly to this factor. Indeed, because the laser energy E_{las} is fixed through the experiment, the initial kinetic energy increases with increasing temperature. However, as made clear in Fig. 6.17, for sample S1A, E_{kin} is not a monotonous function of the temperature, whereas the diffusivity that we measured increases monotonically with the temperature .

Even though our model describes properly the data, it deserves improvements in order to better justify the relation 6.4. Indeed, strictly speaking, diffusing excitons are non radiative ($k \neq 0$). Under the assumption of thermal equilibrium, Eq. 6.4 is correct, as the density of radiative excitons is proportional to the total exciton population. At low temperature, however, without thermalization, the validity of the equation is questioned. We found no evidence of its violation. In particular, the intensities of the signal measured through and without aperture are comparable at low temperature. As all

excitons finally decay radiatively in these conditions, if hot excitons had diffused out of the aperture, it should translate in signal intensity variations. Yet, a finer interpretation of the phenomena at low temperature would require to address this question.

Finally, considering only excitons in our model can be questioned by the fact that excitons are expected to dissociate at increasing temperature. The sharp lines in low-temperature μPL spectra, the regular redshift of the PL line with increasing temperature and the typical resonances in the PLE spectra are all indications that the *optical* properties are dominated by excitons at all temperatures up to 150 K. However, according to the Saha equation [148], at the moderate densities that we used and under the assumption of thermal equilibrium, the electron-hole pair population is larger at temperatures above 50 K. It is now well established that below this temperature (at least) no thermal equilibrium is reached [89,91].

Anyway, once the equilibrium is reached, the conservation of the exciton / e-h pairs ratio requires that a local decrease in the density of one type of pairs (bound or dissociated) triggers the decrease of the other type. An effective diffusivity of excitons and electron-hole pairs is determined and in the absence of a microscopic interpretation of the diffusion mechanisms, we used the term of excitonic diffusion. We keep in mind, however, that ambipolar process can also be involved.

6.5   Chapter summary

We presented systematic measurements of the excitonic diffusion in several V-groove QWR samples. These measurements were based on the time-of-flight method, the principle and limitations of which were thoroughly discussed. At low temperature, no diffusion was observed and other optical properties confirmed that excitons are localized. A clear onset of the diffusion was found above a threshold temperature of about 50 K in the samples exhibiting the largest disorder, independently of their thickness. It is accompanied by a significant reduction of the Stokes shift, indicating that the fraction of delocalized excitons is increasing. Diffusion was setting in at a lower temperature in a sample exhibiting a reduced disorder.

These measurements are discussed in view of the existing theories of exciton diffusion and compared to diffusion measurements made in QWs. We conclude that the diffusion in V-groove QWRs is very similar to that observed in QWs, mainly because it is principally governed by interface roughness scattering.

Chapter 7

Conclusion and outlook

The work described in this thesis offers new insights on the growth of low-dimensional nanostructures by MOVPE. We achieved important improvements of the optical properties of GaAs/AlGaAs QWs and V-groove QWRs and we could relate these advancements to changes in the growth morphology, which determines the interfaces of the heterostructures. These progresses allow to fabricate structures with better controlled excitonic landscapes, which are useful for further studies related to disorder.

We demonstrated that narrow PL linewidth of QWs can be obtained by growing structures on substrates with a small miscut. We correlated this improvement to the settlement of a step-flow growth mode, whereas growth on nominally exact substrates takes place in the 2D mode. Additional transitions of the growth mode occur with increasing miscut angle and result in different types of disorder at the interfaces, which give rise to distinctive optical properties. For the growth conditions that we used, we measured PL linewidth as narrow as 0.5 meV for 15 nm thick QWs grown on 0.2°-off (001) GaAs substrates.

Starting from the improved understanding of the origins of the inhomogeneous linewidth, we discussed the possibilities to further improve the optical characteristics of MOVPE-grown QW samples. Two directions could be particularly worth investigating. First, extending the width of the island-free terraces would decrease the density of longitudinal gaps between the steps at each interface (see Fig. 4.20). The local minima created by these gaps would then be more scarce. This would require exploring the growth parameters space in order to optimize the PL for substrates with $\sim 0.1°$ miscut angle. In that case, fighting atom desorption at higher growth temperature will be crucial. Second, improving the alloy quality of the $Al_xGa_{1-x}As$ could bring further reduction of the PL linewidth, as we suspect it to become crucial for the optical quality of our QWs. Interesting results have been obtained with digital alloys, i.e. barriers composed of GaAs/AlAs superlattices [195] and such structures could be worth exploring.

The data that we presented on the morphology of the interfaces should motivate deeper theoretical studies of the dynamics of MOVPE growth processes. These samples

already allowed the confirmation of an existing growth model [280], but additional informations should be extracted from extending the study to a larger parameter space. The samples that we produced are also ideal for further studies of disorder and its effects, and they could allow to *quantitatively* validate theoretical descriptions. In particular, temperature dependence measurements should allow to distinguish very distinct activation thresholds for phenomena such as motional narrowing or carrier diffusion.

A finer characterization of the purity state of our MOVPE reactor has been made possible by the better reproducibility of routine QW growths. This led to a general improvement of the quality of the structures grown in our group, in particular V-groove QWRs. We reported additional progress in their optical quality. They were obtained by growing the QWRs on vicinal patterned substrates. The narrowest PL linewidths ($<$ 4 meV) were obtained for QWRs grown on a substrate deviating by 8° from the (001) plane toward the $[1\bar{1}0]$ direction. This is the largest miscut angle that we have investigated and it would be definitely worth going beyond this value. In addition, there is certainly room for further optimization of the growth parameters: for GaAs/Al$_x$Ga$_{1-x}$As QWRs, we essentially sticked to fixed V/III ratio and growth temperature; as the linewidth has been now significantly reduced, the present samples might be more sensitive to those parameters.

We also presented a systematic study of the dependence of the PL linewidth on the height of the QWR barriers. We showed that narrow linewidths ($\sim$2 meV) can be obtained for low Al content in the AlGaAs alloy. We evidenced in these samples a reproducible doublet splitting of the PL and μPL line of the QWRs. We proposed to interpret it in terms of a bi-modal distribution of the potential minima. PLE spectra and their evolution as a function of the temperature would be highly beneficial to confirm this interpretation. In that perspective, the low PL intensity of those samples is an issue that has to be solved. The introduction of the backetching procedure is in that case highly advisable, and could be extended to all QWR samples. We also emphasize that, in that case particularly, the effects of internal fields (due to strains or electrostatics) have to be considered carefully.

Temperature dependent PLE experiments should also allow to better relate the doublet observed in these samples to the asymmetric PL lineshape observed in QWR samples with GaAs/Al$_{0.3}$Ga$_{0.7}$As barriers grown on 0.6°-off (001) substrates.

Overall, by combining the two routes that we have investigated, vicinal substrates and low barriers, we believe that V-groove QWRs can reach optical quality comparable to T-shaped QWRs obtained by cleaved-edge overgrowth, for which 1 meV linewidth has been achieved for QWRs emitting at 1.58 eV [72]. Yet, previously unresolved features in the PL and PLE spectra of QWR samples have already been evidenced in the sample presented here and deserve complementary studies. The fine structure of the perpendicularly-polarized transitions in PLE spectra measured on the 8°-off samples brings new insights on the interpretation of PLE spectra. Also, the broadening of the PL linewidth of QWRs is now comparable to the binding energy of charged excitons.

Preparing modulation-doped samples on vicinal substrates could then allow the study of excitonic complexes without having to make use of an opaque mask [88].

In parallel to the changes in the optical properties, we observed important modifications of the morphology of QWR samples grown on substrates with large miscut angles. These changes correspond to modified growth rates on the various facets growing on V-grooved substrates. In regard of our present observations, we cannot attest to a direct correlation between the modification of the morphology and the improvement of the optical properties of the QWRs. More informations on the longitudinal morphology of vicinal QWRs have to be collected. New attempts to apply the selective etching technique for the study of interior QWR interfaces could be considered. Measurements of the PL in a magnetic field could bring indications on the relative depth and extension of localization sites. Such a method was applied to characterize the disorder in QWs, according to the dependence of the diamagnetic shift on the confinement strength [281]. From a modeling point of view, theoretical efforts should focus on the reunion of the growth model explaining the self-organization in the cross-sectional plane of the QWR [176] and that describing the mechanisms taking place on the facets along the QWR direction [181].

Finally, we presented the dependence on temperature of the diffusion of excitons in QWRs. We evidenced that the diffusion is limited by interface roughness and that its activation with temperature is similar to that observed in narrow disordered QWs. In those circumstances, we found no specific sign of a peculiar behavior linked to the one-dimensionality of excitonic diffusion in QWRs. However, the differences observed for samples grown with small ($0.6°$) or large ($6°$) miscut angle have important implications for the standard μPL characterization of QWR samples at low temperature. The larger diffusion coefficient that we measured for the $6°$-off sample implies a wider area probed by the exciton before it recombines. That might explain the relative similarity of the localized exciton lines in the μPL spectra, compared to samples of poorer quality. Making a systematic use of narrow apertures for the low-temperature μPL characterization would remove this bias. Beyond that, extending the investigations of diffusion to (i) samples with different confinements, (ii) higher temperature, and (iii) a broader density range, is necessary to get a better picture of the diffusion mechanisms in V-groove QWRs. We already solved several experimental issues in the experiments presented here. The remaining ones are linked to the weak relative intensity of the QWR PL. Here also, the use of backetched samples could provide more freedom for the choice of experimental parameters.

To conclude, we presented an optical and morphological study of QWs and V-groove QWRs of unprecedented quality. These samples were obtained by MOVPE on vicinal substrates, which allowed to impose different length scales to the fluctuations in nanostructures. The samples and methods achieved through this work offer new opportunities for the study of the physics of excitons in MOVPE grown samples, in particular in 1D V-groove QWRs.

Appendix A

Samples and processes

Samples description

The **TQW structure** is schematized in Fig. A.1(a). It consists in a 500 nm GaAs buffer, a 500 nm $Al_{0.3}Ga_{0.7}As$ lower barrier, followed by three QWs, which are respectively 2, 5 and 15 nm thick and separated by 300 nm $Al_{0.3}Ga_{0.7}As$ barriers. A 300 nm $Al_{0.3}Ga_{0.7}As$ upper barrier is grown after the last 15 nm QW and the sample is finally capped by 30 nm GaAs to prevent surface oxidation. The large barriers allow to absorb most of the photons before reaching the substrate, when exciting above the barriers. We used both semi-insulated and n-doped (001) epi-ready substrates, which undergo a 15 minutes long in-situ thermal desoxidation cycle at 800°C under As flux before growth. For growth conditions, refer to Table 3.1 and Fig. 3.5.

The **DQW structures** have been described in Ch. 4. Refer to Table 4.1 and Fig. 4.9.
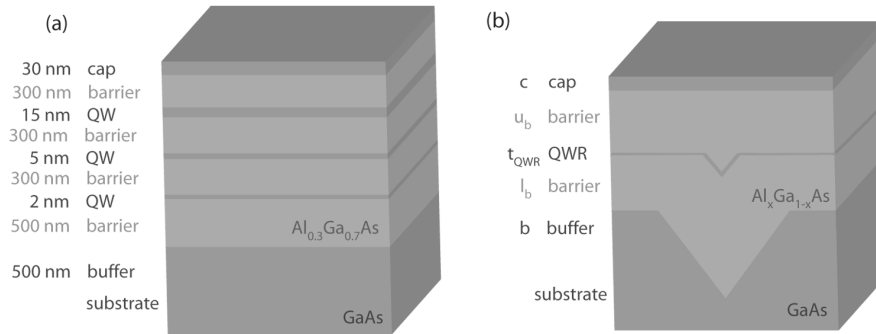
Figure A.1: Scheme of the (a) TQW structure, described in the text and (b) typical QWR structure, whose parameters are detailed in Table A.1

The typical **QWR structure** is represented in Fig. A.1(b). The thicknesses of the layers of the different samples grown with 30% Al content are given in Table A.1. The samples with low Al content are described in Sec. 5.2. The growth of specific structures for morphology investigations is described in Sec. 5.3.2 and Sec. 5.3.3.

Growth run #	Litho.	T_{Growth} °C	Layer thickness [nm]				
			b	l_b	t_{QWR}	u_b	c
1686	opt.	730	30	250	2	50	10
2084	opt.	690	200	1000	2	100	10
2085	opt.	690	200	200	2	100	10
2623 (S1)	eb	690	200	1600	1	500	30
2625	eb	690	200	1600	3	500	30
2671	eb	690	150	1600	0.5	500	30
2673	eb	690	150	1600	2	500	30
2674	eb	690	150	1600	4	500	30
2685 (S2)	eb	690	150	1400	1.5	500	30
2903	eb	690	150	500	2	300	30

Table A.1: List of the QWR samples grown with 30% Al content in the barriers presented in Ch. 5. Opt = optical- ; eb = e-beam lithography.

Fabrication of V-grooves: processing sheets

3µm pitch QWR gratings: e-beam lithography and dry SiO$_2$ etching				
	PROCESS	**EQUIPMENT**	**DETAILS**	
1	Oxide deposition	Oxford PECVD	50 nm SiO$_2$	
2	Cleave			
3	e-beam lithography	PMMA	Various dose and speeds	
	Develop			
4	Plasma-O$_2$	Plasmaline	30s 50W	
5	SiO$_2$ etch	RIE	90s CHF$_3$/Ar	
6	Resist removal	Acetone Isopropanol	Ultrasonic 85% 3 min Ultrasonic 85% 3 min Water rinse	
7	Plasma-O$_2$	Plasmaline	Flux: 0.1; P: 50W; 1min; p $\sim$ 0.3	
8	Plasma-Ar$_2$	RIE	"SiO$_2$ etch Ar" 30s use quarter wafer	
9	Groove etching	HBr:Br:Methanol (40:1:100)	$\sim$ 4 min, substrate dependent 3 water rinses	
	Control	SEM		
10	Lift-off SiO$_2$	BHF	1 min	
11	Plasma-O$_2$	Plasmaline	1 min 50W	
12	Oxide removal	HCl	Until hydrophobic, just before growth	

Figure A.2: V-groove processing sequence, using e-beam lithography and dry etching of the SiO_2 mask.

	PROCESS	EQUIPMENT	DETAILS	NOTES
	3µm pitch QWR gratings: optical lithography and wet etching			
1	Oxide deposition	PECVD	50 nm $\quad$ SiH$_4$: 102 sscm T: 300°C $\quad$ N$_2$O: 338 sscm RF: 110W $\quad$ P: 1000 Torr	
2	Resist spinning	HDMS + S1805	Fast spin for HDMS Δ2 ; 30s ; 800x10 rpm for resist (wafer fully covered)	
	Post-bake		5 min. 90°C	
3	Cleave			
4	Lithography	3µm mask	Align to edges $\quad$ 2s exposure	
	Develop	MF 319	30s	
	Microscope check			
	Annealing	Oven	130°C ; 15min	
5	Plasma-O$_2$	Plasmaline	Flux: 0.1 ; P: 50W ; 1min ; p ~ 0.38	
6	Annealing	Oven	130°C ; 15min	
7	Plasma-O$_2$	Plasmaline	Flux: 0.1 ; P: 50W ; 1min ; p ~ 0.38	
8	Pattern transfer (SiO$_2$ etch)	BHF	35s Water rinse	
	Lift-off resist	Acetone Isopropanol	Ultrasonic 85% 3 min Ultrasonic 85% 3 min Water rinse	
	Plasma-O$_2$	Plasmaline	Flux: 0.1 ; P: 50W ; 3min ; p ~ 0.38	
10	Groove etching	HBr:Br:Methanol (40:1:100)	~ 4min (substrate dependent) 3 water rinses	
	µ-scope check		Density of defects / groove profile	
	Lift-off SiO$_2$	BHF	1min	
	Plasma-O$_2$	Plasmaline	Flux: 0.1 ; P: 50W ; 3min ; p ~ 0.38	
11	Control	SEM		
12	Oxide removal	HCl	Until hydrophobic, just before growth	

Figure A.3: V-groove processing sequence, using optical lithography and wet etching of the SiO_2 mask.

QWR: post-processing sheet

	PROCESS	EQUIPMENT	DETAILS	
	Removing edges and sidewalls in V-groove structures			
1	Cleave		Large piece for resist spinning	
2	Cleaning	Acetone /Isoprop		
3	Pre-bake		115°C 5min	
	Resist spinning	S1805	30s, 6000 rpm	
	Post-bake		90°C 5min / 115°C 15 min	
4	Thin down resist	O$_2$-plasma	Flux: 0.3; p ~ 0.8; P: 75W: ~20min	Until no resist on ridge
5	Etching	H$_2$SO$_4$:H$_2$O$_2$:H$_2$O	(0.5:4:80) ~50s	

Figure A.4: Post-growth processing sequence to remove part of QWs from V-groove samples.

Back-etching of QWR samples

A backetching process is routinely used for quantum dot structures grown in pyramidal recesses to improve the extraction efficiency of the light [186]. We tentatively checked its efficiency for V-groove QWR structures. The principle is to modify the geometry of the surface to create a lens effect. Practically, the structure is turned upside down and the substrate is removed to transform concave corrugations into convex ones.

In order to do so, a particular growth sequence is required. After the usual GaAs buffer layer, a thin $Al_{0.75}Ga_{0.25}As$ layer is grown. It serves as an etch stop when the substrate is removed. Another thin GaAs layer serves as a capping layer to the backetched structure, once the $Al_{0.75}Ga_{0.25}As$ would have been removed, and thus prevent oxidation. The QWR growth then proceeds normally between standard $Al_{0.3}Ga_{0.7}As$ barriers.
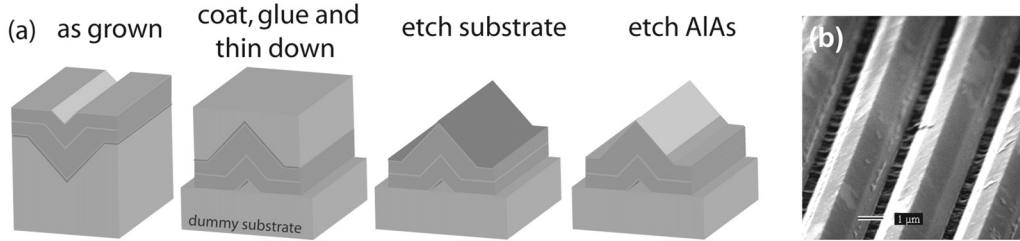
Figure A.5: (a) Post-growth processing steps for substrate removal and upside-down geometry. (b) SEM image of the resulting inverted V-grooves.

The backetching process is illustrated in Fig. A.5(a). First, a metallic coating (20 nm Ti + 200 nm Au) is deposited on the samples surface. It serves as a mirror layer for the photons emitted toward the bottom. The sample is then reverted and glued with wax on a dummy GaAs substrate. It allows to mechanically thin down the sample substrate, and finally to completely remove it by a wet etching in $NH_3 : H_2O_2$ (1:15) (slow etch rate of the order of 1 μm/min). The etch stop layer is finally removed in HF (10%), which leaves grooves with a GaAs cap pointing upwards (Fig. A.5(b)).

The resulting PL spectrum is compared to that of a QWR sample in the usual geometry in Fig. A.6. In that particular case, a thick $Al_{0.6}Ga_{0.4}As$ layer used to planarize the sample prevents a direct comparison of the PL from both geometry on the same sample; this layer is responsible for the peak at 1.875 eV. But the main features of both samples agree nicely. The main difference lies in the intensity of the peaks, and in particular in that of the QWR at 1.604 eV. For the backetched sample it is stronger or at least comparable to all other emission lines, whereas in usual samples the QWR intensity is much weaker. If one defines β as the ratio of the (integrated) QWR intensity to the total PL signal, β is normally only around 0.5% in standard geometry for 3μm grooves. For the backetched sample PL presented here, β is 20%, and even reaches 50% in μPL spectra, where the spatial resolution of the excitation allows to partly eliminate the QWs emission.
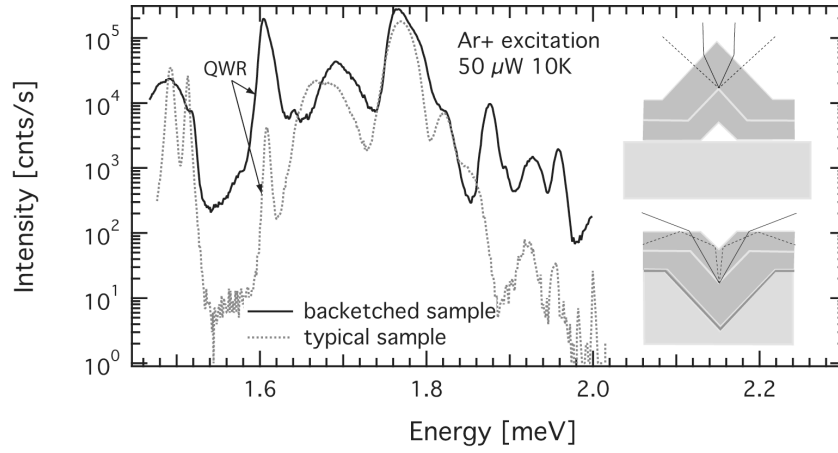
Figure A.6: PL spectra of a backetched QWR, compared to that of a sample with the usual geometry. The insets describe the effect of the surface on the light rays.

The insets in Fig. A.6 indicate how the light rays are refracted at the surface. The solid angle of emission overlapping the collection angle defined by the numerical aperture of the objective is much larger in the backetched geometry than in the non-planarized usual one, which is close to zero in the direction perpendicular to the grooves. This lens effect occurs both for excitation and for collection, and therefore also allows to reach higher carrier densities inside the QWR.

Appendix B

Interior interfaces of V-groove QWRs

As we verified for QWs, the sample surface is not a direct representation of the nanostructure interfaces (Sec. 4.2). In order to check this for QWRs as well, we designed double QWR structures with an AlAs sacrificial layer to investigate the real heterointerface of the QWR layer, in the same way as we did for QWs. The imaging of the interior interface proved however difficult, as dirts and/or etched particles tend to accumulate in the groove, preventing pertinent observations.

We only present here a sample image of the uncovered interface of a nominally exact sample (Fig. B.1(b)). White dots are residual particles, which blur the image in their vicinity. Note, however, that the selectivity of the etch was not checked for surfaces other than (001). As for the QWs, the GaAs cap layer grown above the thick AlAs layer is distorted (a).

We emphasize two observations. First, there is no step-flow pattern on the ridge, but nucleated islands distributed independently of their proximity to the grooves. Second, as is clear from the longitudinal profile (c) and the amplitude image (d), the fluctuations on the sidewalls are systematically correlated. These are two major differences when compared to surface images, and as in the case of QWs, it suggests that the morphology of the samples surface is a result of the annealing taking place during the cooling after growth.
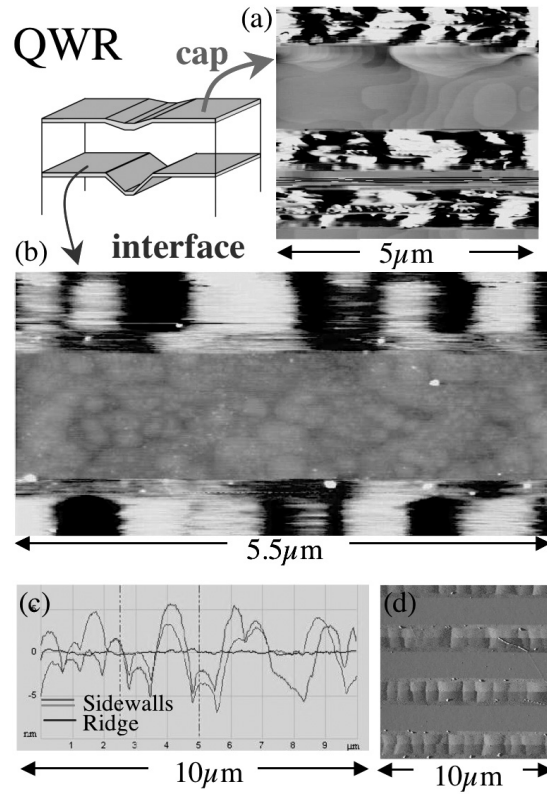
Figure B.1: AFM images of the nominally exact (001) QWR sample from a double QWR structure incorporating a sacrificial AlAs layer (growth #2349). Height images of the cap (a) and buried GaAs layer (b); amplitude image of the buried GaAs layer (d) with corresponding cross-sections (c).

Appendix C

Additional data on diffusion measurements

In order to implement the TOF method as described by Hillmer [261], we started by reproducing measurements on QWs. It allowed us to identify and solve potential issues of the method. Amongst the challenges that we faced were issues related to internal fields in the samples. The observations that we made are relevant to optical characterization of nanostructures in general and we describe and discuss them briefly. Finally we present a few data relative to unintentionally doped QWRs.

Effect of a metallic coating

We described in Sec. 3.1.3 how we prepared opaque masks with apertures on the samples surface. Initially, a thin Ti/Au layer was uniformly deposited below the Al mask. We noticed, however, that this layer had dramatic effects on the optical properties of some samples. This is illustrated in Fig. C.1: the PL lineshape and decay curve of a QW sample coated with 25 Å Ti and 50 Å Au are compared to those of a piece of the same sample without coating. First, we note that the PL lineshape is much different in the two cases (panel (a)). We already mentioned the broader, redshifted PL line obtained when exciting the as-grown sample below the barrier with the Ti-Sa laser (Sec. 4.1). However, the PL spectrum measured from the coated piece under the same conditions is comparable to that resulting from an above-barrier excitation with the Ar+ laser. The temporal decay of the PL is also much affected (Fig. C.1(b)). The decay time is almost twice larger after coating. These differences are not due to a different excitation density resulting from a beam attenuated by the coating, as demonstrated by the measurements made at a lower power on the as-grown sample.

The effect of the coating cannot be explained only by a Stark shift due to an internal electric field. If the redshifted line may arise from band bending, charge separation would result in a longer decay time, opposite to what is measured. Yet, the electrostatic nature of the effect is valid, as the difference can be canceled by exciting at an energy

163
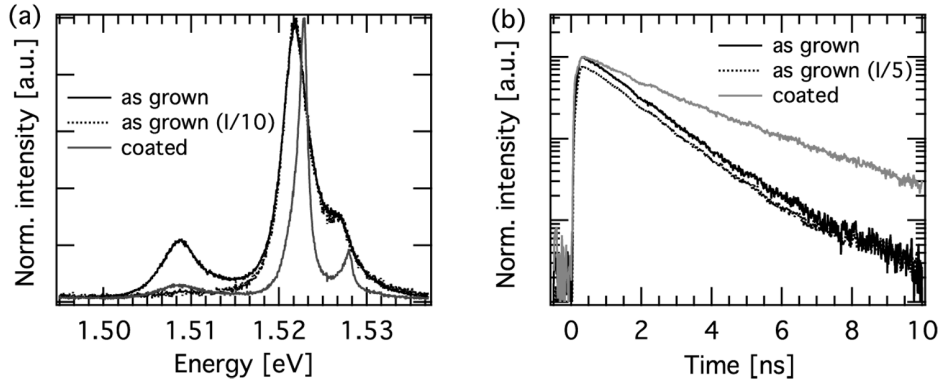
Figure C.1: Effect of a thin metallic coating on the optical properties of a 15 nm-QW grown on 0.2°-off sample: (a) μPL spectra and (b) time-resolved PL decay of the sample as grown (black line) and coated (gray line). Measurements at 50 K with below barrier excitation. Data for two different excitation densities are shown for the 'as grown' sample.

above that of the barriers. We pointed out in Sec. 4.1 that Ti-Sa excitation is likely to favor the formation of charged excitons due to preferential capture of one type of photo-generated carriers. The decay time of such particles is faster than that of the exciton [282]. Alternatively, a similar reduction of the lifetime with increasing electric field has been tentatively explained by the increased leakage of the wavefunction in the barrier or by the tunneling of the carriers out of the QWs [283].

When the excitation is above the barriers, the internal field is screened and flat band conditions are recovered. The effect of the coating is similar to that of screening: the Schottky contact created by the metallic layer compensates the internal field. This type of behavior has already been reported and used in heterostructures.

Effect of the Al mask

Another unanticipated effect was observed in μPL measurements through apertures etched in Al mask. The QW PL line gradually redshifts with decreasing aperture size (Fig.C.2).

The shift is visible already within large apertures, and gets very important for the narrowest ones, for which it reaches 5 meV. Simultaneously, the lineshape changes completely. The three measurement series displayed in Fig. C.2, made in different experimental conditions, indicate that the shift is independent of temperature and excitation conditions. Its origin is therefore different from that of the surface coating.

The PL lines from all structures of the sample redshift. This shift is the largest for the PL of the 15 nm QW closest to the surface, and much smaller for the emission of the GaAs substrate. By changing the thickness of the Al mask layer, we found that the
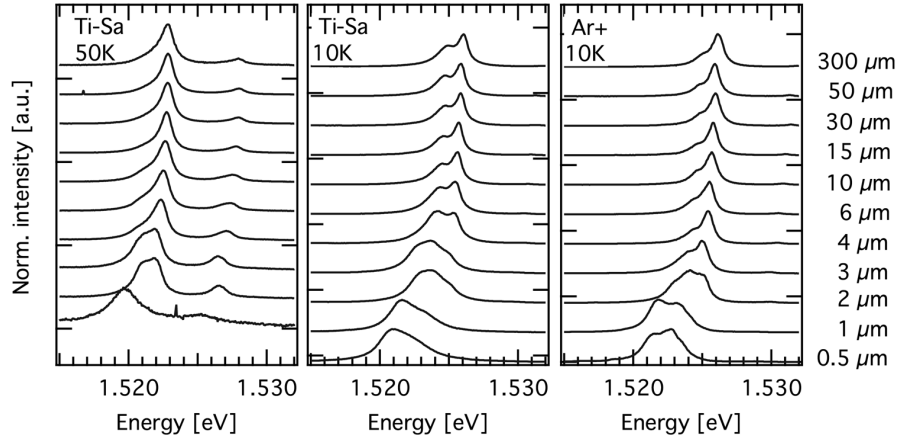
Figure C.2: μPL spectra of a 15 nm QW grown on a 0.2°-off substrate, measured through apertures of decreasing sizes, at different temperature and excitation conditions.

effect is larger for thicker Al layer, and is attenuated when the Ti/Au coating thickness is increased. We therefore attribute this redshift to tensile strains induced by the Al mask [284]. The values of the expansion coefficient of Ti and Au (8.6 and $14 \cdot 10^{-6}$ /C°) are indeed intermediate to those of Al and GaAs (23 and $5.8 \cdot 10^{-6}$ /C°) and the coating layer partially compensate for these strains.

We have strongly reduced the strains by decreasing the Al coverage on the sample surface. New masks were designed with only 20 μm wide Al bands around the apertures. In this way, the redshift was reduced to <1 meV (between 40 and 2 μm apertures). The amplitude of the potential fluctuations induced by the remaining strain are therefore smaller than those due to disorder, and do not perturb the measurements performed on QWRs.

Doped QWR samples

Some QWR samples that have been grown exhibited a peculiar behavior. Their PL was very weak when excited below the barriers. As evidenced by PLE measurements (Fig. C.3, lower spectra), the ground state absorption was completely quenched and an absorption threshold was present close to the light-hole transition energy.

This situation is reminiscent of what was observed in QWs excited below the barriers. For this reason, we deposited a thin coating layer (25 Å Ti, 50 Å Au). In QWs, it was shown in the previous section that the coating compensates the band bending. As visible in Fig.C.3, the PLE of the QWR sample was indeed strongly modified by this coating: the absorption threshold was suppressed and the ground state resonance was recovered, although its intensity was still attenuated. When additionally illuminating the sample with high energy photons ('white light'), the intensity of the first PLE transi-
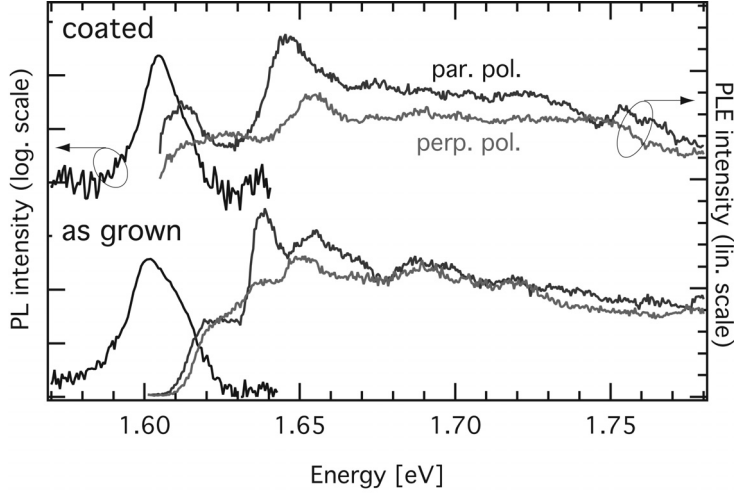
Figure C.3: Ti-Sa excited PL and PLE spectra of a 2 nm QWR before (as grown) and after the surface was coated with thin Ti-Au layers.

tion further increased, which is also consistent with the observations made on QWs. The interpretation in terms of Stark shift and doping is also confirmed by the reduction of the high energy side of the PL line, and the overall blueshift of the PL and PLE spectra.
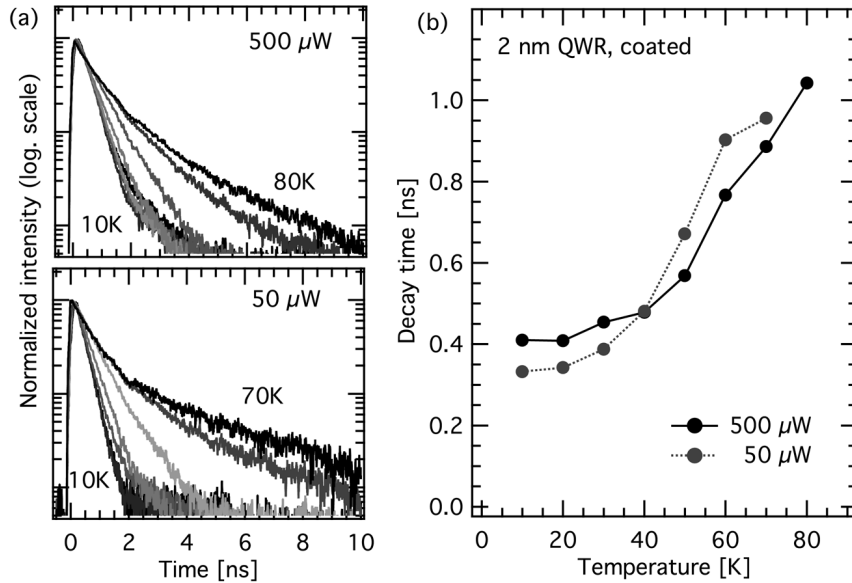
Figure C.4: (a) TR-μPL from a coated 2 nm QWR sample, at two different excitations densities, as a function of temperature. (b) Decay times extracted on the fast decay components of the curves of (a).

Even with this compensation provided by the coating, these samples are not suitable for time-resolved measurements. Example TR-measurements on the same 2 nm QWR samples are shown in Fig. C.4(a). First, we note that the decay is note mono-exponential but has an important slow component, particularly important at the higher temperatures. Second, the time constant extracted from the faster decay segment of the curve depends strongly on the excitation density, with differences up to 150 ps (panel (b)).

The samples that were used in the experiments presented in Ch. 6 do not suffer from these peculiar behaviors and are free of internal electric fields. In particular, we checked on one of them that the deposition of the Ti/Au coating does not change their PL and PLE properties.

Appendix D

Figure / sample correspondence

Figure	Samples
Fig. 4.2	#2025, #2158, #2161, #2163, #2166, #2187,#2190, #2257
Fig. 4.4	#2158, #2161, #2166, #2257
Fig. 4.5	#2095, #2715
Fig. 4.6	#2090
Fig. 4.7	#2166
Fig. 4.8	#2166
Fig. 4.10	#2021
Fig. 4.11	#2081
Fig. 4.12	#2080
Fig. 4.13	#1325, #1776
Fig. 4.14	#2021, #2094, #2111, #2113
Fig. 4.15	#2081
Fig. 4.16	#2018, #2112
Fig. 4.17	#2168

Table D.1: Table indicating the samples, whose data appear in the figures of Ch. 4.

Figure	Samples
Fig. 5.2	#2084, #2085
Fig. 5.3	#2084
Fig. 5.4	#2084, #2085
Fig. 5.5	#2084
Fig. 5.6	#2085
Fig. 5.8	#1686
Fig. 5.3	#2084
Fig. 5.18	#2903
Fig. 5.19	#2903
Fig. 5.20	#2903
Fig. 5.21	#2903
Fig. 5.22	#2623, #2625, #2671, #2673, #2674, #2685
Fig. 5.23	#2685, #2673, #2674
Fig. 5.24	#2671, #2673, #2674, #2685
Fig. 5.25	#2673
Fig. 5.26	#2673
Fig. 5.27	#2903
Fig. 5.28	#2401, #2440
Fig. 5.29	#2488
Fig. 5.30	#2488
Fig. 5.31	#2825, #2674
Fig. 5.32	#2782

Table D.2: Table indicating the samples, whose data appear in the figures of Ch. 5 (except for Sec. 5.2, in which figures are directly labeled).

Bibliography

[1] www.nanotera.ch.

[2] S. R. Forrest. The path to ubiquitous and low-cost organic electronic appliances on plastic. *Nature*, 428:911, 2004.

[3] D. G. Gibson, G. A. Benders, and J. C. Venter. Complete chemical synthesis, assembly, and cloning of a mycoplasma genitalium genome. *Science*, 319:1215, 2008.

[4] www.ieee-virtual-museum.org.

[5] International Technology Roadmap for Semiconductor. Overall Roadmap Technology Characteristics, 2007.

[6] Y. Cui and C. M. Lieber. Functional nanoscale electronic devices assembled using silicon building blocks. *Science*, 291:851, 2001.

[7] D. K. Ferry. Nanowires in nanoelectronics. *Science*, 319:579, 2008.

[8] W. P. McCray. MBE deserves a place in the history books. *Nature Nanotechnology*, 2:269, 2007.

[9] R. Dingle, W. Wiegmann, and C. H. Henry. Quantum states of confined carriers in very thin $Al_xGa_{1-x}As - Al_xGa_{1-x}As$ heterostructures. *Phys Rev Lett*, 33(14):827, 1974.

[10] C. Weisbuch, R. Dingle, A.C. Gossard, and W. Wiegmann. Optical characterization of interface disorder in $GaAs/Ga_{1-x}Al_xAs$ multi-quantum well structures. *Solid State Commun*, 38:709, 1981.

[11] D. Gammon, B.V. Shanabrook, and D.S. Katzer. Interfaces in GaAs/AlAs quantum well structures. *Appl Phys Lett*, 57(25):2710, 1990.

[12] D. Gammon, B.V. Shanabrook, and D.S. Katzer. Excitons, Phonons, and Interfaces in GaAs/AlAs Quantum-Well Structures. *Phys Rev Lett*, 67(12):1547, 1991.

[13] A. Ourmazd, D. W. Taylor, J. Cunningham, and C. W. Tu. Chemical mapping of semiconductor interfaces at near-atomic resolution. *Phys Rev Lett*, 62(8):933, 1989.

[14] B. Deveaud, B. Guenais, A. Poudoulec, A. Regreny, and C. D'Anterroches. Comment on 'Chemical mapping of semiconductor interfaces at near-atomic resolution'. *Phys Rev Lett*, 65(18):2317, 1990.

[15] G. B. Stringfellow. *Organometallic vapor-phase epitaxy*. Academic Press, San Diego, 2nd edition edition, 1999.

[16] R.D. Dupuis, J.G. Neff, and C.J. Pinzone. Very smooth AlGaAs-GaAs quantum wells grown by metalorganic chemical vapor deposition. *J Cryst Growth*, 124:558, 1992.

[17] R.F. Kopf, E.F. Schubert, T. D. Harris, and R.S. Becker. Photoluminescence of GaAs quantum wells grown by molecular beam epitaxy with growth interruptions. *Appl Phys Lett*, 58(6):631, 1991.

[18] L. Gottwaldt, K. Pierz, and F.J. Ahlers et al. Mesoscopic island structure at GaAs/(AlGa)As interfaces grown by MBE. *J Cryst Growth*, 251:85, 2003.

[19] L. Gottwaldt, K. Pierz, and F.J. Ahlers et al. Correlation of the physical properties and the interface morphology of AlGaAs/GaAs heterostructures. *J Appl Phys*, 94(4):2464, 2003.

[20] I. V. Ponomarev, L. I. Deych, and A. A. Lisyansky. Effect of interwall surface roughness correlations on optical spectra of quantum well excitons. *Phys Rev B*, 71:155303, 2005.

[21] N. Néel, T. Maroutian, L. Douillard, and H.-J. Ernst. From meandering to faceting, is step flow growth ever stable ? *Phys Rev Lett*, 91(22):226103, 2003.

[22] H. Omi and Y. Homma. Self-ordering on vicinal Si(111) during molecular beam epitaxy. *Phys Rev B*, 72:195322, 2005.

[23] H. Metiu, Y.-T. YLu, and Z. Zhang. Epitaxial growth and the art of computer simulations. *Science*, 255:1088, 1992.

[24] Y. Horikoshi. Migration-enhanced epitaxy of GaAs and AlGaAs. *Semicond Sci Technol*, 8:1032, 1993.

[25] R. Dettmer. The quest of the quantum dot. *IEEE Review*, November:395, 1988.

[26] G. D. Scholes and G. Rumbles. Excitons in nanoscale systems. *Nature*, 5:683, 2006.

[27] E. Kapon. *Semiconductor lasers I*. Elsevier, San Diego, 1999.

[28] C. L. Tsai, K. Y. Cheng, S. T. Chou, and S. Y. Lin. InGaAs quantum wire infrared photodetector. *Appl Phys Lett*, 91:181105, 2007.

[29] V. Troncale, K. F. Karlsson, E. Pelucchi, A. Rudra, and E. Kapon. Control of valence band states in pyramidal quantum dot-in-dot semiconductor heterostructures. *Appl Phys Lett*, 91:241909, 2007.

[30] N. Akopian, N. H. Lindner, and E. Poem et al. Entangled photon pairs from semiconductor quantum dots. *Phys Rev Lett*, 96:130501, 2006.

[31] R. M. Stevenson, R. J. Young, and P. Atkinson et al. A semiconductor source of triggered entangled photon pairs. *Nature*, 439:179, 2006.

[32] N. Akopian, N. H. Lindner, and E. Poem et al. Correlated and entangled pairs of single photons from semiconductor quantum dots. *J Appl Phys*, 101:081712, 2007.

[33] R. J. Young, R. M. Stevenson, and A. J. Shields et al. Entangled photons from the biexciton cascade of quantum dots. *J Appl Phys*, 101:081711, 2007.

[34] I. Robert, E. Moreau, M. Gallart, J.M. Gérard, and I. Abram. Solid-state triggered single photon sources. *Physica E*, 16:51, 2003.

[35] P. Michler, A. Kiraz, and C. Becher et al. A quantum dot single-photon turnstile device. *Science*, 290:2282, 2000.

[36] M. Asada, Y. Miyamoto, and Y. Suematsu. Gain and the threshold of three-dimensional quantum-box lasers. *IEEE J Quantum Electron*, QE-22(9):1915, 1986.

[37] Y. Arakawa and H. Sakaki. Multidimensional quantum well laser and temperature dependence of its threshold current. *Appl Phys Lett*, 40(11):939, 1982.

[38] H. Sakaki. Scattering suppression and high-mobility effect of size quantized electrons in ultrafine semiconductor wire structures. *Jpn J Appl Phys*, 19(12):L735, 1980.

[39] S. Bandyopadhyay, A. Svizhenko, and M. A. Stroscio. Why would anyone want to build a narrow channel (quantum wire) transistor. *Superlattices Microstruct*, 27(2/3):67, 2000.

[40] R. C. Ashoori. Electrons in artificial atoms. *Nature*, 379:413, 1996.

[41] L. Zhuang, L. Guo, and S. Y. Chou. Silicon single-electron quantum-dot transistor switch operating at room temperature. *Appl Phys Lett*, 72(10):1205, 1998.

[42] E. Knill, R. Laflamme, and G. J. Milburn. A scheme for efficient quantum computation with linear optics. *Nature*, 409:46, 2001.

[43] H. J. Krenner, S. Stufler, and M. Sabathil et al. Recent advancs in exciton-based quantum information processing in quantum dot nanostructures. *New Journal of Physics*, 7:184, 2005.

[44] A. Gustafsson, M.-E. Pistol, L. Montelius, and L. Samuelson. Local probe techniques for luminescence studies of low-dimensional semiconductor structures. *J Appl Phys*, 84(4):1715, 1998.

[45] X. L. Wang and V. Voliotis. Epitaxial growth and optical properties of semiconductor quantum wires. *J Appl Phys*, 99:121301, 2006.

[46] M. Yamamoto, M. Stopa, Y. Tokura, Y. Hiryama, and S. Tarucha. Negative Coulomb drag in a one-dimensional wire. *Science*, 313:204, 2006.

[47] R. Held, T. Heinzel, P. Studerus, and K. Ensslin. Nanolithography by local anodic oxidation of metal films using an atomic force microscope. *Physica E*, 2:748, 1998.

[48] J. Cibert, P. M. Petroff, and G. J. Dolan et al. Optically detected carrier confinement to one and zero dimension in GaAs quantum well wires and boxes. *Appl Phys Lett*, 49(19):1275, 1986.

[49] O. Zsebök, J. V. Thordson, B. Nilsson, and T. G. Andersson. Morphology of InGaAs/GaAs quantum wires prepared by highly controlled deep-etching techniques. *Nanotechnology*, 12:32, 2001.

[50] V. Negoita, D. W. Snoke, and K. Eberl. Stretching quantum wells: A method for trapping free carriers in GaAs heterostructures. *Appl Phys Lett*, 75(14), 1999.

[51] K. Kash, B. P. Van der Gaag, and D. D. Mahoney et al. Observation of quantum confinement by strain effect. *Phys Rev Lett*, 67(10):1326, 1991.

[52] M. S. Miller, H. Weman, and C.E. Pryor et al. Serpentine superlattice quantum-wire arrays of (Al,Ga)As grown on vicinal GaAs substrates. *Phys Rev Lett*, 68(23):3464, 1992.

[53] T. Mélin and F. Laruelle. Optical properties of remotely doped AlAs/GaAs coupled quantum wire arrays. I. Periodic quantum confinement and localization of minority carriers. *Phys Rev B*, 65:195302, 2002.

[54] V.A. Volodin and M.D. Efremov. Photoluminescence study of type-II GaAs quantum well wires grown on nano-faced (311)A surface: Quasi-1D exciton observation ? *Microelectronics Journal*, 37:1557, 2006.

[55] K. Hiruma, M. Yazawa, and T. Katsuyama et al. Growth and optical properties of nanometer-scale GaAs and InAs whiskers. *Appl Phys Lett*, 77(2):447, 1994.

[56] M. T. Borgström, G. Immink, B. Ketelaars, R. Algra, and E. P.A.M. Bakkers. Synergetic nanowire growth. *Nature Nanotechnology*, 2:541, 2007.

[57] H. Akiyama, M. Yoshita, L. N. Pfeiffer, and K. W. West. One-dimensional excitonic states and lasing in highly uniform quantum wires formed by cleaved-edge overgrowth with growth-interrupt annealing. *J Phys: Condens Matter*, 16:S3549, 2004.

[58] K. Y. Cheng, K.C. Hsieh, and J. N. Baillargeon. Formation of lateral quantum wells in vertical short-period superlattices by strained-induced lateral-layer ordering process. *Appl Phys Lett*, 60(23):2892, 1992.

[59] R. Leon, P. M. Petroff, D. Leonard, and S. Fafard. Spatially resolved visible luminescence of self-assembled semiconductor quantum dots. *Science*, 267:1966, 1995.

[60] E. Kapon, E. Pelucchi, and S. Watanabe et al. Site- and energy-controlled pyramidal quantum dot heterostructures. *Physica E*, 25:288, 2004.

[61] Q. Zhu, E. Pelucchi, and S. Dalessi et al. Alloy segregation, quantum confinement, and carrier capture in self-ordered pyramidal quantum wires. *Nano Letters*, 6(5):1036, 2006.

[62] F. Michelini, M.-A. Dupertuis, and E. Kapon. Effect of the one-dimensional quantum barriers in pyramidal quantum dots. *Appl Phys Lett*, 84(20):4086, 2004.

[63] Q. Zhu, F. Karlsson, E. Pelucchi, and E. Kapon. Transition from 2D to 3D quantum confinement in semiconductor quantum wires/quantum dots. *Nano Letters*, 7(8):2227, 2007.

[64] D. Kaufman, Y. Berk, and B. Dwir et al. Conductance quantization in V-groove quantum wires. *Phys Rev B*, 59(16):R10433, 1999.

[65] E. Levy, A. Tsukernik, and M. Karpovski et al. Luttinger-liquid behavior in weakly disordered quantum wires. *Phys Rev Lett*, 97:196802, 2006.

[66] K. A. Atlasov, K. F. Karlsson, and E. Deichsel et al. Site-controlled single quantum wire integrated into a photonic-crystal membrane microcavity. *Appl Phys Lett*, 90:153107, 2007.

[67] C. Constantin, E. Martinet, and D. Y. Oberli et al. Quantum wires in multidimensional microcavities: effects of photon dimensionality on emission properties. *Phys Rev B*, 66:165306, 2002.

[68] T. Giamarchi. *Quantum physics in one dimension*. Oxford Science Publications, 2004.

[69] T. Guillet, J. Berréhar, and R. Grousson et al. Emission of single conjugated polymer chain isolated in its single monomer matrix. *Phys Rev Lett*, 87(8):087401, 2001.

[70] F. Dubin, R. Melet, and T. Barisien et al. Macroscopic coherence of a single exciton state in an organic quantum wire. *Nature*, 2:32, 2006.

[71] T. Ihara, Y. Hayamizu, M. Yoshita, and H. Akiyama. One-dimensional band-edge absorption in a doped quantum wire. *Phys Rev Lett*, 99:126803, 2007.

[72] H. Akiyama, L. N. Pfeiffer, A. Pinczuk, K. W. West, and M. Yoshita. Observation of large many-body Coulomb interaction effects in a doped quantum wire. *Solid State Commun*, 122:169, 2002.

[73] H. Akiyama, M. Yoshita, L. N. Pfeiffer, K. W. West, and A. Pinczuk. One-dimensional continuum and exciton states in quantum wires. *Appl Phys Lett*, 82(3):379, 2003.

[74] H. Itoh, Y. Hayamizu, and M. Yoshita et al. Polarization-dependant photoluminescence-excitation spectra of one-dimensional exciton and continuum states in T-shaped quantum wires. *Appl Phys Lett*, 83(10):2043, 2003.

[75] A. Gold and R. Marty. AlAs quantum wells: transport properties of the two-dimensional electron gas. *J Appl Phys*, 102:083705, 2007.

[76] F. Vouilloz, D. Y. Oberli, and M.-A. Dupertuis et al. Polarization anisotropy and valence band mixing in semiconductor quantum wires. *Phys Rev Lett*, 78(8):1580, 1997.

[77] E. Kapon, D. M. Hwang, and R. Bhat. Stimulated emission in semiconductor quantum wire heterostructures. *Phys Rev Lett*, 63(4):430, 1989.

[78] L. Sirigu, D. Y. Oberli, L. Degiorgi, A. Rudra, and E. Kapon. Excitonic lasing in semiconductor quantum wires. *Phys Rev B*, 61(16):R10575, 2000.

[79] K. Leosson, J.R. Jensen, W. Langbein, and J.M. Hvam. Exciton localization and interface roughness in growth-interrupted GaAs/AlAs quantum wells. *Phys Rev B*, 61(15):10322, 2000.

[80] P. Huai, H. Akiyama, Y. Tomio, and T. Ogawa. Coulomb enhancement and suppression of peak gain in quantum wire lasers. *Jpn J Appl Phys*, 46(44):L1071, 2007.

[81] T. Guillet, R. Grousson, and V. Voliotis et al. Mott transition from a diluted exciton gas to a dense electron-hole plasma in a single V-shaped quantum wire. *Phys Rev B*, 67:235324, 2003.

[82] M. Yoshita, Y. Hayamizu, and H. Akiyama. Exciton-plasma crossover with electron-hole density in T-shaped quantum wires studied by the photoluminescence spectrograph method. *Phys Rev B*, 74:165332, 2006.

[83] M. Yoshita, S.-M. Liu, and M. Okano et al. T-shaped GaAs quantum-wire lasers and the exciton Mott transition. *J Phys: Condens Matter*, 19:295217, 2007.

[84] D. Y. Oberli, A. Rudra, and E. Kapon. Optical studies of modulation-doped V-groove quantum wires: Fermi-edge singularity. *Physica E*, 11:224, 2001.

[85] F. Vouilloz, D. Y. Oberli, F. Lelarge, B. Dwir, and E. Kapon. Observation of many-body effects in the excitonic spectra of semiconductor quantum wires. *Solid State Commun*, 108(12):945, 1998.

[86] T. Otterburg, D. Y. Oberli, and M.-A. Dupertuis et al. Observation of charged excitons in V-groove quantum wires. *Phys stat sol (c)*, 1(3):526, 2004.

[87] A. Feltrin, F. Michelini, and J. L. Staehli et al. Localization-dependent photo-luminescence spectrum of biexcitons in semiconductor quantum wires. *Phys Rev Lett*, 95:177404, 2005.

[88] T. Otterburg, D. Y. Oberli, and M.-A. Dupertuis et al. Enhancement of the binding energy of charged excitons in disordered quantum wires. *Physical Review B*, 71:033301, 2005.

[89] D. Y. Oberli, F. Vouilloz, R. Ambigapathy, B. Deveaud, and E. Kapon. Photo-luminescence study of V-groove quantum wires: the influence of disorder on the optical spectra and the carrier thermalization. *Phys stat sol (a)*, 178:211, 2000.

[90] T. Yasuhira, K. Komori, and R. Akimoto et al. Exciton formation dynamics in crescent-shaped quantum wires. *Appl Phys Lett*, 81(19):3642, 2002.

[91] A. Feltrin, R. Idrissi Kaitouni, and A. Crottini et al. Exciton relaxation and level repulsion in $GaAs/Al_xGa_{1-x}As$ quantum wires. *Phys Rev B*, 69:205321, 2004.

[92] J Bellessa, V Voliotis, and R Grousson et al. Quantum-size effects on radiative lifetimes and relaxation of excitons in semiconductor nanostructures. *Phys Rev B*, 58(15):9933, 1998.

[93] J. Hasen, L. N. Pfeiffer, and A. Pinczuk et al. Metamorphosis of a quantum wire into quantum dots. *Nature*, 390:54, 1997.

[94] B. J. Van Wees, H. Van Houten, and C. W. J. Beenakker et al. Quantized conductance of point contacts in a two-dimensional electron gas. *Phys Rev Lett*, 60(9):848, 1988.

[95] A. Yacoby, H. L. Stormer, and N. S. Wingreen et al. Nonuniversal conductance quantization in quantum wires. *Phys Rev Lett*, 77(22):4612, 1996.

[96] N.I. Cade, M. Hadjipanayi, and R. Roshan et al. Longitudinal photocurrent spectroscopy of a single GaAs/AlGaAs V-groove quantum wire. *Nanotechnology*, 16:307, 2005.

[97] L. Pfeiffer, A. Yacoby, and H. L. Stormer et al. Transport and optics in quantum wires fabricated by MBE overgrowth on the (110) cleaved edge. *Microelectronics Journal*, 28:817, 1997.

[98] T. Guillet, R. Grousson, V. Voliotis, X.-L. Wang, and M. Ogura. Local disorder and optical properties in V-shaped quantum wires: Towards one-dimensional exciton systems. *Phys Rev B*, 68:045319, 2003.

[99] M. A. Herman, D. Bimberg, and J. Christen. Heterointerfaces in quantum wells and epitaxial growth processes: evaluation by epitaxial growth technics. *J Appl Phys*, 70(2):R2, 1991.

[100] G. D. Gilliland. Photoluminescence spectroscopy of crystalline semiconductors. *Materials Science and Engineering*, R18:99, 1997.

[101] K. K. Bajaj. Use of excitons in material characterization of semiconductor system. *Materials Science and Engineering R*, 34:59, 2001.

[102] J. H. Davies. *The physics of low-dimensional semiconductors.* Cambridge University Press, 1998.

[103] C. Bosio, J. L. Staehli, M. Guzzi, G. Burri, and R. A. Logan. Direct-energy-gap dependence on Al concentration in $Al_xGa_{1-x}As$. *Phys Rev B*, 38(5):3263, 1988.

[104] G. Thucydides, J. M. Barnes, and E. Tsui et al. Picosecond photoluminescence studies of carrier escape processes in a $GaAs/Al_{0.3}Ga_{0.7}As$ single quantum well. *Semicond Sci Technol*, 11:331, 1996.

[105] R. Cingolani, H. Lage, and L. Tapfer et al. Quantum confined one-dimensional electron-hole plasma in semiconductor quantum wires. *Phys Rev Lett*, 67(7):891, 1991.

[106] G. Bastard. *Wave mechanics applied to semiconductor heterostructures.* John Wiley and Sons, Inc, Les Ulis, 1990.

[107] U. Bockelmann and G. Bastard. Interband absorption in quantum wires. I. Zero-magnetic-field case. *Phys Rev B*, 45(4):1688, 1992.

[108] P. C. Sercel and K. J. Vahala. Analytical formalism for determining quantum-wire and quantum-dot band structure in the multiband envelope-function approximation. *Phys Rev B*, 42(6):3690, 1990.

[109] R. L. Greene, K. K. Bajaj, and D. E. Phelps. Energy levels of Wannier excitons in $GaAs-Ga_{1-x}Al-xAs$ quantum-well structures. *Phys Rev B*, 29(4):1807, 1984.

[110] M. Gurioli, J. Martinez-Pastor, and M. Colocci et al. Well-width and aluminum-concentration dependence of the exciton binding energies in $GaAs/Al_xGa_{1-x}As$ quantum well. *Phys Rev B*, 47(23):15755, 1993.

[111] F. Rossi, G. Goldoni, and E. Molinari. Shape-independent scaling of excitonic confinement in realistic quantum wires. *Phys Rev Lett*, 78(18):3527, 1997.

[112] H. Akiyama. One-dimensional excitons in GaAs quantum wires. *J Phys: Condens Matter*, 10:3095, 1997.

[113] J. G. Tischler, A.S. Bracker, D. Gammon, and D. Park. Fine structure of trions and excitons in single GaAs quantum dots. *Phys Rev B*, 66:081310, 2002.

[114] T. Ogawa and T. Takagahara. Optical absorption and Sommefeld factor of one-dimensional semiconductors: an exact treatment of excitonic effects. *Phys Rev B*, 44(15):8138, 1991.

[115] J. Feldmann, G. Peter, and E.O. Göbel et al. Linewidth dependence of radiative exciton lifetimes in quantum wells. *Phys Rev Lett*, 59(20):2337, 1987.

[116] H. Akiyama, S. Koshiba, and T. Someya et al. Thermalization effect on radiative decay of excitons in quantum wires. *Phys Rev Lett*, 72(6):924, 1994.

[117] Y. Takahashi, K. Muraki, and S. Fukatsu et al. In-plane transport of excitons in quantum well structures. *Solid State Commun*, 88(9):667, 1993.

[118] Y. Takahashi. Monte Carlo simulations of the spatial transport of excitons in a quantum well structure. *Phys Rev B*, 53(11):7322, 1996.

[119] R. Kumar, A. S. Vengurlekar, and A. Venu Gopal et al. Exciton formation and relaxation dynamics in quantum wires. *Phys Rev Lett*, 81(12):2578, 1998.

[120] A. Venu Gopal, R. Kumar, and A. S. Vengurlekar et al. Exciton-phonon scattering in GaAs/AlAs quantum wires. *Appl Phys Lett*, 24(17):2474, 1999.

[121] L. Rota, F. Rossi, P. Lugli, and E. Molinari. Ultrafast relaxation of photoexcited carriers in semiconductor quantum wires: a Monte Carlo approach. *Phys Rev B*, 52(7):5183, 1995.

[122] J. Singh and K. K. Bajaj. Role of interface roughness and alloy disorder in photoluminescence in QW structures. *J Appl Phys*, 57(12):5433, 1985.

[123] V. Savona and W. Langbein. Realistic heterointerface model for excitonic states in growth-interrupted GaAs quantum well. *Phys Rev B*, 74:075311, 2006.

[124] H. Castella and J. W. Wilkins. Splitting of the excitonic peak in quantum wells with interfacial roughness. *Phys Rev B*, 58(24):16186, 1998.

[125] E. C. Ferreira, J. A. K. Freire, and V. N. Freire et al. Interfacial fluctuations effects on confined excitons in single $GaAs/Al_xGa_{1-x}As$ quantum wells. *Surf Sci*, 532-535:774, 2003.

[126] J.R. Jensen, J.M. Hvam, and W. Langbein. Optical properties of InAlGaAs quantum wells: influence of segregation and band bowing. *J Appl Phys*, 86(5):2584, 1999.

[127] V. Savona. Effect of interface disorder on quantum well excitons and microcavity polaritons. *J Phys: Condens Matter*, 19:295208, 2007.

[128] O. Di Stefano, S. Savasta, and R. Girlanda. Theory of local optical spectroscopy of quantum wires with interface fluctuations. *J Appl Phys*, 91(4):2302, 2002.

[129] A. V. Filinov, C. Riva, F. Peeters, Y.E. Lozovik, and M. Bonitz. Influence of well-width fluctuations on the binding energy of excitons, charged excitons, and biexcitons in GaAs-based quantum wells. *Phys Rev B*, 70:035323, 2004.

[130] L. C. O. Dacal, R. Ferreira, G. Bastard, and J. A. Brun. Binding enery of negatively charged exciton in a semiconductor quantum well: the role of interface defects. *Phys stat sol (a)*, 190(3):799–802, 2001.

[131] A.S. Bracker, E. A. Stinaff, and D. Gammon et al. Binding energies of positive and negative trions: from quantum wells to quantum dots. *Phys Rev B*, 72:035332, 2005.

[132] A. Esser, R. Zimmermann, and E. Runge. Theory of trion spectra in semiconductor nanostructures. *Phys stat sol (b)*, 227(2):317, 2001.

[133] B. Szafran, T. Chwiej, F. Peeters, S. Bednarek, and J. Adamovski. Relative stability of negative and positive trions in model symmetric quantum wires. *Phys Rev B*, 71:235305, 2005.

[134] F. Peeters, B. Szafran, T. Chwiej, S. Bednarek, and J. Adamovski. Stability of charged exciton states in quantum wires. *Few-Body Systems*, 38:121, 2006.

[135] R. Zimmermann and E. Runge. Exciton lineshape in semiconductor quantum structures with interface roughness. *J Lumin*, 60/61(320), 1994.

[136] F. Yang, M. Wilkinson, E. J. Austin, and K. P. O'Donnel. Origin of the Stokes shift: a geometrical model of exciton spectra in 2D semiconductors. *Phys Rev Lett*, 70(3):323, 1993.

[137] M. Gurioli, A. Vinattieri, J. Martinez-Pastor, and M. Colocci. Exciton thermalization in quantum-well structures. *Phys Rev B*, 50(16):11817, 1994.

[138] A. Polimeni, A. Patanè, and M. Grassi Alessi et al. Stokes shift in quantum wells: trapping versus thermalization. *Phys Rev B*, 54(23):16389, 1996.

[139] R. Zimmermann, F. Grosse, and E. Runge. Excitons in semiconductor nanostructure with disorder. *Pure and Appl Chem*, 69(6):1179, 1997.

[140] R. Zimmermann and E. Runge. Excitons in narrow quantum wells: disorder localization and luminescence kinetics. *Phys stat sol (a)*, 164:511, 1997.

[141] H. Wang, M. Jiang, and D. G. Steel. Measurement of phonon-assisted migration of localized excitons in GaAs/AlGaAs multiple-quantum-well structures. *Phys Rev Lett*, 65(10):1255, 1990.

[142] J. Hegarty, L. Goldner, and M. D. Sturge. Localized and delocalized excitons in GaAs-AlGaAs multiple-quantum-well structures. *Phys Rev B*, 30(12):7346, 1984.

[143] D. Gershoni, E. Cohen, and A. Ron. Excitonic mobility edge in $GaAs_xP_{1-x}$. *Phys Rev Lett*, 56(20):2211, 1986.

[144] U. Jahn, M. Ramsteiner, and R. Hey et al. Effective exciton mobility edge in narrow quantum wells. *Phys Rev B*, 56(8):R4387, 1997.

[145] A. Gold and A. Ghazali. Analytical results for semiconductor quantum-well wire: plasmons, shallow impurity states, and mobility. *Phys Rev B*, 41(11):7626, 1990.

[146] H. Hillmer, A. Forchel, and C. W. Tu. An optical study of the lateral motion of the two-dimensional electron-hole pairs in GaAs/AlGaAs quantum wells. *J Phys: Condens Matter*, 5:5563, 1993.

[147] J. Motohisa and H. Sakaki. Interface roughness scattering and electron mobility in quantum wires. *Appl Phys Lett*, 60(11):1315, 1992.

[148] D. Y. Oberli, M.-A. Dupertuis, F. Reinhardt, and E. Kapon. Effect of disorder on the temperature dependence of radiative lifetimes in V-groove quantum wires. *Phys Rev B*, 59(4):2910, 1999.

[149] V. Voliotis, T. Guillet, and R. Grousson et al. Disorder effect on carrier dynamics in a single quantum wire. *Phys stat sol (a)*, 190(3):735, 2002.

[150] D. S. Citrin. Radiative lifetimes of excitons in quantum wells, localization and phase-coherence effects. *Phys Rev B*, 47(7):3832, 1993.

[151] M. Lomascolo, P. Ciccarese, R. Cingolani, R. Rinaldi, and F. K. Reinhardt. Free versus localized exciton in GaAs V-shaped quantum wires. *J Appl Phys*, 83(1):302, 1998.

[152] J. Stangl, V. Holy, and G. Bauer. Structural properties of self-organized semiconductor nanostructures. *Reviews of modern physics*, 76:725, 2004.

[153] F. Nita and A. Pimpinelli. When smoothering makes it rough: unhindered step-edge diffusion and the meandering instability on metal surface. *Phys Rev Lett*, 95:106104, 2005.

[154] M. Vladimirova, A. Pimpinelli, and A. Videcoq. A new model of morphological instabilities during epitaxial growth: from step bunching to mound formation. *J Cryst Growth*, 220:631, 2000.

[155] G. Danker, O. Pierre-Louis, K. Kassner, and C. Misbah. Peculiar effects of anisotropic diffusion on dynamics of vicinal surfaces. *Phys Rev Lett*, 93(18):185504, 2004.

[156] M. Yoon, H. N. Lee, and W. Hong et al. Dynamics of step bunching in heteroepitaxial growth on vicinal substrates. *Phys Rev Lett*, 99:055503, 2007.

[157] P. H. Fuoss, D. W. Kisker, G. B. Stephenson, and S. Brennan. In-situ X-ray studies of organometallic vapor phase epitaxy growth. *Materials Science and Engineering B*, 30:99, 1995.

[158] M. Ebert, K. A. Bell, K. Flock, and D. E. Aspnes. Investigation and control of MOVPE growth by combined spectroscopic ellipsometry and reflectance-difference spectroscopy. *Phys stat sol (a)*, 184(1):79, 2001.

[159] P. D. Dapkus, H. M. Manasevit, K. L. Hess, T. S. Low, and G. E. Stillman. Rich purity GaAs prepared from trimethylgallium and arsine. *J Cryst Growth*, 55:10, 1981.

[160] R. L. Schwoebel. Step motion on crystal surface II. *J Appl Phys*, 40(2):614, 1968.

[161] H. Asai. Anisotropic lateral growth in GaAs MOCVD layers on (001) substrates. *J Cryst Growth*, 80:425, 1987.

[162] R. L. Schwoebel. Step motion on crystal surfaces. *J Appl Phys*, 37(10):3682, 1966.

[163] C. Ratsch, J. Garcia, and R. E. Caflisch. Influence of edge diffusion on the growth mode on vicinal surfaces. *Appl Phys Lett*, 87:141901, 2005.

[164] E. A. Kondrashkina, S. A. Stepanov, and R. Opitz et al. Grazing incidence x-ray scattering from stepped interfaces in AlAs/GaAs superlattices. *Phys Rev B*, 56(16):10469, 1997.

[165] A. Pimpinelli, R. Cadoret, E. Gil-Lafon, J. Napierala, and A. Trassoudaine. Two-particle surface diffusion-reaction models of vapour phase epitaxial growth on vicinal surfaces. *J Cryst Growth*, 258:1, 2003.

[166] A. Pimpinelli and A. Videcoq. Novel mechanism for the onset of morphological instabilities during chemical vapour epitaxial growth. *Surf Sci*, 445:L23, 2000.

[167] K. Fujii, K. Kawamura, and H. Gotoh. Impurity incorporation of unintentionally doped $Al_xGa_{1-x}As$ during MOVPE. *J Cryst Growth*, 221:41, 2000.

[168] J. Van Deelen, G. J. Bauhuis, J. J. Schermer, and P. K. Larsen. Influence of growth parameters on the composition and impurity levels of intrinsically carbon doped $Al_xGa_{1-x}As$. *J Cryst Growth*, 284:28, 2005.

[169] M. Shinohara, M. Tanimoto, H. Yokoyama, and N. Inoue. Behavior and mechanism of wide terrace formation during metalorganic vaopr phase epitaxy of GaAs and related materials. *J Cryst Growth*, 145:113–119, 1994.

[170] P. Tejedor, M. L. Crespillo, and B. A. Joyce. Influence of atomic hydrogen on step stability during homoepitaxial growth on vicinal GaAs surfaces. *Appl Phys Lett*, 88:063101, 2006.

[171] T. Shitara, D. D. Vvedensky, and M. R. Wilby et al. Misorientation dependence of epitaxial growth on vicinal GaAs (001). *Phys Rev B*, 46(11):6825, 1992.

[172] K. Sears, H. H. Tan, J. Wong-Leung, and C. Jagadish. The role of arsine in the self-assembled growth of InAs/GaAs quantum dots by metal organic chemical vapor deposition. *J Appl Phys*, 99:044908, 2006.

[173] H. Reichardt, K. Leifer, and E. Pelucchi et al. Influence of long-range substrate roughness on disorder in V-groove quantum wire structures. *J Appl Phys*, page 123509, 2006.

[174] X.L. Wang, V. Voliotis, R. Grousson, and M. Ogura. Improved heterointerface quality of V-shaped AlGaAs/GaAs quantum wires characterized by atomic force microscopy and micro-photoluminescence. *J Cryst Growth*, 213:19–26, 2000.

[175] G. Biasiol and E. Kapon. Mechanisms of self-ordering of quantum nanostructures grown on nonplanar surfaces. *Phys Rev Lett*, 81(14):2962, 1998.

[176] G. Biasiol, A. Gustafsson, K. Leifer, and E. Kapon. Mechanisms of self-ordering in nonplanar epitaxy of semiconductor nanostructures. *Phys Rev B*, 65(205306), 2002.

[177] G. Biasiol. *Formation mechanisms of low-dimensional semiconductor nanostructures grown by MOCVD on nonplanar substrates*. PhD thesis, Ecole Polytechnique Fédérale de Lausanne, 1998.

[178] G. Biasiol, F. Reinhardt, A. Gustafsson, and E. Kapon. Self-limiting growth of GaAs surfaces on nonplanar substrates. *Appl Phys Lett*, 71(13):1831, 1997.

[179] A. Gustafsson, F. Reinhardt, G. Biasiol, and E. Kapon. Low-pressure organometallic chemical vapor deposition of quantum wires on V-grooved substrates. *Appl Phys Lett*, 67(25):3673, 1995.

[180] G. Biasiol, F. Reinhardt, A. Gustafsson, E. Martinet, and E. Kapon. Structure and formation mechanisms of AlGaAs V-groove vertical quantum wells grown by low pressure organometallic chemical vapor deposition. *Appl Phys Lett*, 69(18):2710, 1996.

[181] A. Dalla Volta, D. D. Vvedensky, and N. Gogneau et al. Step ordering induced by nonplanar patterning of GaAs surfaces. *Appl Phys Lett*, 88:203104, 2006.

[182] T. Otterburg, F. Lelarge, A. Rudra, and E. Kapon. Wide-range tuning of the two-dimensional confinement in V-groove quantum wires. *Appl Phys Lett*, 81(2):274, 2002.

[183] C.-S. Son, S.-I. Kim, and Y. Kim et al. Dependence of carbon incorporation on crytsallographic orientation of GaAs and AlGaAs grown by metalorganic chemical vapor deposition using CBr_4. *J Appl Phys*, 82(3):1205, 1997.

[184] M. Kondo, C. Anayama, and N. Okada et al. Crystallographic orientation dependence of impurity incorporation into III-V compound semiconductors grown by mtalorganic vapor phase epitaxy. *J Appl Phys*, 76(2):914, 1994.

[185] S. Adachi and K. Oe. Chemical etching characteristics of (001) GaAs. *J Electrochem Soc*, 130(12):2427, 1983.

[186] A. Hartmann, Y. Ducommun, K. Leifer, and E. Kapon. Structure and optical properties of semiconductor quantum nanostructures self-formed in inverted tetrahedral pyramids. *J Phys: Condens Matter*, 11:5901, 1999.

[187] G. Bernatz, S. Nau, R. Rettig, H. Jänsch, and W. Stolz. Experimental investigation of structures of interior interfaces in GaAs. *J Appl Phys*, 86(12):6752, 1999.

[188] F. Vouilloz. *Optical spectroscopy study of carriers recombination in quantum wires.* PhD thesis, EPFL, 1998.

[189] C.A. Warwick, W.Y. Jan, A. Ourmazd, and T.D. Harris. Does luminescence show semiconductor interfaces to be atomically smooth. *Appl Phys Lett*, 56(26):2666, 1990.

[190] D. Schmitz, G. Strauch, and J. Knauf et al. Large area growth of extremely uniform AlGaAs/GaAs quantum well structures for laser application by effective LP-MOVPE. *J Cryst Growth*, 93:312, 1988.

[191] N. Watanabe and Y. Mori. Ultrathin GaAs/GaAlAs layers grown by MOCVD and their structural characterization. *Surf Sci*, 174:10, 1986.

[192] H. Kawai, K. Kaneko, and N. Watanabe. Photoluminescence of AlGaAs/GaAs quantum wells grown by metalorganic chemical vapor deposition. *J Appl Phys*, 56(2):463, 1984.

[193] N. Kobayashi, T. Makimoto, Y. Yamauchi, and Y. Horikoshi. Flow-rate modulation epitaxy of GaAs and AlGaAs. *J Appl Phys*, 66(2):640, 1989.

[194] S. Glasberg, G. Finkelstein, H. Shtrikman, and I. Bar-Joseph. Comparative study of the negatively and positively charged excitons in GaAs quantum wells. *Phys Rev B*, 59(16):R10425, 1999.

[195] F.-Y. Juang, Y. Nashimoto, and P. K. Bhattacharya. Molecular beam epitaxial growth and photoluminescence of near-ideal $GaAs/Al_xGa_{1-x}As$ single quantum wells. *J Appl Phys*, 58(5):1986, 1985.

[196] K.T. Shiralagi, R.A. Puechner, K.Y. Choi, R. Droopad, and G.N. Maracas. Narrow photolouminescence linewidth of quantum wells grown by gas source molecular beam epitaxy. *J Cryst Growth*, 114:337, 1991.

[197] M. Yoshita, H. Akiyama, L. N. Pfeiffer, and K. W. West. Quantum wells with atomically smooth interfaces. *Appl Phys Lett*, 81(1):49, 2002.

[198] C. W. Tu, R. C. Miller, and B. A. Wilson et al. Properties of (Al,Ga)As / GaAs heterostructures grown by molecular beam epitaxy with growth interruption. *J Cryst Growth*, 81:159, 1987.

[199] N. Inoue, K. Ikuta, M. Shinohara, and J. Osaka. Interface structures in GaAs/Al(Ga)As quantum wells controlled by metalorganic vapor phase epitaxy and moleclar beam epitaxy. *J Cryst Growth*, 146:379, 1995.

[200] D.C. Reynolds, K.K Bajaj, and C.W. Litton et al. Determination of interfacial quality of GaAs-GaAlAs multi-quantum well structures using photoluminescence spectroscopy. *Appl Phys Lett*, 46(1):51, 1985.

[201] M. Longo, R. Magnanini, and A. Parisini et al. Controlled intrinsic carbon doping in MOVPE-grown GaAs layers by using TMGa and TBAs. *J Cryst Growth*, 248:119, 2003.

[202] H. Saito, K. Uwai, Y. Tokura, and T. Fukui. Step ordering during fractional-layer superlattice growth on GaAs (001) vicinal surfaces by metalorganic chemical vapor deposition. *Appl Phys Lett*, 63(1):72, 1993.

[203] J.-Y. Ishizaki, S. Goto, M. Kishida, T. Fukui, and H. Hasegawa. Mechanism of multiatomic step formation during metalorganic chemical vapor deposition growth of GaAs on (001) vicinal surface studied by atomic force microscopy. 33:721, 1994.

[204] M. Shinohara, H. Yokoyama, and N. Inoue. Effects of interface flatness and abruptness on optical and electrical characteristics of GaAs/AlGaAs quantum structures grown by metalorganic vapor phase epitaxy. *J Vac Sci Technol B*, 13(4):1773, 1995.

[205] K. Ikuta, M. Shinohara, and N. Inoue. Interface structures in AlGaAs/GaAs quantum wells grown by metalorganic chemical vapor deposition (MOCVD). *Jpn J Appl Phys*, 34:L220, 1995.

[206] L. Jiang, A. Mirabedini, and L.J. Mawst et al. Effect of interface roughness on performance of AlGaAs/InGaAs/GaAs resonant tunneling diodes. *J Cryst Growth*, 195:617, 1998.

[207] M. Tanaka and H. Sakaki. Interface roughness of GaAs-AlAs quantum wells grown by molecular-beam epitaxy: Misorientation effects. *J Appl Phys*, 64(9):4503, 1988.

[208] Y. Tokura, T. Saku, and Y. Horikoshi. Electron scattering by steps in a vicinal heterointerface. *Phys Rev B*, 53(16):R10 528, 1996.

[209] E. Pelucchi, N. Moret, and B. Dwir et al. Sub-meV photoluminescence linewidth and $> 10^6 cm^2/Vs$ electron mobility in AlGaAs/GaAs quantum wells grown by metalorganic vapour phase epitaxy on slightly misoriented substrates. *J Appl Phys*, 99:093515, 2006.

[210] F. Martelli, A. Polimeni, and A. Patanè et al. Exciton localization by potential fluctuations at the interface of InGaAs/GaAs quantum wells. *Phys Rev B*, 53(11):7421, 1996.

[211] J. B. B De Oliveira. Magneto-optical studies of the correlation between interface microroughness parameters and the photoluminescence lineshape in $GaAs/Ga_{0.7}As_{0.3}As$ quantum wells. *Phys Rev B*, 60(3):1519, 1999.

[212] P. Borri, M. Gurioli, and M. Colocci et al. Photoinduced structures in the exciton luminescence spectrum of InGaAs/GaAs quantum well heterostructures. *J Appl Phys*, 80(5):3011, 1996.

[213] V. Srinivas, Y. J. Chen, and E. C. Wood. Bound exciton induced photoluminescence linewidth broadening in GaAs quantum wells. *Solid State Commun*, 89(7):611, 1994.

[214] F. J. Teran, L. Eaves, and L. Mansouri et al. Trion formation in narrow GaAs quantum well structures. *Phys Rev B*, 71:161309(R), 2005.

[215] N. N. Sibeldin, M. L. Shorikov, and V. A. Tsvetkov. Formation of charged excitonic complexes in shallow quantum wells of undoped GaAs/AlGaAs structures under below-barrier and above-barrier photoexcitation. *Nanotechnology*, 12:591, 2001.

[216] M. Bayer. *Exciton complexes in self-assembled In(Ga)As/GaAs quantum dots.* Springer-Verlag, Berlin, 2003.

[217] A Esser, E Runge, and R Zimmermann. Photoluminescence and radiative lifetime of trions in GaAs quantum wells. *Phys Rev B*, 62(12):8232, 2000.

[218] T. Nakanisi. The growth and characterization of high quality MOVPE GaAs and AlGaAs. *J Cryst Growth*, 68:282, 1984.

[219] A. Rudra, E. Pelucchi, and D. Y. Oberli et al. Properties of GaAs/AlGaAs quantum wells grown by MOVPE using vicinal GaAs substrates. *Journal of Crystal Growth*, 272:615, 2004.

[220] G. Kocherscheidt, W. Langbein, and V. Savona. Level-statistics in the resonant Rayleigh scattering dynamics of monolayer-split exciton. *Phys stat sol (b)*, 238(3):486, 2003.

[221] A. Videcoq, A. Pimpinelli, and M. Vladimirova. Kinetic Monte Carlo study of the terrace width distribution during step bunching in homoepitaxial growth. *Appl Surf Sci*, 177:213, 2001.

[222] G. Bernatz, S. Nau, R. Rettig, and W. Stolz. Effect of MOVPE growth interruptions on the Gallium Arsenide interior interface morphology. *J Electron Mater*, 29(1):129, 2000.

[223] S. Wüthrich . Influence de la morphologie des interfaces GaAs / AlGaAs sur les propriétés optiques de puits quantiques crus par épitaxie OMCVD, 2006. Master Thesis EPFL.

[224] M. Shinohara and N. Inoue. Behavior and mechanism of step bunching during metalorganic vapor phase epitaxy of GaAs. *Appl Phys Lett*, 66(15):1936, 1995.

[225] K. Hata, H. Shigekawa, T. Okano, T. Ueda, and M. Akiyama. Modeling step bunching formed on vicinal GaAs (001) annealed in AsH_3 and hydrogen ambient. *Phys Rev B*, 55(11):7039, 1997.

[226] P. A. Lee and T. V. Ramakrishnan. Disordered electronic systems. *Rev Mod Phys*, 57(2):287, 1985.

[227] C. Constantin. *Combined electron and photon confinement in quantum wires incorporated in multidimensional microcavities*. PhD thesis, EPFL, 2000.

[228] C. Constantin, E. Martinet, A. Rudra, and E. Kapon. Observation of combined electron and photon confinement in planar microcavities incorporating quantum wires. *Phys Rev B*, 59(12):R7809, 1999.

[229] S. H. Huang, Z. Chen, and F. Z. Wang et al. Carrier transfer and magneto-transport in single modulation-doped V-grooved quantum wire modified by ion implantation. *J Lumin*, 119:198, 2006.

[230] N.I. Cade, R. Roshan, and M. Hauert et al. Carrier relaxation in GaAs V-groove quantum wires and the effects of localization. *Phys Rev B*, 70:195308, 2004.

[231] A.C. Maciel, C. Kiener, and L. Rota et al. Hot carrier relaxation in GaAs V-groove quantum wires. *Appl Phys Lett*, 66(22):3039, 1995.

[232] N.I. Cade, R. Roshan, and J. F. Ryan et al. Optical measurements of carrier relaxation and transport in single GaAs V-groove quantum wire structures. *Physica B*, 314:413, 2002.

[233] S. Palmgren, H. Weman, and A: Schoenberg et al. Polarization-resolved optical absorption in single V-groove quantum wires. *Appl Phys Lett*, 89:191111, 2006.

[234] A. Feltrin. *Near-field microscopy and theoretical modeling of disordered semiconductor quantum wires*. PhD thesis, EPFL, 2004.

[235] T. Otterburg. *Neutral and charged excitons in $Al_xGa_{1-x}As/GaAs$ V-groove quantum wires*. PhD thesis, EPFL, 2004.

[236] R. Rinaldi, P. V. Giugno, and R. Cingolani et al. Thermal ionization of excitons in V-shaped quantum wires. *Phys Rev B*, 53(20):13710, 1996.

[237] X. L. Wang, M. Ogura, T. Guillet, V. Voliotis, and R. Grousson. Strong Fermi-edge singularity in ultra-high-quality AlGaAs/GaAs quantum wires. *Physica E*, 32:329, 2006.

[238] D. Kaufman. *Electron transport in V-groove quantum wires*. PhD thesis, EPFL, 2000.

[239] A. Schwarz, A. Kaluza, and Th. Schäpers et al. Electron transport in modulation-doped GaAs V-groove quantum wires. *Physica E*, 7:760, 2000.

[240] C.-K. Hahn, T. Sugaya, K.-Y. Jang, X. L. Wang, and M. Ogura. Electron transport properties in a GaAs/AlGaAs quantum wire grown on V-grooved GaAs substrate by metalorganic vapor phase epitaxy. *Jpn J Appl Phys*, 42:2399, 2003.

[241] F. Reinhardt, B. Dwir, G. Biasiol, and E. Kapon. Step ordering during OMCVD growth on non-planar substrates. *J Cryst Growth*, 170:689, 1997.

[242] M. Walther, E. Kapon, J. Christen, D. M. Hwang, and R. Bhat. Carrier capture and quantum confinement in GaAs/AlGaAs quantum wire lasers grown on V-grooved substrates. *Appl Phys Lett*, 60(5):521, 1992.

[243] E. Martinet, A. Gustafsson, and G. Biasiol et al. Carrier quantum confinement in self-ordered $Al_xGa_{1-x}As$ V-groove quantum wells. *Phys Rev B*, 56(12):R7096, 1997.

[244] K. Bando, I. Akai, T. Karasawa, K. Maehashi, and H. Nakashima. Dynamical processes on high density indirect and direct excitons in $Al_xGa_{1-x}As/AlAs$ quantum wires. *J Lumin*, 94-95:389, 2001.

[245] U. Bockelmann. Polarization-dependent optical-wave fields in grating structures. *Europhys Lett*, 16(6):601, 1991.

[246] T. Guillet, V. Voliotis, and R. Grousson et al. Exchange-induced splitting of radiative exciton levels in a single quantum wire. *Physica E*, 9:686, 2001.

[247] F. Lelarge, T. Otterburg, D. Y. Oberli, A. Rudra, and E. Kapon. Origin of disorder in self-ordered GaAs / AlGaAs quantum wires grown by OMVPE on V-grooved substrate. *J Cryst Growth*, 221:551, 2000.

[248] R. Nötzel, J. Temmyo, and T. Tamamura. Tunability of one-dimensional self-faceting on GaAs (311)A surfaces by metalorganic vapor-phase epitaxy. *Appl Phys Lett*, 64(26):3557, 1994.

[249] D. Gammon, E. S. Snow, B.V. Shanabrook, D.S. Katzer, and D. Park. Fine structure splitting in the optical spectra of single GaAs quantum dots. *Phys Rev Lett*, 76(16):3005, 1996.

[250] X.L. Wang and M. Ogura. Flow rate modulation epitaxy of high-quality V-shaped AlGaAs/GaAs quantum wires using tertiarybutylarsine as the arsenic source. *J Cryst Growth*, 221:556, 2000.

[251] X.-Q. Liu, X. L. Wang, and M. Ogura. Reduction of nonradiative recombintation centers in V-grooved AlGaAs/GaAs quantum wires grown using tertiarybutylarsine. *Appl Phys Lett*, 79(11):1622, 2001.

[252] S. A. Lourenço, M. A. T. Da Silva, and I. F. L. Dias et al. Correlation between luminescence properties of $Al_xGa_{1-x}As/GaAs$ single quantum wells and barrier composition fluctuation. *J Appl Phys*, 101:113536, 2007.

[253] M.-A. Dupertuis, D.Y. Oberli, and E. Kapon. Computing excitons in V-shaped quantum wires including band-structure and dielectric effects : binding energies and polarization anisotropy of the bright A_1, B_1, A_2 excitons . *Technical Proceedings of the Second ICCN 2002*, Cambridge MA, USA(4):227, 2002.

[254] F. Vouilloz, D. Y. Oberli, and M.-A. Dupertuis et al. Effect of lateral confinement on valence-band mixing and polarization anisotropy in quantum wires. *Phys Rev B*, 57(19):12378, 1998.

[255] K. Leifer, E. Pelucchi, and S. Watanabe et al. Narrow ($\sim$4 meV) inhomogeneous broadening and its correlation with confinement potential of pyramidal quantum dot arrays. *Appl Phys Lett*, 91:081106, 2007.

[256] V. Emiliani, T. Guenther, and C. Lienau. Ultrafast spectroscopy of quasi-one-dimensional transport in a single quantum wire. *Phys Rev B*, 61(16):R10583, 2000.

[257] Y. Tang, D. H. Rich, A. M. Moy, and K. Y. Cheng. An optical method for studying carrier diffusion in strained $(InP)_2/(GaP)_2$ quantum wires. *Appl Phys Lett*, 72(1):55, 1998.

[258] Y. Nagamune, M. Watanabe, and M. Seyama et al. Time-resolved carrier drag effect in quantum wells and wires. *Physica E*, 2:843, 1998.

[259] Y. Nagamune, H. Watabe, F. Sogawa, and Y. Arakawa. One-dimensional exciton diffusion in GaAs quantum wires. *Appl Phys Lett*, 67(11):1535, 1995.

[260] M. Merano, S. Sonderegger, and A. Crottini et al. Time-resolved cathodoluminescence of InGaAs/AlGaAs tetrahedral pyramidal quantum structures. 84:343, 2006.

[261] H. Hillmer, A. Forchel, and S. Hansmann et al. Optical investigations on the mobility of two-dimensional excitons in $GaAs/Ga_{1-x}Al_xAs$ quantum wells. *Phys Rev B*, 39(15):10901, 1989.

[262] H. Akiyama, T. Matsusue, and H. Sakaki. Carrier scattering and excitonic effects on electron-hole-pair diffusion in nondoped and p-type-modulation-doped $GaAs/Al_xGa_{1-x}As$ quantum well structures. *Phys Rev B*, 49(20):14523, 1994.

[263] A. Richter, M. Süptitz, and C. Lienau et al. Time-resolved near-field optics: exciton transport in semiconductor nanostructures. *Journal of Microscopy*, 194(2/3):393, 1999.

[264] H. Hillmer, A. Forchel, T. Kuhn, G. Mahler, and H. P. Meier. Optical studies of vertical ambipolar transport and interface recombination velocities in $GaAs/Al_{0.5}Ga_{0.5}As$ double-quantum-well heterostructures. *Phys Rev B*, 43(17):13992, 1991.

[265] D. Gershoni, M. Katz, and W. Wegscheider et al. Radiative lifetimes of excitons in quantum wires. *Phys Rev B*, 50(12):8930, 1994.

[266] R. Lécuiller, J. Berréhar, and J. D. Ganière et al. Fluorescence yield and lifetime of isolated polydiacetylene chains: Evidence for a one-dimensional exciton band in conjugated polymer. *Phys Rev B*, 66:125205, 2002.

[267] M. Colocci, M. Gurioli, and A. Vinattieri et al. Temperature dependence of exciton lifetimes in GaAs/AlGaAs quantum well structures. *Europhys Lett*, 12(5):417, 1990.

[268] K. Siantidis, V.M. Axt, J. Wühr, and T. Kuhn. Theory of exciton formation and relaxation in quantum wires. *Phys stat sol (a)*, 190(3):743, 2002.

[269] T. C. Damen, J. Shah, and D. Y. Oberli et al. Dynamics of exciton formation and relaxation in GaAs quantum wells. *Phys Rev B*, 42(12):7434, 1990.

[270] A. Feltrin, J. L. Staehli, and B. Deveaud. Modeling the photoluminescence lifetime in realistic quantum wires. *Phys Rev B*, 69:233309, 2004.

[271] T. Guillet. *Nature du désordre et propriétés optiques des excitons dans les fils quantiques semiconducteurs: de la boîte au fil.* PhD thesis, Université Paris VI, 2002.

[272] F. Vouilloz, D. Y. Oberli, and S. Wiesendanger et al. Density dependence of localized excitonic recombination in quantum wires. *Phys stat sol (a)*, 164:259, 1997.

[273] F. Intonti, V. Emiliani, and C. Lienau et al. Near-field optical spectroscopy of localized and delocalized excitons in a single GaAs quantum wire. *Phys Rev B*, 63:075313, 2001.

[274] T. Takagahara. Localization and homogeneous dephasing relaxation of quasi-two dimensional excitons in quantum-well heterostructures. *Phys Rev B*, 32(19):7013, 1985.

[275] H. Hillmer, A. Forchel, R. Sauer, and C. W. Tu. Interface-roughness-controlled exciton mobilities in $GaAs/Al_{0.37}Ga_{0.63}As$ quantum wells. *Phys Rev B*, 42(5):3220, 1990.

[276] M. Tsetseri and G. P. Triberis. Mobility in V-shaped quantum wires due to interface roughness and alloy scattering. *Phys Rev B*, 69:075313, 2004.

[277] J. S. Thakur and D. Neilson. Effect of electron correlations and disorder on mobility and localization in quasi-one-dimensional wires. *Phys Rev B*, 56(12):7485, 1997.

[278] H. Kalt, H. Zhao, and B. Dal Don et al. Quasi-ballistic transport of excitons in quantum wells. *J Lumin*, 112:136, 2005.

[279] H. Tang. Influence of interface roughness on excitonic diffusion in semiconductor QW. *J Phys: Condens Matter*, 15:8137, 2003.

[280] A. L.-S. Chua, E. Pelucchi, and A. Rudra et al. Theory and experiment of step bunching on misoriented GaAs (001) during MOVPE. *Appl Phys Lett*, 92(1):013117, 2008.

[281] M. Erdmann, C. Ropers, and M. Wenderoth et al. Diamagnetic shift of disorder-localized excitons in narrow GaAs/AlGaAs quantum wells. *Phys Rev B*, 74:125412, 2006.

[282] D. Sanvitto, R. A. Hogg, and A. J. Shields et al. Rapid radiative decay of charged excitons. *Phys Rev B*, 62(20):R13294, 2000.

[283] J. A. Kash, E. E. Mendez, and H. Morkoç. Electric field induced decrease of photoluminescence lifetime in GaAs quantum wells. *Appl Phys Lett*, 46(2):173, 1984.

[284] C. P. Kuo, S. K. Vong, R. M. Cohen, and G. B. Stringfellow. Effect of mismatch strain on band gap in III-V semiconductors. *J Appl Phys*, 57(12):5425, 1985.

Publications

Regular papers

Properties of GaAs/AlGaAs quantum wells grown by MOVPE using vicinal GaAs substrates, A. Rudra, E. Pelucchi, D. Y. Oberli, <u>N. Moret</u>, B. Dwir and E. Kapon,
J. Cryst. Growth. **272**, 615 (2004).

Enhancement of the binding energy of charged excitons in disordered quantum wires,
T. Otterburg, D. Y. Oberli, M.-A. Dupertuis, <u>N. Moret</u>, E. Pelucchi, B. Dwir, K. Leifer and E. Kapon,
Phys. Rev. B. **71**, 033301 (2005).

Sub-meV photoluminescence linewidth and $> 10^6 cm^2/Vs$ electron mobility in AlGaAs/GaAs quantum wells grown by metalorganic vapour phase epitaxy on slightly misoriented substrates, E. Pelucchi, <u>N. Moret</u>, B. Dwir, D. Y. Oberli, A. Rudra, N. Gogneau A. Kumar,
E. Kapon, E. Levy, A. Palevski,
J. Appl. Phys. **99**, 093515 (2006).

Correlation between optical properties and interface morphology of GaAs/AlGaAs quantum wells, <u>N. Moret</u>, D. Y. Oberli, E. Pelucchi, N. Gogneau, A. Rudra and E. Kapon,
Appl. Phys. Lett. **88**, 141917 (2006).

Conferences and seminars

Excitons and trions localized in quantum wires, <u>N. Moret</u>, D. Y. Oberli, T. Otterburg, A. Rudra, A. Malko, E. Pelucchi, M.-A. Dupertuis, B. Dwir, E. Kapon,
Summer School on Semiconductor Quantum Dots, Ascona, Switzerland, September 2004 (poster presentation).

Correlation of interfaces morphologies and optical properties of GaAs/AlGaAs quantum wells grown by MOVPE on vicinal substrates, <u>N. Moret</u>, D. Y. Oberli, E. Pelucchi, N. Gogneau, A. Rudra, E. Kapon,
28th International Conference on the Physics of Semiconductor, Vienna, Austria, August 2006 (poster presentation).

Tuning of the exciton potential landscape in GaAs/AlGaAs quantum wells and correlation between optical properties and interface morphology, <u>N. Moret</u>, D. Y. Oberli, E. Pelucchi, N. Gogneau, A. Rudra, E. Kapon,
Russian-Swiss Seminar on Exciton and Exciton Condensates in Confined Semiconductor Systems, Moscow, Russia, September 2006 (poster presentation).

Thermally activated electron-hole pair diffusion in V-groove quantum wires, <u>N. Moret</u>, D. Y. Oberli, B. Dwir, A. Rudra, E. Kapon,
Second International Conference on 1D Nanomaterials, Malmö, Sweden, October 2007 (poster presentation).

Remerciements

Mon dur labeur au laboratoire de physique des nanostructures n'aurait sans doute pas été aussi fructueux sans le concours des nombreuses personnes qui m'ont entourées pendant ces quatres années.

Tout d'abord, je tiens à remercier le Prof. Eli Kapon qui a guidé avec une grande compétence mon travail de thèse, tout en me laissant beaucoup de liberté dans mes recherches. Je lui suis particulièrement reconnaissant d'avoir développé les infrastructures exceptionnelles qui sont à disposition de notre groupe, et dont j'ai pu pleinement profiter.

Je remercie les professeurs Akiyama, Savona et Wegscheider pour avoir accepté de faire partie du jury, et pour avoir lu et commenté de façon enrichissante mon travail, ainsi que le Prof. Schaller pour avoir présidé ce comité lors de l'examen.

J'ai beaucoup appris des discussions avec Daniel Oberli, qui m'a fait bénéficier de son expertise en physique des semiconducteurs. De plus, j'ai beaucoup aimé sa rigueur et son soucis de précision, notamment lors de la rédaction d'articles ou de sa relecture de cette thèse.

Aucun travail experimental ne serait possible dans notre groupe si Alok Rudra n'apportait pas les plus grands soins à notre réacteur de MOVPE. Il a su surmonter tous les caprices de la croissance épitaxiale pour me procurer des échantillons d'excellente qualité. Emanuele Pelucchi et Noëlle Gogneau m'ont également été très précieux pour la croissance et la caractérisation par AFM, ainsi que pour la compréhension des mécanismes de croissance.

Benjamin Dwir est quelqu'un d'indispensable pour le groupe, et pour moi en particulier. Je le remercie non seulement de s'être chargé de la lithographie e-beam, mais également pour ses conseils techniques et dépannages d'appareils de toute sorte. Au même titre, Nicolas Leiser et les frères Trolliet ont toute ma gratitude pour leur entretien irréprochable de nos salles blanches.

J'aurais aimé travailler plus longtemps avec Marc-André Dupertuis et Fredrik Karlsson. Leurs modélisations, et les explications qui allaient avec, ont apporté un peu de magie dans mon univers experimental.

Merci à Sébastien Wüthrich pour avoir développé notre étude sur les puits quantiques lors de son travail de diplôme. Merci à Sanna, Hakon et Kirill pour avoir partagé leur science des V-grooves. Merci aussi à Tim Otterburg pour m'avoir initié, lors de mon travail de diplôme, puis en début de thèse, à ce domaine et au travail dans ce groupe; pendant ces quatre ans j'ai souvent repensé à une certaine discussion de l'automne 2003 sur la terrasse de l'Arcadie !

Grâce aux compétences et à la gentillesse des secrétaires de notre groupe, les problèmes administratifs n'en furent jamais: merci à Denise et Gabriella, ainsi qu'à Suada et Anita, pour leur dévouement et leur organisation sans faille.

Merci enfin à tous les autres collaborateurs, post-docs, doctorants et étudiants avec qui j'ai partagé le quotidien pendant tout ou partie de ces quatres dernières années: Alessandro, Alexandru, Alexei, Andrei, Anton, Arun, Avijit, Benjamin, Dany, Dmitri, Eckard, Elodie, Fabienne, Gilles, Guillaume, Helge, Julien, Lars, Lukas, Marcin, Marco, Martin(s), Pascal, Qing, Romain, Shinichi, Valentina, Vlad et Zhen.

Sascha Dalessi mérite des remerciements spéciaux, puisque j'ai partagé avec lui notre bureau pendant plus de trois ans. J'aime à me rappeler de nos mémorable discussions de mécanique générale et de thermodynamique, mais surtout de pédagogie. Plus que cela, il m'a encouragé tout au long de ces quatres années, et a toujours su me montrer la lumière (de Sat) quand j'étais égaré dans le noir (du labo).

Pour terminer, j'espère ne pas avoir trop négligé mes amis et ma famille, qui m'ont permis de varier mes intérêts et mes occupations. En particulier, je remercie du fond du coeur mes parents et mon frère pour leur soutien et leur confiance, et ma femme Kozue sans qui cette thèse n'aurait jamais été achevée.

MORET Nicolas

Born 7th February 1979, in Aigle, Switzerland
Swiss citizen
Married

E-mail: nicolas.moret@a3.epfl.ch

Education	PHYSICS ENGINEER	*Oct 1997 - Apr 2002*
	Swiss Federal Institute of Technology, Lausanne (EPFL) Diploma at the Laboratory of Physics of Nanostructures (Prof E. Kapon), on the control of the carrier density in V-groove quantum wires.	
	SCIENTIFIC HIGH-SCHOOL DIPLOMA	*Aug 1994 - Jun 1997*
	CESSEV (Gymnase de Burier), La Tour-de-Peilz	
Professional	SWISS FEDERAL INSTITUTE OF TECHNOLOGY (Lausanne, Switzerland)	*Oct 2003 – Jun 2008*
	Research assistant at the Institute of Quantum Photonics and Electronics, Laboratory of Physics of Nanostructures (Prof E. Kapon) Teaching assistant for undergraduate courses (General Physics)	
	MITSUBISHI ELECTRIC CO. (Amagasaki, Japan)	*Jul 2002 - Jun 2003*
	Intern process engineer in the MEMS processing group. Development of silicon master for polymer molding. Development of micro-fluidics devices for biological assays	
	ANDROMIS S.A. (Geneva, Switzerland)	*Jul 2000 - Aug 2000*
	Intern in a startup manufacturing micro-endoscopes. Design and implementation of a testing ground for microlenses.	
	PAUL SCHERRER INSTITUTE (Villigen, Switzerland)	*Jul 1999 - Aug 1999*
	Intern at the Research Centre in Plasma Physics. Mechanical tests on irradiated steels for nuclear fusion technology.	
Languages	French mother tongue English fluent German good knowledge Japanese simple conversation	
Interests	Soccer (competition), skiing, hiking	